

Magnetic Resonance Imaging of Muscle Structure and Function

DISSERTATION

zur Erlangung des akademischen Grades Doktoringenieur (Dr.-Ing.)

eingereicht von

Dipl.-Ing. (FH) Patrick Hiepe

geboren am 27. September 1984 in Gera, Thüringen

vorgelegt der Fakultät für Informatik und Automatisierung
der Technischen Universität Ilmenau

urn:nbn:de:gbv:ilm1-2017000387

Tag der Einreichung: 3. März 2017

Tag der wissenschaftlichen Aussprache: 5. Oktober 2017

1. Gutachter: Prof. Dr.-Ing. habil. Jens Haueisen

2. Gutachter: Prof. Dr. rer. nat. med. habil. Jürgen R. Reichenbach

3. Gutachter: Prof. Dr. med. Dr. rer. nat. Fritz Schick

Zusammenfassung

Ziel dieser Arbeit ist die Implementierung und kombinierte Anwendung verschiedener MRT-Techniken zur Untersuchung der Struktur und Funktion der humanen Skelettmuskulatur. Insbesondere steht deren Applikation an der Rückenmuskulatur im Vordergrund, um auf Basis dieser Untersuchungen einen Beitrag zur Ursachenforschung des unspezifischen - meist chronifizierten - Rückenschmerzes zu leisten. Vor diesem Hintergrund wurden in der vorliegenden Dissertation dezidierte MR-Pulssequenzen und Bildrekonstruktionsverfahren entwickelt, welche unter Verwendung der diffusionsgewichteten MR-Bildgebung (*diffusion-weighted imaging*, DWI) die 3D-Rekonstruktion der Muskelfaserarchitektur sowie die Quantifizierung der muskulären Vaskularität ermöglichen. Die Erfassung der Faserarchitektur basiert auf der Diffusionstensorbildgebung (*diffusion tensor imaging*, DTI) - einer Weiterentwicklung der DWI - und wurde am Tiermodell anhand sequentiell durchgeführter *in vivo* und *post mortem* Messungen validiert. Anschließend wurde diese Methode in einer Pilotstudie genutzt, um degenerative Veränderungen bei Patienten nach Wirbelsäulenoperation zu erfassen. Im zweiten Schritt dieser Arbeit, wurde ein Messprotokoll zur funktionellen MR-Untersuchung implementiert, welches Messungen vor, während und nach willkürlicher Muskelkontraktion beinhaltet. Dieses Protokoll sieht weiterhin die Applikation einer neuartigen perfusions sensitiven DWI-Sequenz sowie optimierten Sequenzen zur quantitativen T₂-gewichteten MR-Bildgebung und ort aufgelösten ³¹P-MR-Spektroskopie vor, wobei die beiden letztgenannten Techniken es erlauben, komplexe funktionelle Vorgänge, wie beispielsweise die des Energiemetabolismus, unter Einfluss einer Belastungssituation zu untersuchen. Diese funktionellen MR-Messprinzipien werden in der Regel unter dem Begriff *muscle functional MRI* (mfMRI) subsumiert und ermöglichen die multi-parametrische Erfassung unterschiedlicher funktioneller und struktureller Eigenschaften der Muskelphysiologie. Dies wird in der vorliegenden Arbeit anhand einer gerontologischen Studie demonstriert, wobei die hierbei gewonnenen Ergebnisse Einblick in zahlreiche altersassoziierte Aspekte der Rückenphysiologie geben. Zusammenfassend werden in dieser Dissertation verschiedene Ansätze der MR-Bildgebung und MR-Spektroskopie vorgestellt, die einerseits für grundlagenwissenschaftliche Fragestellungen zum unspezifischen Rückenschmerz, andererseits aber auch in der klinischen Routine zur Untersuchung degenerativer Veränderungen der Skelettmuskulatur herangezogen werden können.

Abstract

The aim of this work is the implementation and combined application of different MRI-based methods, which facilitate the comprehensive assessment of the skeletal muscle structure and function. Especially, the application of these MRI techniques to human back muscles has been put into focus, which may provide deeper insights into the origin of non-specific - and in most cases chronic - back pain. To this end, dedicated MRI sequences and quantitative image reconstruction approaches were developed in this work, which are based on *diffusion-weighted imaging* (DWI) and enable the 3D reconstruction of the muscle fiber architecture as well as the assessment of a surrogate measure of the vascular capacity. The MRI-based reconstruction of the fiber architecture relies on *diffusion tensor imaging* (DTI) - an extension of DWI - and was validated by successive *in vivo* and *post mortem* measurements. Afterwards, this method was employed in a pre-clinical pilot study in order to assess surgery-related degenerative changes of the back muscles in patients after spinal surgery. In the second step of this work, functional measurements of the human skeletal muscles, which means quantitative measurements prior to, during and after muscular loading, were performed by using a novel perfusion-sensitive DWI sequence as well as optimized sequence protocols of quantitative T_2 -weighted MRI and spatially resolved ^{31}P -MR spectroscopy. The latter two methods allow the quantification of complex physiological processes, such as of the high-energy metabolism, during the exercise of skeletal muscles, and are often subsumed under the term *muscle functional MRI* (mfMRI). Combined application of these mfMRI techniques provides multi-parametric evaluation of several structural and functional determinants and, thus, allows comprehensive characterization of the muscle physiology. In order to demonstrate the capabilities of the proposed multi-parametric mfMRI approach, a gerontological study is performed in this work, while the obtained results indicate several age-related aspects of the human back muscle physiology. Overall, this thesis introduces MR imaging and MR spectroscopy techniques, which may, on the one hand, contribute to research of low back pain and, on the other hand, serve as basis of clinical investigations in order to investigate degenerative processes of skeletal muscles.

Acronyms and abbreviations

ADC	apparent diffusion coefficient
ATP	adenosine triphosphate
CSI	chemical shift imaging
CK	creatine kinase
CP	planar index
FA	fractional anisotropy
FE	finite element
FWHM	full width at half maximum
FID	free induction decay
FOV	field of view
FT	Fourier transform
DW	diffusion-weighted
DWI	diffusion-weighted imaging
DTI	diffusion tensor imaging
IVIM	intravoxel incoherent motion
mfMRI	muscle functional MRI
MHC	myosin heavy chains
MRI	magnetic resonance imaging
MRS	magnetic resonance spectroscopy
NMR	nuclear magnetic resonance
PCr	phosphorylcreatine
PE	phase encoding
PGSE	pulsed-gradient spin-echo
PSF	point spread function
rf	radio frequency
SE	spin echo
STE	stimulated echo
STEAM	stimulated echo acquisition mode
S-EMG	surface electromyography
TE	echo time
T_1	spin-lattice (or longitudinal) relaxation time constant
T_2	spin-spin (or transverse) relaxation time constant

Contents

1	Introduction	1
2	Fundamentals	5
2.1	Skeletal muscle	5
2.1.1	Muscle types	5
2.1.2	Muscle architecture	5
2.1.3	Muscle contraction	6
2.1.4	Muscular energy supply	7
2.1.5	Motor unit and fiber types	8
2.2	Magnetic resonance imaging	9
2.2.1	Nuclear magnetic resonance	9
2.2.2	Spatial encoding of the MR signal	12
2.2.3	k -space and image reconstruction	15
2.3	Diffusion-weighted imaging	16
2.3.1	Brownian motion and diffusion	16
2.3.2	Bloch-Torrey equation	18
2.3.3	Concept of DWI	19
3	Diffusion-weighted MRI of muscle structure	23
3.1	Introduction	23
3.1.1	Diffusion tensor imaging	24
3.1.2	DTI of skeletal muscles	26
3.2	Concept of turbo-STEAM DTI	29
3.2.1	Diffusion-weighted stimulated echo preparation	29
3.2.2	Single-shot FLASH readout of the diffusion-encoded STEAM signal	32
3.3	DTI and Tractography of a rabbit shank	33
3.3.1	Materials and Methods	33
3.3.2	Results	37
3.3.3	Discussion	44
3.3.4	Histological validation	47
3.4	Application to human lower back muscles	50
3.4.1	Materials and Methods	51
3.4.2	Results	52

3.4.3	Discussion	55
3.5	Future directions	57
4	Quantitative MRI and MRS of muscle function	61
4.1	Introduction	61
4.2	Quantification of high-energy metabolism using ³¹ P-MRS	64
4.2.1	MR spectrum of phosphorous-containing compounds	64
4.2.2	Muscular bioenergetics observed by ³¹ P-MRS	65
4.2.3	Non-localized ³¹ P-MR spectroscopy	66
4.2.4	³¹ P-chemical shift imaging	68
4.3	Quantitation of muscle activity based on T ₂ - and diffusion-weighted MRI	70
4.3.1	Origin of exercise-induced T ₂ -changes	70
4.3.2	Relationship between T ₂ and diffusion or perfusion changes	71
4.3.3	Quantitative T ₂ -weighted MRI	73
4.3.4	Intra-voxel incoherent motion model in DWI	77
4.4	Interrelations of ³¹ P-CSI, T ₂ - and diffusion-weighted MRI in low back muscles	89
4.4.1	Materials and Methods	90
4.4.2	Results	97
4.4.3	Discussion	103
4.5	Age-related changes in muscle function and structure of low back muscles	107
4.5.1	Materials and Methods	107
4.5.2	Results	111
4.5.3	Discussion	117
4.6	Limitations and open questions	123
5	Conclusion and Outlook	125
	Bibliography	145
	List of figures	148
	List of tables	149
	Curriculum Vitae	151
	Prices	151
	Original Papers	152
	Conference Proceedings	152
	Book Chapters	154
	Ehrenwörtliche Erklärung	155
	Danksagung	157

1 Introduction

Skeletal muscles are essential for many mechanical functions and physiological aspects of the human body, including force generation, actuated movement, glucose uptake and storage, thermogenesis and total body water balance [DAMON et al., 2013]. They are specialized to convert chemical energy into mechanical work: during intense exercise, blood perfusion and metabolic demand can increase 10- to 100-fold or more, respectively, compared to resting state conditions. Consequently, proper functioning of skeletal muscles has an important impact on human health and well-being, and any impairment for that matter may result in alterations of muscle strength and endurance, changes in the associated lipid- and carbohydrate metabolism or even in immobility [CRANE et al., 2010; CSAPO et al., 2014].

Skeletal muscles together with bones and joints form the musculoskeletal system of the human body. The muscle architecture, which is characterized by the macroscopic arrangement of muscle fibers relative to the axis of force generation (i.e., the pennation angle), represents the main determinant of a muscle's mechanical function [DAMON et al., 2002a]. Hence, quantitative description of structural properties, such as of the fiber pennation angle, the fiber length, or the muscle volume, may help to better understand normal muscular function as well as clinical manifestations [LIEBER and FRIDEN, 2000]. Given the relationship between muscle architecture and mechanical output that originates from the underlying complex muscle recruitment patterns, it appears both obvious and important to comprehensively characterize muscle structure and function. Applying non-invasive modalities is promising in this endeavor to obtain deeper insight of the relationship of both quantities in healthy and diseased states.

Architectural and functional parameters are traditionally assessed by means of 2D ultrasound imaging [FORNAGE, 2000] and surface electromyography (S-EMG) [HAGBERG, 1981], respectively. However, these techniques are not specifically suited to study multiple muscles or muscle groups because they are limited in their ability to record deeper lying or larger extended anatomical structures. Alternative, powerful modalities, which elegantly enable non-invasive investigations of muscle structure and function, are magnetic resonance imaging (MRI) and magnetic resonance spectroscopy (MRS). Both techniques date back to 1946 in history when pioneering research discovered the nuclear magnetic resonance (NMR) phenomenon which arises from the interaction of magnetic moments of atomic nuclei with static magnetic fields and tuned radio frequency excitation [BLOCH, 1946; PURCELL et al., 1946]. The spatially resolved mapping of NMR signals is made possible by applying additional magnetic field gradients that modulate the resonance frequency of atomic nuclei as a function of spatial position [LAUTERBUR, 1973; MANSFIELD and GRANNELL, 1973]. The most abundant isotope in biological tissue

that gives rise to an NMR signal is hydrogen, and tomographic imaging based on ^1H -MRI or proton MRI is nowadays a well-established tool in medical diagnostics. Being indisputably the superior imaging modality for visualizing anatomical soft tissue features of the human body, MRI has lately been increasingly used for functional imaging of skeletal muscles.

In addition, with the purpose to study muscle recruitment and activity of metabolites, MRS has also gained wide-spread interest [BOESCH, 2007]. Especially, phosphorus MR spectroscopy (^{31}P -MRS) introduced in 1974 has been applied in order to detect high-energy phosphate compounds during non-invasive functional measurements of exercising muscles [HOULT et al., 1974]. Since that time, numerous functional ^{31}P -MRS studies have been conducted to investigate the metabolic aspects of exercising muscle under various conditions including effects of high training level or different muscular diseases [BENDAHAN et al., 2004]. Despite being able to provide specific 3D spatial information, the inherently low sensitivity of ^{31}P -MRS due to the relatively low abundance of phosphorus compounds *in vivo* limits the spatial resolution to the cm-range for typical voxel dimensions during functional examinations. Thus, the recorded signals often represent a superimposition of signals originating from activated and resting, or less active muscles, which may complicate the signal interpretation.

Imaging methods based on ^1H -MRI are better suited to overcome the spatial resolution issue. In particular, quantitative imaging of the intrinsic spin-spin relaxation time constant T_2 , which primarily determines muscle MRI contrast, has turned out to be a powerful tool in order to map muscle activation patterns with good spatial resolution. The transient effects of exercise on T_2 values of loaded muscles were first reported in 1988 [FLECKENSTEIN et al., 1988] and quantitative comparison of their relative involvement in different muscles recruited during exercise is nowadays well established, while being denoted as muscle functional MRI (mfMRI) [MEYER and PRIOR, 2000]. The superior spatial resolution of mfMRI provides a unique opportunity to study multiple muscles under load conditions and to investigate whether and which of the target muscles has been used, how effectively it has been activated, and whether substitution has potentially occurred [PATTEN et al., 2003]. Mapping of T_2 in muscles has not only demonstrated some of the inaccuracies associated with MRS but has also provided insight into the relative participation of muscles during specific activities, including, e.g., hand-grip exercises [MORVAN and LEROY-WILLIG, 1995] or lumbar extensions [MAYER et al., 2005].

Measurements based on mfMRI are sensitive to several of the metabolic and hemodynamic processes accompanying muscle activation and thus portray the complex functional interplay of muscle cell metabolism and fluid uptake from the vascular system [DAMON and GORE, 2005]. During intense exercise, both the intra-cellular tissue water content and acidity increases lead to exercise-induced T_2 increases [BENDAHAN et al., 2004; DAMON et al., 2002b]. In addition, increases of blood flow, blood volume, and blood oxygen extraction are supposed to cause blood-oxygenation level-dependent (BOLD) contrast changes which, in turn, also alter muscle T_2 [DAMON and GORE, 2005; NOSEWORTHY et al., 2003]. Although increased extra-cellular and/or blood volumes have been hypothesized as contributors to the observed T_2 changes by other authors as well [ABABNEH et al., 2008; MORVAN and LEROY-WILLIG, 1995], an unequivocal

interpretation of the underlying mechanisms of mfMRI is still open to date. Simultaneous measurements of metabolic, T_2 and vascular changes should be able in this context to provide improved and more comprehensive interpretation of mfMRI data.

One important physical property that is non-invasively accessible by means of NMR and MRI is the diffusion of water molecules. With the introduction of diffusion-weighted imaging (DWI) in 1985, the quantification of diffusion became possible [LE BIHAN and BRETON, 1985]. In an immediate follow-up publication in 1986, intravoxel incoherent motion (IVIM) imaging was proposed, which refers to a two-compartment model that considers contributions of both diffusion and perfusion to the signal decay observed with DWI [LE BIHAN et al., 1986]. Part of the work presented in this thesis was driven by recent findings that implied that IVIM employed on modern MRI systems with high field and gradient strengths can be used to determine vascular volume fractions in perfused organs [LE BIHAN, 2008]. Previous IVIM studies in skeletal muscles demonstrated the feasibility of extracting both diffusion and perfusion properties in the resting and exercised state [MORVAN, 1995; YANAGISAWA et al., 2009]. The current work was also motivated by more recent developments of diffusion tensor imaging (DTI), originally introduced in 1994 and representing an extension of DWI [BASSER et al., 1994], which demonstrated the possibility to assess and visualize the muscle fiber architecture with great accuracy in 3D *in vivo* [DAMON et al., 2002a]. In particular, DTI exploits the property that the diffusion of water is largest along the dominant muscle fiber direction by means of a diffusion tensor which is reconstructed from a series of diffusion-weighted MR images acquired along non-collinear diffusion-encoding directions. An eigenvalue analysis of the tensor in each voxel yields the spatially resolved principal axes of diffusion, which are supposed to parallel the local muscle fiber orientation [NAPADOW et al., 2001; VAN DONKELAAR et al., 1999]. Principal diffusion directions of neighboring voxels can then be combined for 3D fiber tractography [MORI et al., 1999].

The main goal of this thesis has been the development and application of MR-based methods to assess several aspects of muscle structure and function in a novel, combined way. Specifically, the work aimed to implement diffusion tensor imaging to study muscular structure and to determine vascular volume fractions in skeletal muscles by using IVIM-based DWI. In addition, a protocol was set-up enabling combined ^{31}P -MR spectroscopic, T_2 and IVIM-based mfMRI investigations. This approach required the implementation of the corresponding MR pulse sequences together with appropriate post-processing procedures for analyzing the data. The accuracy of the muscle architecture parameters extracted with the implemented DTI sequence was assessed by performing an experiment both *in vivo* and subsequently *post mortem* in the same animal. In an attempt to improve our understanding of the mechanisms underlying mfMRI, comprehensive functional MRS/MRI and IVIM investigations of human back muscles were performed in a volunteer study. Furthermore, it was intended to demonstrate the capability of the implemented mfMRI methods to identify age-related degenerative changes of muscle structure and function in normal state by comparing two age groups of young and late-middle-aged healthy subjects.

The thesis is organized as follows: Following this introductory chapter, Chapter 2 provides a short overview of some essentials of skeletal muscles and the concepts underlying MRI, MRS and DWI. Chapter 3 describes the implemented DTI sequence, the validation of the muscle architecture parameters derived in the animal experiment as well as an application study that investigated the back muscles of a volunteer group after surgical vertebrae stabilization using the sequence. Future applications of muscle DTI are also briefly presented. In Chapter 4, an overview of existing methods to quantitatively analyze muscle function is presented and the interrelation of MRS, MRI and IVIM examinations in exercised human back muscles is demonstrated. This chapter also contains and discusses the results of a study of back muscle exercise in two healthy age groups of volunteers and closes with an outlook of potential future examinations and required technical developments. Finally, Chapter 5 provides a brief summary of the presented work.

2 Fundamentals

2.1 Skeletal muscle

Skeletal muscles serve the most critical mechanical and physiological roles in the body [DAMON et al., 2013]. Important mechanical functions are force generation and actuation of movement, which are typically accomplished by muscles with different architectural properties. Furthermore, skeletal muscles represent the primary site of glucose uptake and disposal, and they participate in total body water balance and in the thermoregulatory system. This chapter is based on excellent reviews of muscle architecture and physiology given by [LIEBER and FRIDEN, 2000] and [BARRETT et al., 2003], respectively. In particular, the focus is put on important structural and functional aspects of skeletal muscles, which are relevant for quantitative mfMRI.

2.1.1 Muscle types

There are three basic types of vertebrate muscles:

- **Skeletal muscles**, which make up the great mass of the somatic musculature and are attached to the bony skeleton, while being responsible for voluntary movements.
- **Cardiac muscles**, which are similar to skeletal muscles, but are not under conscious control, and are found in the walls and histological foundation of the heart.
- **Smooth muscles**, which are found in the walls of hollow organs, blood vessels, skin and eye pupils and subserve all internal, involuntary functions (with the exception of the movements during breathing and the heartbeat).

2.1.2 Muscle architecture

This thesis focuses on investigations regarding skeletal muscles of the human body. They connect to the skeleton via tendons and form muscle-tendon units that run from a point of origin to a point of insertion [DAMON et al., 2013]. The coordinates of these connections define the mechanical line-of-action. Two basic architectural sub-types can be distinguished:

- **Parallel muscles**, which comprise muscle fibers that are oriented along the muscles' line-of-action enabling more muscle fibers to be arrayed in series causing their displacements to add. Thus, this sub-type is designed for high shortening velocities and length excursions. Prominent examples are the *M. biceps brachii* and *M. sartorius* in humans.

- **Pennate muscles**, which have fibers with their long axis oriented oblique to the line-of-action. This allows placing more fibers in parallel, leading to an adding of corresponding forces. Consequently, pennate muscles, such as the *M. gastrocnemius lateralis* and *M. vastus lateralis*, are optimized for high force production.

In general, skeletal muscles comprise the same hierarchical organization (see Fig. 2.1). The whole muscle is surrounded by a sheet of connective tissue, known as the epimysium, which is formed mainly by collagen fibers. The muscle belly consists of hundreds of muscle fiber bundles, the so-called fascicles. These structures are again surrounded by a sheet of connective tissue, the perimysium. A fascicle itself consists of thousands of muscle fiber cells. These cells show diameters ranging between 10–100 μm and lengths of up to tens of cm (i.e., 30 cm as found, for instance, in human thigh muscles). They are covered by a connective tissue sheet, the endomysium, as well as by capillary and neuronal networks. The fiber cells are made of about a thousand contractile protein filaments, the myofibrils, oriented parallel to each other. The myofibrils consist of a series of sarcomeres, the smallest functioning unit of contraction, which are composed of actin and myosin filaments. The sarcomere is responsible for the striated appearance of skeletal muscles and forms the basic contractile machinery required for muscle contraction. Due to the parallel arrangement between the tendinous ends, the force of contraction of these units is additive. The myofibrils are surrounded by structures of the sarcotubular system, which is made up of a T system and a sarcoplasmic reticulum. In particular, the T system provides a path for the rapid transmission of action potentials from the cell membrane to all muscle fibrils, and the sarcoplasmic reticulum is an important store of Ca^{2+} , which is used for muscle contraction and participates in muscle metabolism [BARRETT et al., 2003].

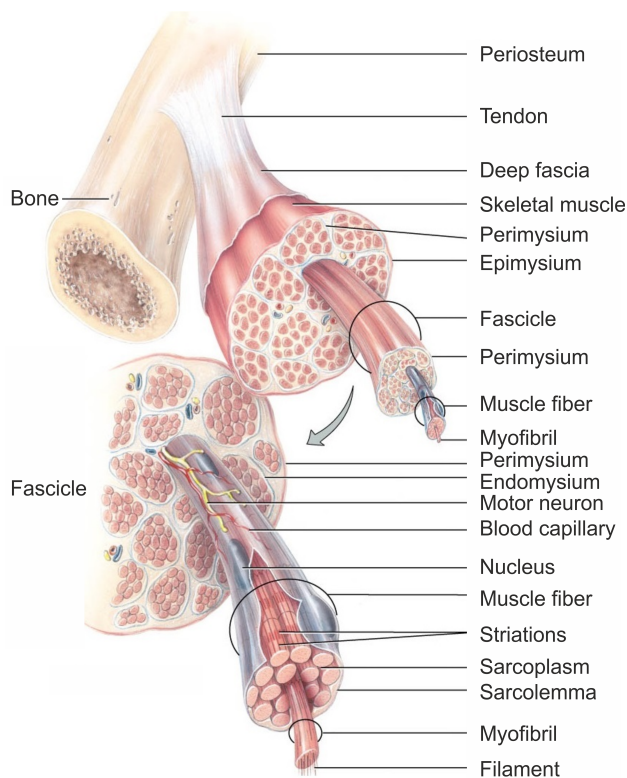


Figure 2.1: Hierarchical organization of skeletal muscle (schematic illustration taken from <http://classroom.sdmesa.edu/eschmid/chapter8-zoo145.htm>).

2.1.3 Muscle contraction

The term 'muscle contraction' encompasses multiple biological processes that result in active force generation, and is used regardless of whether the muscle-tendon unit shortens (concentric

contraction), lengthens (eccentric contraction), or does not change in length (isometric contraction). The muscle contraction itself is triggered by a transient rise in the intra-cellular Ca^{2+} concentration induced by an action potential, which is a fiber membrane depolarization that is transmitted along the T system of a muscle fiber cell. The Ca^{2+} release from the sarcoplasmic reticulum causes the sarcomere proteins actin and myosin to interact, which, in turn, results in force generation and muscle displacement [BARRETT et al., 2003]. According to the cross-bridge theory of muscle contraction it is assumed that the muscle force is generated by a cyclic formation of cross-bridges between actin and myosin filaments [HUXLEY, 1957], in which the myosin filament heads bind to the actin filament at specific sites (forming cross-bridges) and pull the latter by head rotation [HUXLEY, 1969].

2.1.4 Muscular energy supply

The chemical potential energy of adenosine triphosphate (ATP) provides the energy for the actin-myosin interaction (hydrolyzing one ATP during one cycle) and maintenance of the ion gradients [BARRETT et al., 2003]. ATP is resynthesized by an increased flux through the creatine kinase (CK), glycolytic and oxidative phosphorylation reactions. It is assumed that all physical activities derive their energy from each of these energy-supplying processes, which contribute sequentially but in a temporally overlapping manner to the energy demands caused by the exercise [GASTIN, 2001]. Contrary to the anaerobic system, including the CK reaction and anaerobic glycolysis, both of which are capable of responding immediately to an energy demand, the aerobic system (aerobic glycolysis, oxidative phosphorylation) responds more slowly and does not contribute significantly to short-term performances (Fig. 2.2).

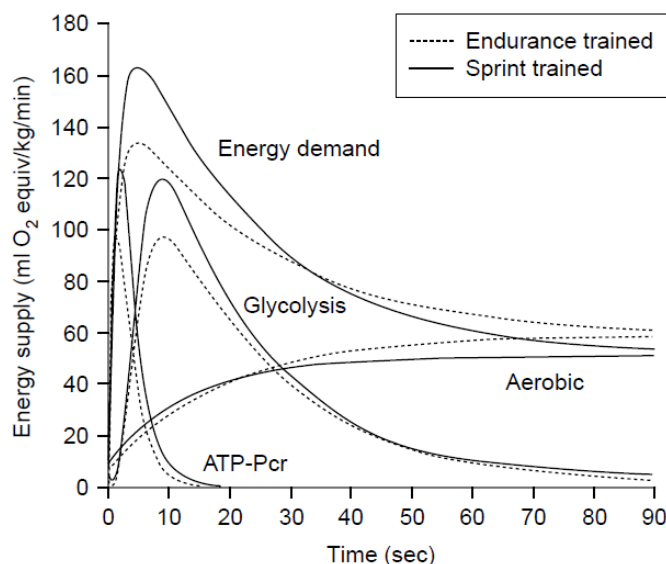


Figure 2.2: Relative contributions of the CK reaction (ATP-PCr), glycolytic and aerobic energy pathways to the total energy supply during 90 seconds of an all-out cycle exercise (taken from [GASTIN, 2001]). The energy supply is given in oxygen equivalents basically derived from VO_2 measurements and was determined for two differently trained groups of six male sprint-trained cyclists (mean maximal oxygen uptake $\text{VO}_{2\text{max}} = 58 \text{ ml/kg/min}$) and eight endurance-trained triathletes ($\text{VO}_{2\text{max}} = 65 \text{ ml/kg/min}$).

In order to match the demand and supply of oxygen during sustained efforts, increased blood flow is required. Consequently, blood vessels in the muscle dilate during exercise, which is induced by extracellular concentration changes of metabolic products [BARRETT et al., 2003].

This process of vasodilation regulated by muscle metabolism influences the muscular micro-circulation [KRIX et al., 2010], while blood flow and the concomitant available O₂ supply are increased until the energy needs are met by the aerobic processes [BARRETT et al., 2003]. However, during muscular exertion the aerobic resynthesis of the energy stores can not keep pace with their utilization, and phosphorylcreatine (PCr), an energy-rich phosphate compound that supplies this needed energy for short periods, is then still used to resynthesize ATP through the CK reaction [GASTIN, 2001]. In addition, part of the ATP synthesis is accomplished by utilizing the energy released by the anaerobic breakdown of glucose to lactate (anaerobic glycolysis). This anaerobic pathway is, however, self-limited because despite rapid diffusion of lactate into the bloodstream, enough of it accumulates in the muscles to eventually exceed the capacity of the tissue buffers and produce an enzyme-inhibiting decline in pH. A more detailed description of the various reactions involved in the supply of energy to skeletal muscle will be given later in this work.

2.1.5 Motor unit and fiber types

Most muscles contain a mixture of different fiber types, while their differences stem from differences in the proteins within them. The vast majority of these proteins are encoded by multigene families. For instance, ten different isoforms of the myosin heavy chains (MHCs) have been characterized [BARRETT et al., 2003]. The pattern of gene expression within a muscle cell is governed by the firing pattern of its single motor neuron. The motor neurons branch within their target muscle, thereby controlling several muscle fibers, known as a motor unit. For example, the high precision eye muscles have only a few fibers in each motor unit, whereas skeletal back muscles comprise thousands of fibers within each unit. Thus, all muscle cells in a motor unit contract in unison and belong to the same fiber type specialized for particular tasks. The following fiber types are commonly defined [BARRETT et al., 2003]:

- **Type 1 or slow oxidative fibers** have a slow contraction speed, a low myosin ATPase activity and are rich in mitochondria. These cells are built for aerobic metabolism yielding high resistance to fatigue and high specialization for steady, continuous activities. Their motor neurons are often active with a low firing frequency and the cells are thin with a good capillary supply for efficient gas exchange. Fat represents the major source of energy for these cells.
- **Type 2a or fast oxidative-glycolytic fibers** have a fast contraction speed, a high myosin ATPase activity and are rich in mitochondria. They are mainly built for aerobic metabolism and are very resistant to fatigue. During muscular loading they are progressively recruited when additional effort is required, while the motor neurons show bursts of intermittent activity. These cells are thin with a good capillary supply and can use either glucose or fat as an energy source.
- **Type 2b or fast glycolytic fibers** have a fast contraction speed, a high myosin ATPase

activity and only few mitochondria. They generate ATP by the anaerobic fermentation of glucose to lactic acid and thus fatigue quickly. They are only recruited for brief maximal efforts with motor neurons transmitting occasional bursts of very high frequency impulses. These fiber cells are large and show only limited capillary supply that slows the delivery process of oxygen and removal of waste products.

2.2 Magnetic resonance imaging

This section briefly introduces the basic principles of signal formation in magnetic resonance imaging (MRI) and magnetic resonance spectroscopy (MRS). The last part focuses on the diffusion-weighted MRI technique, which is of particular interest with respect to the present work. More detailed explanations regarding MR physics and many different available MR pulse sequences can be found in the literature [HAACKE et al., 1999; BERNSTEIN et al., 2004].

2.2.1 Nuclear magnetic resonance

Magnetic moment and macroscopic magnetization

The wide range of MR methods has its origin in the interaction between elementary nuclear particles and externally applied magnetic fields by utilizing the fundamental principle of nuclear magnetic resonance (NMR). The NMR effect relies on quantum mechanics and the existence of an intrinsic angular momentum or spin \vec{I} that is immanent to all atomic and subatomic particles with a spin quantum number I other than 0 [BLOCH, 1946; PURCELL et al., 1946]. Such atomic nuclei possess a nuclear magnetic dipole moment $\vec{\mu}$, which interacts with an external static magnetic field \vec{B}_0 and is given by

$$\vec{\mu} = -\gamma \cdot \vec{I}, \quad (2.1)$$

where the gyromagnetic ratio γ denotes the isotope-specific proportionality constant between the two quantities $\vec{\mu}$ and \vec{I} (Tab. 2.1). The interaction between an individual magnetic moment $\vec{\mu}$ and \vec{B}_0 leads to a precession of $\vec{\mu}$ around \vec{B}_0 with the characteristic Larmor frequency

$$\vec{\omega}_L = \gamma \cdot \vec{B}_0. \quad (2.2)$$

When an ensemble of randomly distributed spins is placed in a strong external static magnetic field \vec{B}_0 , such as typically produced by a superconducting coil, the direction of their rotation axes will be affected and the spins will align parallel or anti-parallel with respect to \vec{B}_0 . Since the magnitude and the direction of \vec{I} , and thus of $\vec{\mu}$, are both quantized, this alignment of the magnetic moments is associated with different discrete energy levels, which are separated by an energy difference ΔE (described by the Zeeman effect). According to the laws of thermodynamics, the number of spins in the lower energy level (parallel spins) slightly outnumber the number of spins in the upper level (anti-parallel spins). In thermal equilibrium the population

Table 2.1: List of isotopes that are relevant for NMR experiments (taken from [HAACKE et al., 1999]) and [REISER and SEMMLER, 2002]).

Isotope	I	γ [MHz/T]	natural abundance [%]	abundance <i>in vivo</i>	ω_L at 3 T [MHz]
1H	1/2	42.58	99.985	88 M	127.7
^{19}F	1/2	40.08	100.00	4 μ M	120.2
^{23}Na	3/2	11.27	100.00	80 mM	33.8
^{31}P	1/2	17.25	100.00	75 mM	51.8

of the states follows the Boltzmann statistics, which in the case of a two-level system (such as, e.g., the proton) leads to

$$\frac{N_{-\frac{1}{2}}}{N_{+\frac{1}{2}}} = e^{-\frac{\Delta E}{kT}}, \quad (2.3)$$

where $N_{-\frac{1}{2}}$ represents the number of spins in the upper energy level, $N_{+\frac{1}{2}}$ the number of spins in the lower energy level, $k = 1.38066 \cdot 10^{-23} \frac{J}{K}$ is the Boltzmann constant and T is the absolute temperature in Kelvin. Hydrogen nuclei in human tissue ($T = 310$ K) investigated at $B_0 = 3$ T show a ratio between $N_{-\frac{1}{2}}$ and $N_{+\frac{1}{2}}$ of ≈ 0.99998024 indicating that only 20 ppm more hydrogen spins are oriented parallel than anti-parallel with respect to \vec{B}_0 . However, due to the large number of nuclei usually encountered in MRI, this small excess of parallel oriented spins nevertheless produces a detectable net (macroscopic) magnetization \vec{M}_0 . In thermodynamic equilibrium \vec{M}_0 has only a longitudinal, non-zero component \vec{M}_z (parallel to \vec{B}_0) but no transverse macroscopic magnetization component \vec{M}_{xy} , which is due to the uniform distribution of the individual phase angles of the precessing spins (phase incoherence).

Magnetic resonance excitation

In order to assess the macroscopic magnetization \vec{M}_0 , a transverse magnetization component \vec{M}_{xy} is necessary, which rotates with $\vec{\omega}_L$ in the transverse xy -plane. The formation of \vec{M}_{xy} requires phase coherence of precessing spins and can be achieved by an additional interaction with an oscillating magnetic radio frequency (rf) field $\vec{B}_1(t)$. This rf field has to be applied perpendicularly to \vec{B}_0 with an excitation frequency ω_{rf} that matches the Larmor frequency ω_L of the spins (thus fulfilling the resonance condition $\omega_{rf} = \omega_L$):

$$\vec{B}(t) = \vec{B}_0 + \vec{B}_1(t) = \begin{pmatrix} 0 \\ 0 \\ B_0 \end{pmatrix} + \begin{pmatrix} B_1 \cdot \cos(\omega_L \cdot t) \\ B_1 \cdot \sin(\omega_L \cdot t) \\ 0 \end{pmatrix}. \quad (2.4)$$

The magnetic rf field induces transitions between the spin states until the occupation numbers are either identical (90° rf pulse) or inverted (180° rf pulse). In addition, irradiation of a 90° rf pulse results in a phase synchronization of the nuclear magnetic moments of the sample and thus yields a macroscopic \vec{M}_{xy} . From the macroscopic point of view, $\vec{B}_1(t)$ exerts a torque on

the magnetization, which turns the magnetization vector \vec{M} away from its orientation along the \vec{B}_0 axis. The description of this temporal evolution of \vec{M} is provided in mathematical form by the Bloch equations [BLOCH, 1946]:

$$\frac{d\vec{M}(t)}{dt} = \vec{\omega}_L \times \vec{M}(t) = \gamma \cdot [\vec{M}(t) \times \vec{B}(t)] = \gamma \cdot \left[\vec{M}(t) \times \begin{pmatrix} B_1 \cdot \cos(\omega_L \cdot t) \\ B_1 \cdot \sin(\omega_L \cdot t) \\ B_0 \end{pmatrix} \right]. \quad (2.5)$$

The \vec{B}_1 -induced directional change of the main orientation of the precessing \vec{M} with respect to the z -axis is characterized by the rf flip angle α , which depends on the \vec{B}_1 pulse magnitude and the duration t :

$$\alpha = \omega_L \cdot t = \gamma \cdot |\vec{B}_1| \cdot t. \quad (2.6)$$

In the case of a 90° rf pulse, \vec{M} is tilted completely into the transverse plane and the magnitude of generated transverse magnetization \vec{M}_{xy} equals the magnitude of \vec{M}_z in the thermal equilibrium state. Contrary, in the case of an 180° rf pulse, \vec{M} is inverted and points along the negative z -axis:

$$M_{xy} = M_0 \cdot \sin \alpha, \quad (2.7)$$

$$M_z = M_0 \cdot \cos \alpha. \quad (2.8)$$

Relaxation and signal detection

With the \vec{B}_1 field being switched off, the magnetization starts to return to thermal equilibrium. The dynamics of this process can be again described phenomenologically by the Bloch equations, which are now extended by additional first order relaxation terms [BLOCH, 1946]:

$$\frac{dM_x(t)}{dt} = \gamma \cdot [\vec{M}(t) \times \vec{B}(t)]_x - \frac{M_x(t)}{T_2} \quad (2.9)$$

$$\frac{dM_y(t)}{dt} = \gamma \cdot [\vec{M}(t) \times \vec{B}(t)]_y - \frac{M_y(t)}{T_2} \quad (2.10)$$

$$\frac{dM_z(t)}{dt} = \gamma \cdot [\vec{M}(t) \times \vec{B}(t)]_z - \frac{M_z(t) - M_0}{T_1}. \quad (2.11)$$

The parameters T_1 and T_2 denote the longitudinal and transverse relaxation time constants, which characterize the medium-specific effects of spin interactions with the environment (the so-called lattice) and among the spins themselves, respectively. **The longitudinal time constant** T_1 is thus also known as the spin-lattice relaxation time constant and is a measure of the time required for the longitudinal magnetization M_z after having been tilted to the transverse plane to recover in its thermal equilibrium state M_0 :

$$M_z(t) = M_0 \left(1 - e^{-\frac{t}{T_1}} \right). \quad (2.12)$$

The transverse time constant T_2 , also called spin-spin relaxation time, is a measure of the temporal evolution of dipole-dipole interactions, which cause variations of the precessing frequencies of the spin isochromates. As a consequence, isochromates lose their initial phase coherence, which, in turn, results in a gradual loss of the net transverse magnetization M_{xy} , i.e. signal dephasing. This process depends on intrinsic factors, such as, e.g. size of molecules or tissue type, and follows in many instances an exponential decay after excitation

$$M_{xy}(t) = M_{xy}(t = 0) \cdot e^{-\frac{t}{T_2}}. \quad (2.13)$$

In practice, the effective transverse relaxation time, however, is shorter due to existing main field inhomogeneities, which accelerate the dephasing process. The effective time constant T_2^* describes the actual decay of the transverse magnetization and follows the relation

$$\frac{1}{T_2^*} = \frac{1}{T_2} + \frac{1}{T_2'} \quad (2.14)$$

with T_2' representing the external field induced effects. The resulting time course of the signal $S(t)$ is named free induction decay (FID) and is given by:

$$M_{xy}(t) = M_{xy}(t = 0) \cdot e^{-\frac{t}{T_2^*}}. \quad (2.15)$$

After rf irradiation generated by a transmit coil, the transverse component of the precessing magnetization vector \vec{M} can be measured with rf receiver coils. According to Faraday's law of induction an electromotive force is induced in the rf coils due to the time-varying (oscillating) magnetic field of \vec{M} . The alternating voltage induced in the receiver coils is measured, amplified, filtered and digitized (using an analog-digital-converter, ADC). The measured MR signal $S(t)$ has the form of a damped oscillation: oscillating with ω_L and decaying with T_2^* . Its initial amplitude is proportional to the number of the excited spins in the sample. The time domain data $S(t)$ can be analyzed by means of the Fourier transform (FT) that yields the complex spectrum of the probed MR signal (frequency domain):

$$I(\omega) = \int_{-\infty}^{+\infty} S(t) \cdot e^{-i\omega t} dt. \quad (2.16)$$

The resulting Fourier spectrum has its center at the Larmor frequency and its full width at half maximum (FWHM) is related to T_2^* ($\Delta\omega = 2/T_2^*$).

2.2.2 Spatial encoding of the MR signal

In order to obtain magnetic resonance images or localized NMR spectra it is necessary to determine the spatial location of the measured signal in a volume. To this end, spatial encoding has to be applied. In general, this is accomplished by spatially selective excitation of the magnetization followed by subsequent spatial encoding of the MR signal using additional magnetic

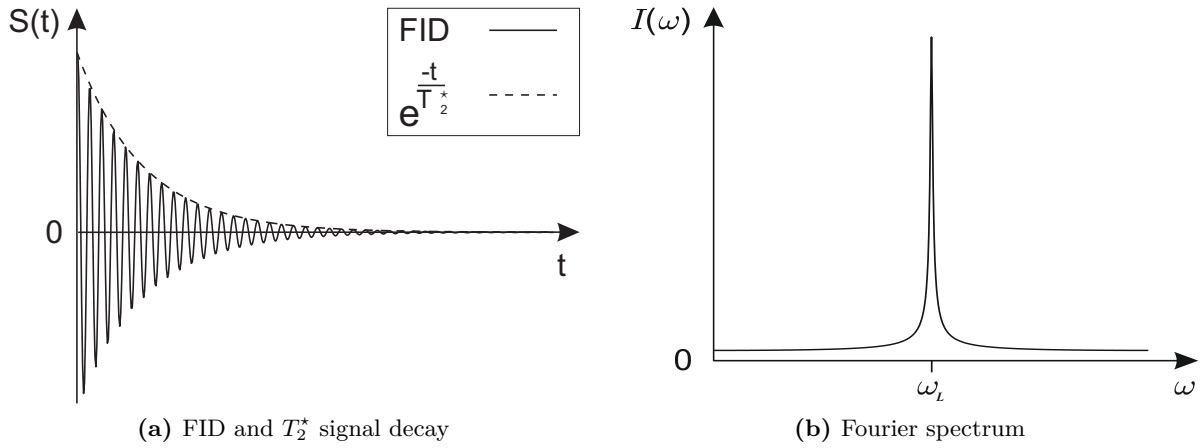


Figure 2.3: Free induction decay (FID) signal and its Fourier spectrum, which is characterized by the Larmor frequency ω_L and the intensity I (the latter defined by the area under the spectrum; illustration adapted from [REISER and SEMMLER, 2002]).

field gradients [LAUTERBUR, 1973; MANSFIELD and GRANNELL, 1973]. Therefore, the static magnetic field $\vec{B}_0 = (0, 0, B_0)^T$ is transiently superposed with a linearly varying field produced by gradient coils, which generate a linear field gradient $\vec{G} = (G_x, G_y, G_z)^T$:

$$G_x = \frac{dB_z}{dx}, \quad G_y = \frac{dB_z}{dy}, \quad G_z = \frac{dB_z}{dz}. \quad (2.17)$$

There are three sets of gradient coils built into an MRI scanner, one for each spatial direction. The magnitudes of the applied linear field gradients G_x , G_y and G_z determine the degree of the induced spatial variation of the z -component of the B_0 -field. This implies that spins at different spatial locations (x, y, z) can in principle be distinguished by means of their characteristic Larmor frequencies (based on Eq. 2.2):

$$\omega_L(x, y, z) = \gamma \cdot (B_0 + G_x x + G_y y + G_z z). \quad (2.18)$$

Slice selection

Applying an rf pulse with the bandwidth $\Delta\omega_L$ and a linear field gradient, e.g., in z -direction ($B_z = G_z z$), enables selective excitation of the magnetization within a slice of thickness Δz :

$$\Delta z = \Delta\omega_L \cdot (\gamma G_z)^{-1} \quad (2.19)$$

Thus, in the presence of a slice-selective gradient the resonance frequency becomes spatially dependent along the z -axis with

$$\omega_L(z) = \omega_0 + \gamma \cdot G_z z. \quad (2.20)$$

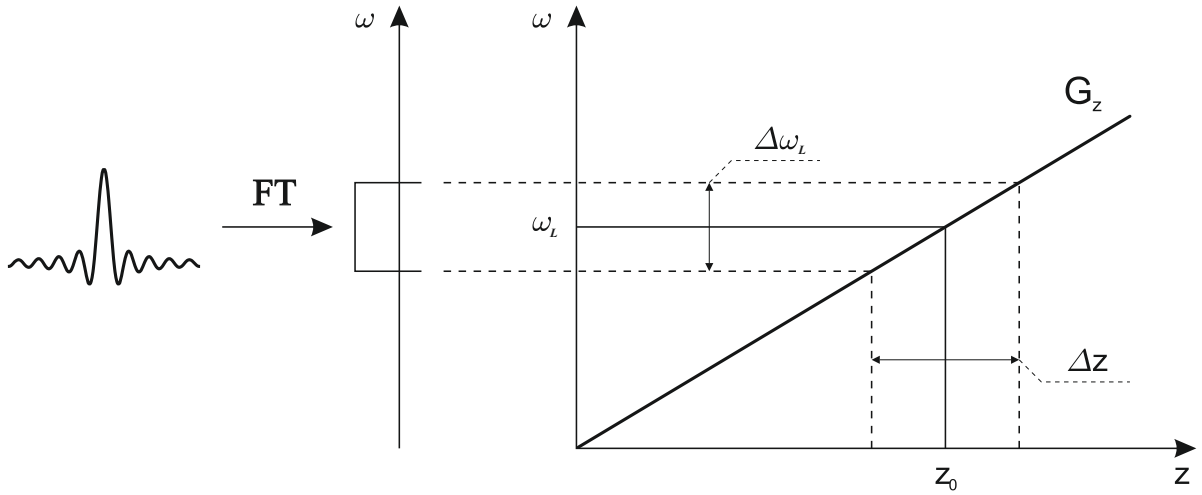


Figure 2.4: Slice-selective spatial encoding by applying a gradient field G_z in z -direction during rf excitation with a *sinc*-shaped rf pulse. Thereby, only magnetization in the spatial range $z_0 - \frac{\Delta z}{2} \leq z \leq z_0 + \frac{\Delta z}{2}$ is excited (adapted from [HAACKE et al., 1999]).

Magnetization adjacent to the selected slice, whose Larmor frequencies does not match the bandwidth of the rf pulse, is not excited and does not contribute to the MR signal. According to Eq. 2.19, the slice thickness can be adjusted by varying the strength G_z or the bandwidth $\Delta\omega_L$ (Fig. 2.4). To obtain a rectangular slice profile, $\Delta\omega_L$ has to match the corresponding resonance frequencies. Since the slice profile in the frequency domain corresponds to the FT of the rf pulse envelope (at least in the low flip angle regime), a uniform slice profile with a rectangular frequency bandwidth is generated by a *sinc*-shaped rf pulse.

Frequency encoding

Image formation, for instance, is based on frequency encoding, which is performed during signal readout by applying a time-invariant linear field gradient in x -direction $B_x = G_x x$. Thus, the precession frequency of the excited magnetization depends on the location along the x -direction

$$\omega_L(x) = \omega_0 + \gamma \cdot G_x x. \quad (2.21)$$

Hence, the recorded signal during the readout time contains different frequencies, which allows the assignment of the signal along the x -axis (illustrated in Fig. 2.5).

Phase encoding

Phase encoding (PE) is accomplished by a linear gradient $B_y = G_y y$ in y -direction, which is applied for a fixed time t_y after selective excitation and prior to the signal readout. Under the effect of this PE gradient, magnetization at position y advances by the phase angle

$$\phi(y) = \phi_0 + \gamma \cdot G_y y \cdot t_y. \quad (2.22)$$

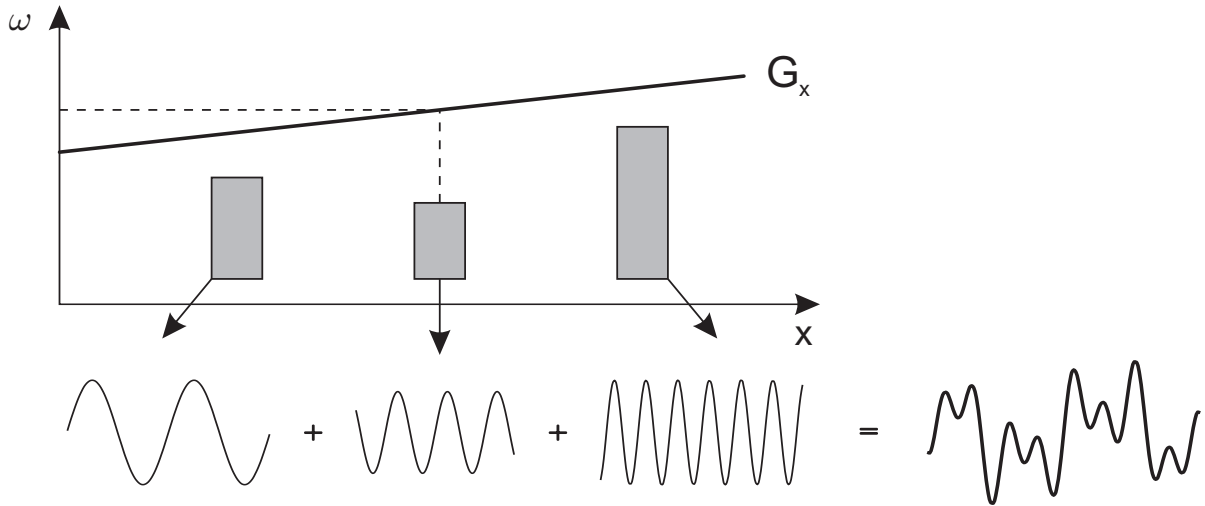


Figure 2.5: Principle of frequency encoding, where the signal amplitude is related to the number of excited spins and its oscillating frequency linearly depends on the x -position. The acquired signal is given by the superposition of all contributing signals at different locations along the x -axis and the bandwidth of the sum signal depends on the applied gradient strength.

Therefore, all magnetization components contribute to the detected MR signal with the same frequency but with differing phases $\phi(y)$. In order to achieve spatial encoding in the PE direction, the selected MR sequence is repeated N times with different spatial frequencies $k_n = n(\gamma\Delta G_y t_y) = n\Delta k$ ($1 \leq n \leq N$). In 3D imaging, the volume may be separated into partitions by using a second phase encoding gradient along the slice encoding axis. The advantage of 3D imaging compared to 2D imaging is that it allows the acquisition of thinner contiguous slices because in 2D imaging the SNR is lower and the imperfect slice selection profile due to truncation of the rf pulse often requires a gap between neighboring slices.

2.2.3 k -space and image reconstruction

The measured MR signal from the sample $S(x, y, z)$ is spatially encoded in three dimensions and recorded as a 3D complex-valued data array, $s(k_x, k_y, k_z)$, known as k -space:

$$s(k_x, k_y, k_z) = \int_x \int_y \int_z S(x, y, z) \cdot e^{-i \cdot 2\pi \cdot (k_x x + k_y y + k_z z)} dx dy dz, \quad (2.23)$$

where k_x , k_y and k_z represent the spatial frequencies, which are defined by the temporal characteristics of the gradients applied in each particular direction after rf excitation ($t = 0$):

$$k_x = \gamma \cdot \int_0^t G_x(t) dt, \quad k_y = \gamma \cdot \int_0^t G_y(t) dt, \quad k_z = \gamma \cdot \int_0^t G_z(t) dt. \quad (2.24)$$

The image volume $S(x, y, z)$ is then obtained by inverse FT of the signal in k -space (Fig. 2.6):

$$S(x, y, z) = \int_{k_x} \int_{k_y} \int_{k_z} s(k_x, k_y, k_z) \cdot e^{i \cdot 2\pi \cdot (k_x x + k_y y + k_z z)} dk_x dk_y dk_z. \quad (2.25)$$

The chronological filling of the k -space (trajectory) is specified by the gradients and can employ Cartesian, spiral, radial, or propeller-like sampling. In practice, the collected data represent a discretized and truncated version of $s(k_x, k_y, k_z)$ resulting in several ramifications for the imaging process. First, sampling of the continuous signal in k -space with equally-spaced *dirac*-functions yields an infinite number of copies of the sampled object in the image space. The displacement of these copies in image space along the particular spatial encoding directions depends on the distance between two neighboring *dirac*-functions

$$\Delta k_x = \gamma \cdot G_x \cdot \Delta t, \quad \Delta k_y = \gamma \cdot \Delta G_y \cdot t_y, \quad \Delta k_z = \gamma \cdot \Delta G_z \cdot t_z. \quad (2.26)$$

Therefore, the periodical shifts along each image dimension are given by integer multiples of the sampling rate $n/\Delta k_d$ (with $n \in \mathbb{Z}$; $d \in x, y, z$). According to the Nyquist sampling criterion overlapping of copies of the sampled object (aliasing) is avoided if the signal contributing parts of the sample (with spatial dimension w_d) are located within the field-of-view (FOV):

$$\text{FOV}_d > w_d \quad \text{with} \quad \text{FOV}_d = \frac{1}{\Delta k_d}. \quad (2.27)$$

Second, the use of a finite number of sampling points leads to a sampling with a *sinc*-function rather than a *dirac*-function and introduces blurring, which is described by the point spread function (PSF).

2.3 Diffusion-weighted imaging

2.3.1 Brownian motion and diffusion

Diffusion refers to the undirected stochastic thermal motion of molecules or atoms in fluids and gases due to their thermal energy. This physical phenomenon was first discovered by Robert Brown in 1827, who observed wondrous random migration of pollen grains under the microscope [BROWN, 1828], and is thus called Brownian motion. It is related to random translational displacements of molecules (illustrated in Fig. 2.7a) caused by constantly colliding particles and is strictly to be distinguished from any kind of directional flow of a liquid. In the presence of thermal energy, a tracer such as a droplet of ink put into water will diffuse into its surroundings, resulting in spatially and temporally changing tracer concentrations, until the ink is diluted homogeneously in the water [REISER and SEMMLER, 2002]. However, the phenomenon of diffusion does not necessarily require concentration gradients but may also occur in mono-molecular media, in which macroscopic concentration gradients are absent (so-called self-diffusion). A general, quantitative description of diffusion processes was introduced by [FICK, 1855], who defined in his first law the diffusion coefficient D by relating a concentration gradient ∇n to a diffusion flux \mathbf{j} (i.e. amount of substance per unit area per unit time):

$$\mathbf{j} = -D\nabla n. \quad (2.28)$$

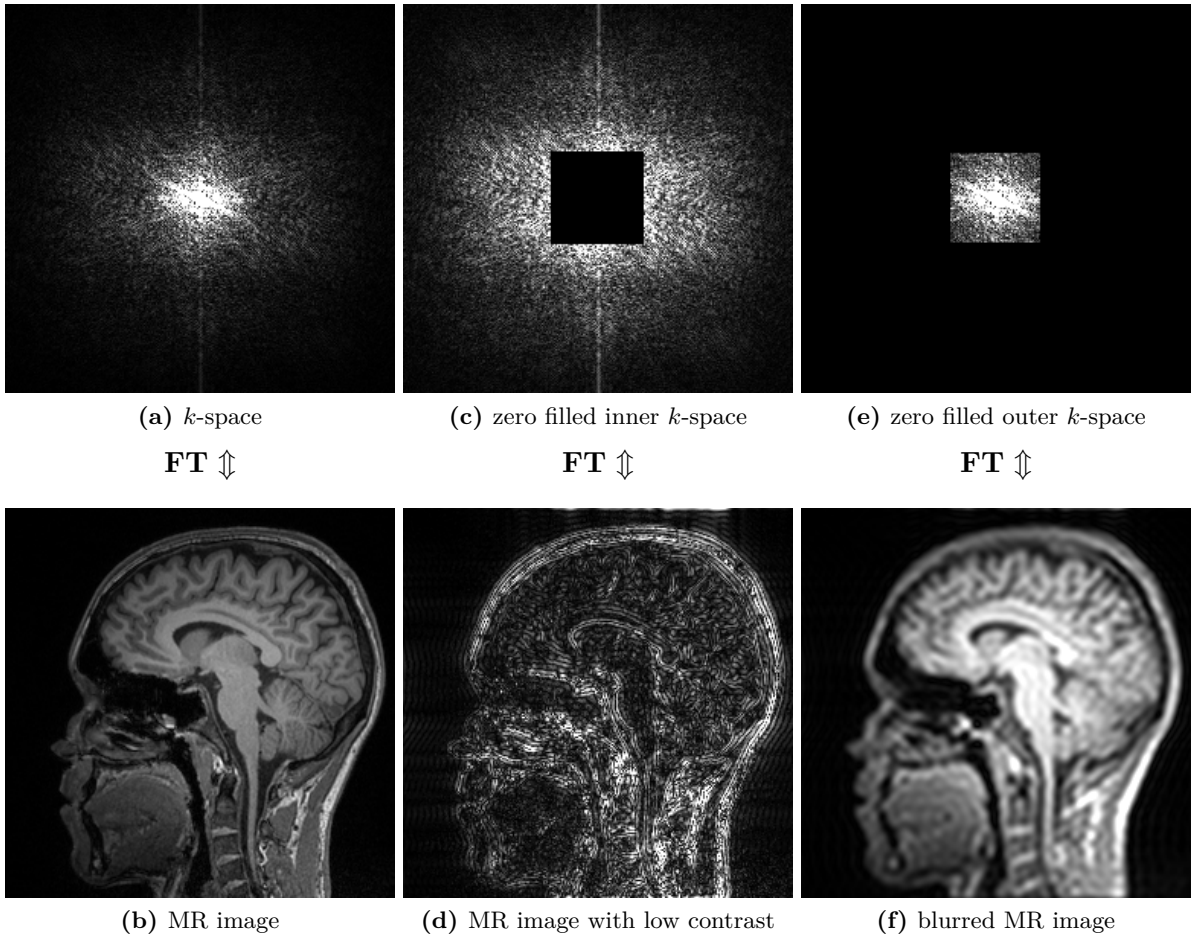


Figure 2.6: MR image reconstruction based on k -space data obtained through 3D MRI of a human head by means of inverse FT. The k -space center includes information about image brightness and contrast (low spatial frequencies), whilst the outer k -space data determine the spatial resolution of the object (high spatial frequencies).

Based on the continuity equation

$$\frac{\delta n(\mathbf{r}, t)}{\delta t} + \nabla \mathbf{j}(\mathbf{r}, t) = 0, \quad (2.29)$$

which states that a change in density in any part of the system is due to inflow and outflow of material into and out of that part of the system [URSELL, 2011], Fick's second law is formulated in order to describe the concentration change with time t at position \mathbf{r} :

$$\frac{\delta n(\mathbf{r}, t)}{\delta t} = D \nabla^2 n(\mathbf{r}, t). \quad (2.30)$$

Assuming a specific number of particles M as a Dirac function at the origin $\mathbf{r} = 0$, an initial time point $t = 0$ and that the medium is isotropic and, thus, the diffusion coefficient directionally independent, the solution to the diffusion equation (Eq. 2.30) is given by [EINSTEIN, 1905;

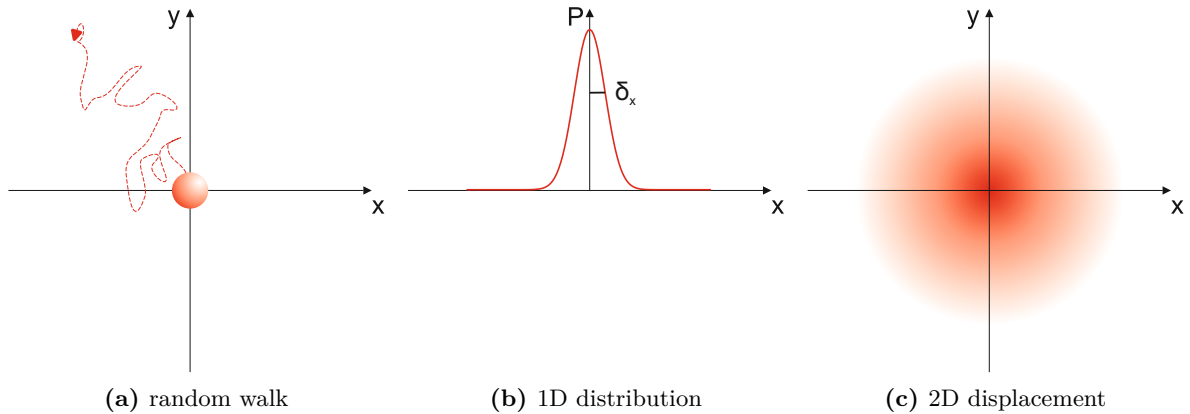


Figure 2.7: Schematic illustration of Brownian motion and the resulting 1D and 2D Gaussian distribution of diffusing particles. In 3D space, the particles show so-called isotropic diffusion.

URSELL, 2011]:

$$n(\mathbf{r}, t) = \frac{M}{(4\pi Dt)^{3/2}} e^{-\frac{r^2}{4Dt}}. \quad (2.31)$$

It follows that the distribution of the particles is Gaussian with increasing width of the distribution with time. Considering the distribution only in one dimension x , yields a Gaussian distribution with the mean of this distribution $r = 0$ and the standard deviation δ_x (Fig. 2.7b). In this case, the mean square displacement of the particles after time T is given by the Einstein equation [EINSTEIN, 1905]:

$$\delta_x^2 = \langle x^2 \rangle_{1D} = 2DT. \quad (2.32)$$

Hence, the mean square displacement increases linearly with time T (two-dimensional distribution after a certain T illustrated in Fig. 2.7c). In the case of three-dimensional displacements, one obtains a mean diffusion distance of:

$$\delta^2 = \langle x^2 \rangle_{3D} = 6DT. \quad (2.33)$$

2.3.2 Bloch-Torrey equation

Similar to spatial encoding in MR imaging sequences, diffusion-weighted imaging (DWI) employs spatially dependent field gradients affecting the spatial distribution of resonance frequencies along the direction of the applied diffusion sensitizing gradient. The influence of the diffusive motion of the particles on the measured signal can be described by adding a diffusion term to the Bloch equations (Eqs. 2.9-2.11). The resulting Bloch-Torrey equation for an

isotropic diffusion coefficient D is given by [TORREY, 1956]:

$$\frac{d\vec{M}(t)}{dt} = \gamma \cdot [\vec{M}(t) \times \vec{B}(t)] - \begin{pmatrix} 1/T_2 & 0 & 0 \\ 0 & 1/T_2 & 0 \\ 0 & 0 & 1/T_1 \end{pmatrix} \vec{M} + \begin{pmatrix} 0 \\ 0 \\ 1/T_1 \end{pmatrix} \vec{M}_0 + \nabla(D\nabla\vec{M}). \quad (2.34)$$

The time-evolution of the transverse magnetization $M_{xy}(\mathbf{r}, t)$ in the presence of both diffusion and a magnetic field gradient $B_z = B_0 + \mathbf{r}\mathbf{G}(t)\hat{z}$ is then given as:

$$\frac{dM_{xy}(\mathbf{r}, t)}{dt} = -i\gamma M_{xy}(\mathbf{r}, t) \cdot [B_0 + \mathbf{r}\mathbf{G}(t)] - \frac{M_{xy}(\mathbf{r}, t)}{T_2} + \nabla[D\nabla M_{xy}(\mathbf{r}, t)]. \quad (2.35)$$

In the absence of diffusion, $M_{xy}(\mathbf{r}, t)$ is exponentially decaying with the characteristic transverse relaxation time T_2 . In the presence of field gradients ($\mathbf{G}(t) \neq 0$), the spins are subjected to an additional precession, and if they also diffuse, $M_{xy}(\mathbf{r}, t)$ is attenuated. According to [TORREY, 1956], the magnitude of the transverse magnetization is defined by:

$$M(T) = M(0) \cdot e^{-D \int_0^T [k(t') \cdot k(t')] dt'}, \quad (2.36)$$

where $M(0)$ corresponds to the unweighted amplitude and k refers to the spatial wave vector of the field gradients \mathbf{G} , which describes the specific time-dependent diffusion gradient shapes applied during the time interval between $t = 0$ and $t = T$ (T ; time between excitation and signal acquisition). The ratio of the weighted ($k > 0$) and unweighted ($k = 0$) signal amplitudes thus depends exponentially on the diffusion coefficient D and on the diffusion weighting of the MR pulse sequence. The latter is typically described by the b-value [in s/mm^2]:

$$b = \int_0^T [k(t') \cdot k(t')] dt' = \gamma^2 \int_0^T \left[\int_0^t G(t') dt' \right]^2 dt. \quad (2.37)$$

For free isotropic diffusion, the signal attenuation observed with DWI is therefore given by the simple mono-exponential function

$$\frac{S(b)}{S_0} = e^{-D \cdot b}. \quad (2.38)$$

2.3.3 Concept of DWI

The effect of stochastic molecular motion on MR signal attenuation was first recognized by Hahn in 1950, who introduced the NMR spin-echo experiment [HAHN, 1950]. A number of more sophisticated experiments were described in the following years that allowed quantitative determination of diffusion coefficients [CARR and PURCELL, 1954; TORREY, 1956]. In particular, the pulsed-gradient spin-echo (PGSE) technique was established, which is most commonly applied in DWI and employs a bipolar diffusion gradient profile [STEJSKAL and TANNER, 1965].

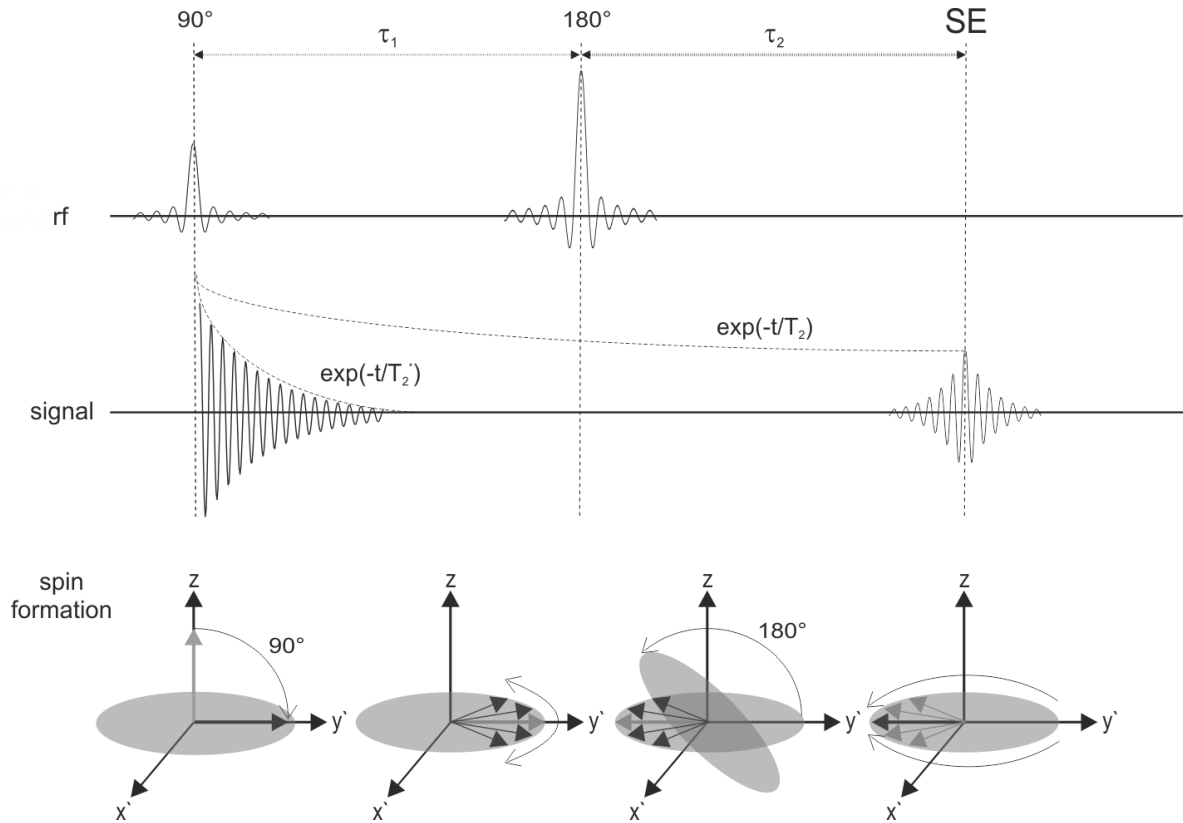


Figure 2.8: Rf pulse scheme of the SE sequence (top) and the temporal evolution of the MR signal (middle) related to the different phases of spin distributions (bottom; visualized based on a rotating frame around the z -axis and by neglecting T_2 relaxation processes; adapted from [REISER and SEMMLER, 2002]). After 90° rf excitation, M_{xy} dephases and decays with the time constant T_2^* . The 180° rf pulse, which is drawn at twice the height but with the same width and duration as the 90° pulse, mirrors the dephased magnetization vectors resulting in a regeneration of M_{xy} after τ_2 . The denoted spin-echo signal is independent of static B_0 inhomogeneities and its magnitude is reduced by the intrinsic T_2 signal decay. After $TE = \tau_1 + \tau_2$, the echo diminishes - as the original FID does - with the time constant T_2^* .

Spin-echo method and T_2 measurement

As explained in section 2.2.1, the temporal decay of M_{xy} is caused by two effects: fluctuating local magnetic fields and static spatial inhomogeneities of the magnetic field B_0 . Consequently, M_{xy} does not relax with the substance-specific relaxation time T_2 but rather with the effective time constant T_2^* . In order to determine T_2 , the effect of field inhomogeneities has to be compensated, which can be achieved by means of the Hahn spin-echo (SE) sequence. This method reverses the T_2^* -related phase coherence loss and the signal amplitude thus only depends on the irreversible stochastic T_2 signal loss. The SE experiment is based on a 90° rf excitation followed by magnetization refocusing with a 180° rf pulse after half the echo time TE (Fig. 2.8). At $t = 0$, the 90° rf pulse rotates the initial (longitudinal) magnetization M_0 into the $x'y'$ -plane, with all magnetization components (isochromates) contributing to the transverse magnetization

M_{xy} pointing along one direction. If the magnetic field of the excitation pulse is applied along the x' -direction in the rotating frame of reference, which precesses with ω_L around \vec{B}_0 , the initial direction of the M_{xy} vector corresponds to the y' -axis. Following excitation, the magnetization components at different positions \mathbf{r} begin to precess with different ω_L as they experience different field strengths, which, in turn, leads to a loss of the initial phase coherence:

$$\phi(\mathbf{r}, t) = -\gamma\Delta B(\mathbf{r})t \quad \text{with} \quad 0 < t < \tau. \quad (2.39)$$

This phase shift continues until the application of the 180° rf pulse along the x' -axis after the time interval τ_1 . The refocusing pulse reverses the sign of the phases and the differently located spins start to rephase:

$$\phi(\mathbf{r}, t) = -\gamma\Delta B(\mathbf{r})(t - 2\tau) \quad \text{with} \quad t > \tau. \quad (2.40)$$

At the time point 2τ ($\tau = \tau_1 = \tau_2$), all magnetization components point again in the same direction (their phase shifts due to static B_0 field inhomogeneities are canceled) and generate again a macroscopic transverse magnetization, called 'spin-echo'. Compared to the initial M_{xy} magnitude immediately after the 90° rf excitation, the spin-echo magnitude $S(0)$ is attenuated only according to the irreversible loss of spin phase coherence due to T_2 relaxation (Eq. 2.13):

$$S(\text{TE} = 2\tau) = S(0) \cdot e^{-\text{TE}/T_2}. \quad (2.41)$$

Pulsed-gradient spin-echo diffusion measurement

The most common approach to measure diffusion is a simple modification of the Hahn spin-echo pulse sequence, in which identically rectangular gradient pulses (usually referred to as diffusion gradients) are inserted before and after the 180° rf pulse. This method was introduced by [STEJSKAL and TANNER, 1965] and is schematically illustrated in Fig. 2.9). The basic idea of this 'Stejskal and Tanner sequence' is to measure the Brownian motion as signal attenuation based on the Bloch-Torrey equation (Eq. 2.34). Therefore, after irradiation of the 90° rf pulse causing the magnetization to precess in the xy -plane, the first gradient pulse of duration δ and strength G is applied that induces an additional phase shift of the spins (in addition to the phase dispersion caused by the static inhomogeneities of the main field). The 180° rf pulse applied after time τ_1 reverses the sign of the phases and the application of the second gradient pulse cancels the additional phase shift induced by the first gradient pulse. However, this process is only reversible if the spins are stationary and thus in the absence of translational diffusion (intrinsic T_2 effects are ignored). If the spins change their position due to stochastic motion along the direction of the diffusion gradient during the time interval Δ , the additional phase shift will not be completely refocused, resulting in signal attenuation as given by Eq. 2.38.

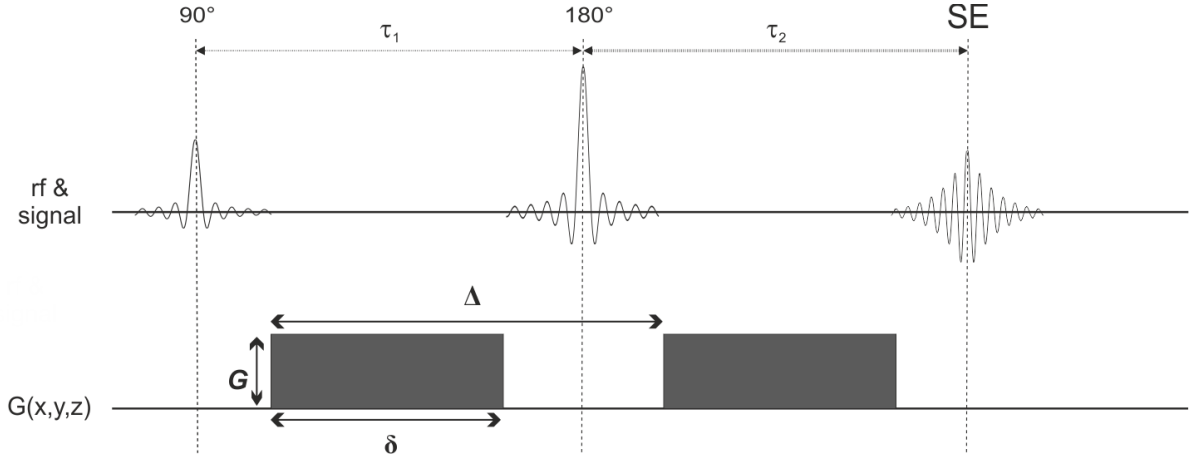


Figure 2.9: PGSE sequence based on Stejskal Tanner method, where the diffusion sensitivity of the sequence depends on the strength G and duration δ of the gradient pulses as well as on their temporal separation Δ (denoted as diffusion time). The second gradient can only compensate the effect of the first one, if the spins do not move between the both gradients. In the case of translational stochastic movement, rephasing is incomplete after the second gradient, resulting in diffusion-dependent signal attenuation of the spin-echo.

Generally, the diffusion weighting of a PGSE sequence is defined by:

$$b = \gamma^2 G^2 \delta^2 \left(\Delta - \frac{\delta}{3} \right) + \frac{\epsilon^2}{30} - \frac{\delta \epsilon^2}{6}, \quad (2.42)$$

where ϵ denotes the ramp times of trapezoidal diffusion gradients. However, since modern MRI scanners provide high gradient slew rates, like > 100 mT/m/ms (at $G_{max} \approx 30$ mT/m), rectangular gradient pulses can be assumed, which, in turn, leads to the following simplified expression for the b-factor in DWI:

$$b = \gamma^2 G^2 \delta^2 \left(\Delta - \frac{\delta}{3} \right). \quad (2.43)$$

3 Diffusion-weighted MRI of muscle structure

In this chapter, an MR technique is introduced, which enables investigation of the muscle fiber architecture. The proposed method is based on diffusion tensor imaging (DTI), which represents an extension of DWI, and provides information about the structural alignment of the examined tissue. The developed DTI sequence utilizes diffusion signal encoding based on stimulated echo acquisition mode (STEAM) and applies a single-shot (turbo) readout of the k -space within less than a second. Following the description of the principle concept of turbo-STEAM DTI (sec. 3.2), this chapter reports an *in vivo* study, which investigates myo-fiber architecture parameters, like fascicle lengths and pennation angles, of a rabbit's hind limb (sec. 3.3). This study was published in 2014 as an article in *NMR in Biomedicine* [HIEPE et al., 2014b]. In addition, the fiber architecture quantities obtained with this animal model were subsequently evaluated through manual dissection/digitization applied to the same fixated muscle [SCHENK et al., 2013]. The results of this validation study are discussed below (sec. 3.3.4). The next section documents an initial pre-clinical study, where turbo-STEAM DTI was applied to patients after posterior spinal fusion in order to identify surgery-related structural changes in back muscles (sec. 3.4). Finally, future applications of turbo-STEAM DTI are discussed (sec. 3.5).

3.1 Introduction

In bio-mechanical research, sophisticated models are applied to investigate the relationship between architectural and functional features of complex muscle structures. The major constituents of muscle architecture are the fascicle lengths and pennation angles, which largely determine muscle function [LIEBER and BLEVINS, 2000]. Information about these structural parameters can be included into 3D finite element (FE) muscle models to investigate their influence on muscle deformation and force development [RÖHRLE et al., 2012b; SIEBERT et al., 2012]. However, current FE models are often suffering from simplified and thus unrealistic muscle architecture definitions by neglecting the complex inner architecture showing fibers with different lengths and varying pennation angles [SIEBERT et al., 2015]. This limitation arises from a lack of adequate methods, which enable non-invasive high-resolution 3D probing of skeletal muscles and thus allow the characterization of muscle architecture *in vivo*.

Meanwhile, assessment of fascicle geometry and musculoskeletal anatomy per se became three-dimensionally possible with several *in vivo* MR imaging techniques [BLEMKER et al., 2007]. In particular, DTI provides valuable information of the muscle fiber arrangement by relying on the directional dependence of diffusion. It has been demonstrated that FE muscle

models may indeed benefit from this information [VAN DONKELAAR et al., 1999]. Generally, two intrinsic properties of water diffusion in muscle fibers allow DTI to be used to study micro- and macro-structure of skeletal muscles [DAMON et al., 2002a]. The first property refers to the observation of reduced diffusion coefficient D for muscle tissue compared to the value for free water, which indicates the existence of barriers to molecular movement in muscle tissue, such as myofibrils and cell membranes. The second property is that water diffusion in muscle is anisotropic as early NMR experiments reported $\approx 40\%$ greater D values parallel to the long axis of the fiber than perpendicular to it [CLEVELAND et al., 1976]. This anisotropic diffusion of water can be characterized by means of a diffusion tensor model derived from DTI [BASSER et al., 1994]. A brief description of the DTI method is given in the following section.

3.1.1 Diffusion tensor imaging

The directional dependence of diffusive water movement is modeled at each point in space ($\mathbf{r} = [x\ y\ z]^T$) as a second order tensor [BASSER et al., 1994]. In the simplest case, the diffusion tensor \mathbf{D} is a 3×3 symmetric matrix containing diffusion coefficients determined in the x , y , z , xy , xz , and yz -directions:

$$\mathbf{D} = \begin{pmatrix} D_{xx} & D_{xy} & D_{xz} \\ D_{yx} & D_{yy} & D_{yz} \\ D_{zx} & D_{zy} & D_{zz} \end{pmatrix}. \quad (3.1)$$

The symmetric diffusion tensor (i.e. $D_{ij} = D_{ji}$) is determined voxel-wise by acquiring a series of diffusion-weighted (DW) images, each with diffusion gradients applied along a different direction [BAMMER et al., 2009; MORI and BARKER, 1999]. Furthermore, non-DW image is acquired for reference (to solve the DWI signal equation; eg. 2.38). In practice, the determination of the diffusion tensor is improved by acquiring more than six directions with the diffusion directions spread isotropically over a sphere. Since any extra encoding direction adds extra time, a trade-off is sought between the optimum number of non-collinear directions and an acceptable scan time. To facilitate the interpretation of the tensor information, it is broken down into single-valued measures that can then be visualized as gray scale maps. To this end, the tensor \mathbf{D} is diagonalized by a standard mathematical matrix operation (singular value decomposition or eigendecomposition) that rotates the coordinate frame of reference independently into the principal axes of the tensor [JOLLIFFE, 1986]. Thereby, eigenvalue and eigenvector matrices are produced, which contain three eigenvalue/eigenvector pairs:

$$\mathbf{D} = [\vec{\nu}_1 \vec{\nu}_2 \vec{\nu}_3] \begin{pmatrix} \lambda_1 & 0 & 0 \\ 0 & \lambda_2 & 0 \\ 0 & 0 & \lambda_3 \end{pmatrix} [\vec{\nu}_1 \vec{\nu}_2 \vec{\nu}_3]^T, \quad (3.2)$$

with the eigenvalues and eigenvectors given by λ_i and $\vec{\nu}_i$, respectively (illustrated in Fig. 3.1a). The subscripts $i = 1 - 3$ denote the descending magnitude order of the eigenvalues. These data describe the characteristics of water diffusion in the tissue, including the degree of diffusion

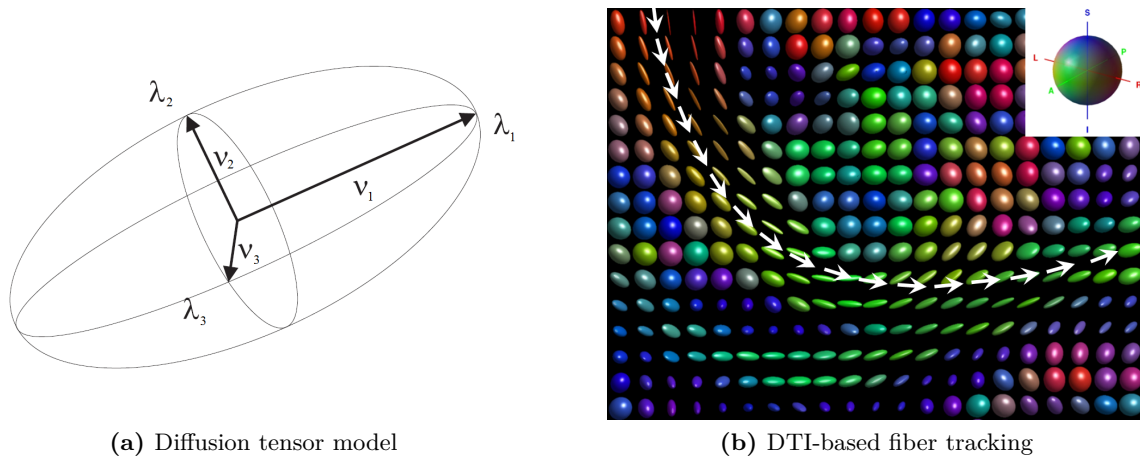


Figure 3.1: Schematic illustrations of the tensor model used in DTI and the fiber tracking approach. The color-coding of the tensors is related to a general definition of color-coding in DTI, where tensors aligned parallel to right-left, anterior-posterior and proximal-distal directions are visualized in red, green and blue, respectively.

anisotropy (typically characterized by the scalar metric fractional anisotropy, FA) and the magnitude and direction of greatest diffusion (λ_1 and \vec{v}_1 , respectively). The FA is defined as follows:

$$\text{FA} = \sqrt{\frac{3}{2}} \cdot \frac{\sqrt{(\lambda_1 - \lambda)^2 + (\lambda_2 - \lambda)^2 + (\lambda_3 - \lambda)^2}}{\sqrt{\lambda_1^2 + \lambda_2^2 + \lambda_3^2}} \quad (3.3)$$

$$\text{with } \lambda = \frac{1}{3}(\lambda_1 + \lambda_2 + \lambda_3), \quad (3.4)$$

where λ represents the rotationally invariant mean diffusibility (or so-called 'apparent diffusion coefficient', ADC). As an extension of DTI, the first eigenvalue/eigenvector pair can be used for fiber tracking, which tracks the mean diffusion direction of the water molecules in each voxel (Fig. 3.1b). In general, fiber tractography approaches provide a map of the structural connectivity within the examined biological tissue by propagating fiber tracts from pre-defined seed points through integration of the first eigenvectors of neighbored voxels [MORI et al., 1999]. Typically, the tract propagation is constrained by termination criteria, such as anatomical boundaries, maximal curvature or minimum FA. In order to characterize skeletal muscle architecture the orientation of the primary eigenvector can be expressed in a given 3D frame of reference by the polar coordinates (Fig. 3.2), the zenith and azimuth angle [KARAMPINOS et al., 2009; KARAMPINOS et al., 2012]. The zenith angle θ is defined as the angle between the first eigenvector \vec{v}_1 and a reference vector \vec{r} :

$$\theta = \arccos \left(\frac{\vec{r} \cdot \vec{v}_1}{|\vec{r}| \cdot |\vec{v}_1|} \right), \quad (3.5)$$

and varies between 0° and 90° . If \vec{r} is oriented along the line-of-action of a particular muscle the zenith angle corresponds to its pennation angle (Fig. 3.2). The azimuth angle ϕ is defined by the angle between the projection of the first eigenvector $\vec{\nu}_1$ onto the transverse plane and the x -axis:

$$\phi = \begin{cases} \arctan\left(\frac{\vec{\nu}_{1y}}{\vec{\nu}_{1x}}\right); & \vec{\nu}_{1y} > 0 \\ \arctan\left(\frac{\vec{\nu}_{1y}}{\vec{\nu}_{1x}}\right) + \pi; & \vec{\nu}_{1y} < 0 \end{cases} \quad (3.6)$$

By computing the angle between the projection of $\vec{\nu}_1$ on the xy -plane and the positive or negative x -axis for eigenvectors with positive or negative y -component, respectively, ϕ varies between 0° and 180° . Furthermore, the difference between the secondary and tertiary eigenvalues, which characterize diffusion in the plane perpendicular to the main muscle fiber orientation and are potentially related to the cross-sectional fiber ellipticity, can be analyzed by means of the planar index CP [KARAMPINOS et al., 2009]:

$$\text{CP} = 2 \cdot \frac{\lambda_2 - \lambda_3}{\lambda_1 + \lambda_2 + \lambda_3}. \quad (3.7)$$

3.1.2 DTI of skeletal muscles

Since the diffusion in very elongated muscle fiber cells is greater in the fiber direction than in others the diffusion tensor may represent the cell geometry within a voxel by yielding a first eigenvector, which is parallel to the mean fiber orientation [DAMON et al., 2002a]. This hypothesis has been supported by histology-DTI comparisons [VAN DONKELAAR et al., 1999; NAPADOW et al., 2001] and direct anatomic inspections [DAMON et al., 2002a]. Recently, DTI and fiber tractography studies have been used to quantify the pennation angle and fiber tract length in human calf [HEEMSKERK et al., 2010; KARAMPINOS et al., 2009; KARAMPINOS et al., 2012; SCHWENZER et al., 2009; SINHA and SINHA, 2011], thigh [BUDZIK et al., 2007; KAN et al., 2009] and forearm muscles [FROELING et al., 2012]. In particular, the heterogeneity of the pennation angle along the muscle was studied, reinforcing the value of a technique having 3D sensitivity and a fixed frame of reference [LANSDOWN et al., 2007; NAPADOW et al., 2001]. Furthermore, the heterogeneity in fiber length was documented [HEEMSKERK et al., 2010] and rigorous reproducibility studies successfully demonstrated the reliability of the muscle DTI parameters [HEEMSKERK et al., 2010; SCHWENZER et al., 2009; SINHA and SINHA, 2011].

However, since fiber tracking is not able to differentiate between tendinous (aponeurosis) and connective tissue (epimysium, endomysium, perimysium), which both separate muscle cells or muscle compartments, it often results in unrealistically long fiber tracts [HEEMSKERK et al., 2010; KHALIL et al., 2010; FROELING et al., 2012]. This limitation is mainly caused by the low spatial resolution typically provided by muscle DTI and which hampers the reliable identification of muscle (fiber) boundaries between equally oriented structures. Additionally, and compared to DTI in the brain, muscle DTI reveals lower SNR due to a lower proton density, stronger

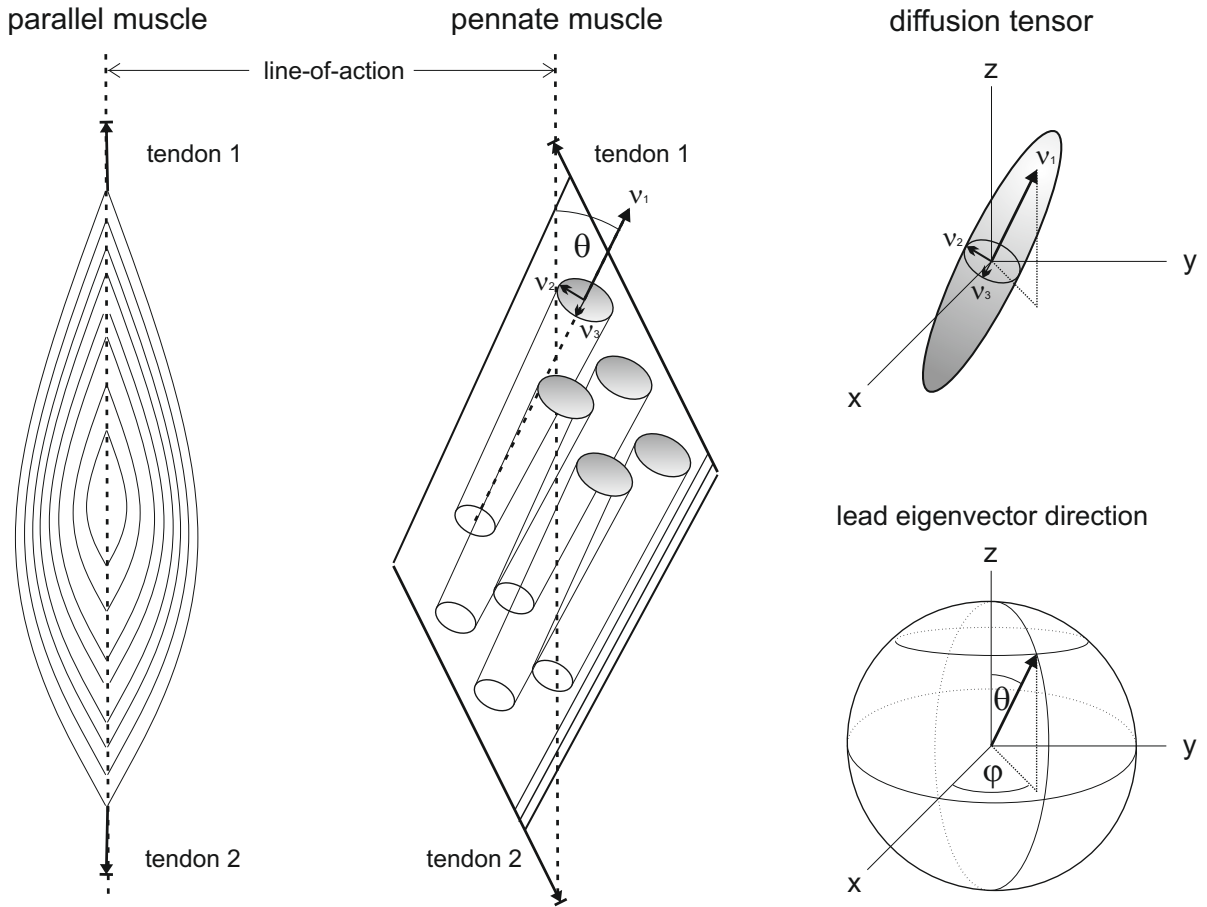


Figure 3.2: Schematic illustration of fascicle orientation patterns in parallel and pennate muscles and how they can be assessed by means of DTI. The lead eigenvector λ_1 of the diffusion tensor is principally aligned parallel to the main fiber direction and its orientation can be described by the zenith θ and azimuth angle ϕ . In the case of parallel alignment of the line-of-action (defined by the endpoints of tendon 1 and tendon 2) and the reference vector \vec{r} the zenith angle corresponds to the pennation angle of the muscle. The diffusion in the plane perpendicular to λ_1 is characterized by the second and third eigenvalue and can be used to determine the planar index CP, which is related to the cross-sectional fiber ellipticity.

T_2 -related signal attenuation and reduced B_0 homogeneity [STEIDLE and SCHICK, 2006]. Using clinical MRI systems, most of the mentioned muscle DTI studies have employed single-shot, diffusion-weighted spin-echo echo planar imaging (SE-EPI) sequences. In fact, rapid EPI acquisition significantly reduces motion sensitivity, but it suffers from B_0 inhomogeneity-induced image distortions, which restrict the available spatial resolution [KARAMPINOS et al., 2012]. In order to account for the T_2 -related SNR loss, the muscle DTI studies referred to above applied moderate b-values ($400 - 500 \text{ s/mm}^2$) and increased slice-thicknesses ($3 - 6 \text{ mm}$), resulting in a low sensitivity to restrictive diffusion and anisotropic voxel dimensions, respectively.

The major disadvantage of SE-based muscle DTI - and moderate diffusion weightings - is the inherent restriction to short diffusion times ($\Delta < 50 \text{ ms}$ at $b = 500 \text{ s/mm}^2$). This results in

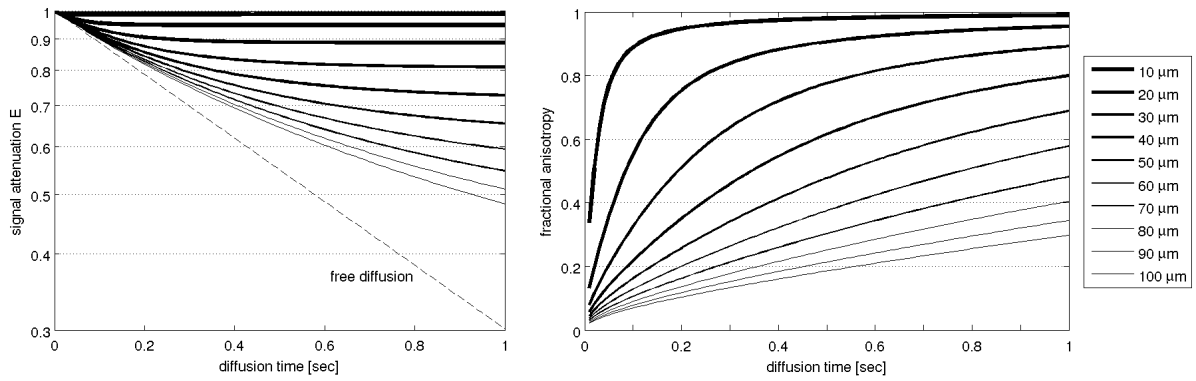


Figure 3.3: Simulated signal attenuation curves (left) and corresponding FA values (right) as function of the diffusion time Δ for different cylinders with diameters ranging between 10–100 μm . Free diffusion along the cylinder direction is assumed to show a diffusion coefficient of $D = 1.8 \times 10^3 \text{ mm}^2/\text{s}$. In essence, structures with a large diameters yield higher signal attenuation and thus lower FA values compared to low-scale structures. Prolonging of Δ simultaneously increases the deviation of the signal attenuation from free diffusion and the FA.

reduced variations between diffusion coefficients of restricted and free diffusion, which is due to the lowered reduction for perpendicular diffusion caused by barriers to water movement at short diffusion times (Fig. 3.3, left). In skeletal muscle tissue, where muscle fiber diameters are in the range of 50 – 200 μm [LIEBER and BLEVINS, 2000], long diffusion times are required to separate the signal attenuation curves obtained for restrictive and free diffusion. Therefore, it has been previously suggested that prolonged diffusion times on the order of $\Delta \approx 1 \text{ s}$ should be used to improve the sensitivity towards detection of hindered diffusion effects in muscle DTI [KIM et al., 2005; SIGMUND et al., 2014]. In particular, long diffusion times increase the sensitivity to structural ordering and thus the structural contrast as quantified by the fractional anisotropy (FA; see Fig. 3.3, right). It is assumed that the muscle fibrils provide the largest contribution to diffusion restriction at short diffusion times with an increasing contribution from the plasma membrane of the fibers at diffusion times $\Delta > 0.5 \text{ s}$ [KIM et al., 2005].

Previously, STEAM-based DTI sequences have been introduced in order to maximize the SNR in muscle DTI [KARAMPINOS et al., 2009; KARAMPINOS et al., 2012; STEIDLE and SCHICK, 2006], because the STEAM-technique is particularly able to provide extended diffusion times such as $\Delta \approx 1 \text{ s}$ without introducing additional T_2 -related signal loss (precise description given in the next section). By applying long diffusion times, STEAM DTI facilitates the detection of restricted diffusion processes within large-scale structures, i.e., revealing intra-cellular spatial extents of up to 100 μm (calculated based Eq. 2.33 by assuming $\Delta = 1 \text{ s}$ and $D = 2 \times 10^3 \text{ mm}^2/\text{s}$). In contrast, conventional SE-EPI sequences, which typically apply relatively short diffusion times ($\Delta \approx 50 \text{ ms}$), are mostly sensitive to structure sizes of up to 25 μm . Previous STEAM DTI studies applied diffusion times in the range of 100 – 300 ms, providing maximum SNR and combined STEAM-based signal preparation with EPI readout, but were not optimized for high structural sensitivity and were prone to image distortions, respectively.

Therefore, an improved muscle DTI sequence is introduced in this thesis, which employs STEAM-based DWI signal preparation with long diffusion times (typically in the order of 1 s) and robust single-shot readout based on fast low-angle shot (FLASH) imaging. This approach provides high-resolution distortion-free DTI images with high sensitivity to muscle tissue architecture. The proposed single-shot STEAM MRI sequence itself was already introduced in 1986 and was based on multiple acquisitions of stimulated echoes [FRAHM et al., 1986]. This so-called turbo-STEAM imaging method employs recording of a number of phase-encoded stimulated echoes after unique signal preparation and provides image acquisition times of about 200 ms to 1 s (depending on the spatial resolution). The imaging part of the sequence is based on repetitive acquisition periods, in which low-flip-angle rf pulses are applied that continuously consume a small part of the initially prepared (diffusion-encoded) magnetization and thereby provides insensitivity to resonance offset effects from chemical shifts or magnetic susceptibility differences. Thus, turbo-STEAM DWI represents a robust alternative to SE-EPI as previously shown for several applications [FINSTERBUSCH and FRAHM, 2000; FINSTERBUSCH and FRAHM, 2002; MERBOLDT et al., 1992; MERBOLDT et al., 2000; NOLTE et al., 2000].

3.2 Concept of turbo-STEAM DTI

3.2.1 Diffusion-weighted stimulated echo preparation

The turbo-STEAM DTI sequence proposed in this work was developed based on a previously implemented single-shot STEAM DWI sequence [HIEPE et al., 2011] using a vendor-specific sequence development environment (IDEA, version VB17, Siemens Healthcare, Erlangen, Germany). The new sequence consists of two modules that generate diffusion-encoded stimulated echoes and provide image formation, respectively (Fig. 3.4). Basically, a stimulated echo (STE) is formed from three rf pulses and its magnitude is defined by [BURSTEIN, 1996]:

$$S = \frac{S_0}{2} \cdot \sin(\phi_1) \cdot \sin(\phi_2) \cdot \sin(\phi_3) \cdot e^{-\left(\frac{TM}{T_1} + \frac{\tau_1 + \tau_2}{T_2}\right)}. \quad (3.8)$$

Hence, the STE amplitude depends on the rf pulse flip angles ϕ_{1-3} as well as on the T_1 - and T_2 -related signal losses during the mixing time TM and the τ intervals, respectively. The most important feature of a STEAM sequence is that the magnetization prevails during the TM interval, where its intensity is only subjected to T_1 relaxation. Although STEAM preparation results in a 50% signal reduction compared to SE sequences (Eq. 3.8), it therefore provides a unique way to apply extraordinarily long diffusion times by using a first diffusion gradient in the τ_1 and a second identical gradient pulse in the τ_2 interval. The benefit from the much slower T_1 signal decay in the TM interval of the STEAM-based DWI preparation over purely T_2 -weighted SE-DWI signal preparation is demonstrated in Fig. 3.5. For instance, signal obtained for muscle tissue by employing STEAM with $TM = 1$ s decreases only to approximately one-half of the signal corresponding to $TM = 10$ ms (at 3T). In comparison, the SE signal would have

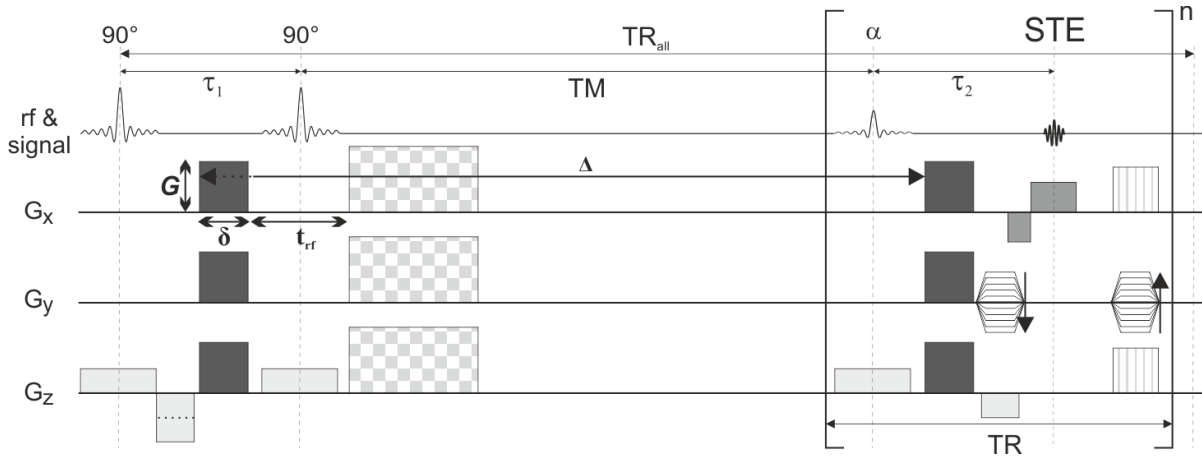


Figure 3.4: Rf pulse and gradient diagram of the turbo-STEAM DTI sequence containing the diffusion-weighted STEAM preparation module and the FLASH-based readout module. Diffusion gradients (dark grey areas) are applied in three orthogonal directions and consist of two gradient slopes with strength G , duration δ and same polarity on each axis (the linear combination of the DW gradients with direction-dependent G 's determines the effective DW direction). The first gradient pulse is applied during τ_1 and the second within the τ_2 interval. The time between the DW gradient-related de- and rephasing of the spin evolution is defined as the diffusion time Δ . The square brackets refer to the FLASH readout interval, which is repeated n -times for n phase-encoded STEs. In the TM interval, crusher gradients are applied to suppress the SE (checkered areas).

decayed completely within 300 ms. The STEAM signal preparation module consists of a slice-selective 90° rf excitation (G_z applied on the slice encoding axis during the rf-pulse), diffusion gradient pulses in predefined directions and a second slice-selective 90° rf pulse (Fig. 3.4). The formation of the diffusion-encoded STE signal is schematically illustrated in Fig. 3.6. During the time interval τ_1 , the transverse magnetization decays as a result of spin dephasing induced

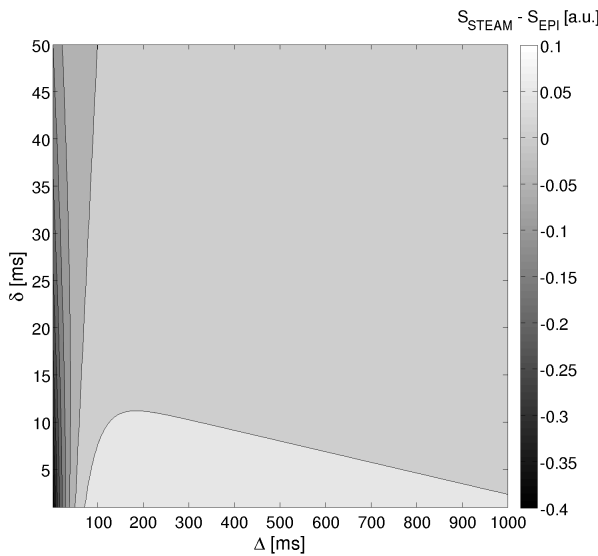


Figure 3.5: Difference between simulated STEAM and SE-based DWI signal amplitudes as function of diffusion time Δ and diffusion gradient duration δ . In SE-EPI, the signal obtained for the k -space center is defined by $S = S_0 \cdot e^{-TE/T_2}$ and $TE = \delta + \Delta + 20$ ms (20 ms required for imaging gradients). The first STE amplitude is given by Eq. 3.8 (with $\phi_{1,2} = 90^\circ$, $\phi_3 = 20^\circ$, $TM = \Delta - t_{rf} - \delta$, $\tau_{1,2} = \delta + 6$ ms). Assuming T_1/T_2 relaxation times of (1420/31.7) ms as typically observed for muscle tissue at 3 T, STEAM yields higher signal amplitudes compared to SE-EPI for diffusion times $\Delta > 50$ ms and is able to maintain this signal for ≥ 1 s (>0 ; light grey area).

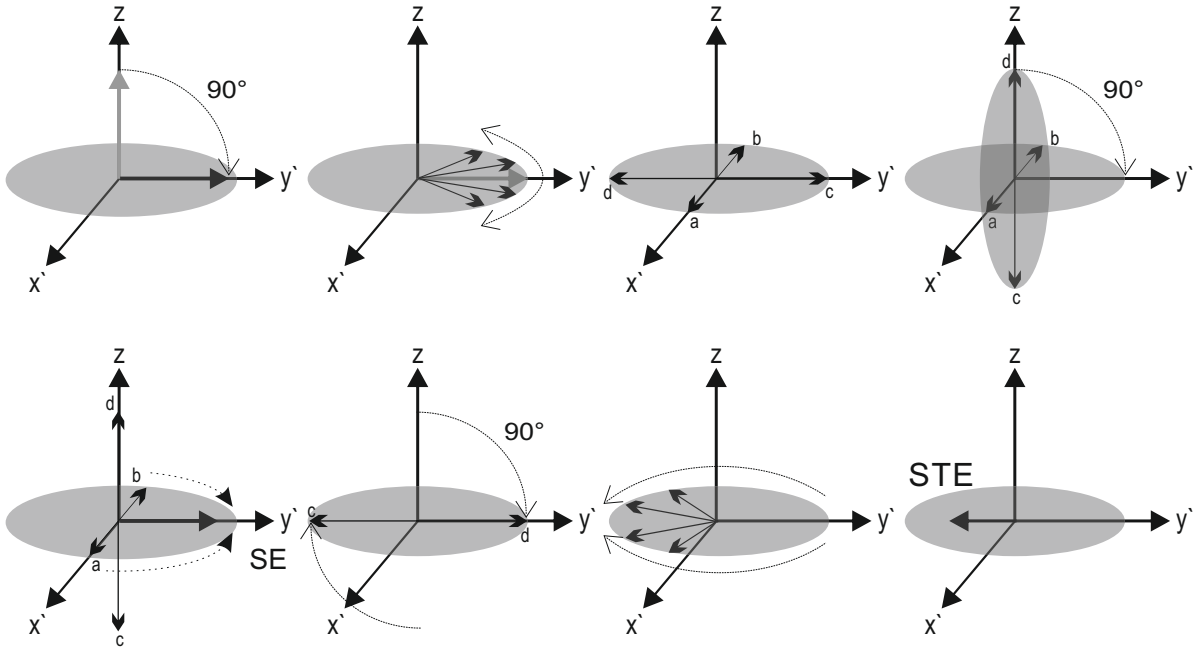


Figure 3.6: Simplified vector diagram illustrating the formation of a stimulated echo (according to [BURSTEIN, 1996]). The first 90° rf pulse (applied along the x' -direction) creates a y' -component to the magnetization. After complete dephasing during τ_1 , represented by four equal-sized magnetization vectors a , b , c , and d , the second 90° pulse (also applied along the x' -axis) flips the spins c and d , but does not affect the a and b (which refocus to form a SE). The third 90° pulse then flips the magnetization vectors c and d back into the xy -plane subsequently resulting in a STE.

by field inhomogeneities due to T_2^* relaxation and the diffusion sensitizing (Fig. 3.6). The second 90° rf pulse rotates the disc of dephased spins and splits the initial magnetization into two components (Fig. 3.6, top right). One component is stored in the z -direction and decays exponentially during TM with the time constant T_1 . The other component remains in the xy -plane and forms an SE (Fig. 3.6, bottom left), which is usually suppressed by crusher gradients (checkered gradients in Fig. 3.4). To provide complete dephasing during τ_1 , which is required for appropriate generation of a STE, small diffusion gradients (5 mT/m) are applied during acquisition of non-DW (reference) images [BURSTEIN, 1996]. Finally, application of the third rf pulse after the mixing time TM leads to the formation of a STE signal (Fig. 3.6, bottom right). The b -value of this STEAM-based DWI sequence is similar to a Stejskal-Tanner PGSE approach, which was described in sec. 2.3.3, and can be approximated by [MERBOLDT et al., 1992]:

$$b = \gamma^2 \delta^2 G^2 \left(t_{\text{rf}} + \delta + \text{TM} - \frac{\delta}{3} \right). \quad (3.9)$$

The diffusion time is given by $\Delta = t_{\text{rf}} + \delta + \text{TM}$ with the pulse duration of the three rf pulses being adjusted to $t_{\text{rf}} = 2.56$ ms for each pulse. The echo time of the first phase-encoded STE is defined by $\text{TE}_{\text{STE}} = (\tau_1 + \text{TM} + \tau_2)$.

3.2.2 Single-shot FLASH readout of the diffusion-encoded STEAM signal

The image acquisition module implemented in this work consists of a series of slice-selective refocusing low-flip angle α pulses that fractionally tip the initially stored magnetization back into the transverse plane in order to generate a series of STEs. Similar to the FLASH imaging technique, spatial encoding is achieved by the application of phase (G_y) and readout gradients (G_x in Fig. 3.4) prior to and during acquisition of the signal, respectively [FRAHM et al., 1986]. Dephasing of the prepared transverse magnetization caused by the slice selection (G_z) and the readout gradient is compensated by two additional inverted gradients (rephasing and pre-dephasing gradients, respectively). The diffusion gradient pulses are applied directly after the α pulses in the τ_2 interval to reverse the spin dephasing previously induced by the diffusion gradients of the first module. In addition, the rephasing diffusion gradient slopes crush the FID signals from each α pulse. Thus, high b-values are mostly self-spoiling. However, to suppress unwanted signal coherence pathways during FLASH-based turbo-STEAM readout, rf spoiling (phase-cycling of the rf pulses) and gradient spoiling (dephasing of M_{xy} in x and z -direction and rephasing on the y -axis after signal acquisition) is applied. In addition, for 'b0' images weak diffusion weightings are applied, which provide dephasing of the FID signals arising due to the repetitive α pulses (with an effective b-value of approx. 25 s/mm^2).

As a result of the long TM, imaging gradients can cause motion artifacts and additional undesirable diffusion weightings. In order to minimize these effects, all dephasing imaging gradient lobes are placed close to their rephasing counterpart preferably within the same τ interval. To render negligible cross-term effects on the diffusion weighting the following strategy was applied: After application of the slice-selection gradient during the first 90° rf excitation pulse the resulting gradient moment (inducing dephasing across the excited volume) is over-compensated by the rewinder in the slice-selection direction by adjusting the gradient moment (area under the lobe) of the rewinder to be equal to the moment of the slice selection gradient (see G_z axis in Fig. 3.4). This rewinder gradient pre-dephases the spins in the xy -plane prior to the application of the second, slice-selective 90° rf pulse in the τ_1 interval. During readout in the τ_2 interval rephasing of the spins that are dephased by the third slice-selective rf pulse is achieved by the slice-selection rewinder, which is applied simultaneously with the PE gradient (G_y axis). Furthermore, the readout dephasing gradient is placed in the τ_2 interval leading to phase coherence of the spin ensemble at the echo time TE (G_x axis).

The FLASH-based readout suffers from blurring artifacts in the PE direction as a result of a broadened point spread function (PSF). This blurring occurs because the available longitudinal magnetization for each α pulse continuously decays with T_1 and is fractionally consumed by a factor proportional to $\cos(\alpha)$. In addition, the magnetization is further reduced by progressive diffusion weighting as a result of the increasing diffusion time Δ over the echo train. Overall, the ratio of subsequently available longitudinal magnetization is given by:

$$\frac{M_{n+1}}{M_n} = \cos(\alpha_n) \cdot e^{-\text{TR}/T_1} \cdot e^{-D(\gamma^2 \delta^2 G^2 \cdot \text{TR})}. \quad (3.10)$$

Thus, by choosing the minimum TR, the decay of the amplitudes of successively produced STEs can be reduced, which results in minimal T_2 signal loss during the 2τ time. In order to enhance the SNR, a centric reordering scheme of the PE gradient table was implemented and readout flip angle of $\alpha = 20^\circ$ was used. The latter requires reduction of the number of PE STEs, which can be achieved by acquiring narrowed rectangular FOVs and by undersampling the k -space along the PE direction, i.e., by applying phase partial Fourier approach or the generalized auto-calibrating partially parallel acquisition (GRAPPA)-based sampling strategy [GRISWOLD et al., 2002].

3.3 DTI and Tractography of a rabbit shank

The feasibility of turbo-STEAM DTI to characterize muscle architecture was evaluated by successively performing *in vivo* DTI and *post mortem* dissection measurements in the hind limb of a rabbit. The data acquired was first assessed in terms of SNR and motion artifacts. Secondly, the images were used to determine FA and ADC parameters as well as the polar coordinates of the primary eigenvector (i.e., estimating the pennation angle etc.). To account for the low SNR a denoising approach was applied to the acquired DW images. In addition, a dedicated fiber tracking procedure was employed, which is based on constraining the tracking processes using the superposition of intensity-corrected high-resolution anatomic MR and (distortion-free) denoised turbo-STEAM images (illustrated in Fig. 3.7). It was hypothesized that this tractography approach provides reliable separation of equally aligned structures during tract propagation and thus reduces the amount of artificially prolonged fiber tracts.

3.3.1 Materials and Methods

Animal preparation and experimental setup

In vivo MRI protocol optimization was performed with four rabbits on a 3 T clinical whole-body MR scanner (TIM Trio; Siemens Healthcare, Erlangen, Germany). All imaging experiments were approved by the local animal care committee. All data presented in this work were acquired in the left shank of a female rabbit (*Oryctolagus cuniculus*, $m = 3.1$ kg). The animal was anesthetized using a mixture of ketamine (10 mg/kg/h) and xylazine (1 mg/kg/h), and fresh oxygen (0.5 L/min) was applied through a nasal tube during the MRI measurement (Fig. 3.8). A custom-made framework immobilized the examined leg of the animal with the leg fixed in a relaxed position (as defined by the deflection of the knee and ankle joint). The shanks of the animal were aligned parallel to the magnetic field of the scanner.

Data acquisition

The MRI system provided a maximum gradient amplitude of 28 mT/m and a maximum gradient slew rate of 178 mT/m/ms. All MRI data were acquired with an eight-channel receive-only

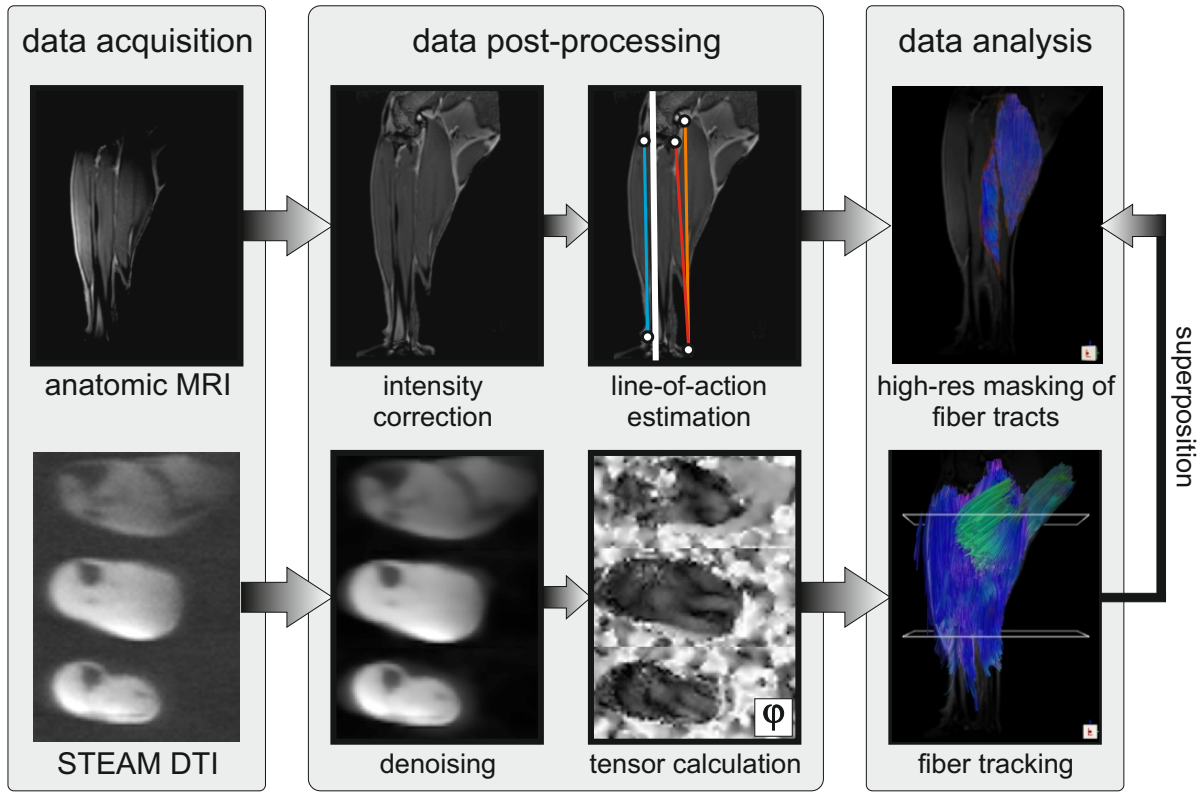


Figure 3.7: Data acquisition and post-processing pipeline for combined anatomic MRI and turbo-STEAM DTI in order to provide quantitative fiber orientation parameters (e.g., the fiber’s azimuth angle ϕ) as well as improved fiber tractography (resulting in less artificially prolonged tracts). The latter is based on the superposition of denoised DTI and intensity-corrected anatomic MRI data and accounts for inter-muscular boundaries identified through high-resolution MRI (showing hyperintense signal produced by connective tissue). By determining muscle-specific lines-of-action and 3D segmentations this post-processing strategy allows the assessment of muscular pennation angles and fascicle lengths, respectively.

coil consisting of two elements each containing four small loop coils (clothes pin coil, Noras MRI Products GmbH, Hochberg, Germany). Imaging of the hind limb anatomy was achieved by T_2 -weighted, high-resolution 3D MRI using a vendor-specific SPACE (spin-echo variant with variable flip angles) sequence with an isotropic resolution of 0.5 mm^3 ($\text{FOV} = 128 \times 116 \text{ mm}^2$; 256×232 pixels; slice thickness of 0.5 mm ; 192 sagittal slices per 3D block; bandwidth of 145 Hz/pixel ; $\text{TR/TE} = 2500/333 \text{ ms}$; $\text{TA} = 69 \text{ min}$). Oversampling in the PE (96%) and slice (8.3%) direction was applied to avoid aliasing artifacts. Finally, the obtained images were intensity corrected to account for coil sensitivity profiles using routines included in the FSL image processing package [SLED et al., 1998].

Following anatomic imaging, four turbo-STEAM DTI data sets were acquired ($\text{NEX} = 4$) each consisting of five low b-value images ($b = 25 \text{ s/mm}^2$, $\delta = 3.7 \text{ ms}$, $G = 5 \text{ mT/m}$) and 30 images with diffusion weighting in 30 different (non-collinear) spatial directions ($b = 600 \text{ s/mm}^2$, $\delta = 3.7 \text{ ms}$, $G = 25 \text{ mT/m}$; G was limited due to stimulation restrictions). The sequence timing

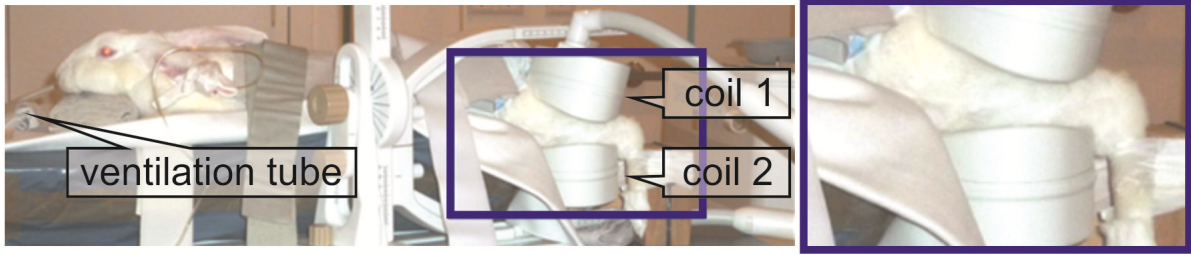


Figure 3.8: Experimental set-up for *in vivo* MRI and DTI in the left hind shank of a rabbit using a clinical human whole-body MR scanner and a two-element multi-purpose coil.

was defined as follows: $TR/TR_{\text{all}}/TM = 14.8/1678/980$ ms; $\tau_{1,2} = 10$ ms. Images were acquired with $FOV = 256 \times 72$ mm² and 256×72 pixel matrices providing an effective in-plane resolution of 1.0×1.0 mm². For complete coverage of the shank, thirty-one slices, each 2 mm-thick, were acquired in the sagittal orientation and parallel to the direction of the tibia bone. Acquisition of overlapping slices by using a negative slice distance factor of -50% during interleaved 2D acquisitions enabled the reconstruction of DTI data with an isotropic resolution of 1.0 mm³.

Undersampling of the k -space was performed by parallel imaging using an GRAPPA acceleration factor of two (thus, 48 STEs are acquired per excitation). This technique utilizes time domain data acquired with different coil elements to reconstruct the missing k -space lines [GRISWOLD et al., 2002]. The total acquisition time for the high-resolution turbo-STEAM DTI data was 128 min, which was tolerated by all examined animals. In order to avoid off-resonance artifacts caused by the chemical shift between the water and fat signal (differences of the Larmor frequencies due to the chemical environment), and due to the low bandwidth (310 Hz/pixel), a fat saturation pulse was applied prior to the STEAM preparation.

Denoising and motion artifact detection

In order to increase the intrinsically reduced SNR the acquired images were processed by using a denoising method, which reduces background noise by means of voxel-wise averaging, non-linear filtering (edge preserving smoothing) and Rician bias correction [HAHN et al., 2010; HAHN et al., 2012]. This denoising approach was implemented in IDL (ITT Visual Information Solutions, Boulder, CO, USA) and achieves an SNR improvement by a factor of 3-6, while keeping the effective DWI resolution practically unchanged. In order to demonstrate this effect the SNR of arithmetically averaged and denoised turbo-STEAM images was determined. To this end, mean intensity values measured in an inner shank muscle (*M. soleus*) were related to the SD of signal intensities in a box of $20 \times 72 \times 31$ pixels containing only background noise. Another important aspect of DTI post-processing relies on the detection of motion artifacts. In particular, application of long image acquisition times ($TE = 1$ s with a 700 ms-long readout period) results in an increased sensitivity to coherent macroscopic or bulk motion, such as due to periodic tissue motion, spontaneous muscle twitching or animal movement. Since even very small (sub-millimeter) object displacements during the diffusion-encoding period will

cause signal loss and phase changes in the resulting STE signal, motion-induced artifacts like ghosting along the PE direction can occur. Therefore, variance analyses of the multiple DTI acquisitions was performed in order to detect motion artifacts. For this purpose, pixel-wise SD calculation and 2D correlation analysis between the multiple DTI data sets ($DTI_{NEX} = 1, 2, 3, 4$) were added to the post-processing pipeline. The correlation analysis was used to assess the similarity between the images of data set $DTI_{NEX} = 1$ and the subsequent acquisitions $DTI_{NEX} = 2, 3, 4$. Both methods were performed for the entire image volume (along the slice direction) and for each DW image index (different DW directions). The (three) determined correlation coefficients were used to calculate their mean value ρ_{mean} and range $\rho_{max}-\rho_{min}$, which both provide measures for random image artifacts.

Tensor reconstruction and quantification

The tensor reconstruction was performed by using the Diffusion Toolkit (R. Wang, Athinoula A. Martinos Center for Biomedical Imaging, Massachusetts General Hospital, Boston, MA, USA). Thereby, the tensor eigenvalues λ_{1-3} and eigenvectors \vec{v}_{1-3} were determined in each voxel, and ADC, FA, CP as well as first eigenvector orientation maps were derived from these data. The latter were reconstructed by calculating the zenith and azimuth angle of \vec{v}_1 (described in sec. 3.1.1). The reference vector \vec{r} was defined by the readout direction of the DTI volume, which corresponds to the proximal-distal direction and thus to the direction of the tibia. Hence, the zenith angle represents an estimate of the pennation angle for the majority of shank muscles whose line-of-action are equally oriented along the tibia direction. However, the force-axes of the *M. soleus* (SOL), *M. tibialis* (TA) and *M. gastrocnemius medialis* (GM) were precisely determined by analyzing the anatomic MRI data. This analysis was performed by an experienced bio-mechanic scientist and was used to correct the muscle-specific θ values (yielding θ_{corr}). The maps of the zenith angle θ as well as of the azimuth angle ϕ and the planar index CP were calculated by using self-written MATLAB routines.

ROI-based analysis of the tensor metrics

The DTI parameters (ADC, FA, CP, θ and ϕ) were determined separately in three manually segmented ROIs comprising the SOL, TA and GM muscles. The segmentation of each muscle was performed slice-by-slice using the reformatted transverse images of the high-resolution anatomic MRI. After applying a closing procedure to the segmented ROIs (including eroding and dilating to smooth the object boundaries) they were rigidly registered to the DTI volume. To assess inter-muscular differences the mean DTI parameter values were compared between the ROIs by means of a two-sample *t*-test with the null hypothesis that the data of each muscle are independent random samples from normal distributions with equal means (using MATLAB). As a result of the large number of analyzed ROI voxels, a Bonferroni correction was performed and the statistical significance level was defined as $p < .001$.

Fiber tractography

The connectivity and structural alignment of the muscle fibers was assessed by fiber tracking using the deterministic Fiber Assignment by Continuous Tracking (FACT) algorithm [MORI et al., 1999]. Based on an initial ROI-analysis a FA-value of $FA = 0.3$ as well as a maximum change in direction angle of 7° per iteration step (0.1 voxel; both suggested by a bio-mechanic scientist) served as stopping criteria for the fiber tract progression during tractography. In addition, the reconstructed fiber tracts were optionally constrained by T_2 -weighted anatomic MR images to exclude artificially prolonged tracts with unexpected transitions between adjacent muscles with similar orientation. To this end, the high-resolution T_2 -weighted MRI data set was intensity-corrected and registered to the DTI data. Since connective and tendinous tissue, which separates the muscle compartments, appears bright (hyperintense) on T_2 -weighted images, the threshold for T_2 masking was successively increased until no prolonged, non-anatomical fiber tracts were detected. In order to visualize and evaluate muscle-specific fibers (obtained with or without additional T_2 masking), the corresponding tracts were overlaid onto the corresponding manually segmented ROI and displayed using the 3D tractography viewer software TrackVis (R. Wang, Athinoula A. Martinos Center for Biomedical Imaging). In accordance with the general definition of color coding of fiber directions, fibers aligned parallel to right-left, anterior-posterior and proximal-distal directions were visualized in red, green and blue, respectively. Mean fiber lengths of the examined muscles were determined by separately performing fiber tracking in one particular ROI. These ROI-based tracking results were then compared with the fiber tracts obtained through T_2 -masked fiber tracking.

3.3.2 Results

Correction and analysis of anatomic MR images

Figure 3.9 displays sagittal T_2 -weighted images of the left rabbit's shank together with three reformatted transverse slices and corresponding cross sections of examined muscles. Due to the non-uniform sensitivity profile of the rf coil the original images contain inhomogeneous intensity distributions, which were corrected by applying an intensity correction (Fig. 3.9b). The knee and ankle joints were deflected by 127° and 94° , respectively, indicating that the muscles were relaxed without significant passive shortening or stretching. The tendons at both joints were determined (marked by white circles) and used to define the line-of-action of the TA (blue), GM (orange) and SOL muscle (red). In contrast to the TA and GM muscles, whose force axes are aligned parallel to the tibia bone (blue and orange lines), the SOL muscle reveals a slight deflection of its line-of-action by $\epsilon = 2^\circ$ relative to the tibial axis (red line).

Motion artifact detection of DTI data

Native sagittal turbo-STEAM DW images as shown in Fig. 3.10 ($b = 25$ and 600 s/mm^2) were free of motion-induced phase errors (no destructive phase interferences that lead to signal losses)

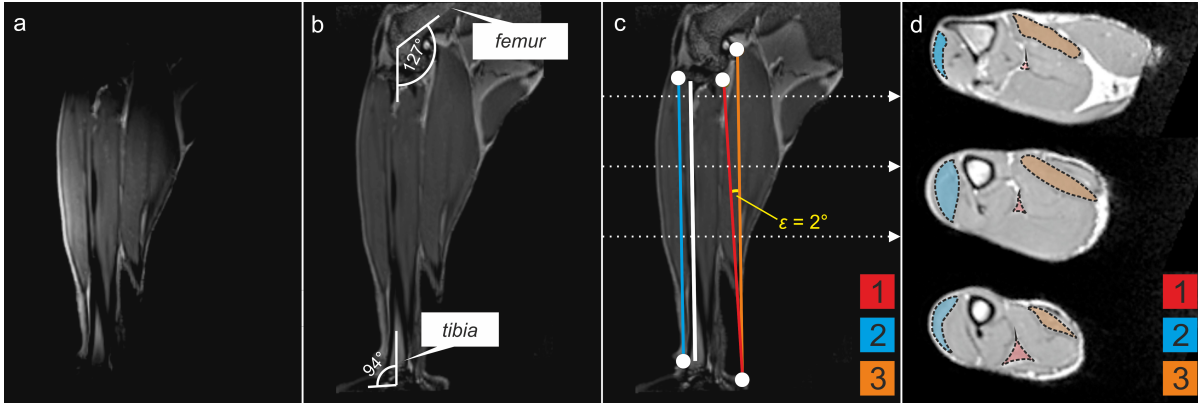


Figure 3.9: T_2 -weighted high-resolution MR images of a rabbit's shank before (a) and after (b-d) intensity correction. In (b) and (c), the joint angles and the lines-of-action of the SOL (red, 1), TA (blue, 2) and GM muscle (orange, 3) are illustrated, respectively. The force axes of the TA and GM are aligned parallel to the tibia (thick white line), whereas the line-of-action of the SOL muscle is slightly deflected relative to the tibial axis ($\epsilon = 2^\circ$). The dotted white lines indicate the planes of the transverse slices shown in (d), where overlaid ROIs mark the three examined shank muscles.

and had sufficient SNR ($\text{SNR}_{b25} = 19$, $\text{SNR}_{b600} = 13$). The corresponding (representative) SD maps of multiple low b-value images show only slight and local SD increases in the anterior region of the shank indicating motion artifacts due to arterial pulsation in this area. The mean correlation coefficients found for central sagittal slices of the low and high-DW images are in the range of $\rho_{mean} = 0.9 - 0.95$ and $\rho_{mean} = 0.8 - 0.9$, respectively. Generally, slices with less signal originating from muscle tissue (slice index 1-15 and 28-31) yielded decreased ρ_{mean} values. Thus, ρ_{mean} is primarily linked to the signal fraction imaged in the particular slice. However, differences of the correlation coefficients are very small ($\rho_{max} - \rho_{min} < 0.02$ for central slices) and also systematic (SNR dependent). Motion-induced phase errors, which should appear as random deviations, are therefore not observable.

SNR and tensor analysis of raw and denoised DTI data

Figure 3.11 displays transverse slices of the turbo-STEAM images, corresponding ADC, FA and CP maps as well as the mapped polar coordinates of the first eigenvector θ and ϕ . The first and second rows contain images and maps derived from original noisy and denoised data, respectively. The slice positions in Fig. 3.11 were selected similarly to the positions of the three transverse slices shown in Fig. 3.9d. Compared with arithmetically averaged raw data ($\text{SNR}_{b25} = 29$, $\text{SNR}_{b600} = 18$), the denoised images yield significantly increased SNR ($\text{SNR}_{b25} = 202$, $\text{SNR}_{b600} = 102$), which, in turn, significantly enhanced the quality of the derived CP, θ and ϕ maps and resulted in a superior delineation of the different muscles (in contrast to uncorrected data). For instance, as illustrated in the third row of Fig. 3.11, the SOL and GM muscle (1 and 3, respectively) show variations in θ and ϕ compared to adja-

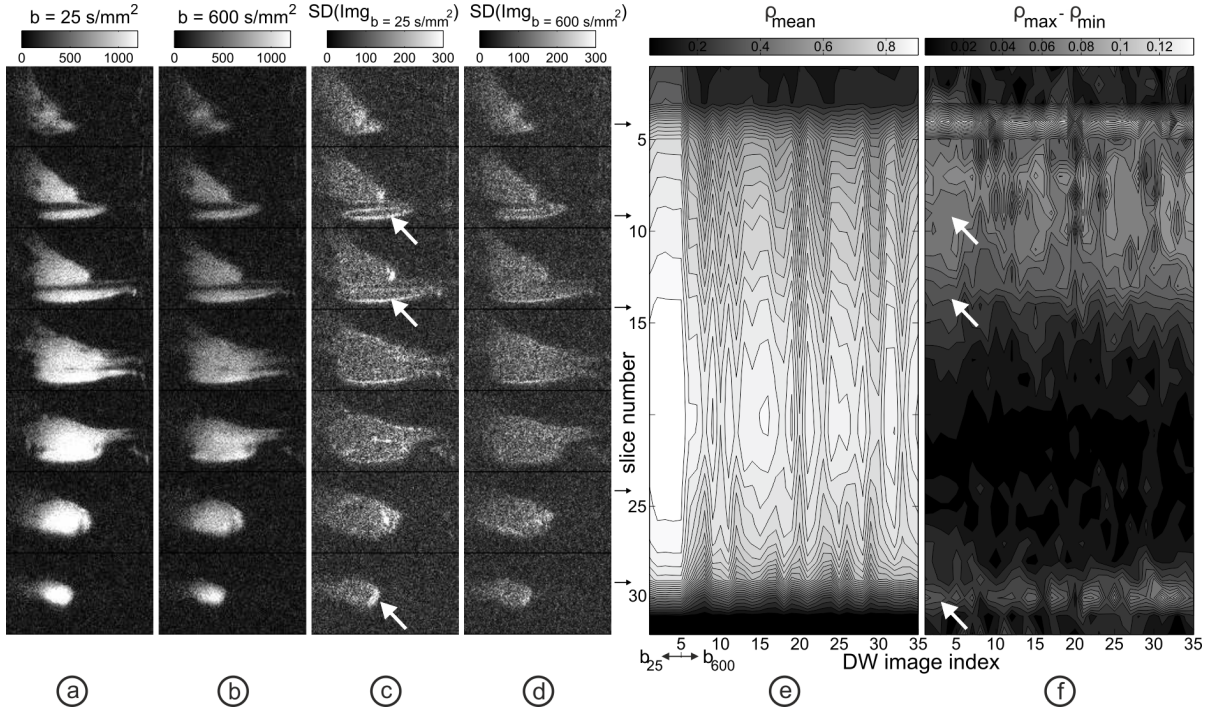


Figure 3.10: Native turbo-STEAM DW images of a rabbit shank with low (a) and high DW (b), which show sufficient SNR (a, SNR = 19; b, SNR = 12) and are free from motion-induced artifacts. The SD maps of the multiple data sets (c,d) yield only small variations in the anterior and lateral regions (white arrows in $b = 25 \text{ s/mm}^2$ images). Variations in the mean 2D correlation coefficients ρ_{mean} (e) and in the maximum coefficient changes (f) are linked to the signal observed within the particular DW image. However, central slices show high ρ_{mean} values and only small variations of $\rho_{max} - \rho_{min}$. Although motion-induced ρ changes are also observable for the anterior and lateral regions (arrows in f), no random phase errors are presented for central slices, indicating the absence of significant subject movements.

cent muscles, which are most probably caused by differences in the muscle fiber orientation. Table 3.1 summarizes the ROI-based mean and SD values of the DTI parameters for the three shank muscles. Besides reducing inner-ROI variation (SD), the denoising correction resulted in an increase of the mean ADC (and mean eigenvalues) compared to the results obtained with unfiltered data. Bonferroni-corrected pair-wise t -test comparisons partially revealed significant differences of the determined mean DTI measures between specific muscles ($p < .001$), whilst applied denoising helped to detect significant inter-muscular differences (e.g. compare FA and CP of raw and denoised data). The highest inter-muscular parameter variations were obtained for θ and ϕ . As a result of the deflected line-of-action of the SOL muscle, the corresponding zenith angle were corrected for $\epsilon = 2^\circ$ leading to $\theta_{corr} = (11.3 \pm 6.1)^\circ$. However, the TA muscle yielded the lowest zenith angles ($p < .001$).

The muscle-specific variations of the first eigenvector orientation, indicated by the high standard deviations of the calculated mean θ and ϕ values, were further investigated by slice-wise analysis. To this end, ROI-specific θ and ϕ values were averaged slice-by-slice (in axial

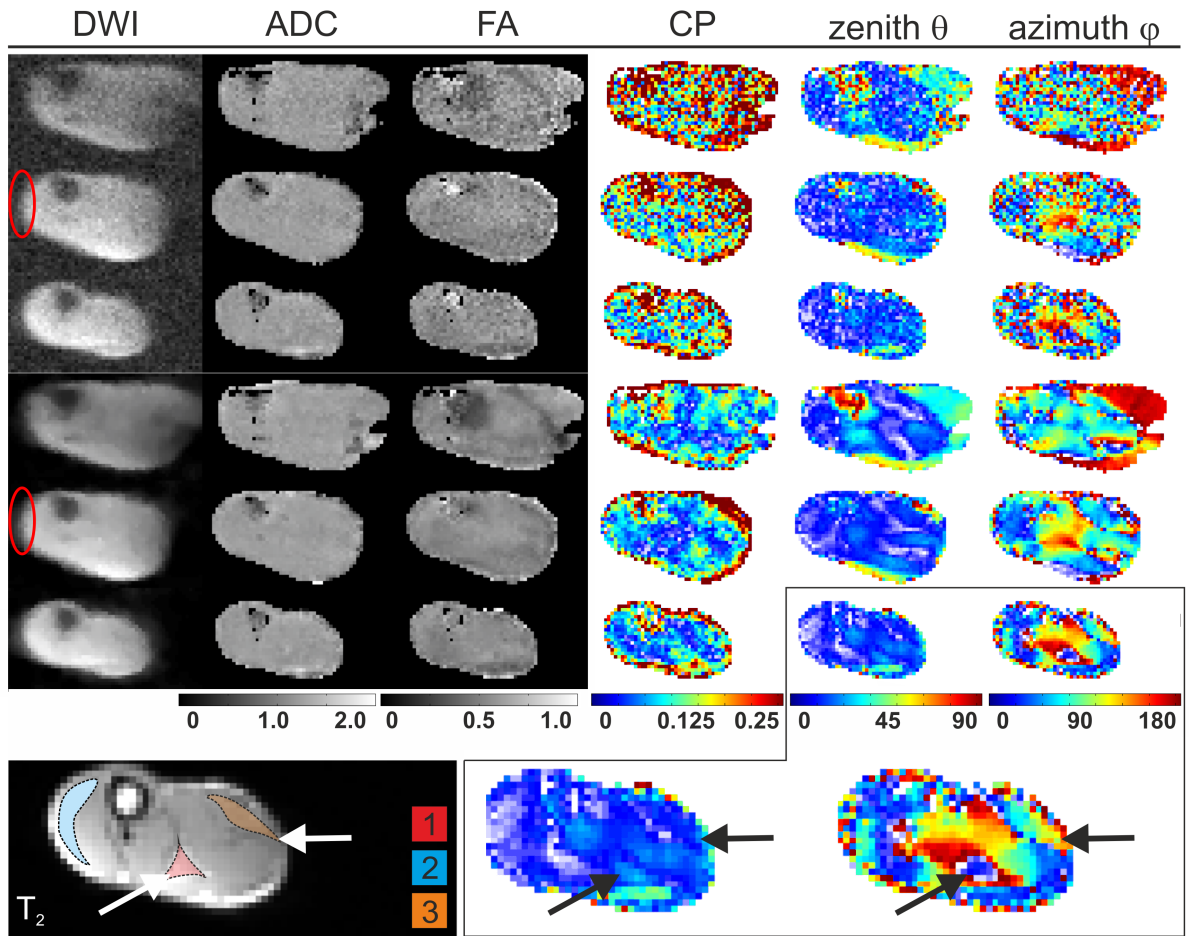


Figure 3.11: Reformatted transverse images obtained through turbo-STEAM DTI based on raw (first row) and denoised data (second row). The columns contain from left to right: DW images ($b = 600 \text{ s/mm}^2$ with DW in a single direction, ADC, FA, CP, θ and ϕ maps. Raw and denoised DW images show blurring artifacts mainly in PE direction (left-right direction, encircled in red). After denoising, particularly the maps of CP, θ and ϕ show improved inter-muscular contrasts. The bottom row shows a T_2 -weighted image and corresponding θ and ϕ maps, where the SOL (1 in T_2) and GM (3 in T_2) can be clearly distinguished from surrounding muscles (see arrows).

direction) for the different muscles. The results are given in Figure 3.12 (top). In addition, θ and ϕ were mapped in a representative sagittal slice using the segmented muscles as input mask (Fig. 3.12, bottom). Both plots indicate that the highest spatial variations of θ and ϕ occur close to the muscle boundaries. I.e., θ (left) yields the most prominent variations at the superior and inferior tips of each muscle. However, ϕ (right) also reveals a monotonic variation, particularly for GM, indicating twisting of fibers along the line-of-action. The strong orientation changes directly at muscular boundaries may be caused by partial volume effects.

Table 3.1: Mean values and SD of ADC, FA, three eigenvalues (λ_{1-3}), planar index CP, zenith θ and azimuth angle ϕ , which were calculated by using raw and denoised turbo-STEAM data for manually segmented ROIs of the SOL, TA and GM muscles.

	data	SOL	TA	GM
ADC [10^{-3} mm ² /s]	raw	0.96 ± 0.12^b	0.96 ± 0.09^c	0.94 ± 0.18
	denoised	$0.96 \pm .012^{ab}$	0.98 ± 0.09	0.99 ± 0.17
FA [a.u.]	raw	0.44 ± 0.08	0.43 ± 0.08^c	0.44 ± 0.13
	denoised	0.43 ± 0.07^{ab}	0.42 ± 0.06^c	0.40 ± 0.09
λ_1 [10^{-3} mm ² /s]	raw	1.46 ± 0.16^{ab}	1.45 ± 0.15^c	1.40 ± 0.26
	denoised	1.46 ± 0.14^{ab}	1.48 ± 0.11^c	1.44 ± 0.23
λ_2 [10^{-3} mm ² /s]	raw	0.79 ± 0.14^{ab}	0.81 ± 0.12^c	0.83 ± 0.21
	denoised	0.78 ± 0.12^{ab}	0.81 ± 0.12^c	0.85 ± 0.21
λ_3 [10^{-3} mm ² /s]	raw	0.62 ± 0.14^b	0.62 ± 0.11^c	0.56 ± 0.22
	denoised	0.65 ± 0.13	0.66 ± 0.10	0.66 ± 0.19
CP [a.u.]	raw	0.13 ± 0.08^b	0.14 ± 0.08^c	0.22 ± 0.48
	denoised	0.09 ± 0.06^{ab}	0.10 ± 0.06^c	0.14 ± 0.21
zenith angle θ [deg]	raw	14.7 ± 7.2^{ab}	10.7 ± 7.3^c	20.6 ± 16.4
	denoised	13.3 ± 6.1^a	8.3 ± 4.6^c	14.4 ± 13.0
azimuth angle ϕ [deg]	raw	98.8 ± 59.9^{ab}	78.3 ± 53.6	83.8 ± 51.1
	denoised	104.3 ± 59.8^{ab}	65.3 ± 51.6^c	81.2 ± 45.8

^a Statistical difference ($p > .001$) between SOL and TA, ^b statistical difference ($p > .001$) between SOL and GM, ^c statistical difference ($p > .001$) between TA and GM.

Evaluation of reconstructed fiber tracts

Figure 3.13 illustrates the muscle fiber tracts reconstructed by means of the turbo-STEAM DTI data (without additional T_2 masking) in the left hind leg of the rabbit that pass through either the proximal or distal transverse slice (which correspond to the top and bottom transverse images in Fig. 3.9). Fiber tracts with different orientations can be distinguished. In particular, the tracts of the TA muscle, which are aligned almost parallel to the tibia, can be separated from the tracts of the GM, which show a greater deflection relative to the leg axis (see arrows in Fig. 3.13a). This indicates different pennation angles for the different shank muscles and is in agreement with the reported θ values (in Tab. 3.1), where the TA muscle reveals a smaller mean θ compared to the SOL or GM muscle. Of special note is the bipennate structure of the *M. gastrocnemius* including the medial and lateral head, which is clearly visible in the posterior view (thick arrows in Fig. 3.13b). Tracts passing both muscles continue until they merge in the Achilles tendon (thin arrow in Fig. 3.13b).

Reconstructed fiber tracts of the isolated SOL and GM muscles are shown in greater detail in Fig. 3.14. Figure 3.14a shows the tracts using $FA > 0.3$ and a maximum tracking angle difference of 7° as thresholds for the tracking procedure, and which pass through an axial slice

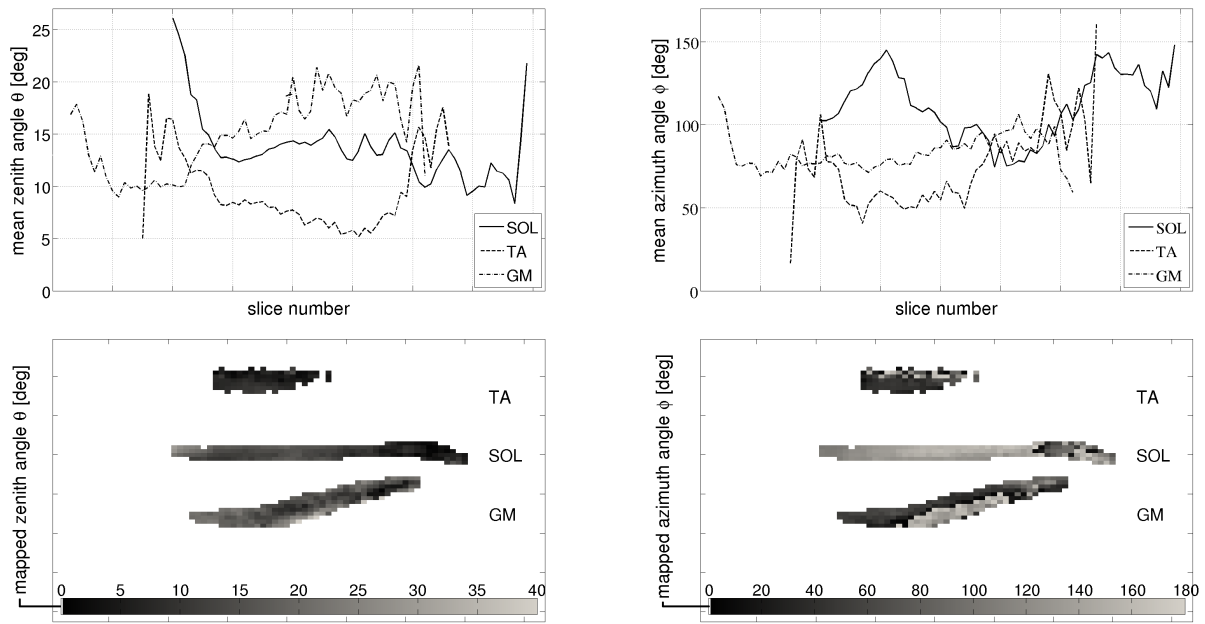


Figure 3.12: Detailed tensor orientation analyses based on denoised data showing the zenith θ (left column) and azimuth ϕ (right column) angles. The polar coordinates of the three examined muscles are averaged in each transverse plane of the corresponding ROI (top row) and mapped in a representative sagittal slice (bottom row). High deviations of the mapped θ angle can be observed at muscular boundaries, while ϕ varies along the muscle's long axis.

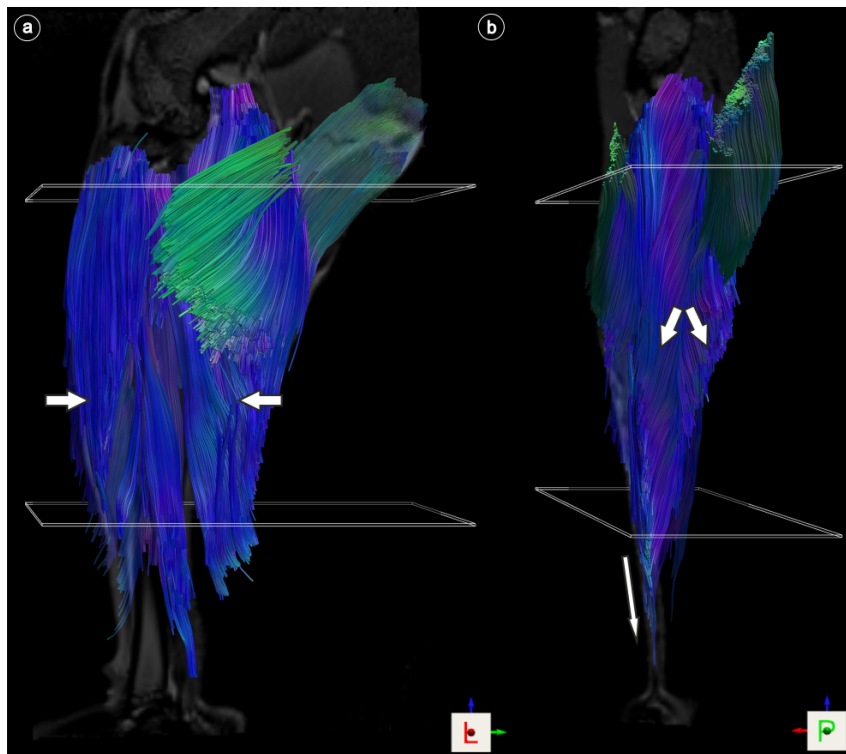


Figure 3.13: Directional color-coded fiber tracts of a rabbit's hind leg based on turbo-STEAM DTI in sagittal (a) and coronal view (b). Fiber tracts passing either one of the two transparent slices show variously deflected paths [i.e., TA and GM; see arrows in (a)]. The bi-pennate build-up of the *M. gastrocnemius* including medial and lateral head is visible [thick arrows in (b)] with tracts continuing until merging in the Achilles tendon [thin arrow in (b)].

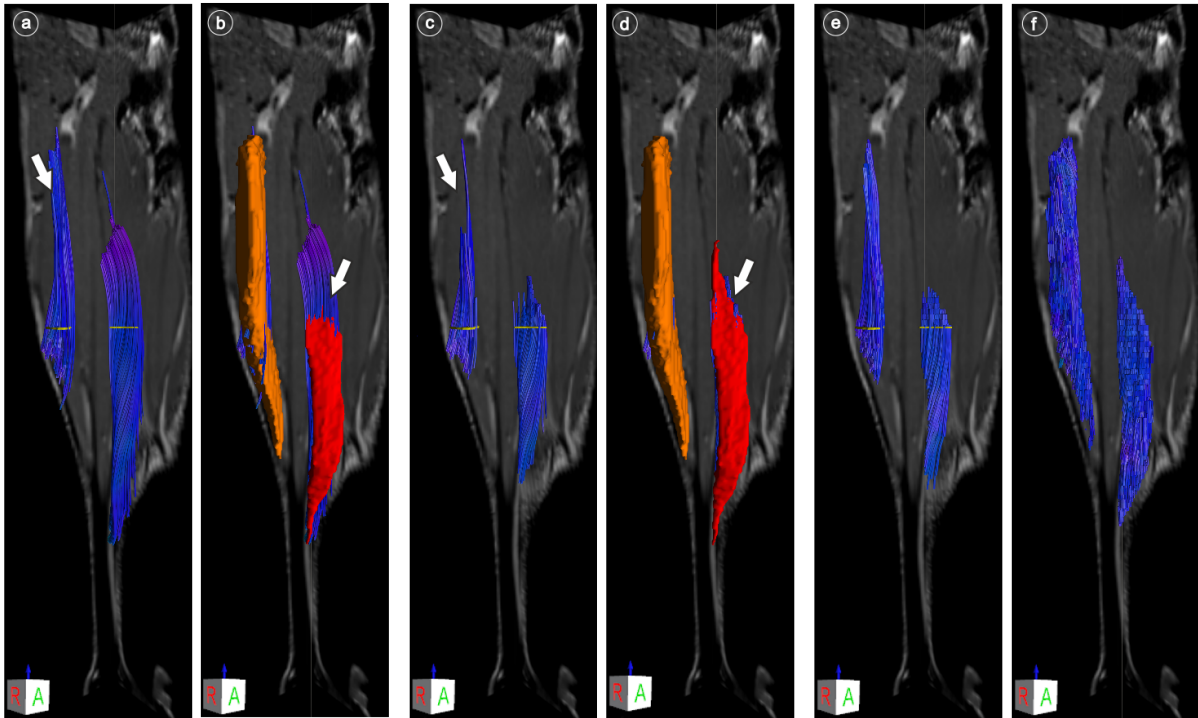


Figure 3.14: Reconstructed tracts for the SOL (red) and GM (orange) muscles, which pass through the selected transverse slices (yellow), without (a,c) and with (b,d) overlaid 3D ROIs. Tracking was performed without (a,b) and with (c,d) additional masking using anatomic image information [tracking stop criteria: $FA = 0.3$; maximum angle deviation 7°]. In (e,f), ROI-based fiber tracking results are displayed, which can be used to quantify the mean fiber lengths. For the SOL and GM mean lengths of (11.2 ± 6.2) mm and (16.2 ± 9.1) mm were determined, respectively. The TA (not shown here) revealed a mean fiber tract length of (19.2 ± 11.5) mm.

of the segmented muscles. Figure 3.14b visualizes the same tracts together with the 3D volumes of the GM (orange) and SOL (red). Fiber paths with great deflection and twisting arrangement relative to the leg's long-axis are observable, respectively. There are also some tracts that falsely cross boundaries between different muscles (white arrow in Fig. 3.14b for the SOL). This is most likely due to parallelly aligned muscle structures and/or partial volume effects. However, application of an additional mask obtained from thresholding the high-resolution T_2 -weighted MR images removed false tracts (white arrows in Fig. 3.14b and d), albeit this procedure reduced the number of fiber tracts within a muscle (resulting in less compact fiber bundles as visible for the GM; top left arrows in Fig. 3.14a and c).

To extract architectural parameters of the reconstructed muscle fibers, such as the mean fiber length, which is of particular interest in bio-mechanical studies, as accurately as possible and to evaluate the initial tracking results, tracking was confined to the manually segmented ROIs instead of using additional T_2 masking. The ROI-based tracking results for the SOL and GM muscles are shown in Fig. 3.14e and f, whereas Fig. 3.14e shows, analogously to Fig. 3.14a-d, slice-filtered fiber tracts. The T_2 - and ROI-masked fiber tracts reveal comparable results indicating that T_2 masking provides complete boundary detection but - as shown above - at

the cost of true fiber tracts within the GM (compare Fig. 3.14c and e). Based on the results shown in Figure 3.14f, where all fiber tracts within the two ROIs are illustrated, fiber tract lengths of the SOL and GM were determined yielding mean values of (11.2 ± 6.2) mm and (16.2 ± 9.1) mm, respectively. The TA (whose fiber tracts are not shown in this figure due to illustrative purposes) yielded a mean fiber tract length of (19.2 ± 11.5) mm.

3.3.3 Discussion

This animal study demonstrates the capability of STEAM-DTI to extract muscle architecture parameters, like fiber orientation and fascicle length. The single-shot images of the implemented turbo-STEAM DTI sequence do not suffer from geometric distortions, motion-induced phase errors, and have sufficient SNR. Compared to previous STEAM-EPI implementations, which were applied in human calf muscles [KARAMPINOS et al., 2012; STEIDLE and SCHICK, 2006], the proposed sequence provides improved spatial resolution for DW images without increased off-resonance-induced geometric distortions. In addition, employing long diffusion times provided high micro-structural contrast resulting in realistic fiber pathways.

The optimized turbo-STEAM DTI protocol yielded an effective isotropic resolution of 1 mm^3 by using a negative slice distance of -50% for (overlapping) 2-mm-thick slices and acquisition of a 256×72 pixel matrix. Nevertheless, turbo-STEAM DTI is affected by partial volume effects in slice and - more prominent - in PE direction (Fig. 3.10, Fig. 3.11). This is caused by imperfect slice excitation profiles and the decaying longitudinal magnetization, respectively. The latter limits the in-plane resolution along the PE direction and represents the major limitation of the proposed readout method. As each refocusing pulse successively expends the prepared STEAM magnetization within the repetitive FLASH readout interval, the actual signal distribution in k -space strongly depends on the applied rf flip angle of the α pulse, affecting the PSF in PE direction, thus limiting the feasible number of PE steps [HIEPE et al., 2011; FINSTERBUSCH and FRAHM, 2002]. Furthermore, intrinsic T_1 relaxation effects and diffusion-related signal losses contribute to blurring effects. Consequently, in this work the number of PE steps was minimized using parallel imaging and by acquiring a rectangular FOV. Although the number of acquired STEs was reduced to $n = 48$, a distinct signal decay over the echo train and therefore a reduced resolution in PE direction, was observed in this study. Retrospective simulations demonstrated a reduction factor of approx. 50% (Fig. 3.15).

Nevertheless, the achieved effective spatial resolution of approximately $1 \times 2 \times 1 \text{ mm}^3$ is, to the best of our knowledge, higher than in any previously published muscle DTI study conducted with clinical MRI scanners. Major future application of the turbo-STEAM sequence can be seen in small-FOV acquisitions, with low numbers of PE steps. Additionally, in order to reduce blurring by shaping the PSF, variable flip angles can be applied along the echo train [FRAHM et al., 1986]. This approach was, however, not applicable in the present experiments since it leads to a markedly reduced SNR due to a small starting flip angle ($\alpha_1 = 8.6^\circ$ for $n = 48$ echoes). Future sequence developments should explore alternative sampling schemes for the

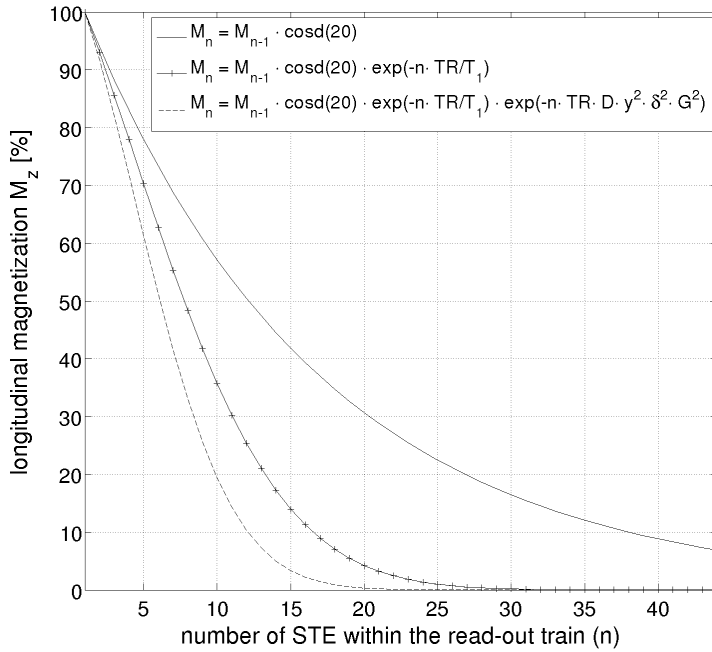


Figure 3.15: Simulated evolution of the longitudinal STEAM magnetization M_z during FLASH readout as a function of the stimulated echo number based on Eq. 3.10. Equal rf flip angles of the α pulses were assumed ($\alpha = 20^\circ$). Although the fractional consumption of the uniquely prepared M_z provides signal for more than $n = 48$ STEs, additive T_1 and diffusion-related signal losses result theoretically in totally consumed M_z already after ≈ 24 echoes. This lowers the spatial resolution in PE direction and, in turn, results in an effective spatial resolution of $\approx 1 \times 2 \times 1 \text{ mm}^3$.

readout module, such as radial trajectories [BLOCK et al., 2007], which are capable to minimize PSF blurring. In particular, PROPELLER trajectories would allow segmentation of the data acquisition into multiple shots [KRÄMER et al., 2012], thereby overcoming the limited number of PE lines and improving spatial resolution. At the same time, the repeated scanning of the k -space center with PROPELLER could improve SNR without increasing PSF blur, albeit at the cost of longer acquisition times. In *in vivo* experiments with minimum macroscopic motion, multi-shot acquisition technique based on segmented readout may represent an alternative. For instance, navigator-corrected DW-EPI provides a fast and motion-insensitive readout technique [JIANG et al., 2002]. This approach can be combined with DW-STEAM signal preparation, while accounting for eddy currents, B_0 -induced distortions and T_2^* -related blurring. Moreover, high-resolution DTI of larger objects containing small structures may be realized by interleaved inner volume imaging based on DW-EPI, which provides reduced geometric distortion and blurring [JEONG et al., 2006].

Previously proposed STEAM-DTI approaches were optimized for SNR of muscle tissue *in vivo* by employing b-values of $b \approx 600 \text{ s/mm}^2$ and diffusion times in the range 150 – 480 ms [KARAMPINOS et al., 2012; SCHWENZER et al., 2009; STEIDLE and SCHICK, 2006]. However, *ex vivo* measurements demonstrated that with increased diffusion time, the diffusion in the plane perpendicular to the mean fiber orientation becomes more restricted and the second and third eigenvalues decrease, whereas FA increases [KIM et al., 2005]. As such, it has been proposed to use long diffusion times, e.g. $\Delta \approx 1 \text{ s}$, to increase the FA and to decrease the cone of uncertainty in skeletal muscle DTI [SIGMUND et al., 2014]. In this study a diffusion time of $\Delta \approx 1 \text{ s}$ was chosen using the STEAM-DTI preparation module. The reduced SNR due to the increased mixing time TM was compensated by averaging and denoising based on Rician bias

correction and edge-preserving nonlinear image smoothing [HAHN et al., 2010]. The resulting images showed sufficient SNR (Fig. 3.10, Fig. 3.11) and provide fiber tracts with high structural integrity (Fig. 3.13, Fig. 3.14). In future studies, simulation of SNR and FA as functions of TM are beneficial required to minimize the SD of FA for a constant total scan time.

The long acquisition times of approximately 1.7 s per turbo-STEAM image did not result in significant motion-induced phase errors such as ghosting along the PE image direction (Fig. 3.10). However, residual motion artifacts in low-DW images, most likely resulting from arterial pulsation, may affect the determination of diffusion parameters (marked with arrows in Fig. 3.10). These effects can be eliminated in future studies by applying higher b-values for low-DW images or by electrocardiogram triggering. For human application, the proposed sequence may be problematic since nonrigid body motion during long scan times can not be completely avoided. Of note, the accuracy of ADC values measured by means of turbo-STEAM DTI is intrinsically limited because of the imprecise estimation of the effective b-value (leading to an overestimation of ADC values since the b-value is estimated for the first STE only) and the violation of the mono-exponential DWI signal equation (which is only applicable for free isotropic diffusion, thereby leading to an underestimation of the ADCs). However, the ADC values determined in this study (Tab. 3.1) are in the range of previously reported *in vivo* DTI studies, such as acquired in a mouse hind leg [HEEMSKERK et al., 2005] and human thigh muscles [BUDZIK et al., 2007].

Compared to ADC, the FA maps yielded increased inter-muscular contrast, probably corresponding to inter-muscular architectural differences (Fig. 3.11). In addition to local FA variations observed at muscle boundaries caused by different fiber orientation patterns of adjacent muscles (and partial volume effects), slight FA differences were found for different shank muscles. In particular, the TA (non-pennate) muscle revealed a significantly increased FA compared to the GM (pennate) muscle ($p < .001$). This is in line with results obtained in a cadaveric DTI study of human muscles [BUDZIK et al., 2007]. High inter-muscular contrast was also seen in CP, θ and ϕ maps (Fig. 3.11). The CP index, which accounts for diffusion perpendicular to the main fiber direction and is thus related to the fiber cross-sectional ellipticity [DEUX et al., 2008; HEEMSKERK et al., 2010], revealed higher values in the pennate muscle (GM) than in parallel muscles (SOL, TA; Tab. 3.1). This finding is in accordance with a previous DTI study [KARAMPINOS et al., 2009].

Complementary, the GM, which is involved in rapid leg movement, e.g. during jumping (plantar flexion), yielded higher zenith angles compared to the TA muscle (which is mainly involved in less powerful dorsal flexion). The pennation angles θ_{corr} of the TA, SOL and GM muscles were determined as $(8.3 \pm 4.6)^\circ$, $(11.3 \pm 6.1)^\circ$ and $(14.4 \pm 13.0)^\circ$, respectively. These results are similar to previously reported angles $[(3.0 \pm 1.0)^\circ, (8.5 \pm 1.5)^\circ$ and $(13.8 \pm 1.7)^\circ$, respectively], which, however, were measured (only) on the muscle surface by means of a dissecting microscope and a goniometer [LIEBER and BLEVINS, 2000]. Of note, the pennation angles of the SOL muscle were subsequently evaluated by manual dissection of the same probe and the corresponding results are reported in section 3.3.4.

Slice-by-slice analysis of the high-resolution θ and ϕ maps yielded further information about spatial fiber orientation patterns. Variations of the parameters were observed along the muscle's long axis with largest changes at the muscle boundaries (Fig. 3.12). In accordance, previous human DTI and fiber tracking studies have demonstrated physiological pennation angle heterogeneity caused by variations in the orientation of aponeuroses [LANSDOWN et al., 2007; HEEMSKERK et al., 2010]. Smooth variation of the azimuth angle ϕ in the inner muscular regions, i.e., of the SOL muscle, may be attributed to physiologically twisted fibers along the long axis. The structural connectivity of the shank muscles was further assessed by fiber tractography (Fig. 3.13). In particular, the GM and SOL muscles were evaluated and confirmed the presence of strongly deflected and twisted fiber paths relative to the long axis, respectively (Fig. 3.14). However, although fiber tracking was performed based on high-resolution DTI data, erroneously prolonged fiber tracts were obtained for both muscles. This phenomenon has already been reported in previous muscle DTI studies and is generally related to equally aligned structures imaged with a limited (effective) DTI resolution [HEEMSKERK et al., 2005; HEEMSKERK et al., 2010; KHALIL et al., 2010; FROELING et al., 2012].

For detailed delineation of fiber patterns and contraction-induced deformations of different muscle compartments, it is essential to track muscle compartments individually. Therefore, in this work, a combination of directional constraints, FA thresholding and additional T_2 masking based on anatomical T_2 -weighted MRI data was employed as stop criterion for the tract propagation process. The latter was enabled by the acquisition of geometrically undistorted MR images by using turbo-FLASH readout, which resulted in rigid matching between anatomical MRI and DWI data. This approach facilitates the reconstruction of fiber tracts with a reduced number of erroneously prolonged fiber tracts. Compared with ROI-based constrained fiber tracking using automatic muscle segmentation, which to our knowledge is still not straightforward to implement, T_2 masking of DTI data provides an alternative method to create muscle-specific fiber representations, which can be used in bio-mechanical models in the future (see sec. 3.5). Another parameter of particular interest in sophisticated bio-mechanical models is the muscle fiber length. For the SOL, GM and TA muscles, mean fiber lengths were determined as (11.2 ± 6.2) mm, (16.2 ± 9.1) mm and (19.2 ± 11.5) mm, respectively. These results are in good agreement with those obtained from *post mortem* studies reporting mean lengths of (13.8 ± 0.8) mm, (14.7 ± 0.7) mm and (38.1 ± 3.0) mm, respectively [LIEBER and BLEVINS, 2000]. The determined fascicle lengths reconstructed for the SOL (together with the corresponding pennation angles) were thoroughly evaluated by dissection of the fiber bundles from the same SOL muscle. The results of this validation study are presented in the next section.

3.3.4 Histological validation

Different attempts have been undertaken to validate DTI regarding determination of muscle architectural parameters. Initially, principal eigenvector directions in *ex vivo* rat TA muscle were compared with fascicle striation patterns visible on high-resolution MRI and on a longitu-

dinal section [VAN DONKELAAR et al., 1999]. These authors reported an acceptable accuracy of DTI fiber directions (error below $\pm 5^\circ$). Subsequently, Damon *et al.* studied the pennation angles of a rat GM by means of DTI and direct anatomical inspection using a protractor on the surface of the thickest part of the muscle belly [DAMON et al., 2002a]. They found a high correlation between the pennation angles determined with both methods ($\rho = 0.89$). However, both studies did not account for the high architectural diversity in skeletal muscles and may thus not be representative for the entire muscle volume. Larger muscular regions were examined in a pig tongue and almost equal fascicle angles measured with DTI and photon microscopy were reported [NAPADOW et al., 2001]. Unfortunately, these researchers did not perform statistical analysis. Further qualitative analyses were performed for human forearm [FROELING et al., 2012] and back muscles [SIEBEN et al., 2016] with good correspondences between photographs of dissected cadaver muscles and the reconstructed fiber tracts. Moreover, several *ex vivo* DTI-histology studies with fixed hearts documented statistically similar fiber orientations of the ventricular architecture (helix fiber orientation) for both methods [KUNG et al., 2011]. Hitherto, no study exists that validated 3-dimensionally both the pennation angles and fascicle lengths determined from *in vivo* DTI. Therefore, the present study aimed to compare quantitatively the pennation angles and fiber lengths of an entire muscle volume determined by means of turbo-STEAM DTI and histological examinations. The obtained results have been published in 2013 as an article in *Journal of Anatomy* [SCHENK et al., 2013].

Methodology

After the *in vivo* MRI measurements, the same animal was used to reconstruct the architecture of the SOL muscle using an established manual dissection/digitization method of fiber bundles from fixated muscle [ROSATELLI et al., 2008]. For *post mortem* manual digitization of the fascicles, the rabbit was euthanized with an overdose of pentobarbital, its leg was amputated above the knee, the skin removed and the preparation histologically fixed in Bouin solution for two days. Except for the SOL, all shank muscles were removed after muscle fixation and the preparation was cast in wax to provide additional mechanical stability during the digitizing process (Fig. 3.16). Small fascicle bundles were successively dissected with a micro forceps and their original position was recorded by using a manual digitizer (MicroScribe MLX®). This process was repeated until all fascicles of the muscle were recorded. In addition to the fascicle bundle positions, the insertion (calcaneus) and origin of the muscle (caput fibulae) were recorded to define the line-of-action (force axis). A detailed description of the data post-processing including 3rd order polynomial fitting of the fiber paths reconstructed from DTI and manual digitization as well as of the applied statistical methods is given in the paper of [SCHENK et al., 2013].

Results

Figure 3.16 illustrates the dissection of the cadaver muscle and the fascicle paths obtained with both methods. MicroScribe digitization and DTI yielded 131 fascicle bundles and 1606 tracts, respectively. The Kolmogorov-Smirnov test revealed that the pennation angle ($p = .59$) and the fascicle length ($p = .69$) determined by MicroScribe were normally distributed, whereas the DTI estimates did not show a Gaussian distribution ($p < .001$). Although the median pennation angles of both methods are close to each other (MicroScribe: median 9.7° , first quartile $Q_1 : 7.6^\circ$, third quartile $Q_3 : 12.0^\circ$; DTI: median 8.5° , $Q_1 : 6.7^\circ$, $Q_3 : 10.7^\circ$), the Mann-Whitney U-test revealed a significant differences in the pennation angle ($p < .001$). The median fascicle length measured with the MicroScribe system was 16.8 mm ($Q_1 : 15.5$ mm, $Q_3 : 18.5$ mm) compared with 18.2 mm ($Q_1 : 10.5$ mm, $Q_3 : 26.1$ mm) as determined with the DTI. In contrast to the pennation angles, the fascicle lengths did not differ significantly ($p = .22$) between both methods.

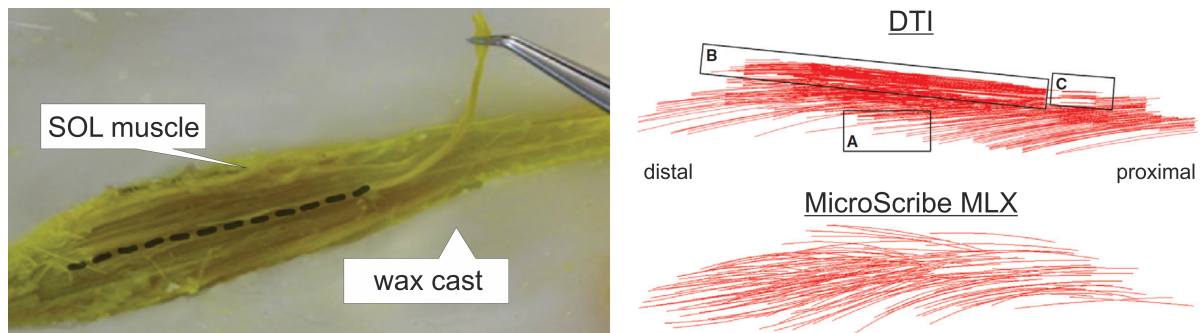


Figure 3.16: Anatomical preparation of the histologically fixed SOL muscle embedded in wax (left) and lateral view of the fiber tracts (right) determined with DTI and manual digitization (taken from [SCHENK et al., 2013]). The fascicle bundles were dissected using a micro forceps, whilst their original position was manually digitized by tracking the dashed line using the MicroScribe system. The comparison of reconstructed fibers between both methods indicates the gradual cut-off of the DTI tracts (A), the aggregation of non-physiological long DTI tracts at the anterior boundary of the muscle (B) and non-physiological short DTI tracts due to limited spatial resolution (C). Note that for illustration purposes only every third DTI fascicle tract is shown.

Discussion

Although the difference between the median pennation angles was small (1.2°), it was significant, which may be related to the unequal sample sizes (MicroScribe: $n = 131$ vs. DTI: $n = 1606$). It can be further explained by deviations of the force axis estimation with both methods. This interpretation is supported by the minimum and maximum pennation angles determined with both methods [MicroScribe: median = 9.7° , range between $(3.5 - 22.1)^\circ$ vs. DTI: median = 8.5° , range between $(0.9 - 20.7)^\circ$]. The deviation of the line-of-action estimation is due to the following reason: The distal tendon of the SOL is only a small part of the Achilles

tendon and is located at the lateral border of the Achilles tendon. The insertion area of the Achilles tendon at the calcaneus is about 5 mm wide, whereas the insertion area of the SOL tendon is limited to 1 – 2 mm within the Achilles tendon. Whilst during manual preparation it is possible to separate the tendon of the muscle from the other parts of the Achilles tendon and mark the muscle insertion very precisely, it is not possible with MRI to differentiate between the various components of the Achilles tendon due to the limited resolution and the low contrast between these structures. In future, ultra-short echo time (UTE) MRI sequences may provide superior delineation of tendinous tissue, as described in the last section of this chapter (sec. 3.5). Note, however, that deviations of the force axis may also result from slight differences of the ankle deflection between the measurements (MicroScribe: 83° vs. DTI: 94°).

The median fascicle lengths showed no statistical difference between both methods. DTI, however, showed a higher variance of the fiber lengths compared to manual digitization [MicroScribe: range between (12.5 – 23.1) mm vs. DTI: range between (2.7 – 61.5) mm]. Although fiber tracking was only applied within the ROI of the SOL, whilst the muscle surface served as stop criterion during the fiber tracking process, it resulted in artificially long fiber tracts, which can be attributed to equally oriented adjacent structures within the muscle. Such artificially prolonged tracts were reconstructed, e.g., on the anterior margin of the SOL (Fig. 3.16, B). Too short fascicle fragments near the muscle surface resulted from limited spatial resolution of DTI (Fig. 3.16, C). Despite these limitations, STEAM-based DTI represents an excellent tool to capture certain aspects of the inner muscle architecture, and differences in the observed pennation angle may have no true relevance for muscle (FE) simulation studies. Further, the proposed DTI sequence enables clinical investigations of muscle injuries as exemplarily demonstrated in the next section (3.4).

3.4 Application to human lower back muscles

Beyond application in animal studies the proposed turbo-STEAM DTI technique may also provide valuable information for characterizing degenerative changes in skeletal muscles, such as due to muscle injuries. For instance, DTI may allow the assessment of atrophic processes, which may be induced by direct injuries during surgery and are related to muscle denervations and ischemic impairments. One prominent example for such pathologies is back muscle atrophy after posterior spinal fusion of multiple spine segments caused by muscle retraction with long hours of excessive pressure [MIN et al., 2009; SUWA et al., 2000]. Despite being an established surgical approach to stabilize the spine after trauma or in degenerative diseases, a subset of patients suffers from chronic low back pain (LBP) after spinal fusion. Development of LBP in such cases is suspected to emerge from atrophy of injured back muscles and instabilities in adjacent vertebrae segments. Electro-physiological investigations recently performed in our lab characterized these atrophic changes by detecting altered muscle activation patterns in the back muscles of patients with spine fusion during isometric and dynamic loads. Subsequent bio-mechanical simulations using a human torso FE model ascribed these electro-physiological

alterations to increased muscular stress in the region of the implant (results not published yet). In line with these observations, posterior spinal fusion applied to rabbits resulted in atrophy of their back muscles (reduction in fiber size) and reduced adjacent paraspinal activity (decrease of EMG median frequency) with simultaneously higher muscle activity in the adjacent caudal and cranial regions [HU et al., 2008]. Furthermore, several studies were performed to compare the outcomes of conventional (open) and minimally invasive (percutaneous) surgery procedures. Although there are reports showing that less invasive approaches can reduce muscular injury and systemic inflammatory response immediately after surgery [KIM et al., 2006], no significant differences in the level of muscle degeneration measured by means of muscular fat infiltration and cross-sectional area were found between both surgery approaches in an one-year follow-up evaluation [MIN et al., 2009].

Generally, questions related to different factors affecting the severity of degenerative muscle impairments as well as to surgery-related effects on LBP development remain open to date. Against this background, DTI may provide a powerful, non-invasive tool to investigate degenerative changes of muscle architecture and thus to characterize surgery-related atrophic processes. Therefore, turbo-STEAM DTI was applied in a pilot study on healthy volunteers and patients with spine fusion in order to identify surgery-induced changes of architectural DTI parameters like FA, which is thought to indicate structural abnormalities of muscle tissue [NOSEWORTHY et al., 2010]. Besides being able to characterize structural ordering of skeletal muscles by using long diffusion times, turbo-STEAM DTI additionally provides low sensitivity to B_0 inhomogeneities, which is particularly beneficial in MRI of anatomies located near metal implants. In this initial study, it was hypothesized that both open and minimally invasive surgery induces similar modifications to the muscle micro-structural integrity, such as caused by the disruption of muscle cell membranes, which, in turn, result in changes of FA and fiber tractography.

3.4.1 Materials and Methods

Five patients with spinal fusion (2-4 weeks after surgery, three open and two percutaneous fusions of two or three lumbar segments) and five age-, gender- and BMI-matched healthy subjects (three male, two female, 31 – 59 years, BMI: 22-28) were examined on a clinical 3 T whole-body MRI scanner (TIM Trio; Siemens Healthcare, Erlangen, Germany) by using a standard spine coil. After anatomic imaging (T_1 -weighted VIBE sequence; 1.0 mm^3 , TE/TR = 0.8/5 ms, TA = 8.5 min), two turbo-STEAM DTI data sets were acquired (NEX = 2) each consisting of five low b-value images ($b = 5 \text{ s/mm}^2$, $\delta = 2 \text{ ms}$, $G = 5 \text{ mT/m}$) and 30 images with diffusion weighting in 30 different spatial directions ($b = 160 \text{ s/mm}^2$, $\delta = 2 \text{ ms}$, $G = 26.6 \text{ mT/m}$). Further sequence parameters were: TR/TR_{all}/TM = 11.9/1503/985 ms; $\tau_1 = \tau_2 = 7.5 \text{ ms}$; FOV = $336 \times 222 \text{ mm}^2$; 112×74 pixels; in-plane resolution of $3.0 \times 3.0 \text{ mm}^2$; bandwidth of 450 Hz/pixel. Twenty-two 6 mm-thick slices were acquired in coronal orientation aligned to the spine. Using a negative slice distance factor of -50% during interleaved 2D

acquisitions provided an effective isotropic resolution of 3.0 mm^3 . Parallel imaging was applied using a GRAPPA factor of three resulting in a turbo factor of 38 (number of acquired STEs with different PE). To avoid chemical shift artifacts, which can lead to mismapped fat compartments with distinctly lower diffusion coefficients than muscle tissue, fat suppression was applied using frequency-selective water excitation pulses. The total DTI acquisition time was 38 min.

For post-processing, DTI data were denoised using a local principle component analysis (PCA) approach, which filters the multi-directional data according to the strongest component (first eigenvector) within a moving 3D patch [MANJON et al., 2013]. This edge-preserving denoising method will be described in greater detail in the next chapter (sec. 4.3.4). Afterwards, the tensor was reconstructed using the Diffusion Toolkit (R. Wang, Athinoula A. Martinos Center for Biomedical Imaging, Massachusetts General Hospital, Boston, USA). ADC, FA and eigenvalue maps were calculated and subsequently analyzed by slice-wise ROI analysis. To this end, ROIs were defined in the anatomic MR images comprising the entire left and right back muscles using a manual segmentation software (<http://www.mitk.org/>). The ROIs were transferred to the DTI image space. In order to account for implant-induced image distortions and low SNR in DW images, corresponding voxels were excluded from the analysis. The identification of corrupted voxels was based on histogram analysis of the ROI voxel intensities normalized to their mean intensity value. As illustrated in Fig. 3.17, voxels with intensities below the 10% quantile and above the 90% quantile were excluded from further analysis. This allows to account for voxels showing a low SNR and/or image distortions, respectively. The latter criterion was only applied to the patient data. In the next step, a logical 3D mask defined by the remaining voxels was used to mask the DTI maps (ADC, FA, eigenvalues). The filtered data served as basis for slice-wise ROI analysis, which was performed along the head-feet direction. Mean and SD values of the DTI parameters were determined in three consecutive transverse slices, whilst the positions of the corresponding slices were defined by anatomic landmarks (center of vertebrae bodies). Finally, fiber tracking was performed using the FACT algorithm [MORI et al., 1999] with the surface of the muscle ROI and a maximum orientation change of 8° per iteration step (0.1 voxel) serving as stop criteria.

3.4.2 Results

Figure 3.18 shows representative T_1 -weighted MR images of a patient whose vertebrae bodies L1-L3 were fixed by a metal implant. In addition, bilaterally determined FA values for the five patients and the corresponding healthy controls are illustrated. As shown in Fig. 3.18a, morphological structures of the spine can be imaged with high spatial resolution, while signal cancellations and image distortions did only occur close to the metal implant restricted to a few millimeters around the lesion. Similar image artifacts are observable in turbo-STEAM images, which, however, were corrected by applying the histogram-based artifact detection (compare top and bottom row in Fig. 3.17). Corresponding anatomic images and mean FA values in Fig. 3.18a and Fig. 3.18b, respectively, exemplarily show that this patient data yields lower FA

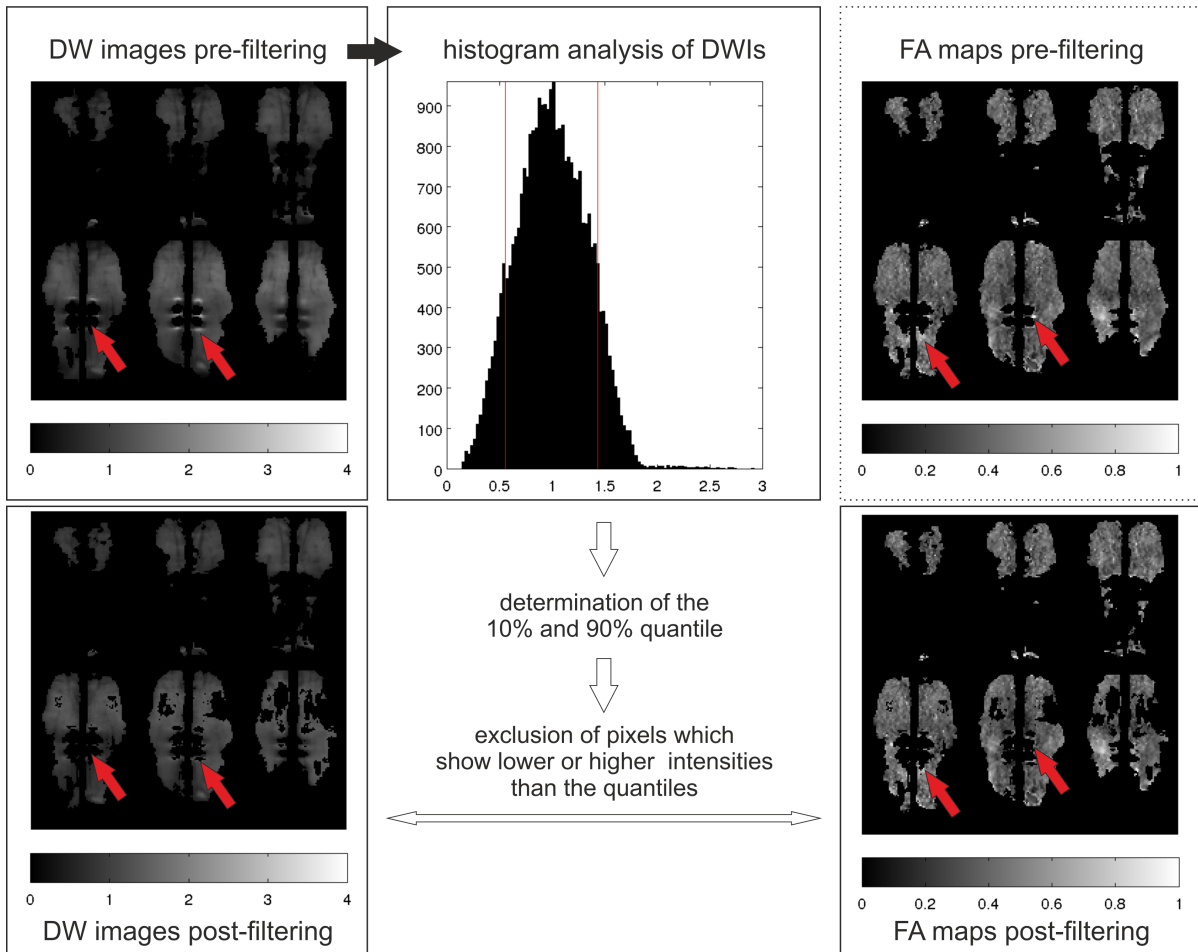


Figure 3.17: Representative multi-slice, coronal turbo-STEAM images ($b = 160 \text{ s/mm}^2$) and corresponding FA maps of a patient with fused vertebrae segments. All images were overlaid with the manually segmented ROI of the back muscles. It is visible that the implant induces signal alterations in adjacent muscles, which affect the FA maps (see red arrows). To account for the low SNR and the metal-induced signal alterations voxels of lowest ($<10\%$ quantile) and highest intensity ($>90\%$ q.) were detected by means of histogram analysis, respectively. Hereinafter, these voxels were excluded from ROI-based analysis.

values in the back muscles close to the fused vertebrae (marked as gray area) compared to his matched control. Contrary, no significant FA differences were observed in regions located below and above the fused segments. Additionally, both subjects show higher FAs cranial to the position of L2, which will be discussed later. As shown in Fig. 3.18c-3.18f, similar FA distributions were observed for the other patients and their matched controls. However, no obvious differences were found for ADC and tensor eigenvalues (thus these results are not shown here). Finally, back muscle fibers were tracked based on DTI data to visualize the surgery-related changes of the fiber architecture. The reconstructed fiber tracts of a representative control subject were compared with photographs of dissected lumbar muscles yielding close correspondence between DTI-based tractography and dissection results (compare Fig. 3.19a

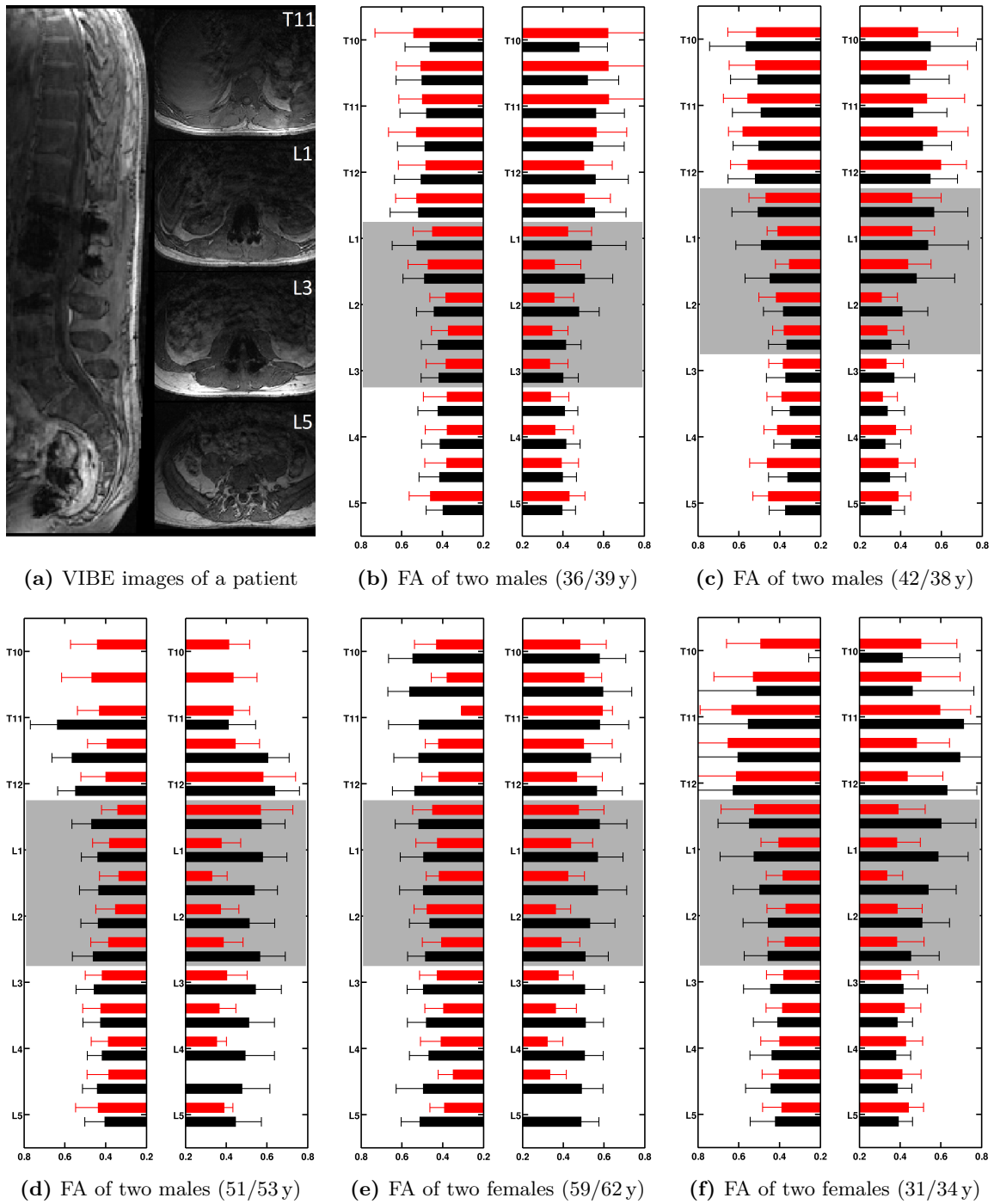


Figure 3.18: Representative mid-sagittal and transverse T_1 -weighted images of a patient after lumbar stabilization as well as bar plots of bilaterally determined FA values as a function of the anatomic position (defined by the vertebrae bodies) each including the results of one patient (red) and his or her matched control (black). The mean FA values (together with their SDs indicated by errorbars) predominately show differences between patients and controls at the position of the implant (marked as gray area).

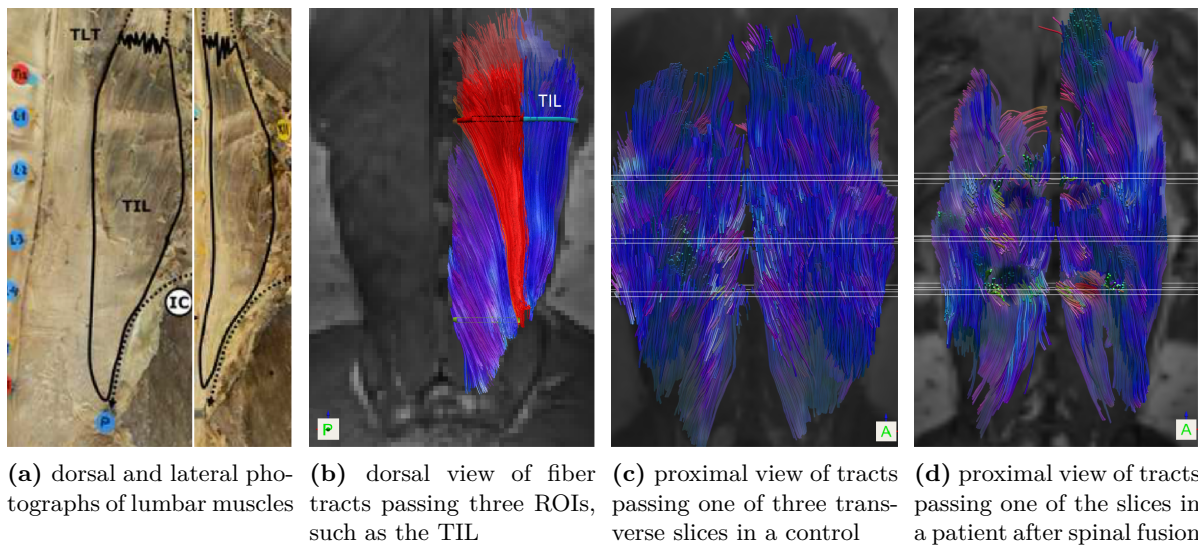


Figure 3.19: Photographs and reconstructed fiber tracts of back muscles. In (a) the dissected vertebrae bodies T12-S1, the iliac crest (IC), the thoracic part of *M. iliocostalis lumborum* (TIL) and the posterior superior iliac spine are marked (taken from [SIEBEN et al., 2016]). Images in (b-d) show tractography results overlaid on anatomic coronal images. The fascicle paths of the TIL muscle are closely corresponding between the photographs and the fiber tracts (a,b). Qualitative comparison of tracts obtained in a representative patient and in his healthy control (c,d) yields fewer and disordered fiber tracts in the case of spinal fusion (for illustration purposes only every fifth tract is shown).

and Fig. 3.19b). In particular, the tracts of the thoracic part of the superficial *M. iliocostalis lumborum* (TIL), which attaches the iliac crest (IC), show similar orientation patterns. The fiber paths given in Fig. 3.19b-Fig. 3.19c provide an impression of the architecture of deep and superficial back muscles. Assuming that fibers within each type of muscle are oriented equally and form a well organized and ordered structure in healthy state, regionally damaged muscle zones can be identified in patients based on Fig. 3.19d and 3.19c. These changes as well as the reported FA changes indicate a loss in the micro-structural integrity of back muscles in the surgical area.

3.4.3 Discussion

This pilot study demonstrates the feasibility of turbo-STEAM DTI to monitor surgery-related micro-structural changes in the back muscles of patients with spinal fusion. Combining STEAM-based DWI with FLASH-readout enabled quantification of DTI parameters even in muscle parts located close to metal implants. Furthermore, the application of long diffusion times during STEAM preparation facilitated the identification of structural changes, such as affected directional integrity of muscle fibers as quantified by the fractional anisotropy (FA). In particular, reduced FA values were found in the patients' back muscles with largest differences observed close to the implant. Together with representative tractography illustrations, which are prin-

cipally in good accordance with previous fiber tracking studies of lower back muscles [SIEBEN et al., 2016], the present results indicate a surgery-related loss of structural integrity.

In line with these results, similar observations have been made in previous DTI studies that reported lower FA values and disordered fiber structures in injured human calf muscles after muscle-tears [ZARAIKAYA et al., 2006] or by means of animal models [HEEMSKERK et al., 2006; HEEMSKERK et al., 2007]. Using an ischemic mouse muscle damage model, reduced FAs (and simultaneously increased ADCs) were documented that predominantly arose from increases of the second and third eigenvalue [HEEMSKERK et al., 2006]. These changes were associated significantly with the level of tissue damage as quantified by histology. Further, by using a femoral artery ligation model complex temporal and spatial patterns of the diffusion changes were reported [HEEMSKERK et al., 2007]. After induced ischemia, ADC, λ_2 , λ_3 as well as muscle T_2 increased significantly, with a maximum change at 3 days, when most muscle damage was observed with histologic analysis. At day 10, diffusion values were reduced overall, whereas T_2 remained increased, and at day 21, all parameters had largely returned to their normal values. Additionally, transient changes in the direction of the principal eigenvector during the period of maximum muscle damage were reported with more heterogeneous direction maps compared to the normal state, in which a well organized (ordered) fiber structure was observed.

Although only five patients were included in this pilot study with each being measured only once post surgery (2-4 weeks after intervention), and acknowledging that the processes due to (direct or indirect) muscle damage during posterior spinal fusion are potentially different from the processes occurring after muscle-tear or ischemia-induced injury, the presented results support the notion of structural disordering due to surgery. However, it is still unclear whether the FA changes remain constant and whether the structural changes can be ascribed to muscle denervations and/or ischemic impairments. Further limitations of the present study are related to the ROI-based analysis, which was restricted in patients to superficial muscle compartments that were not affected by the metal-induced image artifacts. It may be argued that this restriction introduces a systematic bias in the FA estimation since deep back muscles potentially show higher FA compared to the superficial compartments. However, qualitative comparisons of FA maps of patients and controls did not reveal systematic differences between both muscle regions. Thus, this effect was neglected in this pilot study. The interpretation of pathological changes is further complicated due to the high diversity of FA values along the head-feet direction (i.e., trend of higher FA values cranial to L2). By considering previously described FA increases in passively stretched muscles [SCHWENZER et al., 2009], spatially dependent FA alterations along H-F direction may be ascribed to pressure-induced passive deformation of the muscles while lying in the MR scanner (indicated by Fig. 3.18a). Furthermore, higher fractions of connective tissue, such as aponeuroses, may result in lowered FA values in these regions (caudal to L2).

In conclusion, turbo-STEAM DTI can be used to study changes of micro-structural integrity after muscle damage, such as due to surgery, whilst DTI quantities, like FA, may serve as quantitative markers for muscle damage with potential applicability in (pre-)clinical therapeutic

screening studies. In follow-up studies, larger patient cohorts with different surgical approaches (open vs. percutaneous) have to be investigated, while accounting for the post-surgical period and the applied treatment strategy. Future examinations in our lab will aim to evaluate structural and metabolic turnover changes of back muscles after surgery by means of combined DTI and ^{31}P -MR spectroscopy (the latter will be introduced in the next chapter). This may provide deeper insights into muscle damage and repair mechanisms. Further, it may allow to monitor therapy-induced improvements of muscle function and to optimize therapy strategies. The DTI-based fiber path information can be used to assess functional implications of muscle (sub-)compartments and thus to constrain individualized bio-mechanical models, which are promising tools in movement sciences and LBP research (see next section).

3.5 Future directions

Since diffusion tensor changes are related to muscle contraction, DTI might become an important tool for the evaluation of muscle function in the future [DEUX et al., 2008; SCHWENZER et al., 2009; SINHA and SINHA, 2011]. In particular, the proposed turbo-STEAM DTI provides information of the individual deformation of fiber bundles during contraction with respect to the intrinsic architectural diversity. This sequence also provides high sensitivity against restricted diffusion processes resulting in high FA values, large numbers of tracked muscle fiber bundles over long distances and a low within-subject dispersion of the pennation angle [NOEHREN et al., 2015]. Hence, turbo-STEAM DTI enables valid 3D reconstruction of the muscle architecture and assessment of structural parameters that may serve as the basis for individualized 3D bio-mechanical finite element (FE) models [BLEMKER et al., 2007; SIEBEN et al., 2016]. Such models help to simulate realistically contractile behavior and are consequently of special interest for bio-mechanical researchers.

Although FE models already appear in various domains of our daily routine - from optimized objects, like footwear, orthopedic arch support, prostheses, over films and video games to areas, such as medical device design, surgery simulations and ergonomics - they are limited to the usage of simplified and therefore, in most cases, unrealistic muscle architectures [BÖL et al., 2013]. In addition, the models are not validated in such a way that they are able to predict correct muscle forces and shapes of muscle packages during contraction periods so far. In order to shed light on such evolution processes and to allow more accurate simulations of muscle properties, the development and utilization of 3D muscle models is required based on comprehensive data sets including information about force evolution (force-velocity, force-length and force-strain relations), active muscle force response and alignment of the fibers measured from the same muscle [BÖL et al., 2013]. The latter, which is enabled by means of DTI, has already been successfully applied in bio-mechanical research by generating accurately shaped FE meshes of a rat GM muscle and including DTI information of the muscle fiber architecture [VAN DONKELAAR et al., 1999]. The results of this and subsequent research indicate that, besides morphological information (muscle volume, tissue composition), knowledge of the fiber

orientation may significantly improve the model-based simulations of force development and transmission [BÖL et al., 2011].

Recent attempts to generate comprehensive multi-scale 3D FE models incorporating muscle fiber and motor-unit distributions or consisting of data describing characteristic force responses, 3D muscle shapes during isometric, isotonic and isokinetic contractions as well as fascicle orientation throughout the whole muscle are limited to generalized structural information taken from the literature [RÖHRLE et al., 2012b] or isolated muscles only [BÖL et al., 2013]. This information, however, may significantly differ from integrative muscle structure *in vivo* and may thus potentially limit the accuracy of muscle deformation and force generation simulations [SIEBERT et al., 2014]. Therefore, DTI-based *in vivo* measurements of muscle architecture obtained from multiple members of a synergistic group of muscles may offer a spectrum of new and exciting possibilities to generate adequate 3D bio-mechanical FE models. Such models may benefit, for instance, from multi-parametric MRI, which is able to provide information about muscle volumes, muscle moment arms, muscle geometry, joint kinematics and fascicle architectures at the same time [BLEMKER et al., 2007]. Furthermore, dynamic imaging techniques, such as kinematic MRI (acquisition of static images at multiple joint positions), cine phase-contrast MRI and real-time MRI can be combined to characterize strain fields predicted by the models. However, conclusions drawn from current MRI measurements of muscle motion are limited by inaccurately measured velocities or displacements within tendons that play an important role in muscle mechanics. Therefore, ultra-short echo-time (UTE) pulse sequences, which provide reliable imaging of tendinous tissue [ROBSON et al., 2004], may enhance the value of dynamic MRI in the future. Once a detailed FE muscle model is available, which would reproduce experimental findings, such as force evolution, it could be used to intensify our understanding of muscle deformations, strain fields, functional implications, internal muscle forces and the influence of muscle architecture on contraction dynamics [BÖL et al., 2013]. It could also be used to obtain deeper insights into fatigue effects [RÖHRLE et al., 2012a; BÖL et al., 2011], growth phenomena [ZÖLLNER et al., 2012], damage aspects [ITO et al., 2010] and electro-mechanical activation behavior of muscles [RÖHRLE, 2010].

Future muscle DTI examinations may benefit from an analysis of the muscle fiber curvature, which characterizes the stresses developed by intra-cellular contractile proteins [DAMON et al., 2013]. Development of alternative acquisition techniques (discussed in sec. 3.3.3) in conjunction with dedicated tensor models may provide more precise estimation of muscle DTI parameters. E.g., using a two-compartment model for tensor reconstruction considering anisotropic diffusion in the intra- (muscle fiber cell) and isotropic diffusion in the extra-cellular space (endomysium/perimysium) may allow to account for intra-muscular fat infiltration, which represents an important determinant of muscle atrophy [SINHA et al., 2015]. Such advancements may also improve the estimation of tensor-based structural parameters like the planar index CP [KARAMPINOS et al., 2009]. In addition, diffusion time and diffusion weighting-dependent DTI can be applied to enhance the micro-structural specificity by assessing muscle fiber diameters [SIGMUND et al., 2014] and tissue heterogeneity [MARSCHAR et al., 2015], respectively. The

latter is assessable by means of diffusion kurtosis imaging (DKI), which quantifies the dependence of diffusion parameters on the diffusion weighting and, thereby, provides micro-structural information [MARSCHAR et al., 2015]. Of note, future DTI studies may also benefit from moving to higher field and gradient strengths ($> 7\text{ T}$, $> 1\text{ T/m}$) by overcoming the major challenge of limited SNR as prevailing in muscle DTI. This would facilitate DTI acquisition with higher spatial and temporal resolution allowing to assess skeletal muscle function in greater detail [GONDIN et al., 2014].

Last but not least, recent studies have already demonstrated the clinical usefulness of muscle DTI, such as in monitoring degenerative muscle diseases [HOLL et al., 2008], in planning of tendon transposition surgery [KREULEN and SMEULDERS, 2008] or in the evaluation of acute muscle injury [ZARAISKAYA et al., 2006], ischemia [HEEMSKERK et al., 2006], dystrophy [MCMILLAN et al., 2011], inflammation [QI et al., 2008] and aging [SINHA et al., 2015]. Furthermore, the capability of muscle DTI in characterizing the atrophy due to denervation [ZHANG et al., 2008], ischemic infarction of heart muscle [WU et al., 2011] and muscle adaptations induced by training or rehabilitation [OKAMOTO et al., 2012] was demonstrated. And despite many difficulties, DTI can be applied in the field of *in vivo* cardiac imaging to better understand cardiac function, characterize cardiac pathology, and understand muscle fiber remodeling in response to injury or disease [KUNG et al., 2011]. Overall, basic and clinical research studies based on DTI and appropriate muscle models may contribute to a deeper understanding of bio-mechanics and widespread diseases, and thus are a key factor of future musculoskeletal examinations.

4 Quantitative MRI and MRS of muscle function

In addition to muscle morphology and fiber architecture, muscle function characterized by metabolic and vascular properties represents the major determinate of muscular capacity. Against this background, this chapter introduces muscle functional MRI (mfMRI) techniques, which enable the quantitative assessment of muscle function with high spatial resolution. After a brief introduction of the technical principle and the clinical relevance of mfMRI (sec. 4.1), phosphorus MR spectroscopy (^{31}P -MRS) based on chemical shift imaging (CSI) and quantitative T_2 -weighted MRI will be introduced in more detail (sec. 4.2, sec. 4.3). While ^{31}P -CSI enables spatially resolved quantification of load-induced metabolic changes, the T_2 -based mfMRI provides high-resolution activation maps, which are determined by a mixture of metabolic and vascular responses to muscular loading. In the subsequent section, a novel DWI-based mfMRI approach will be introduced, which relies on an analytic model allowing quantitative differentiation between load-induced diffusion and perfusion changes (sec. 4.3.4). After explaining its physiological basis and technical principle, an *in vivo* study including ^{31}P -CSI, T_2 and DWI-based mfMRI applied to healthy, human back muscles will be presented (sec. 4.4). This study aims at the evaluation of interrelated, load-induced T_2 , metabolic, perfusion and diffusion changes in a cohort of young, healthy volunteers, and was published in 2014 as an article in *NMR in Biomedicine* [HIEPE et al., 2014a]. In order to investigate age-related changes of the back muscle morphology and function, the proposed multi-parametric mfMRI approach was extended in a subsequent study by morphological MRI and applied to two different age groups (sec. 4.5). This study was published in 2015 as an article in *Experimental Gerontology* [HIEPE et al., 2015]. Finally, the results of both studies will be discussed in terms of their significance for understanding multi-focal mechanisms occurring during healthy aging as well as in diseased states, such as in the case of non-specific low back pain (sec. 4.6).

4.1 Introduction

Non-invasive mfMRI enables identification of activated muscles and has been increasingly used in recent years to resolve spatial patterns of muscular involvement in exercising human leg [ABABNEH et al., 2008; DAMON et al., 2003; TAWARA et al., 2011; VANDENBORNE et al., 2000] and lower back muscles [CLARK et al., 2009; D’HOOGHE et al., 2013; DICKX et al., 2010a; MAYER et al., 2005]. By regarding recently documented increased mfMRI activation [D’HOOGHE

et al., 2013] and more asymmetric mfMRI activation patterns [CLARK et al., 2009] in loaded low back muscles of patients suffering from low back pain (LBP), mfMRI seems to be of advantage for assessment of muscle impairments during manifestation of chronic non-specific LBP. Furthermore, little is known to date about the physiological determinants affecting muscle function during healthy aging. Generally, it is assumed that functional impairments result in reduced maximum force capacity, while endurance, such as assessed with moderate back extension exercises, is widely preserved during aging [CHAMPAGNE et al., 2009; YASSIERLI et al., 2007]. Functional determinants showing age-related changes are, e.g., the vascular and metabolic capacities in the loaded state, such as previously reported for human calf [WRAY et al., 2009] and back muscles [YANAGISAWA et al., 2009]. In addition, LBP patients reveal increased fatigability during isometric endurance tests [BIERING-SORENSEN, 1984; PANJABI, 2003]. Hence, non-invasive measurement of muscle functional determinants by means of mfMRI potentially represents an important tool to investigate degenerative modifications in both normal and pathological state.

The mfMRI technique is based on the acquisition of T_2 -weighted MR images before and after muscular loading and subsequent quantitation of the spin-spin transverse relaxation times T_2 (details given in sec. 4.3.3). Thereby, on the one hand, the activated muscles can be visually identified by enhanced signal intensity on T_2 -weighted images and, on the other hand, the T_2 time constants calculated from a series of T_2 -weighted images with different echo times provide a direct quantitative measure of muscular activation. The latter can be used to compare muscle recruitment in different muscles and in different functional examinations. Previously, transient activity-induced T_2 increases were observed in skeletal muscles already after few contractions, rising to a work-dependent steady-state within a few minutes of repeated contractions, and recovering completely within 20 – 30 min following exercise [PATTEN et al., 2003]. Over a finite range of sub-maximal workloads, the relationship between increased signal intensity and muscle work was linear as reported for human calf [FISHER et al., 1990] and back muscles [DICKX et al., 2010b]. Although the full set of mechanisms influencing T_2 is not yet fully understood (discussed in sec. 4.3.1), osmotically driven water shifts from extra- into intra-cellular spaces have been reported as important determinants in response to the intra-muscular accumulation of hydrogen ions and small metabolic osmolites [BENDAHAN et al., 2004; DAMON et al., 2003; DAMON and GORE, 2005; SAAB et al., 2000]. These conclusions were driven from previous studies that combined mfMRI and dynamic ^{31}P -MRS, where the latter enables quantitation of energy metabolites, including inorganic phosphate, phosphocreatine, adenosine triphosphate, and pH changes in loaded muscles (further details given in sec. 4.2).

Recently, it was, however, demonstrated that load-induced T_2 changes are not completely explained by metabolic changes as observed with localized ^{31}P -MRS [CANNON et al., 2013]. Alternatively, the effect of increased extra-cellular and/or blood volume, which results in increased molecular diffusibility and elevated vascular volume fraction, has been hypothesized by several authors to additionally contribute to the T_2 changes in exercised muscles [ABABNEH et al., 2008; DAMON and GORE, 2005; MORVAN and LEROY-WILLIG, 1995; MORVAN, 1995]. Using modern

MR scanners molecular diffusion and vascular volume fraction of skeletal muscles became assessable by applying DWI in combination with the intra-voxel incoherent motion (IVIM) model (sec. 4.3.4). Recent muscle IVIM studies demonstrated the feasibility of extracting diffusion and perfusion properties in the resting [CALLOT et al., 2003; KARAMPINOS et al., 2010] and exercised state [FILLI et al., 2015; YANAGISAWA et al., 2009]. However, combined analyses of T_2 - and DWI-based mfMRI in exercised skeletal muscles have not been performed yet and experimental verification of an association between exercise-induced T_2 and diffusion or vascular volume changes is still required.

The primary goals of this work were therefore, first, to demonstrate the application of mfMRI in combination with dynamic ^{31}P -CSI and IVIM-based DWI for improved differentiation between diffusion, perfusion and metabolic effects in exercised low back muscles by using an isometric trunk-extension exercise with potentially high clinical relevance in diagnosing LBP, and second, to explore changes of structural and functional MR parameters between different age groups in order to investigate mechanisms of impaired muscle function. To this end, changes of T_2 , high-energy metabolism, molecular diffusion coefficients and vascular volume fractions were determined in the lower back muscles *M. multifidus* and *M. erector spinae* of young and late-middle-aged healthy subjects by using a self-constructed MR-compatible ergometer (which is presented in sec. 4.4.1). In a first step, the previously reported hypothesis that changes in metabolism and vascular volume fraction are underlying the T_2 alterations in activated muscles was evaluated based on data obtained in the young cohort by means of multi-factorial mixed models, in which changes in T_2 were related to changes in metabolism, molecular diffusion and vascular volume fraction (results given in sec. 4.4).

In a second step, the multi-parametric mfMRI approach was applied to a second age group of late-middle-aged subjects and extended by high-resolution T_1 -weighted anatomic MRI in order to determine muscle cross-sectional areas and fat infiltration, which both represent important biological contributors to the age-related loss of muscle strength [GOODPASTER et al., 2006; KORHONEN et al., 2006; NILWIK et al., 2013] and are potentially related to the development of LBP [D'HOOGHE et al., 2012; FISCHER et al., 2013; HEBERT et al., 2014; KJAER et al., 2007]. Hitherto, comprehensive analyses of age-related structural (muscle cross-sectional area, fat infiltration, fiber structure and composition) and functional alterations (load-induced vascular and metabolic changes) in skeletal muscles have so far not been performed. Therefore, the obtained structural and functional MR quantities were compared between the two age groups allowing to explore (i) age-related changes of vascular volume fraction and metabolic turnover, (ii) effects of these changes on load-induced alterations of T_2 relaxation as well as (iii) associations between age-related changes of structural and functional parameters (findings reported in sec. 4.5). It was hypothesized that functional determinants show age-related changes, whilst the fatigability, however, remains practically unchanged (preserving of muscle endurance), and that the functional impairments are related to structural changes, such as quantified via perfusion-sensitive mfMRI (providing a surrogate for muscular vascularity) and fat infiltration measurement (surrogate for muscle atrophy).

4.2 Quantification of high-energy metabolism using ^{31}P -MRS

In order to provide a basic understanding of the physiological principle of mfMRI, this section introduces metabolic processes of skeletal muscles in greater detail (based on sec. 2.1.4), and describes, how they can be non-invasively assessed by means of phosphorus magnetic resonance spectroscopy (^{31}P -MRS).

4.2.1 MR spectrum of phosphorous-containing compounds

Studies of muscular bioenergetics were among the first applications of *in vivo* ^{31}P -MRS in humans, while this method was - for over a decade - the workhorse for muscle physiologists who investigated high-energy phosphates and intra-cellular pH at different physiological and pathological conditions [BOESCH, 2007]. Although the number of phosphorus-containing compounds in muscle is quite large, the *in vivo* ^{31}P -MR spectrum is rather simple and mainly comprises signals of adenosine triphosphate (ATP), phosphocreatine (PCr) and inorganic phosphate (Pi), metabolites that play central roles in tissue energetics (Fig. 4.1). The following compounds are present in lower concentrations and do not contribute significantly to the signal of the spectrum: phosphomonoesters (PME; including glucose-6-P, fructose-6-P, inosine monophosphate and adenosine monophosphate) and phosphodiester (PDE; such as membrane and bone phospholipids).

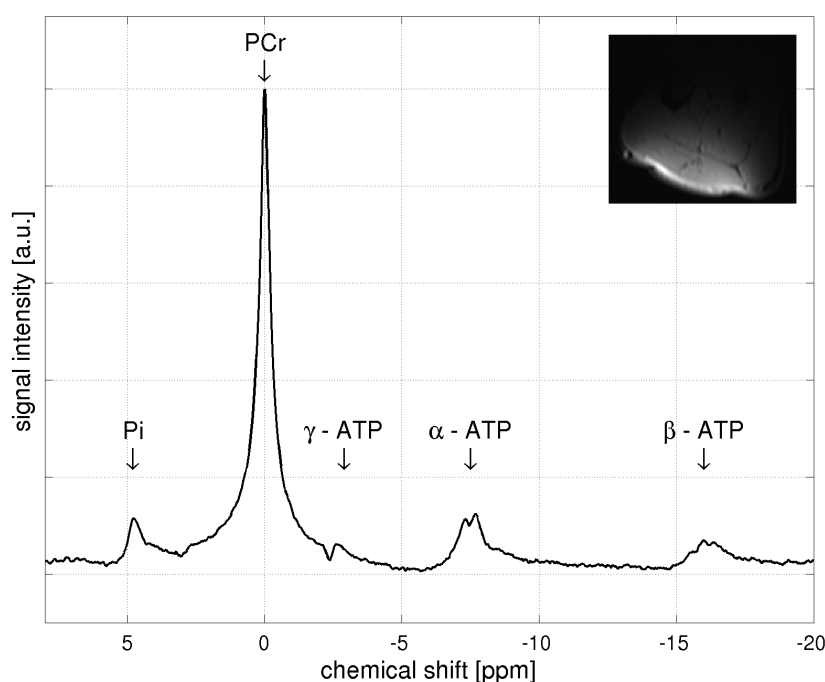


Figure 4.1: Non-localized ^{31}P -MR spectrum of resting human calf muscles acquired at 3 T by using a small ring coil. The spectrum was frequency-, phase- and baseline-corrected and contains peaks of the high-energy metabolites PCr, Pi and ATP. The α , β and γ -ATP peaks refer to the different phosphoryl groups starting with the group closest to the ribose (sugar molecule).

In general, MRS utilizes the effect that different chemical bonds create different shieldings of the main magnetic field at the location of the nucleus and thus lead to shifts of its Larmor frequency [HAACKE et al., 1999]. The distance of the resonance frequencies from a chosen reference frequency (ν_{ref} ; in ^{31}P -MRS typically corresponding to the PCr resonance) is termed

chemical shift δ and is expressed in parts per million (ppm) relative to the system operating frequency (ν_0):

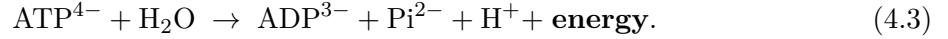
$$\delta = \frac{\nu - \nu_{\text{ref}}}{\nu_0} \times 10^6. \quad (4.1)$$

The Fourier Transform of the acquired spectroscopic FID signal results in an MR line spectrum, where the areas under the peaks are directly related to the metabolite concentrations in the sample. Although the determination of absolute metabolic concentrations is feasible because the resting ATP concentration in muscle is relatively constant at 8.2 mM [DAWSON, 1982], it is notoriously difficult since effects of T_1 and T_2 relaxation and signal overlapping, such as of Pi and PDE, during intense loads, have to be taken into account. For this reason, relative signal intensities normalized to the sum of the ATP peak integrals are used in this work to compare dynamic spectra. In addition, ^{31}P -MRS allows determining intra-cellular pH, which is based on the fact that the Pi peak shifts in response to different concentrations of the mono- and di-protonated forms of Pi ($[\text{HPO}_4^{2-}]$ and $[\text{H}_2\text{PO}_4^-]$) and can be derived from the Henderson-Hasselbalch equation [DAWSON, 1982]:

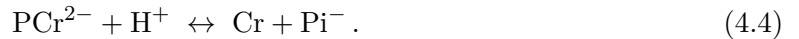
$$\text{pH} = 6.75 + \log \left[\frac{\delta - 3.27}{5.69 - \delta} \right]. \quad (4.2)$$

4.2.2 Muscular bioenergetics observed by ^{31}P -MRS

High-energy phosphates and pH dynamics are important indicators for the energy supply of muscles during load, which is based on the splitting of ATP into adenosine diphosphate (ADP) and inorganic phosphate [BARRETT et al., 2003]:



The additional omitting of H^+ ions leads to pH decrease in loaded muscles. In order to maintain a constant ATP level, ATP is re-synthesized by means of PCr hydrolysis, anaerobic and aerobic glycolysis as well as by oxidative splitting of fatty acids [BARRETT et al., 2003]. As the latter two processes need some starting time, the initial ATP demand during workload is buffered by PCr hydrolysis to compensate for a temporary ATP shortfall immediately after the onset of exercise:



Hence, PCr serves as a short-term Pi reservoir, which will be metabolized in the creatine kinase (CK) reaction to re-synthesize ATP from ADP with an additional release of creatine:



This process allows high-intensity workload of short duration, i.e. 10 – 20 s, until the PCr pool is depleted [GASTIN, 2001]. Therefore, an increased ADP concentration triggers anaerobic glycolysis, which metabolizes the cellular glycogen to lactic acid via glucose-6-phosphate (with a

net yield of only 2 ATP/glucose) with its peak after ≈ 0.5 min. After ≈ 1 min, the most efficient aerobic decomposition of glucose and fatty acids (aerobic respiration yields 34 ATP/glucose) supersedes the glycolytic ATP production, while pulse- and respiratory frequency are increased until the requirements of muscle metabolism are met by aerobic ATP re-synthesis (equilibrium is achieved after several minutes). Only during high-intensity loads, when the aerobic pathway is insufficient, glycolysis continues by decomposing glucose delivered by the blood. With aerobic ATP synthesis reaching a steady-state, the PCr decline stops and the remaining PCr pool behaves as a shuttle for the transport of high-energy phosphates between the sites of production and utilization of ATP [BARRETT et al., 2003].

The dynamics of load-induced PCr depletion, Pi accumulation and pH alterations can be directly observed with dynamic ^{31}P -MRS by regarding, however, the limitation that the measured time courses reflect the superposition of the processes in multiple muscle fibers with different bioenergetic properties [RZANNY et al., 2016]. A representative stack-plot of ^{31}P -MR spectra obtained in exercising human calf muscles is given in Fig. 4.2. It can be seen that during onset of exercise, PCr degradation (through the CK reaction) is the major source of Pi, and the time course of Pi is almost stoichiometric with the breakdown of PCr. Due to the accumulation of degradation products, such as Pi and lactate, the Pi peak increases and shifts towards lower δ , indicating tissue acidification [TSCHIESCHE et al., 2014].

The rates of PCr breakdown and Pi accumulation together with the pH shift are associated with the exercise-induced metabolic stress defined by the exercise conditions, such as workload and oxygen supply to the muscle. At low exercise intensities, homeostasis of the ATP concentration leads to moderate PCr decline without significant pH changes [ROUSSEL et al., 2003]. Strong workloads, as demonstrated in Fig. 4.2, result in completely consumed PCr and significantly reduced post-exercise pH values due to the higher rate of anaerobic glycolysis [TSCHIESCHE et al., 2014]. In general, the transition phase of progressive PCr decline to reach a steady-state (PCr hydrolysis equilibrium) normally follow a mono-exponential time-course with time constants typically ranging from 20 – 70 s (Fig. 4.2). In order to extract these time constants a temporal resolution of the spectroscopic measurements of 5 – 15 s is required.

4.2.3 Non-localized ^{31}P -MR spectroscopy

Combining surface coil based localization with ^{31}P -MRS without any volume selection represents a most suitable approach for functional, high-temporal-resolution measurements in skin adjacent muscles. Thereby, the volume-of-interest selection is intrinsically defined by the sensitivity profile of the surface coil and no spatial encoding of the signal is required. When acting as transmitter and receiver, the sensitivity profile of a circular coil forms a hemisphere penetrating into the volume with a radius approximately equal to the coil radius [ACKERMAN et al., 1980]. Since no preparation time due to gradient switching is required, acquisition of the FID follows immediately the 90° rf pulse. This intrinsically avoids any T_2 weighting of the recorded signal and provides high SNR in spectra even when selecting short repetition times

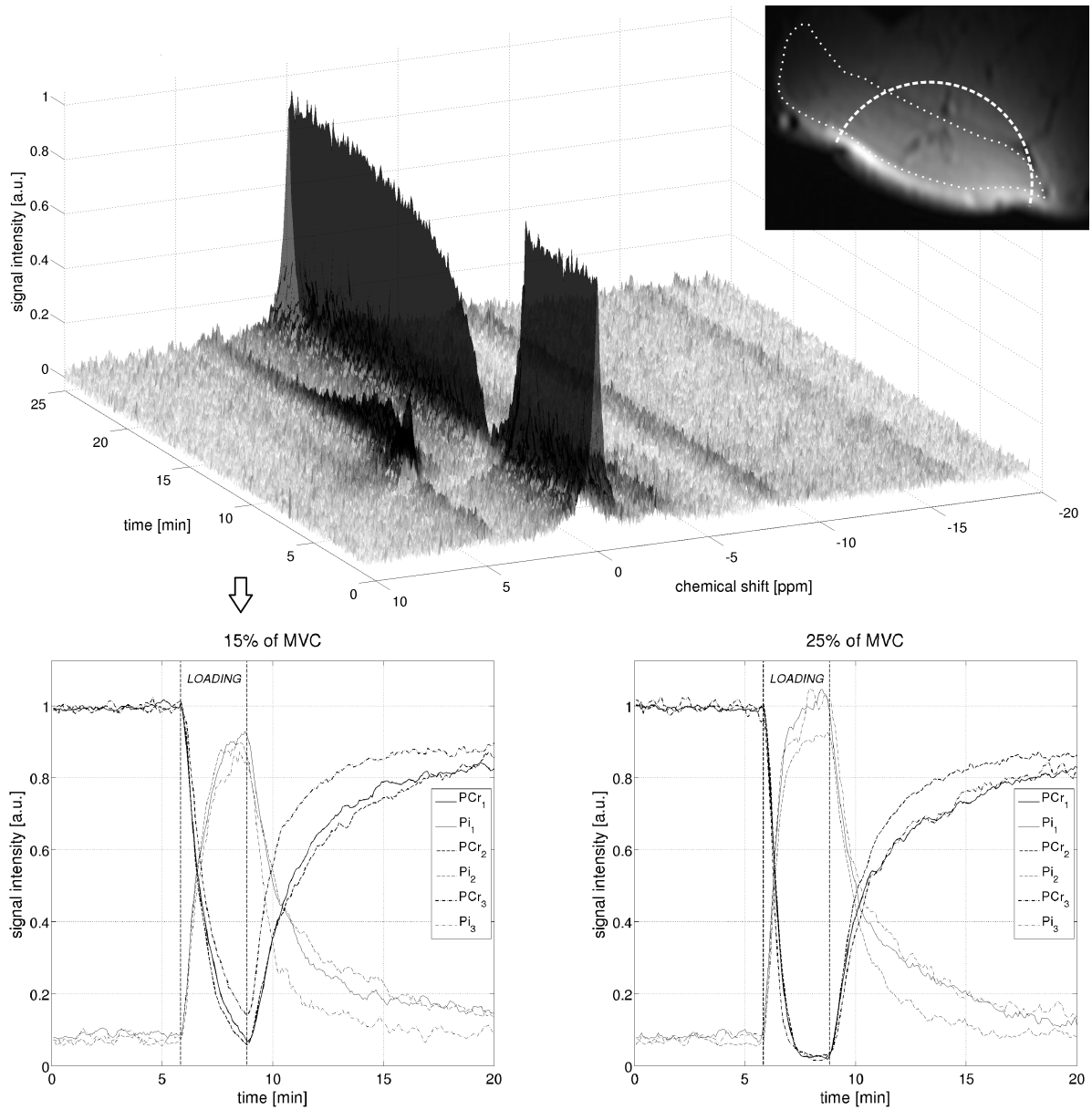


Figure 4.2: Dynamic ^{31}P -MRS in human calf muscles. Top: A representative stack-plot of non-localized ^{31}P -MR spectra showing declining PCr and increasing Pi intensities as well as a significant Pi signal shift during the exercise period (6 – 9 min). Bottom: Multiple time courses of PCr and Pi intensities that were quantified based on data acquired at two different work-levels (15% and 25% of maximum voluntary contraction, MVC) and smoothed by moving averaging of five consecutive spectra (adapted from [TSCHIESCHE et al., 2014]). Results of the repetitively performed measurements ($n = 3$) indicate the reproducibility of metabolic quantities measured by means of dynamic ^{31}P -MRS. Higher loading (25% of MVC) yielded faster mean PCr and Pi changes ($\tau_{\text{PCr}} = 27.6\text{ s}$, $\tau_{\text{Pi}} = 28.0\text{ s}$) and higher mean pH changes ($\Delta\text{pH} = 0.37$) as compared to the lower load-level ($\tau_{\text{PCr}} = 65.1\text{ s}$, $\tau_{\text{Pi}} = 45.6\text{ s}$, $\Delta\text{pH} = 0.16$).

(TR). Due to the fact that skeletal muscles are often located close to the skin surface and (at least at first glance) relatively homogeneous, application of transmit/receive surface coils for volume selection is tempting for dynamic ^{31}P -MRS. However, as seen in the top right image of Fig. 4.2, surface coil localization using a ring coil with a diameter of $\varnothing = 8\text{ cm}$ results in an estimated sensitivity volume (dotted half circle), which is larger than the outlined region-of-interest (ROI), i.e., the *M. gastrocnemius medialis* (GM). Hence, adjacent muscles like the weaker-exercising *M. soleus* (SOL) also contribute to the non-localized ^{31}P -MR spectra, which in turn potentially leads to partial volume contamination that can cause wrongly determined spectroscopic parameters [RZANNY et al., 2016]. To overcome this major disadvantage caused by the signal heterogeneity, volume selection is required, which can be achieved by single-voxel techniques, such as point-resolved spectroscopy (PRESS) based on spin-echo or stimulated echoes, and by chemical shift imaging (CSI). The latter allows simultaneous measurement of a voxel matrix and will be introduced in the next section. Single-voxel techniques, which are based on SE or STE acquisition, are less suitable for ^{31}P -MRS owing to the short T_2 relaxation times of most phosphorus compounds.

4.2.4 ^{31}P -chemical shift imaging

To acquire spectroscopic signals from a selected volume, gradient-controlled high-frequency pulses are applied after frequency selective slice excitation. In chemical shift imaging (CSI), gradient-mediated localization is realized by means of phase-encoding gradients prior to the read-out [BROWN et al., 1982]. Since frequency encoding can not be applied because the spectral information is needed for chemical shift related separation of the different metabolites, CSI measurements require long acquisition times depending on the number of PE steps in the spatial dimensions. The spectroscopic information can be derived from a slice (2D-CSI) or a volume (3D-CSI) by applying two or three PE tables, respectively. Due to the major limiting factor of ^{31}P -MRS, its inherent low sensitivity, ^{31}P -CSI sequences typically acquire spatially phase-encoded FID signals (instead of SEs) and, however, provide only limited spatial and/or temporal resolution (which are inversely proportional to each other).

In order to achieve sufficient temporal resolution, the acquisition time (TA) of a complete k -space needs to be shorter than 1 min. Therefore, compared to non-localized ^{31}P -MRS, where an optimum SNR per unit of measurement time is obtained when TR approximately corresponds to the T_1 relaxation time of the metabolites to be examined, a reduced TR has to be applied with dynamic ^{31}P -CSI. Considering the relatively long T_1 times of phosphorus metabolites in muscle (4 – 7 s at 3 T), this results in significant T_1 signal weighting of the equilibrium magnetization and thus distinctly lower SNR. Typical voxel sizes in dynamic ^{31}P -CSI investigations are 20 – 40 cm^3 based on a 8×8 voxel acquisition matrix obtained within $\text{TA} \approx 30\text{ s}$. Figure 4.3 shows an exemplary stack-plot of localized ^{31}P -MR spectra obtained unilaterally in the inner low back muscles during moderate isometric loading (back extension). Compared to the non-localized ^{31}P -MRS in the dynamically loaded calf muscles (Fig. 4.2), the stack-plot shows reduced SNR

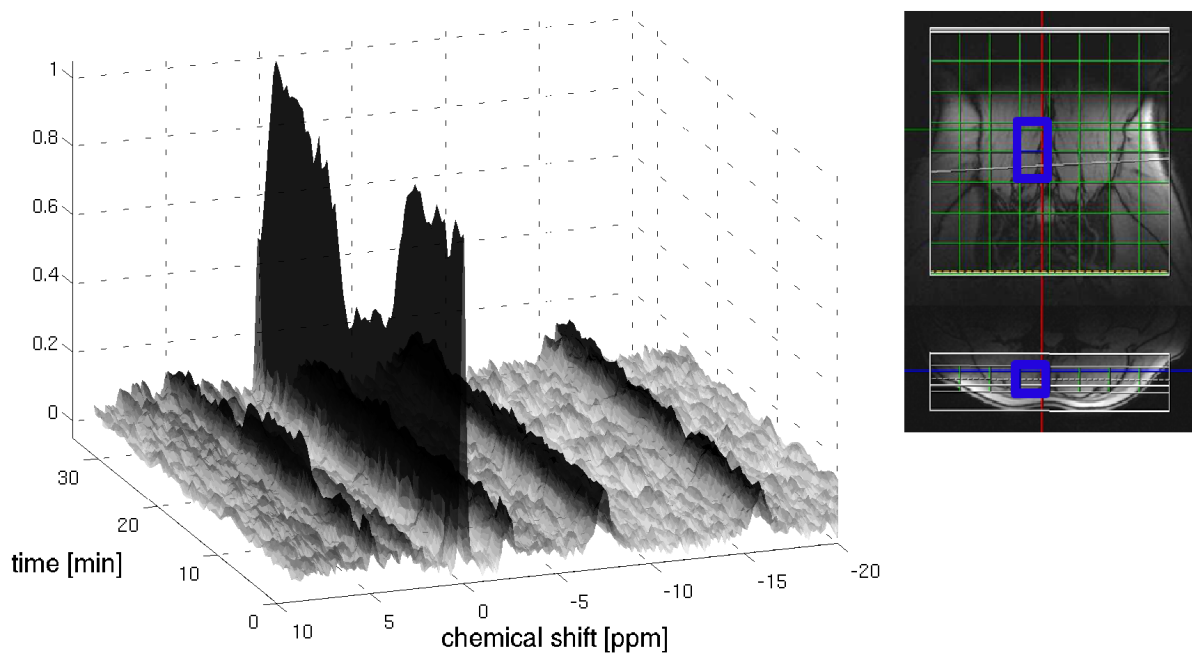


Figure 4.3: Stack-plot of localized ^{31}P -MR spectra acquired in moderately exercised low back muscles (right *M. multifidus* within blue voxels) using a ^{31}P -CSI-FID sequence. Intensities were normalized to the mean PCr intensity during rest. PCr depletion as well as Pi accumulation exhibit two phases during exercise (10 – 20 min): an initial rapid phase during the first 1-2 minutes, followed by a second phase during which PCr and Pi concentration reach a steady state. The native spatial and temporal resolution of the coronal CSI slice were $(30 \times 30 \times 25) \text{ mm}^3$ (8×8 voxel matrix) and $\text{TA} = 27 \text{ s}$ ($\text{TR} = 920 \text{ ms}$, elliptical k -space sampling), respectively. Due to spatial averaging (2 voxels in H-F direction), PSF blurring and sliding window reconstruction of 5 consecutive spectra the effective spatial and temporal resolution were $(45 \times 90 \times 25) \text{ mm}^3$ and $\text{TA} = 135 \text{ s}$, respectively.

and a lowered temporal resolution ($\text{TA} = 27 \text{ s}$). As described before, temporal resolutions below 15 s do not allow reliable determination of mono-exponential time constants of the transient PCr and Pi changes. At least, however, it provides an estimate of resting-state PCr and Pi values as well as magnitudes of PCr and Pi changes during load, averaged over the PCr hydrolysis equilibrium phase. The latter, in turn, requires moderate exercise intensities causing aerobic energy supply (as performed in this work).

Besides the low spatial resolution, signal bleeding from outside the voxels into other parts of the acquisition matrix grid due to the broad point-spread function (PSF) represents another major limitation of ^{31}P -CSI. This further reduces the (effective) spatial resolution of metabolic measurements as the real voxel size is much larger than the nominal voxel size. For instance, acquisition of an 8×8 voxel matrix (using elliptical k -space sampling) leads to a PSF with a full width half maximum (FWHM) of approximately 1.5 voxel and thus to an enlargement of the nominal voxel size by 50% (after Hamming filtering with a filter width of 50% that suppresses the PSF side lobes; information provided by the vendor, TIM Trio; Siemens Health-

care, Erlangen, Germany). This low effective spatial resolution in dynamic ^{31}P -CSI limits the inter-muscular differentiation of spectroscopic parameters acquired with the volume and may lead to wrong results and misinterpretations.

4.3 Quantitation of muscle activity based on T_2 - and diffusion-weighted MRI

Since ^{31}P -MRS investigations suffer from low spatial resolution, new MR techniques for imaging water protons were introduced during the past two decades in order to assess the spatial pattern and extent of muscle utilization. The direct effects of exercise on T_2 -weighted MRI contrast in skeletal muscles were first reported in 1988 [FLECKENSTEIN et al., 1988]. From that time on, it has been recognized that MRI could be used to distinguish between active and nonactive muscle groups and provides functional information about exercising muscles. Hence, *muscle functional MRI* (mfMRI), which is based on the acquisition of differently T_2 -weighted MR images and subsequent quantitation of the T_2 relaxation constant before and after muscle loading, has emerged as a promising tool for studying the involvement of muscles during exercise. However, this approach is limited by a missing full theoretical understanding which physiological variables produce the mfMRI response and how their contributions may differ during and after exercise [DAMON et al., 2003]. Furthermore, the inherent difficulty of MRI of being often unable to separate the compartments of multi-compartmental biological samples results in measurements, which depend on multiple intrinsic parameters [MORVAN, 1995]. For instance, compartments, which can be distinguished on a spatial, chemico-physical, or functional basis, and the effects of exchanges between these compartments complicate the possibility of deriving intrinsic parameters from MRI signal analysis, implying that the extracted parameters, like T_2 , should be only considered as apparent ones.

4.3.1 Origin of exercise-induced T_2 -changes

The mechanisms influencing T_2 in skeletal muscle are highly complex and remain an intense area of investigation. Early *in vitro* NMR relaxometry studies performed on isolated excised muscles demonstrated that the T_2 relaxation decay curve is multi-exponential and characterized by three distinct T_2 components of < 5 ms, $20 - 40$ ms, and > 80 ms, with the intermediate component comprising the majority of the signal [BELTON et al., 1972; HAZLEWOOD et al., 1974]. Contrary, due to limited echo spacings and low SNR, conventional T_2 -weighted MRI protocols do not show multi-component T_2 relaxation of muscle tissue and the measured signal decay appears to be mono-exponential. Recently, combined *in vivo* T_2 -weighted MRI and NMR relaxometry was performed and it was demonstrated that intense exercise has a profound effect on the multi-component muscle T_2 with changes in the magnitudes of all the T_2 components, synergistically increasing T_2 extracted from T_2 -weighted MRI [SAAB et al., 2000]. These authors reported changes for two intermediate T_2 components (found at ≈ 20 ms and 40 ms), which were both

considered to be of intra-cellular origin, and for the third component ($T_2 > 100$ ms), which was attributed to extra-cellular fluid, of -44% , $+52\%$, and $+23\%$, respectively. The corresponding magnitudes of these components were 34% , 49% , and 14% of the total MRI signal, which indicates that the major contribution to mfMRI signal changes stems from increased T_2 of intra-cellular water protons. Of note, an increase of the total signal magnitude by $8 - 9\%$ was attributed to an uptake of fluid from the vasculature.

Multi-component T_2 investigations during exercise were extended by subsequent research revealing additional insight into the mechanisms that underlie the increase of intra-muscular T_2 during load. In particular, accumulation of metabolic end products was found to be responsible for the water movement into the cells due to osmotically driven fluid shifts [DAMON et al., 2003; LOUIE et al., 2009; VANDENBORNE et al., 2000]. These water shifts mainly occur from one intra-cellular compartment possessing a short T_2 (≈ 20 ms) to a second intra-cellular compartment having a longer T_2 (≈ 40 ms). These results were supported by *ex vivo* investigations that identified the intra-cellular compartments as the primary site of activity-induced T_2 changes [DAMON et al., 2002a]. Additionally, it was reported that changes of both intra-cellular pH (due to accumulation of lactate) and cellular volume predicted the intra-cellular T_2 changes by accounting for 70% of their variance. The residual contribution to the T_2 alterations was again attributed to increased extra-cellular and/or vascular fluid volumes.

Although skeletal muscle tissue comprises only low interstitial volume fractions, it is known that changes of the extra-cellular space affect the mfMRI signal, and it was hypothesized by several authors that increased extra-cellular, vascular volume changes also contribute to T_2 alterations during exercise [ABABNEH et al., 2008; DAMON et al., 2003; DAMON and GORE, 2005; SAAB et al., 2000]. A computer model, which was developed to examine how physiological factors altered during exercise affect the mfMRI signal, included metabolic (PCr, pH, lactate) and vascular parameters (capillary recruitment, blood volume, blood oxygen extraction) and well predicted experimental data [DAMON and GORE, 2005]. It was shown that load-induced increases of blood oxygenation, blood flow and blood volume are directly related to the (intra-vascular) blood-oxygenation level-dependent (BOLD) contrast, which is expressed in altered blood T_2^* constant and thus also in whole-tissue T_2 relaxation times. Consequently, the superposition of intra and extra-cellular phenomena results in a complex signal-time-course providing information of metabolic and hemodynamic muscle tissue response during exercise. The hypothesis of extra-cellular and/or vascular contributions to T_2 changes has, however, not been fully tested. In order to resolve this lack of information, mfMRI was applied in this work in conjunction with a novel perfusion-sensitive DWI sequence.

4.3.2 Relationship between T_2 and diffusion or perfusion changes

The relatively short T_2 of muscle is an indicative of restricted water mobility and the lengthening of T_2 with exercise can arguably be rationalized as an overall increase in water mobility. If so, the water diffusion coefficient would then be expected to increase after muscular loading. An

early attempt of simultaneous T_2 and diffusion measurements performed in exercised forearm muscles showed that both parameters increased with exercise [MORVAN and LEROY-WILLIG, 1995]. The authors attributed the changes of T_2 to changes in water content, and changes of the molecular diffusion coefficient were suggested to reflect temperature variations. More recent work demonstrated a correlation between T_2 and diffusion changes in exercised skeletal muscles and reported similar recovery times of both measures [ABABNEH et al., 2008]. These authors attributed the T_2 and diffusion changes to more 'free' and less macro-molecular 'bound' water after exercise and confirmed the hypothesis that load-induced lengthening of T_2 is caused by an overall increase in water mobility.

Similar to T_2 , the diffusion coefficient D varies between muscle tissue compartments and thus an apparent diffusion coefficient (ADC) is registered by means of DWI, which represents the averaged value of different compartments within a voxel. Although T_2 relaxation times strongly vary between intra- and extra-cellular compartments in skeletal muscle tissue, this insight is less established for the ADC. The most interesting condition involving a strong difference between ADC values is that of the vascular and the extra-vascular tissue compartmentalization as proposed by Denis Le Bihan in 1986. By introducing the intra-voxel incoherent motion (IVIM) model, differentiation between these compartments is enabled using DWI in combination with a two-compartment model, which considers both the diffusion of water molecules in intra- or extra-cellular spaces and the micro-circulation of blood in the capillary network [LE BIHAN et al., 1986]. According to the follow-up publication [LE BIHAN et al., 1988], the signal attenuation in DWI also depends on the timescale of the incoherent motion of water molecules in the vasculature. If this timescale is much shorter than the time during which diffusion sensitizing gradients are applied, the signal decay can be described by a bi-exponential function. Therefore, the IVIM model enables quantitative assessment of the respective signal fractions and ADCs of the vascular and extra-vascular compartment, and its application to skeletal muscle potentially provides information about the underlying mechanisms of mfMRI.

Although an early one-dimensional IVIM-based DWI study of exercised skeletal muscles was published showing significantly modified attenuation curves between rest and shortly after exercise [MORVAN, 1995], IVIM has not been frequently applied in skeletal muscle studies since then. Only few studies have investigated the attenuation pattern (as a function of the b-value) in skeletal muscles in detail [CALLOT et al., 2003; KARAMPINOS et al., 2010] and reported exercise-induced changes within the vascular and extra-vascular compartments [FILLI et al., 2015; YANAGISAWA et al., 2009]. In the present work, a detailed description of the IVIM approach and its application to skeletal muscle tissue is given in section 4.3.4. Following the introduction of IVIM, combined T_2 and IVIM-based DWI measurements is presented in order to examine the mechanisms observed in mfMRI. The proposed multi-parametric mfMRI examination is extended by ^{31}P -CSI and is applied to exercised back muscles. This comprehensive study, which is presented in chap. 4.4, provides improved differentiation between diffusion, perfusion and metabolic effects affecting mfMRI.

4.3.3 Quantitative T_2 -weighted MRI

Quantitative *in vivo* T_2 mapping is notoriously difficult since conventional MRI techniques, like spin-echo (SE) or multiple spin-echo (MSE) MRI, allow application of only a limited number of echoes, and thus provide only an apparent T_2 time constant reflecting an average T_2 from all contributing compartments. In addition to the low SNR obtained at long echo times, conventional MRI techniques require long read-out periods inducing significant susceptibility to respiration and arterial motion artifacts. Therefore, new mfMRI techniques have been introduced in the past, which utilize rapid MRI in order to provide high temporal resolution and robust signal read-outs [PLOUTZ-SNYDER et al., 1997; TAWARA et al., 2009]. In the next paragraph, a brief introduction of rapid imaging strategies is given. For more details regarding the principle concepts of rapid MRI, interested readers are referred to the comprehensive books regarding MRI pulse sequences [BERNSTEIN et al., 2004; HAACKE et al., 1999].

Rapid imaging approaches

One prominent rapid imaging method is the fast spin-echo MRI sequence (FSE, alternatively turbo-SE or TSE), which has widely replaced conventional SE imaging in clinical routine [REISER and SEMMLER, 2002]. This T_2 -weighted MRI sequence acquires an echo train to fill k -space lines in the same slice (Car-Purcell-Meiboom-Gill echo train acquisition). Therefore, 180° pulses are applied, which continually refocus the decaying transverse magnetization and produce phase-encoded SEs (Fig. 4.4). The PE gradients are applied in each repetitive read-out interval, while the induced phase shift is canceled after each echo (see y -axis in Fig. 4.4). This sequence requires a low number of repetitive excitations to achieve k -space filling and thus provides accelerated data acquisition (echo train length of $n = 5$ yields a scan time of one fifth of the time needed without acceleration). However, compared to the conventional SE sequence, FSE-MRI reveals modified image contrast due to the acquisition of the differently phase-encoded echoes at different echo times. Echoes which correspond to central k -space lines primarily determine image contrast, whereas echoes acquired in the periphery of the k -space define spatial image resolution, but also induce changes of the T_2 weighting [REISER and SEMMLER, 2002]. Hence, only an effective echo time can be defined as the time to the echo showing minimal phase encoding.

The major disadvantage of this sequence, however, is that imperfectly refocusing 180° rf pulses lead to stimulated echoes, which introduce mixed T_1 and T_2 contrast into the image and thus may result in an overestimation of T_2 relaxation times as assessed via quantitative T_2 -weighted MRI [MAIER et al., 2003; TAWARA et al., 2011]. Briefly explained, this is due to incomplete refocusing of spins throughout the slice, which, in turn, create some magnetization along the longitudinal axis (instead of in the transverse plane) that is stored and subsequently flipped back into the transverse plane by subsequent imperfect rf pulses. Hence, later echoes contain a stimulated echo contribution in addition to the SE signal that finally affects the T_2 measurement. Additionally, uncertainties of T_2 quantitation are related to the different

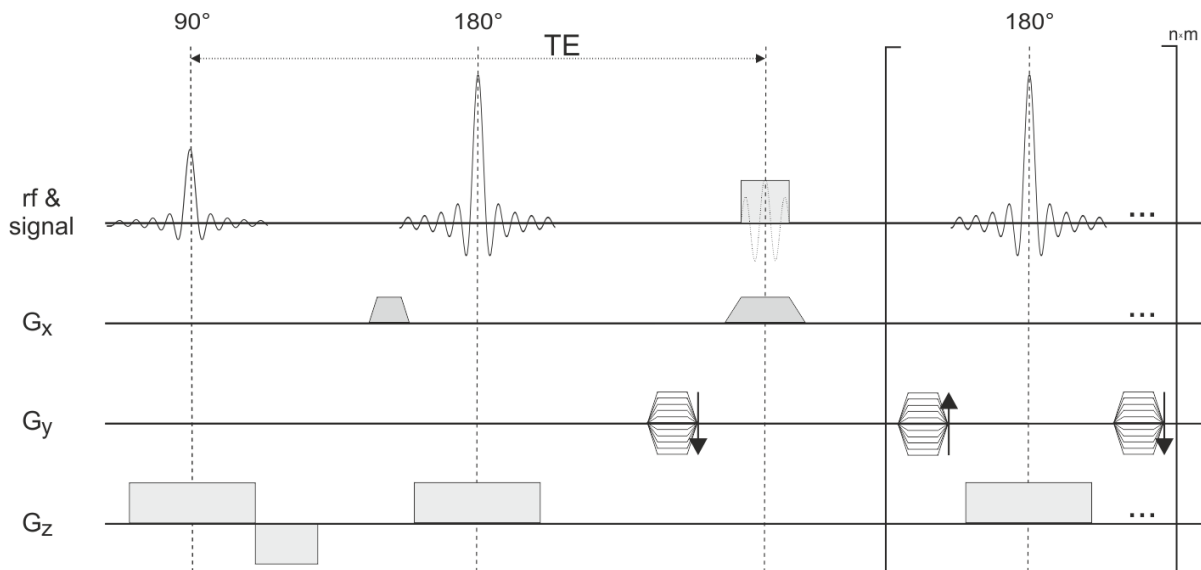


Figure 4.4: Simplified pulse timing diagram of a FSE-MRI sequence, which employs slice-selective excitation (rf pulse plus G_z), frequency (G_x), and phase-encoding gradients (G_y) like conventional SE-MRI, but applies multiple 180° rf pulses after an excitation with de- and rephasing PE gradients utilized after and prior to each refocusing pulse, respectively. Thereby, multiple phase-encoded SEs are acquired during an echo-train (the sequence part in brackets further includes frequency-encoding gradients applied during data acquisition). Depending on the echo-train length n , the repetitive read-out interval is applied 8, 16, 32 or more times during each TR interval, while the SE amplitudes diminish following T_2 decay (leading to image blurring). In order to acquire multiple FSE images with different T_2 weightings the echo-train is repeated m -times, whilst the time between the initial excitation and the acquisition of the m -th central k -space line primarily defines the image contrast.

T_2 constants of fat and water (with higher T_2 values for fat) as well as to J-coupling within the lipid molecules, and thus to partial volume effects between fat and water signals. E.g., J-coupling, which leads to dephasing of the fat signal in conventional SE-MRI, is disturbed in FSE-MRI (due to the short inter-rf-refocusing intervals), in turn, resulting in artificially increased T_2 relaxation times for fat [REISER and SEMMLER, 2002]. Overall, modifications in contrast and fat signal must be taken into account when interpreting FSE images.

An alternative fast and quantitative T_2 measurement approach is given by spin-echo echo planar imaging (SE-EPI). The basic idea of EPI is to generate a series of spin or gradient echoes in a short period of time after an uniquely applied rf excitation. This is achieved by the acquisition of differently phase-encoded echoes according to a gradient-switching scheme [MANSFIELD and GRANNELL, 1973]. In this way, all rows of the k -space matrix are acquired within one single sequence repetition. As illustrated in Fig. 4.5, the EPI read-out applied after SE preparation collects phase-encoded gradient echoes (GREs) beneath an SE envelope, while the central k -space line contains information about the T_2 contrast and the PE is realized by short gradient pulses (blips). The advantages of SE-EPI are very short acquisition times of less than 200 ms per slice and thus an inherent low sensitivity to motion [REISER and SEMMLER,

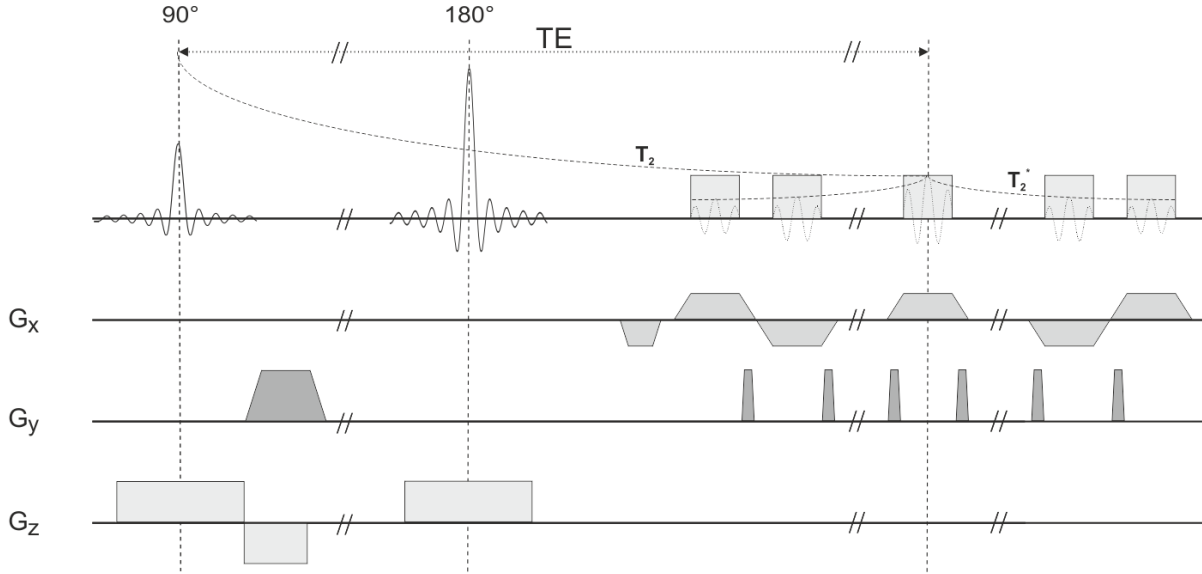


Figure 4.5: Pulse timing diagram of the SE-EPI sequence generating multiple GREs after slice-selective excitation (G_z) by means of an oscillating frequency-encoding gradient (G_x). PE is achieved by using small gradient blips (G_y) during ramping of G_x . These blips successively compensate the initial gradient moment applied prior to the 180° rf pulse. The central k -space line is thus acquired when the PE pre-dephasing is completely rephased and the GRE amplitude is maximized. The latter is defined by the TE-dependent T_2 decay. The subsequently acquired GRE amplitudes diminish following T_2^* decay (inducing image blurring).

2002]. However, due to T_2^* effects during the read-out period the sequence is very sensitive to magnetic susceptibility variations leading to severe image distortions and signal loss. This limitation is caused by the acquisition strategy itself where the signal is collected by reversing gradient fields after applying a single 180° refocusing pulse. Therefore, this sequence cannot reverse the dephasing resulting from susceptibility differences of adjacent tissues, which, in turn, lead to geometrical image distortions and signal cancellations particularly close to interfaces between, i.e., soft tissue, air and bones. As a consequence, outer k -space lines are not only affected by T_2 but also by T_2^* relaxation yielding T_2^* -related PSF blurring that limits the spatial resolution [HAACKE et al., 1999]. In order to account for this major limitation, EPI acquisitions are typically limited to 128×128 pixels per slice and, since T_2^* -related blurring becomes larger with increasing TE, short echo times are typically applied, which are in the range of the tissue's T_2 [REISER and SEMMLER, 2002]. Distortion artifacts can be reduced by k -space under-sampling as possible with phase-partial-Fourier or parallel imaging techniques, such as SENSE [PRUESSMANN et al., 1999] or GRAPPA [GRISWOLD et al., 2002].

T_2 -quantitation

T_2 -mapping is typically based on the signal analysis of a series of T_2 -weighted images with incrementally increased echo times. In this work, T_2 -weighted images were acquired by means of a multi-slice SE-EPI sequence as supplied by the vendor. To demonstrate mfMRI an initial

study of exercised human calf muscles was performed with loading achieved by repetitive extension of the ankle joint (plantar flexion). T_2 -weighted images of 3 mm-thick transverse slices ($n = 24$) were obtained prior to and post exercise with an in-plane resolution of $1.5 \times 1.5 \text{ mm}^2$ (FOV = $258 \times 144 \text{ mm}^2$; 172×96 voxel matrix). The shortest echo time was $TE_1 = 23 \text{ ms}$ using k -space under-sampling based on phase-partial-Fourier (factor 5/8). Each set of multi-echo data ($TE_{1-5} = 23, 33, 43, 53, 63 \text{ ms}$) was acquired within $TA_{\text{all}} = 100 \text{ s}$ (TR = 2.5 s; NEX = 6, TA = 20 s per echo). In order to reduce chemical shift artifacts and potential partial volume effects affecting the T_2 -estimation in voxels containing subcutaneous or intra-muscular fat, the fat signal was suppressed by means of frequency selective water excitation. For voxel-wise T_2 -quantitation the sampled signal decays were mono-exponentially fitted based on (sec. 2.2.1):

$$S(TE_i) = S(0) \cdot e^{-\frac{TE_i}{T_2}}. \quad (4.6)$$

In addition, non-negative least square (NNLS) fitting was performed using the multi-echo data in order to determine multiple T_2 components of the signal decay (in the pre-defined range between 1 – 150 ms). Images of the central transverse slice are shown in Fig. 4.6. Whilst signals, such as originating from the *M. gastrocnemius medialis* (GM, right arrow), increased due to exercise, other muscular regions did not show signal alterations. Muscles, such as the *M. tibialis anterior* (TA, left arrow), are typically not involved during plantar flexion. Mono-exponential fitting of the mean signal-time-course of the GM (averaged across the voxels in this particular ROI) yielded pre- and post-exercise transverse relaxation times of $T_{2,\text{pre}} = 30.8 \text{ ms}$ and $T_{2,\text{post}} = 35.9 \text{ ms}$, respectively. NNLS fitting based on averaged pre- and post-exercise ROI data resulted accordingly in line spectra with a single peak shifted from $T_{2,\text{pre}} = 29.5 \text{ ms}$ to $T_{2,\text{post}} = 33.5 \text{ ms}$. Furthermore, voxel-wise NNLS fitting of the GM data revealed that the T_2 components mainly distributed within the range between 25 – 40 ms. These components can be ascribed to intra-cellular (bound and unbound) water fractions (as described in sec. 4.3.1). The T_2 shift observed by both fitting methods typically corresponds to high workloads, such as applied in this experiment and which leads to totally exhausted calf muscles.

The reconstructed multi-slice T_2 maps of the exercised calf given in Fig. 4.7 further demonstrate that T_2 increased over a wide range of calf muscles, which, in turn, indicates activation/recruitment of these muscle compartments during load. In particular, the highest post-exercise T_2 values were observed in the GM (up arrow), whereas the T_2 estimates of the TA muscle remained nearly constant (left arrow). In essence, the initially reported findings indicate that mono-exponential T_2 fitting based on SE-EPI employing echo times in the range of $TE = 20 - 100 \text{ ms}$ is sensitive to intra-cellular water components, whilst extra-cellular components, such as intra-vascular water ($T_2 > 100 \text{ ms}$), do not significantly contribute to muscle T_2 as determined by SE-EPI. Furthermore, load-induced changes of these 'visible' components can be imaged with high spatial resolution.

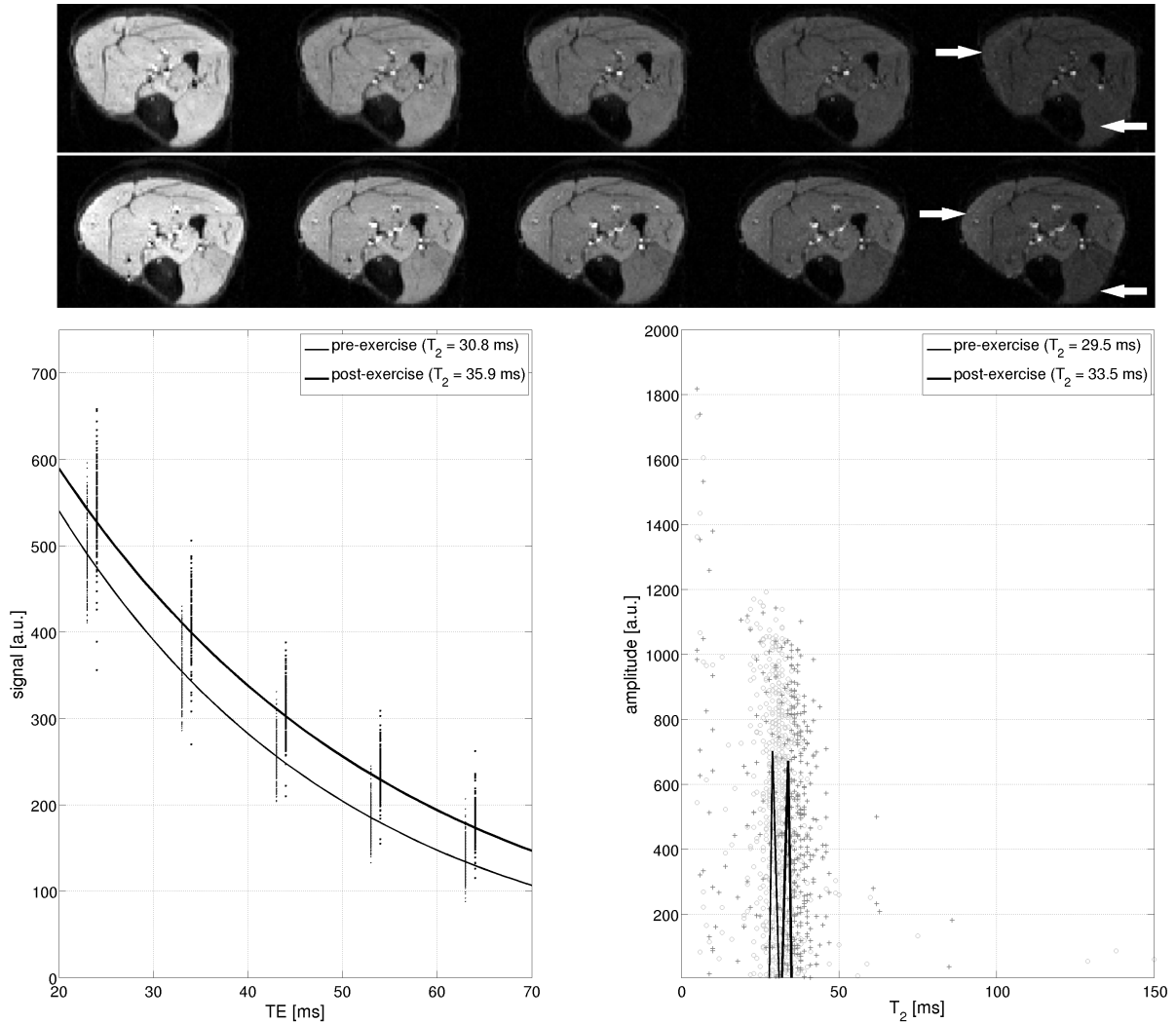


Figure 4.6: Transverse T_2 -weighted MR images of the human calf acquired pre- (top) and post-exercise (bottom) at different echo times (from left to right: $TE_{1-5} = 23, 33, 43, 53, 63$ ms). In addition, ROI-based analysis of signal obtained in the GM muscle is presented below, where the signal-time-course of the corresponding voxels was used for mono-exponential (left) and NLS fitting (right). For illustrative purposes, pre- (grey dots) and post-load data (black dots) are slightly shifted around the actual TE (left graph). NLS fitting was performed voxel-wisely (results marked as circles and crosses for pre- and post-exercise data, respectively) and for the mean signal of the GM (illustrated as T_2 line spectra). The pre- and post-load T_2 values obtained with both fitting routines agree well showing similar exercise-induced increases. The T_2 spectra also indicate the shift toward higher T_2 components with the majority of components ranging between 25 – 40 ms.

4.3.4 Intra-voxel incoherent motion model in DWI

MRI offers several non-invasive approaches to quantify muscle perfusion. Recently, arterial spin labeling (ASL) imaging has been proposed to investigate local perfusion changes in muscle tissue with high spatial and temporal resolution [BOSS et al., 2006; FROUIN et al., 2006; SCHRAML

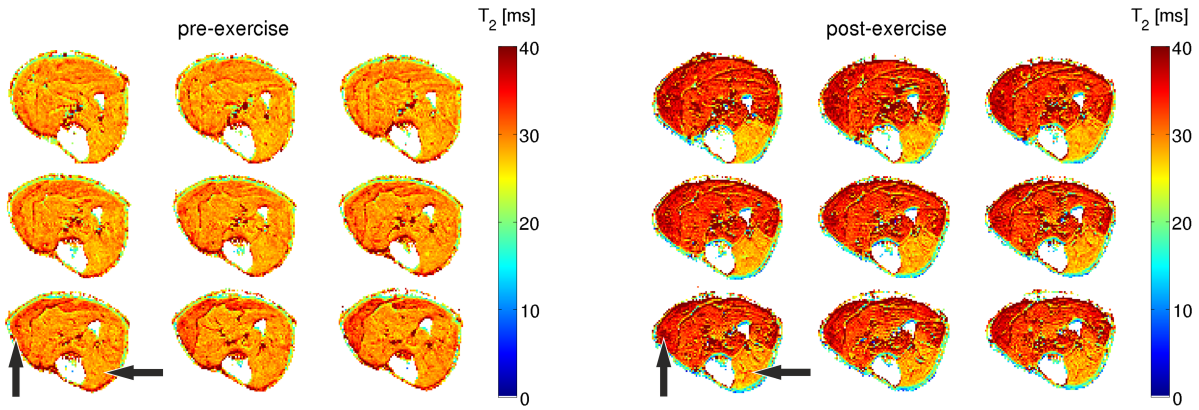


Figure 4.7: Reconstructed multi-slice T_2 maps of human calf muscles acquired pre- (left) and post-exercise (right) based on data shown in Fig. 4.6. The color-coded T_2 maps, which were obtained by voxel-wise fitting of the signal course as function of TE (Eq. 4.6), indicate, e.g., significantly recruited muscles (GM, up arrow) and less activated muscles (TA, left arrow).

et al., 2011; WRAY et al., 2009]. However, ASL-based perfusion quantitation is limited by early magnetization decay of the tagged spins, low SNR and relaxation time changes during exercise. The latter includes the change of the effective transverse relaxation time T_2^* due to the blood-oxygen level dependent (BOLD) effect. This effect is characterized by changes in the micro-vascular ratio of diamagnetic oxyhemoglobin (oxyHb) to paramagnetic deoxyhemoglobin (deoxyHb), and represents the basis of functional T_2^* -weighted MRI, which is an alternative approach to measure oxygen saturation of hemoglobin and micro-circulation in skeletal muscles [DAMON et al., 2007; NOSEWORTHY et al., 2003]. The main limitation of this method is, however, that it measures a mixture of several effects, such as oxygen consumption, blood content and metabolically driven T_2 increases, rather than 'pure' tissue perfusion.

In search of reliable non-invasive tools for perfusion imaging and quantification, recently the focus has been put on intravoxel incoherent motion (IVIM) imaging, a concept that was first described by Denis Le Bihan [LE BIHAN et al., 1986]. The IVIM technique is based on DWI acquired at different b-values and refers to a two-compartment model taking into account contributions of both diffusion and perfusion to the signal attenuation in DWI. The diffusion and perfusion-related signal attenuations are related to the Brownian motion of intra- and extra-cellular water and to the micro-circulation of blood in the capillary network, respectively. The circulation of water molecules in the vasculature is considered as incoherent motion due to the pseudo-random orientation of capillaries at the voxel level (Fig. 4.8), and its fractional volume is called perfusion fraction f (or vascular volume fraction), which typically involves only a few percent of the total water content within the voxel. The superimposed diffusion and perfusion-related signal decay can be expressed by using a bi-exponential model [LE BIHAN et al., 1988]:

$$\frac{S_b}{S_0} = (1 - f) \cdot e^{-bD} + f \cdot e^{-bD} \cdot F, \quad (4.7)$$

where the signal attenuation of the tissue fraction $(1 - f)$ is described by the 'pure' molecular diffusion coefficient D and the perfusion fraction f undergoes additional perfusion-related dephasing which, in turn, results in additional signal attenuation with the expectation value

$$F = \left| \langle e^{i\phi} \rangle \right| = \left| \int \rho(\phi) e^{i\phi} d\phi \right|. \quad (4.8)$$

The perfusion-related signal attenuation thus depends on the phase distribution $\rho(\phi)$ of water molecules in blood during the diffusion sensitizing, which is determined by the blood velocity \vec{v} and the capillary geometry. Assuming that the capillary network can be modeled by a network made of straight capillary segments (first and second model in Fig. 4.8), F will depend on the mean segment length l and mean velocity \vec{v} of blood in vasculature (both averaged over the voxel dimension) as well as on the measurement time T (corresponding approximately to the echo time TE). Further assumptions of the IVIM theory are:

- Blood particles move with $\vec{v} = |\mathbf{v}|$ during the total duration T of the diffusion gradients, which is either the same for all particles or follows a distribution.
- After a characteristic time τ or a capillary segment length l has passed, particles change their movement direction (but not its $|\mathbf{v}|$), which happens multiple times during T .
- Due to the pseudo-random orientation of the capillaries at the voxel level the velocity directions are randomly distributed. The distribution of velocities is isotropic and the velocity directions before and after a change are uncorrelated.
- The vascular volume fraction f and the intra- and extra-cellular water fraction $(1 - f)$ are assumed to have similar values for D and exchange between water in- and outside capillaries is neglected (Fig. 4.8, right).

Regarding the geometry of vascular networks, two extreme cases can be distinguished: The first model assumes that τ is several times smaller than the diffusion time T (approx. $T/\tau > 7$). Then the movement of water in the capillary network mimics the diffusion process as phase distributions become approximately Gaussian (Fig. 4.8, left). The signal attenuation in this case is then described by a pseudo-diffusion coefficient $D^* = vl/6 = v^2\tau/6$ of the vascular fraction and defined by $F = e^{-bD^*}$. This results in the following signal intensity equation:

$$\frac{S_b}{S_0} = (1 - f) \cdot e^{-bD} + f \cdot e^{-b(D+D^*)}. \quad (4.9)$$

The second model refers to cases, when the capillary segments l (or τ) are longer, the blood velocity \vec{v} is slower, or the measurement time T is shorter, as then the blood flow directions do not change multiple times during T (Fig. 4.8, middle) and the echo attenuation F becomes different. In these scenarios only a very small fraction of the protons change their movement during the applications of the diffusion gradients, while the majority of particles acquire a phase, which is proportional to the cosine of the angle between movement direction and the

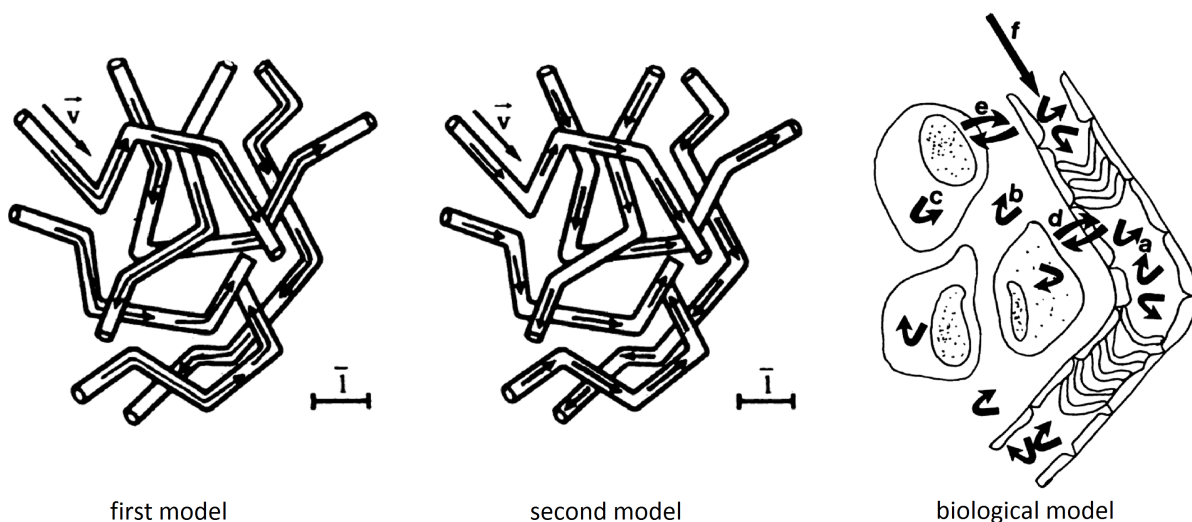


Figure 4.8: Two models of a capillary network composed of straight capillary segments as well as a simplified biological model (taken from [LE BIHAN et al., 1988]). Left: In the first model blood flow directions change several times during T and the movement of water is thus described by a pseudo-diffusion coefficient. Middle: In the second model the blood flow directions do not change during T (indicated by the shorter arrows) and signal attenuation different from the pseudo-diffusion will be observed. Right: The biological model is described by a vascular volume fraction f with protons diffusing in capillaries (a) and an extra-vascular volume fraction, which is only involved in diffusion. The latter comprises extra- (b) and intra-cellular (c) spaces with exchange between these two compartments (e). Exchange between inside capillaries and outside capillaries (d) is neglected due to slow exchange regime between both compartments.

axis of the diffusion gradients. Assuming pseudo-random orientations of the capillary segments, the average dephasing of the transverse magnetization remains zero ($F \rightarrow 1$) and the effect of the capillary flow is a pure signal amplitude attenuation (similar to the diffusion or pseudo-diffusion approach). If net flows persist, i.e. if voxels include small vessels rather than capillaries only, a non-zero average dephasing will contribute to the signal attenuation. However, in both these scenarios the perfusion-related signal decay will occur faster than the diffusion-related attenuation allowing them to be separated on a quantitative basis by means of the IVIM model. Typical signal curves as a function of the b-value are illustrated for brain and liver in Fig. 4.9 (IVIM parameters taken from [LE BIHAN, 2008]). It is clearly visible that the signal attenuation due to the blood flow is an order of magnitude faster than the diffusion-associated signal decay ($D^* \gg D$) and thus dominates signal behavior in the low b-value regime ($b < 100 \text{ s/mm}^2$). Furthermore, the signal fraction of the perfusion compartment contributing to the non-weighted signal S_0 is higher in the liver ($f = 15\%$) than in the brain ($f = 8\%$), and the higher f as well as D^* values in the liver results in stronger perfusion-related signal losses at low b-values.

Previously, IVIM was used to investigate the structure and vascularity of human brain and

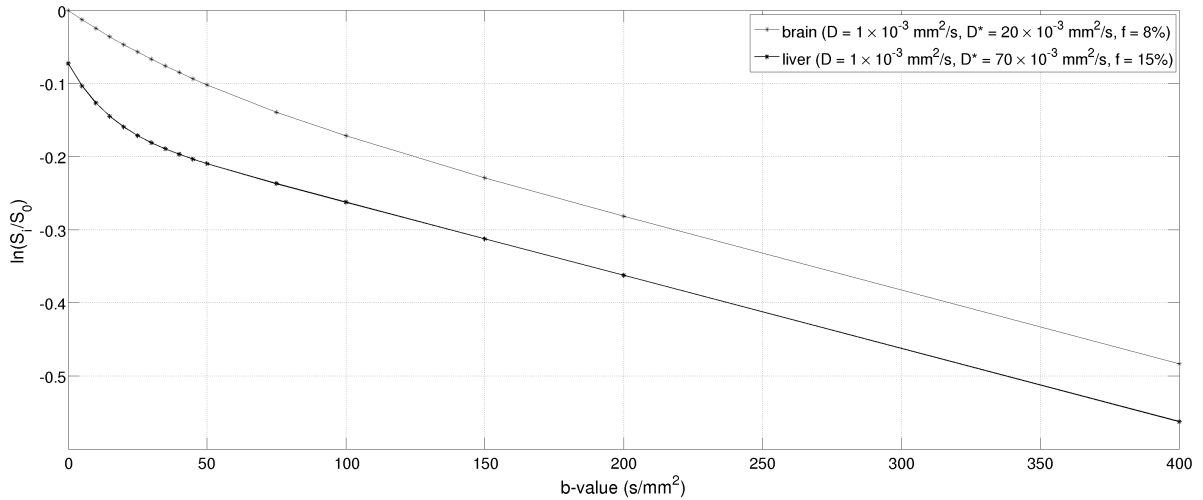


Figure 4.9: Simulated DWI signal attenuation curves for brain and liver as a function of the diffusion weighting (b-value) as proposed by the bi-exponential IVIM model. The signal behavior is determined by the self-diffusion coefficient D based on Brownian motion, by the much faster pseudo-diffusion coefficient D^* and by the vascular volume fraction f , which represents a surrogate of tissue perfusion.

tumor tissue [LE BIHAN et al., 1988]. However, due to its high sensitivity against SNR [PEKAR et al., 1992], IVIM imaging was not frequently used in (pre-)clinical studies until recent scanner developments, such as higher field and gradient strengths, have enabled its application a few years ago [LE BIHAN, 2008]. Recent studies have shown the effectiveness and sensitivity of IVIM as a marker of vascularity in abdominal organs, such as liver, pancreas and kidney [LEMKE et al., 2009; LEMKE et al., 2011; LUCIANI et al., 2008; ZHANG et al., 2010]. In addition, numerous IVIM models and theories have been suggested and investigated using flow phantoms or flow models to better understand perfusion/diffusion contrast as influenced by flow velocity distributions and geometry of the flow branches and segments [CHO et al., 2012; HENKELMAN et al., 1994; KENNAN et al., 1994]. However, the determination of IVIM parameters was found to be challenging. For instance, a recent study reported poor measurement reproducibility of f and D^* estimates in normal liver and metastases [ANDREOU et al., 2013]. Regarding the SNR dependency, simulations suggested the acquisition of a minimum of 10 b-values when performing single signal-averaged IVIM imaging [LEMKE et al., 2011]. In particular, it was shown that estimation of D^* is even more demanding than estimation of f by fully fitting noisy data to Eq. 4.9 [PEKAR et al., 1992]. Overcoming the ambiguity of the fit solutions has been a prevailing research topic but recent research provided an explanation of the large variation of D^* values reported in literature. It was found that the characteristic timescale of the incoherent motion is not in the appropriate range ($T/\tau > 7$) for assuming the pseudo-diffusion limit with typical DWI experiments in liver and pancreas [WETSCHEREK et al., 2015]. The authors concluded that the bi-exponential description does not adequately model the diffusion signal and that the signal attenuation of the perfusion compartment can not be described solely by D^* . Therefore,

and as stated early [LE BIHAN et al., 1988], the main purpose of IVIM imaging in this work is to generate separate maps of the diffusion coefficient D and the perfusion fraction f by robust voxel-wise parameter fitting of multiple DW images, regardless of capillary geometry or blood velocity. The obtained perfusion fraction maps can then be interpreted as density maps of active capillaries in which blood is flowing. The implementation of D^* -measurement was not within the scope of the present work. The IVIM fitting approach allowing reliable D and f mapping in muscles is presented in the next section (sec. 4.3.4). This method enables the interrelation of muscle functional diffusion and perfusion measurements with T_2 -based mfMRI in order to gain better understanding of the origin of exercise-induced T_2 -changes (results given in sec. 4.4).

IVIM in skeletal muscles

To investigate whether diffusion-related compartmentalization could be observed in skeletal muscle and whether this compartmentalization was affected by exercising, attenuation curves of signal against diffusion weighting were initially analyzed based on 1D measurements in human forearm muscles [MORVAN, 1995]. The author reported exercise-dependent bi-exponential signal behavior and addressed the question of the appropriateness of bi-exponential signal modeling for muscle tissue. One particular concern was related to the distribution of convective micro-circulatory displacements, which would justify a bi-exponential model. A Gaussian distribution of velocity directions, which is implicit to the pseudo-diffusion concept and not appropriate in the case of regular capillary ordering, may not be valid in skeletal muscles as they reveal an anisotropic capillary bed with $\approx 3/4$ of capillaries being parallelly aligned to the muscle fibers [MATHIEU-COSTELLO, 1987]. However, since the micro-circulation in muscle is organized in bundles with lateral cross-connections of capillaries [SKALAK and SCHMID-SCHINBEIN, 1986], it was concluded that the vascular geometry of muscles does not preclude a pseudo-diffusion process [MORVAN, 1995].

Subsequent studies of the myocardium of dogs [CALLOT et al., 2003] and human calf muscles [KARAMPINOS et al., 2010] reported, however, anisotropic IVIM signal with highest f values in the main direction of the muscle fibers. These authors defined an apparent (or 'visible') intra-vascular fraction f_a depending on the angle between the average micro-vasculature orientation and the applied diffusion encoding direction. This estimate represents the signal-weighted fraction of intra-vascular spins moving in a specific diffusion-encoding direction, which is the contribution mostly from spins contained within capillaries oriented along that specific direction. It has been suggested that the variation of f_a for different diffusion-encoding directions characterizes the degree of micro-vascular anisotropy by taking into account the underlying fiber orientation, while the (apparent) D is independent on the degree of vascular geometry [KARAMPINOS et al., 2010].

As stated in the previous section, the main challenge for *in vivo* IVIM imaging of skeletal muscles is the low sensitivity of the diffusion signal to micro-circulatory flow effects and the

inherent low SNR due to T_2 -related signal loss [PEKAR et al., 1992]. Both factors affect the amount of perfusion-related signal variations and thus complicate a straight forward application of the bi-exponential fit model. This issue is illustrated in Fig. 4.10 showing representative IVIM data, which were obtained prior to and post exercise of the human calf muscle *M. gastrocnemius medialis* (GM). The voxel values of the ROI (marked as thin and thick black crosses for data obtained pre- and post-exercise, respectively) are used to determine the mean S_i/S_0 signal curves as a function of the b-value, which are then fitted to the bi-exponential IVIM model according to Eq. 4.9 (black lines). It is clearly visible that the perfusion-related signal loss - especially in the resting state - is much smaller in skeletal muscles than compared to brain or liver ($f < 8\%$). However, since typical D^* values in skeletal muscles are also much higher than D (approx. ten-fold) diffusion-related compartmentalization is visible showing much faster decay of the signal originating from the intra-vascular space than of the signal from the extra-vascular space. Consequently, signal originating from the micro-circulatory network can be assumed to be totally attenuated in the high b-value regime ($b > 100 \text{ s/mm}^2$) and the pseudo-diffusion D^* can be separated from molecular diffusion. The latter can be quantified by using the asymptotic limit expression of Eq. 4.9:

$$\frac{S_b}{S_0} = (1 - f) \cdot e^{-bD}, \quad (4.10)$$

where f describes the deviation of the asymptotic extrapolation of the high b-value behavior from unity and D determines the slow mono-exponential tail of the (theoretical) bi-exponential curve (also demonstrated in Fig. 4.10). The initial faster signal attenuation in the low b-value regime ($b < 100 \text{ s/mm}^2$), which is related to D^* , is, however, not accessible using this mono-exponential approximation. Contrary, mono-exponential curve fits provide reliable extraction of the vascular volume fraction f and the molecular diffusion coefficient D as demonstrated by similar estimates for bi- and mono-exponential curve fitting (see legend in Fig. 4.10). In addition, simulations supported the validity of the separation between the perfusive and diffusive signal loss by mono-exponential fitting of high b-value data (see Fig. 4.11).

IVIM parameter mapping in muscles

In order to provide reliable (directional independent) f and D mapping based on voxel-wise mono-exponential fitting a series of diffusion-weighted images has to be acquired comprising multi-b-value measurements in at least three non-collinear directions with high SNR. Therefore, IVIM images were acquired in this work by means of diffusion-weighted spin-echo twice-refocused EPI, which is based on the diffusion sensitizing Stjeskal-Tanner sequence (sec. 2.3.3) and provides the temporal resolution needed for mfMRI. To overcome the violation of the pre-condition of a Gaussian (normal) distribution of the convective micro-circulatory displacements due to the anisotropic capillary bed in muscles, trace-weighted DWI with diffusion sensitizing in three orthogonal directions was applied in the present experiments as previously suggested

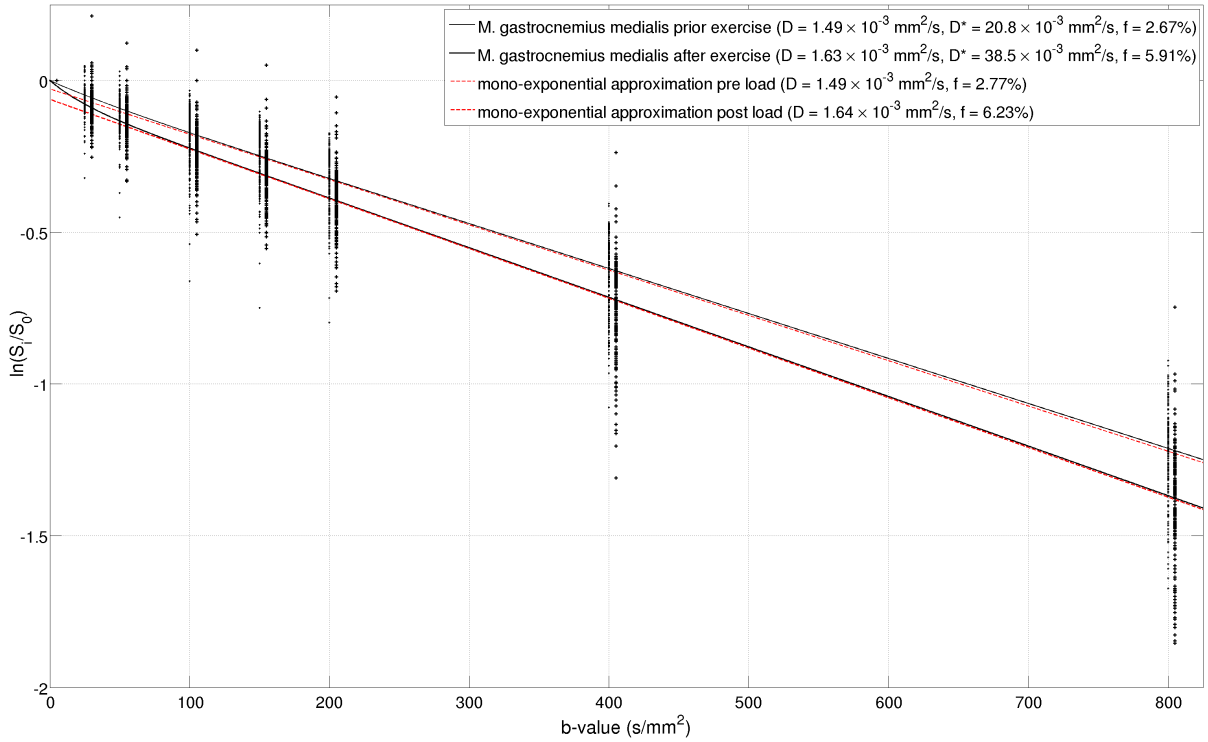


Figure 4.10: DWI signal attenuation curves obtained pre- (thin crosses) and post-exercise (thick crosses) in a human calf muscle (GM), which were fitted by means of mono- (red lines) and bi-exponential IVIM functions (black lines). For illustrative purpose, post-exercise data were shifted by $\Delta b = 10 \text{ s/mm}^2$. Since in skeletal muscle tissue pseudo-diffusion D^* is typically an order of magnitude higher compared to molecular diffusion D , the perfusion-related signal attenuation becomes only significant at low b -values ($b < 100 \text{ s/mm}^2$). Therefore, f and D can be quantified either by fitting the complete signal decay based on Eq. 4.9 or by mono-exponential fitting of the high b -value regime ($b > 100 \text{ s/mm}^2$) according to Eq. 4.10. As indicated by similar D and f estimates obtained by both approaches (see legend), it can be assumed that the contribution of the signal originating from the micro-circulatory network can be safely neglected in the high b -value regime and mono-exponential fitting represents a valid approximation in IVIM quantitation.

[CALLOT et al., 2003; FILLI et al., 2015]. An initial feasibility study was carried out by performing multi- b -value SE-EPI in exercised human calf muscles (loading due to repetitive plantar flexion). This experiment aimed at evaluating the sensitivity of the proposed IVIM sequence protocol to exercise-induced perfusion changes as indicated by changes of the perfusion fraction f . Therefore, pre- and post-load DWI data were acquired ($1.5 \times 1.5 \text{ mm}^2$; $\text{FOV} = 258 \times 144 \text{ mm}^2$; 3 mm-thick transverse slices) each within $\text{TA} = 7 \text{ min}$ ($\text{TE}_{\min} = 72 \text{ ms}$; $\text{TR} = 3 \text{ s}$; $\text{NEX} = 3$). The data sets included 12 trace-weighted acquisitions with linearly increased b -values between $(0 - 550) \text{ s/mm}^2$ (increment of $b_{\text{inc}} = 50 \text{ s/mm}^2$) and were used for voxel-wise fitting of the magnitude data by using Eq. 4.10. The reconstructed D and f maps of multiple transverse slices of are shown in Fig. 4.12. As it can be clearly seen in the D maps, this parameter increased with exercise over a wide range of muscles with largest changes in the GM muscle (up

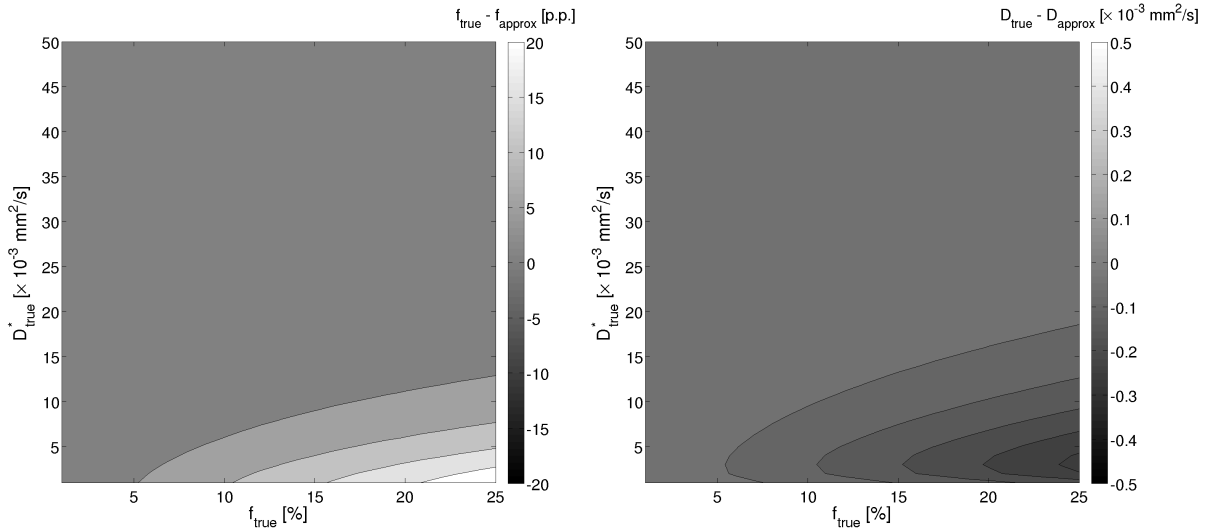


Figure 4.11: Error of D and f estimates obtained by mono-exponential approximation based on simulated (noise-free) bi-exponential IVIM data. The error of both parameters was determined for different perfusion fractions and pseudo-diffusion coefficients ($f_{true} = (1 - 25)\%$ and $D_{true}^* = (1 - 50) \times 10^{-3} \text{ mm}^2/\text{s}$ with constant $D_{true} = 1.5 \times 10^{-3} \text{ mm}^2/\text{s}$). In essence, differences of $f_{true} - f_{approx}$ (given in percentage points, p.p.) and $D_{true} - D_{approx}$ show substantial deviation from zero only for $f_{true} > 5\%$ and simultaneously for $D_{true}^* < 15 \times 10^{-3} \text{ mm}^2/\text{s}$. This is due to the remaining perfusion-related signal attenuation in the high b-value regime. However, such low D_{true}^* values for $f > 5\%$ are far away from previously reported values in muscles [FILLI et al., 2015; MORVAN, 1995].

arrow). Contrary, f maps showed only slight increases in the GM with highest f values in medial calf regions, which can be attributed to large vessels (down arrows). Muscles, normally not exercised during plantar flexion, like the *M. tibialis anterior* (TA), showed no significant D and f changes (left arrow). However, identification of recruited (sub-)muscle compartments based on f maps is complicated due to heterogeneous distributions with several voxels showing physiologically non-plausible f values below 0% (white voxels). This may hide valuable information and limits the interpretation of DWI-based mfMRI. Therefore, a denoising approach was implemented in this work, which enables filtering of the signal attenuation curves within a spatial kernel and thus provides improved mapping quality (see next section).

Denoising of IVIM images

Compared to conventional MRI, diffusion-weighted images suffer from inherently low SNR due to low signal amplitudes. In general, low SNR impairs DWI analysis by biasing the quantitation of the diffusion coefficients [JONES and BASSER, 2004]. Many denoising approaches, like spatial Gaussian filters, use signal averaging based on the natural spatial pattern redundancy in the images [MANJON et al., 2009]. However, they have the disadvantage of blurring edges due to averaging of non-similar patterns. More appropriate edge preserving filters reduce this effect but do not taking advantage of the multi-component intrinsic nature of MRI studies, which allows

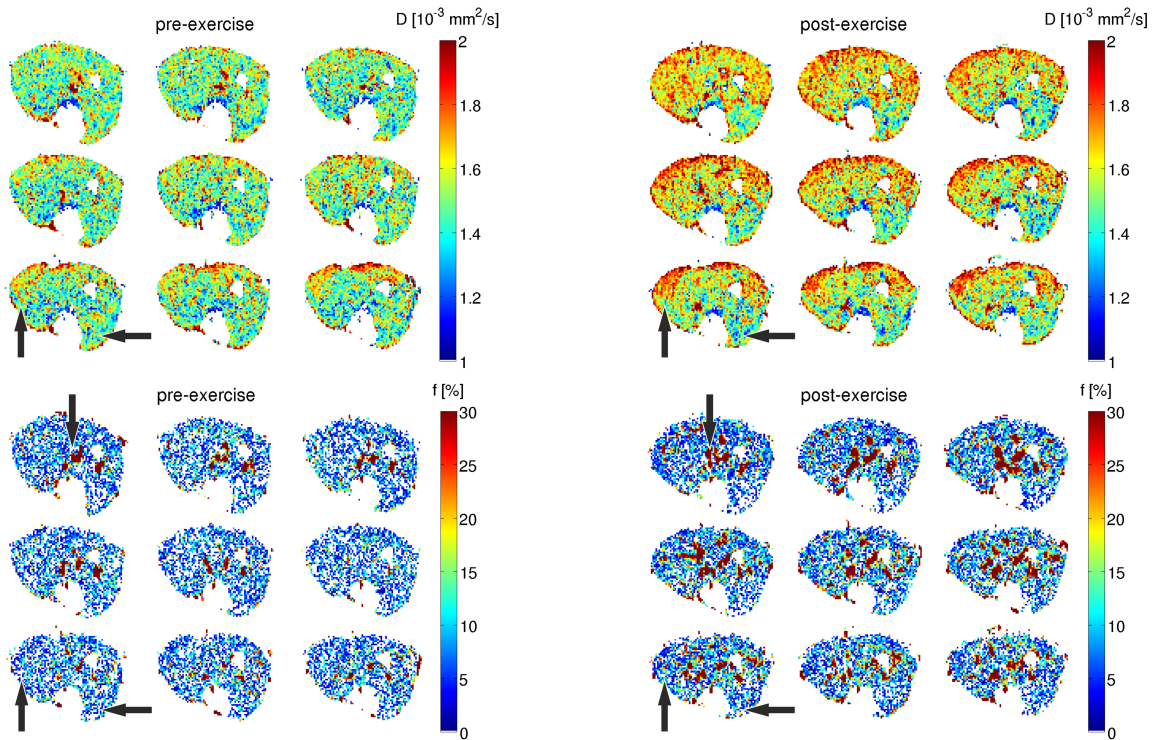


Figure 4.12: Reconstructed multi-slice D (top) and f maps (bottom) of human calf muscles acquired pre- (left) and post-exercise (right). Except for the TA (left arrow), all calf muscles show increased D values with the largest changes in the GM (up arrow). The f maps show highest values in areas of the inner muscles, which can be ascribed to signal originating from large vessels (down arrow) and slight load-induced changes in the GM (up arrow).

to consider spatial intensity variations by analyzing the image series instead of a single image. Recently, it was suggested that series of MR images comprising different contrasts/weightings but revealing the same spatial information can be used to identify structure edges that allows to restore image sharpness by image denoising using the correlated information in such images. This approach was originally proposed for multi-contrast MRI [MANJON et al., 2009] and multi-directional DTI data [MANJON et al., 2013]. It is based on principal component analysis (PCA) and provides noise removal by locally shrinking less significant principal components of the multi-contrast MRI data. In order to filter IVIM images this denoising method was applied in this work by taking into account multi-b-value DWI data, thus reducing random noise of the signal attenuation patterns.

PCA represents an orthogonal linear transformation that converts a set of observations of possibly correlated variables into a set of values of linearly uncorrelated variables called principal components [JOLLIFFE, 1986]. Thereby, it maps the data into a new coordinate system such that the greatest variance, by any projection of the data, comes to lie along the first axis (called the first principal component), the second greatest variance along the second coordinate (second principal component), and so on. In general, the number of images for PCA has to be larger than the number of independent significant image components. This theoretical issue

can be overcome by performing PCA decomposition over small local windows instead of the whole image [MANJON et al., 2013]. The basic idea of using local image patches for PCA of IVIM images is that every voxel signal can be filtered by decomposing the local surrounding square window for the multi-b-value image series and subsequently attenuate the less significant principle components. In this work, 3D decomposition patches were defined for each voxel x_i of the image domain in each diffusion-weighted image k . Afterwards, the voxel values within the patch surrounding x_i are reordered as a column vector yielding the matrix

$$X = N \times K \quad (4.11)$$

with N being the number of voxels of the local window and K the number of applied diffusion-weightings. Then PCA is performed based on this local matrix X (based on eigenvalue decomposition as described in [JOLLIFFE, 1986]). The calculated (orthogonal) eigenvectors are stored as columns in a squared matrix U (size of $K \times K$) and the associated eigenvalues, which correspond to the amount of variation of the new components, are stored in a diagonal matrix S (size of $K \times K$). The new coordinates of the original data are computed by a simple matrix product:

$$Y = XU. \quad (4.12)$$

In order to reduce the noise, the obtained components can be processed (in several ways) and subsequently used for recombination of the original matrix. Since multi-b-value data typically show only one dominant component, which represents the signal attenuation as a function of the b-value, thresholding of the eigenvalue matrix S is performed by canceling all coefficients except the first eigenvalue (values in the diagonal of S are set to zero). The modified diagonal matrix \hat{S} is then used to obtain the denoised original matrix through inverse PCA transformation:

$$\hat{X} = YU^T \hat{S}. \quad (4.13)$$

Since local PCA denoising based on overlapping patches provides multiple estimations for a particular voxel, the filtered intensity value can be obtained through averaging over the multiple overlapping windows estimates. Initially, the noise reduction due to the proposed PCA approach was evaluated by simulations based on $N = 27$ noisy bi-exponential signal attenuation curves ($b = 0 - 400 \text{ s/mm}^2$, $b_{inc} = 50 \text{ s/mm}^2$, $K = 9$). The number of multiple observations N corresponds to a $3 \times 3 \times 3$ voxel window. Each curve was composed as a sum of ideal data (defined by $f = 5\%$, $D^* = 50 \times 10^{-3} \text{ mm}^2/\text{s}$, $D = 1.5 \times 10^{-3} \text{ mm}^2/\text{s}$ as typically observed in muscles) and additive Gaussian noise ($SD_{noise} = 3 \cdot f$). As shown in Fig. 4.13, decomposing of these curves into the underlying components and using the first (strongest) principal component to recombine the denoised signal courses resulted in a significant reduction of the standard deviation (SD) for $\ln(S_i/S_0)$ at each i -th b-value (indicated by smaller errorbars of the denoised data compared to noisy data). This demonstrates that the proposed PCA denoising algorithm provides SNR improvement in signal attenuation courses.

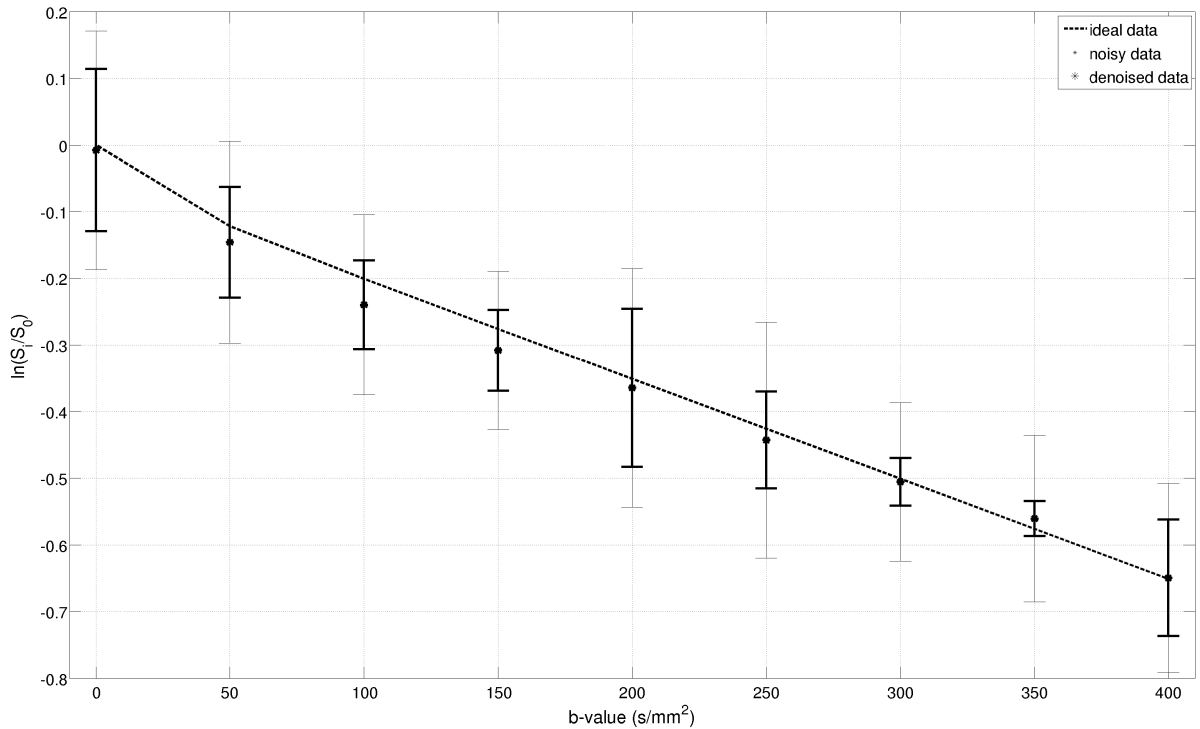


Figure 4.13: Noise reduction of simulated signal attenuation curves by PCA based on simulated ideal (dashed line), noisy (gray errorbars) and denoised IVIM data (black errorbars). Whilst the mean signal S_i/S_0 is not affected due to PCA denoising, the standard deviation across the $N = 27$ intensity values at each b-value is markedly reduced (indicated by lower errorbars). Principally, the noise removal is done by decomposing the multi-b-value signal into the principal components, attenuating less relevant components and reconstructing again.

However, since reduction of the principal components to the first eigenvalue results in spatial filter characteristics, such as blurring, and because the sampling density of diffusion weightings is limited due to the restricted acquisition time frame available during functional measurements, an appropriate trade-off between patch size N and the number of employed diffusion weightings K has to be considered for sufficient PCA-based denoising. Thus, further simulations were performed with the same parameters above (b , D , etc.) but with varying numbers of N and K . Resulting SD differences across N intensity values based on noisy and denoised data with respect to K different b-values [difference of $SD_{\text{raw data}}(b)$ and $SD_{\text{denoised}}(b)$] are illustrated in Fig. 4.14. The results show that increasing the voxel number N reduces the mean SD (across different b-values) as indicated by a larger difference $\overline{SD}_{\text{raw}} - \overline{SD}_{\text{den}}$. A similar trend is visible for lower b-value increments and thus for higher sampling densities of diffusion weightings. For a patch size of $3 \times 3 \times 3$ voxels ($N = 27$) a b-value increment of $b_{\text{inc}} < 50 \text{ s/mm}^2$ ($K = 9$) yields distinct noise reduction, which is, however, higher than for lower DWI sampling density. This level of noise removal remains constant for a wide range of higher N (at constant K) or for lower b_{inc} (at constant N). Only for $b_{\text{inc}} < 20 \text{ s/mm}^2$ a significantly higher noise reduction is achieved, which would, however, result in an exorbitantly long acquisition time that is not

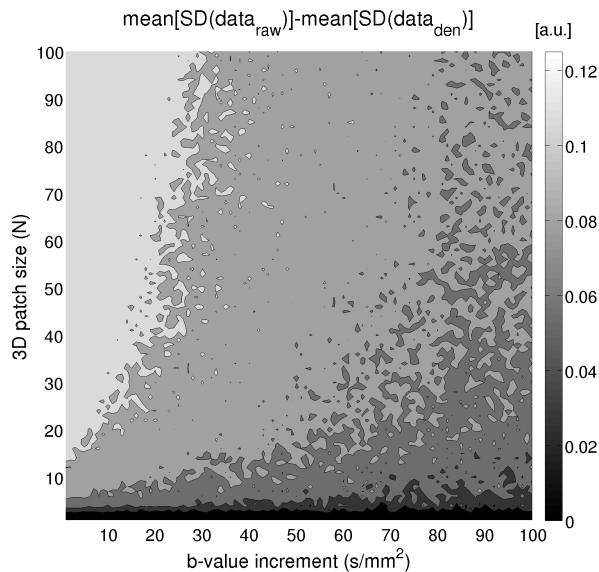


Figure 4.14: Noise reduction by local PCA denoising as a function of the number of considered b-value samples K (defined by the b-value increment) and of the patch size taking into account N simulated signal bi-exponential attenuation curves (parameters given in the text). The noise reduction is determined by the difference between the standard deviation (SD) across N intensity values of raw (noisy) and denoised data both averaged over K b-values. Highest improvement is provided for low b-value increments and a high number of considered voxels. A distinct noise reduction is already achieved for $b_{inc} < 50 \text{ s/mm}^2$ and $N = 20$ voxels, which represents a reasonable trade-off between noise suppression and the limited spatial and temporal resolution in mfMRI.

applicable in mfMRI. Therefore, DWI sampling densities of $b_{inc} \approx 50 \text{ s/mm}^2$ represent a proper choice when performing noise removal by means of the proposed local PCA denoising approach analyzing a $3 \times 3 \times 3$ voxel kernel in the image domain.

The local PCA denoising based on a $3 \times 3 \times 3$ patch was finally applied to the previously shown IVIM data of exercised calf muscles ($b_{inc} = 50 \text{ s/mm}^2$). The D and f maps reconstructed based on raw and denoised data are shown in Fig. 4.12 and Fig. 4.15, respectively. Improvement of the mapping quality due to filtering is clearly visible. Especially the f maps show less non-physiological values ($f < 0\%$) and provide improved visualization of local exercise-induced f changes. It can be concluded that the proposed local PCA algorithm robustly reduces noise by using information not only in the spatial domain but also in the inter-component (b-value) domain without significantly affecting the original image resolution.

4.4 Interrelations of ^{31}P -CSI, T_2 - and diffusion-weighted MRI in low back muscles

Since investigations of back muscle physiology are important for understanding the role of muscle strain in the development of low back pain, T_2 - and diffusion-weighted MRI as well as ^{31}P -CSI were applied in exercised back muscles of volunteers using an exercise protocol with potentially high clinical relevance (the methodology is described in sec. 4.4.1). In a first study, young, healthy subjects were examined by analyzing differences between pre- and post-exercise MR parameters as well as between the different back muscles (sec. 4.4.2). Furthermore, associations between the degree of perceived exertion and different MR parameter changes (independent of muscles) were evaluated; in particular, to test the hypothesis that changes in

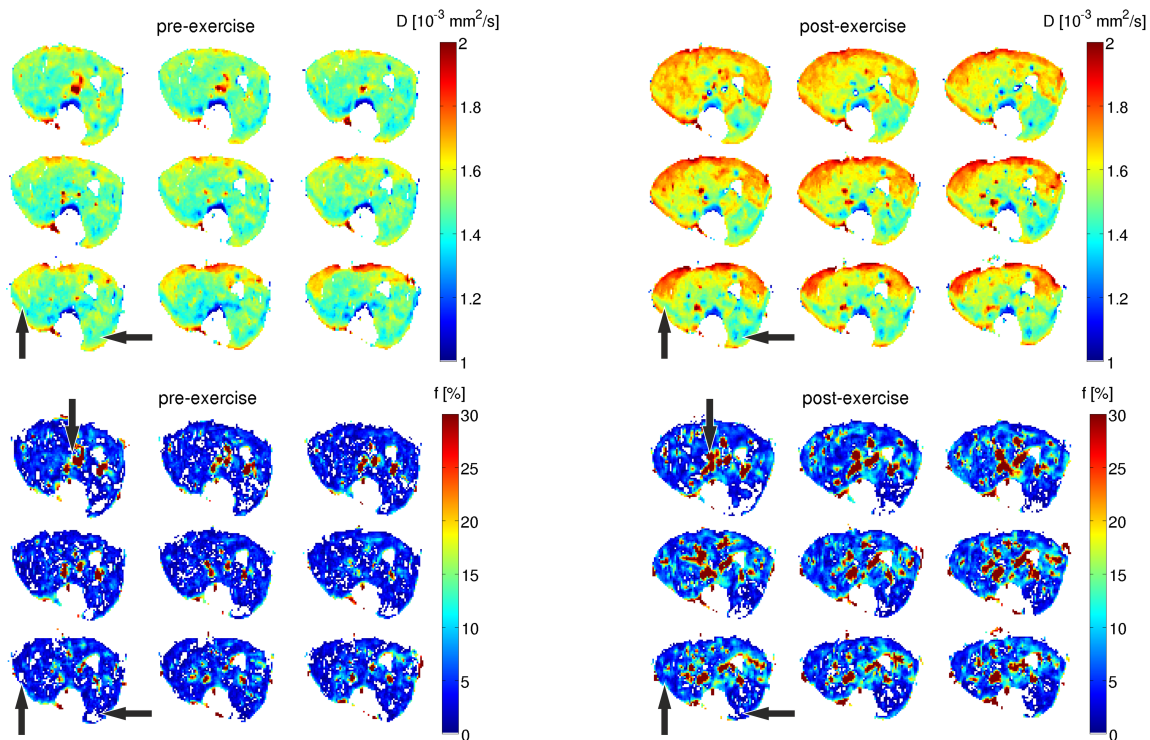


Figure 4.15: Reconstructed D (top) and f maps (bottom) of exercised calf muscles based on denoised data by means of the local PCA approach. Compared to Fig. 4.12, an improved quality of the maps is noticeable, which facilitates the separation of exercise-induced parameter changes (see arrows and text for description).

metabolism, diffusion and/or vascular volume fraction underlie T_2 alterations [HIEPE et al., 2014a]. Subsequently, a second study was carried out in order to assess age-related changes of functional and structural parameters [HIEPE et al., 2015]. The results are given in sec. 4.5.

4.4.1 Materials and Methods

Fourteen healthy subjects were examined with the following subject specifications (mean \pm SD): 22.5 ± 1.4 years; 179.2 ± 5.8 cm; 74.7 ± 7.5 kg; only male right-hander.

Exercise protocol

A modified Biering-Sørensen test [BIERING-SØRENSEN, 1984] was chosen, which is a sustained isometric back extension exercise that can be performed inside an MR scanner. Supported by a self-designed wooden rocker frame (illustrated in Fig. 4.16), the volunteer contracts his lower back muscles to keep his upper body part in a horizontal position. The upper body part rests on a support frame that is constructed in a way to enable variable load removals by means of adjustable counterweights. The ergometer can be used inside or outside the MR scanner. In the present study, a moderate intensity of physical activity was adjusted by applying a load removal of 50% of the volunteer's upper body weight. The latter was determined in

a separate experiment by using the computer-supported test and training device Centaur® (BfMC, Leipzig, Germany) [ANDERS et al., 2008]. The ergometer is equipped with an angle sensor to monitor the upper body position (via a potentiometer on the rocker axis). This information is visually fed back to the volunteer via a self-written graphical user interface (MATLAB, The Mathworks, Inc., USA) and an MR-compatible video system (Virtual Stim Digital, Resonance Technologies Inc., USA) to enable interactive self-adjustment of the body position (Fig. 4.16, bottom right).

The exercise was performed over a time period of 10 min and was repeated for each volunteer in two separate sessions on different days (see Fig. 4.16, top row): During the MRS session, the modified Biering-Sørensen test was performed inside the scanner and ^{31}P -MR spectra were continuously acquired before, during and after the exercise. The rocker was fixed before and after the exercise to avoid any additional loads. During the MRI session, T_2 - and diffusion-weighted MR data were collected before and after the exercise with subjects lying in supine position to reduce breathing motion artifacts that typically occur in prone position. The exercise itself was performed outside the scanner in the scanner room. Post-exercise data acquisition started 1.5 min after the end of the exercise. This delay was necessary to position the subject in the scanner and to select the image volume position. Each session took about one hour and both were performed within one week. At the end of the exercise volunteers had to rate their individual perceived exertion (rated perceived exertion, RPE) on a standardized Borg scale ranging from 6 - "no exertion at all" - to 20 - "maximal exertion" [BORG, 1990].

MR spectroscopy

All MR data were collected on a 3 T whole-body MR scanner (TIM Trio; Siemens Healthcare, Erlangen, Germany). In the MRS session, T_1 -weighted localization images and MR spectra were measured in the low back muscles with a double tuned ($^1\text{H}/^{31}\text{P}$) flexible surface coil (RAPID Biomedical GmbH, Würzburg-Rimpar, Germany), which was aligned symmetrically to the volunteer's lumbar spine. Spectra were acquired using a 2D ^{31}P -CSI-FID sequence (FOV = $240 \times 240 \text{ mm}^2$; matrix = 8×8 ; voxel volume = $30 \times 30 \times 25 \text{ mm}^3$; TR = 920 ms; TA = 27 s; elliptical k -space sampling scheme and Hamming filtering). The coronal CSI slice was aligned parallel to the spine at the height of the intervertebral disk L3-L4 such that the two center CSI grid rows contained 2×4 voxels covering the inner (*M. multifidus*, MF) and outer (*M. erector spinae*, ES) regions of the lower back skeletal muscles (demonstrated in Fig. 4.17; MF and ES marked in red and blue, respectively). Voxels (4,4) and (5,4) correspond to the right, and voxels (4,5) and (5,5) to the left MF, whereas the left and right ES are represented by the voxels (4,3), (5,3) and (4,6), (5,6), respectively. Measurement series of 22, 22 and 36 single CSI acquisitions were continuously performed prior, during and post exercise, respectively.

All spectra were post-processed using a self-written MATLAB routine including frequency, phase and baseline corrections as well as exponential apodization with a 20 Hz damping constant. In order to exclude motion-induced signal changes during exercise, the SNR of the β - and

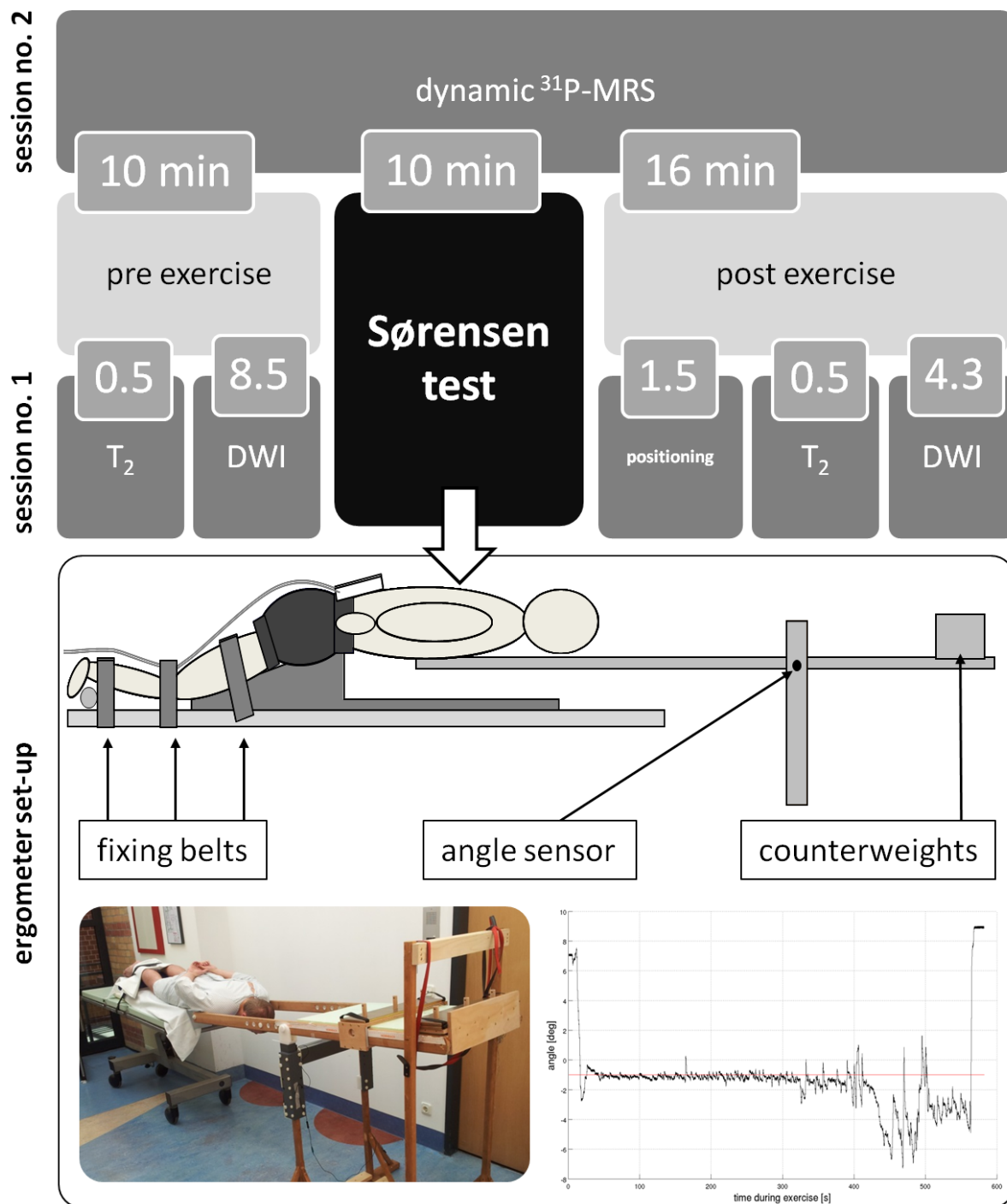


Figure 4.16: MR examination protocol including an MRS session, during which ^{31}P -MR spectra were continuously acquired during rest (10 min), exercise (10 min) and post exercise (16 min), and an MRI session, during which T_2 -weighted and DW data were collected before and after the exercise that was performed outside the scanner (re-positioning of the subject in the scanner resulted in an MRI acquisition delay of 1.5 min and 2 min, respectively). The exercise was arranged as a modified Biering-Sørensen test using an MR compatible ergometer equipped with an angle sensor on the ergometer stilt for interactive self-adjustment of the upper body position during the exercise (red line represents the target position of the rocker). The counterweights were adjusted to 50% of the upper body weight.

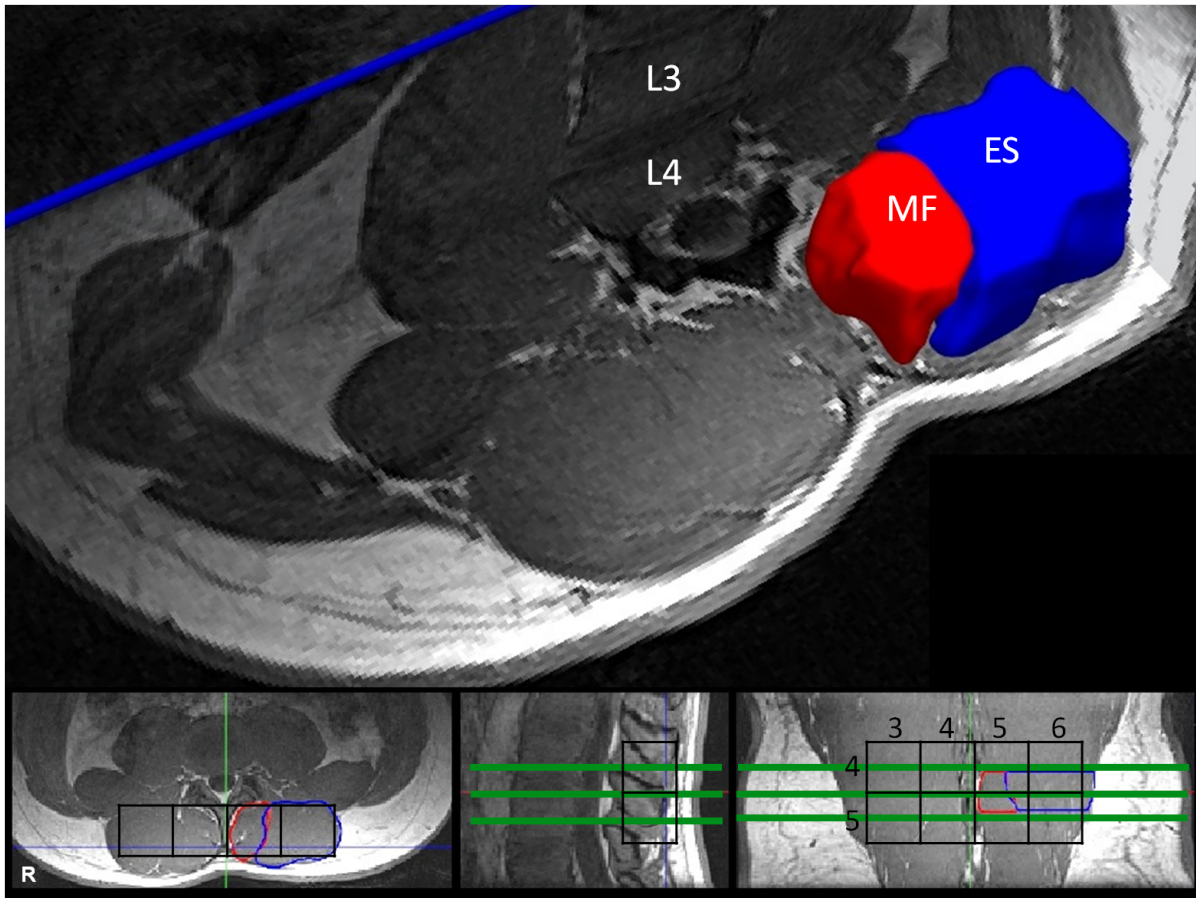


Figure 4.17: Position of the coronal ^{31}P -CSI slice (illustration of the inner 2×4 voxels of the 8×8 grid, black) and the axial mfMRI slices (green) using the intervertebral disk L3-L4 as anatomic reference. The colored 3D ROIs correspond to the *M. multifidus* (MF, red) and *M. erector spinae* (ES, blue). The ROIs outlining the right and left MF are mainly located in the central CSI voxels (4-5,4) and (4-5,5), respectively, whereas the outer CSI voxels (4-5,3) and (4-5,6) mainly cover the ES muscles.

γ -ATP multiplets was determined by assuming constant ATP concentrations during rest and load [TAYLOR et al., 1986]. Only spectra with $\text{SNR}_{\text{ATP}} > 6$ were included for further analysis. To improve SNR, spectra of the same CSI grid columns were spatially averaged [voxels (4,3) and (5,3); (4,4) and (5,4); (4,5) and (5,5); (4,6) and (5,6)], followed by temporal sliding-window averaging of five consecutive spectra. All metabolites were corrected for saturation effects by using recently reported T_1 -values of human calf muscles [BOGNER et al., 2009]. This correction method was also successfully evaluated based on an additional ^{31}P -CSI measurement in the lower back muscles of a 23 year-old male volunteer using the proposed sequence protocol with two different repetition times of $\text{TR}_1 = 920$ ms (as usually applied) and $\text{TR}_2 = 30$ s. Peak integrals of PCr, Pi and the three ATP groups were quantified using the AMARES routine of the MR spectra processing toolbox jMRUI [VANHAMME et al., 1997]. PCr and Pi peaks were fitted as single Lorentzians, whereas γ - and α -ATP signals were fitted as Lorentzian doublets

and β -ATP as a Lorentzian triplet. Quantification was constrained by using an appropriate, previously described prior knowledge database of constant intensity ratios within the multiplets [SCHRODER et al., 2005]. To account for the intrinsic motion-sensitivity of the ^{31}P -CSI sequence, which can cause motion-induced SNR alterations during exercise, PCr and Pi signals were normalized with the corresponding mean intensity of ATP, whose concentration was assumed to remain constant during muscle load [TAYLOR et al., 1986].

Changes between normalized PCr and Pi intensities pre- ($\text{PCr}_{\text{rest}}/\text{ATP}_{\text{rest}}$, $\text{Pi}_{\text{rest}}/\text{ATP}_{\text{rest}}$) and post-exercise ($\text{PCr}_{\text{load}}/\text{ATP}_{\text{load}}$, $\text{Pi}_{\text{load}}/\text{ATP}_{\text{load}}$) were determined by comparing their mean resting-state values to the average ratios during the second half of the exercise, respectively, while assuming a PCr equilibrium in the second half of loading (described in section 4.2.4). Relative PCr and Pi changes (PCr_{drop} , Pi_{inc}) were determined as follows:

$$\text{PCr}_{\text{drop}} = 100 \cdot \left(1 - \frac{\text{PCr}_{\text{load}}/\text{ATP}_{\text{load}}}{\text{PCr}_{\text{rest}}/\text{ATP}_{\text{rest}}} \right), \quad (4.14)$$

$$\text{Pi}_{\text{inc}} = 100 \cdot \left(\frac{\text{Pi}_{\text{load}}/\text{ATP}_{\text{load}}}{\text{Pi}_{\text{rest}}/\text{ATP}_{\text{rest}}} - 1 \right). \quad (4.15)$$

The chemical shift between Pi and PCr was used to calculate the intra-cellular pH according to the Henderson-Hasselbalch equation (Eq. 4.2) and exercise-induced pH changes were calculated by subtracting the mean pH during the second half of the exercise (pH_{load}) from the mean pH during rest (pH_{rest}):

$$\Delta\text{pH} = \text{pH}_{\text{load}} - \text{pH}_{\text{rest}}. \quad (4.16)$$

MR imaging

In analogy to the spectroscopic session, the intervertebral disk L3-L4 was chosen as anatomic reference to select the image position (Fig. 4.17). All MR images were acquired in transverse orientation using a spine coil array and slice positions were aligned perpendicularly to the lumbar spine of the subject. To prevent inclusion of subjects with pathological changes, such as disk degeneration diseases, high-resolution anatomic MR images were acquired using a T_1 -weighted 3D GRE sequence (VIBE sequence; single 3D slab of 96 transverse partitions; FOV = $352 \times 352 \times 96 \text{ mm}^3$; voxel matrix = $352 \times 352 \times 96$; voxel size = 1 mm^3 ; 6/8 slice-PF; TR = 4 ms; TE = 2.3 ms; NEX = 2; TA = 5.18 min).

T_2 - and diffusion-weighted MR images were measured before and after exercise. T_2 mapping was based on a series of five T_2 -weighted data sets with incrementally increased echo times that were acquired with a multi-slice SE-EPI sequence as supplied by the vendor (three 10 mm-thick transverse slices without inter-slice gap; FOV = $330 \times 276 \text{ mm}^2$; 110×92 voxel matrix, $3 \times 3 \text{ mm}^2$ in-plane resolution; TR = 500 ms; TE₁₋₅ = 32, 40, 48, 56, 64 ms; NEX = 6; TA = 32.5 s; 7 preparation scans per slice). Trace-weighted IVIM images were obtained with a twice-refocused SE-EPI sequence of the same three slices with identical spatial resolution and sequence timing (TR = 2 s; TE = 68 ms; GRAPPA factor = 2; 1 preparation scan per slice)

including 16 acquisitions with incrementally increased b-values in three orthogonal directions ($b = 0, 5, 10, 15, 20, 25, 30, 35, 40, 45, 50, 75, 100, 200, 400, 600 \text{ s/mm}^2$). Due to the low perfusion-related signal decay during rest $\text{NEX}_{\text{pre}} = 6$ ($\text{TA}_{\text{pre}} = 8.5 \text{ min}$) and $\text{NEX}_{\text{post}} = 3$ ($\text{TA}_{\text{post}} = 4.3 \text{ min}$) multiple data sets were acquired prior to and post exercise, respectively. To avoid signal contamination from vascular flow in large blood vessels two transverse oriented saturation pulses were applied caudally and cranially to the acquired transverse DWI slices. Furthermore, T_2 - and diffusion-weighted MR images were acquired by means of frequency selective water excitation, which reduces chemical shift artifacts of fat signals and partial volume effects in voxels containing subcutaneous or intra-muscular fat both potentially affecting the T_2 and IVIM quantitation.

In order to correct for image displacements resulting from the re-positioning of subjects, all pre- and post-exercise images were co-aligned intra-individually using a non-linear image registration method [AVANTS et al., 2008]. Maps of T_2 , molecular diffusion coefficient D and vascular volume fraction f were all calculated from the aligned image data sets. T_2 maps were calculated voxel-wise using a mono-exponential fit function (Eq. 4.6). The DWI data were denoised by performing the local PCA approach (described in sec. 4.3.4) and maps of the IVIM parameters D and f were calculated based on mono-exponential fitting (Eq. 4.10) of DWI data with $b > 100 \text{ s/mm}^2$ (sec. 4.3.4). ROIs defining the MF and ES (compare Fig. 4.17) were outlined once on the averaged b_0 images of the DW data set and subsequently copied to the T_2 , D and f maps. To reduce partial volume effects, ROIs were eroded using a kernel size of two voxels (FSL 4.1, FMRIB Software Library, University of Oxford, UK). To examine exercise-induced changes of T_2 , D and f , the median of the ROI values on the corresponding maps was calculated before and after the exercise and the parameter changes were defined as follows:

$$T_{2,\text{inc}} = 100 \cdot \left(\frac{T_{2,\text{load}}}{T_{2,\text{rest}}} - 1 \right), \quad (4.17)$$

$$D_{\text{inc}} = 100 \cdot \left(\frac{D_{\text{load}}}{D_{\text{rest}}} - 1 \right), \quad (4.18)$$

$$\Delta f = f_{\text{load}} - f_{\text{rest}}. \quad (4.19)$$

In addition, the mean squared errors (MSE) of the fits were calculated for all IVIM and T_2 estimates. Voxels with MSE exceeding an empirically chosen threshold (T_2 : 10 a.u.; DWI: 0.0005 a.u.) were excluded from the ROI analysis described before. The MSE values were averaged over the ROIs and also compared to the results of the IVIM maps calculated without applying the denoising procedure to assess the effect of denoising on the enhancement accuracy.

Statistical analysis

All results including pre- and post-exercise MR parameters as well as exercise-induced changes are presented as mean and standard deviation (SD). Based on the obtained data several sta-

tistical analyses were performed:

- Differences between pre- ($\text{PCr}_{\text{rest}}/\text{ATP}_{\text{rest}}$, $\text{Pi}_{\text{rest}}/\text{ATP}_{\text{rest}}$, pH_{rest} , $T_{2,\text{rest}}$, D_{rest} , f_{rest}) and post-exercise values ($\text{PCr}_{\text{load}}/\text{ATP}_{\text{load}}$, $\text{Pi}_{\text{load}}/\text{ATP}_{\text{load}}$, pH_{load} , $T_{2,\text{load}}$, D_{load} , f_{load}) as well as between muscles were evaluated by using linear mixed models allowing flexible modeling of correlated data with non-constant variability. To account for different variability in each state as observed by exploring individual profile diagrams with respect to the four muscles, state-specific random effects were included in the model. The model also accounted for correlation between the states and between the muscles by incorporating correlation between the random effects.
- Due to the limited number of observations an interaction between the mixed model effects of *state* and *muscle* was not included into the above-described models. Possible differences between the muscles with respect to the exercise-induced MR changes were evaluated by means of one-way repeated measurements ANOVA of the MR response factors PCr_{drop} , Pi_{inc} , ΔpH , $T_{2,\text{inc}}$, D_{inc} and Δf .
- To test for associations between the rate of perceived exertion (RPE) and different MR parameter changes (averaged over the different muscles), pairwise Pearson correlations were performed between RPE values determined in the MRI or in the MRS session and $T_{2,\text{inc}}$, D_{inc} , Δf or PCr_{drop} , Pi_{inc} and ΔpH , respectively. In addition, to assess associations between activation levels as characterized by ^{31}P -CSI, T_2 - or diffusion-weighted MRI independent of muscle, pairwise Pearson correlations were calculated between intra-individually averaged mfMR response factors (mean values across the muscles).
- The effects of metabolic, diffusion and vascular changes on T_2 alterations with respect to the muscles were evaluated using a linear mixed model, in which $T_{2,\text{inc}}$ served as the dependent variable, and PCr_{drop} , Pi_{inc} , ΔpH , D_{inc} and Δf as covariates. To account for correlation between the muscles, the model also included a muscle-specific random intercept. Finally, the hypotheses that (i) changes in metabolism and vascular volume fraction and (ii) changes in diffusion and blood volume underlie T_2 alterations ($T_{2,\text{inc}}$) were tested by evaluating two reduced linear mixed models, first including PCr_{drop} and Δf and second D_{inc} and Δf as covariates, respectively.

All statistical analyses were carried out by SAS 9.4 using PROC MIXED. In all linear mixed models Q-Q-plots of the residuals and random effects were examined to confirm model assumptions visually. The level of significance was set to 0.05. In case of multiple comparisons the corresponding p -values were Bonferroni-corrected (α adjustment).

4.4.2 Results

Dynamic ^{31}P -MR spectroscopy

Mean ATP-normalized PCr and Pi time-courses averaged over all subjects are shown in Fig. 4.18 for the four investigated muscles. The time courses show similar transient changes in all muscles with approximately the same PCr/Pi equilibrium level during the second half of the exercise. Table 4.1 summarizes the results for the different metabolic parameters. The applied mixed model of PCr/ATP levels yielded significantly higher PCr/ATP ratios in the right lower back muscles (ES and MF) compared to the left body side ($p < .009$) both at rest and during exercise. Furthermore, the significant effect of model factor *state* clearly indicated differences between PCr/ATP ratios during rest and exercise ($p < .001$). Mixed model analyses of PCr decreases (PCr_{drop}) resulted in non-significant differences between the muscles ($p = .225$), with PCr_{drop} ranging from $\approx 30\%$ in the ES muscles [right: $(29.8 \pm 10.5)\%$; left: $(29.7 \pm 12.5)\%$] to $\approx 34\%$ in the MF muscles [right: $(33.4 \pm 11.9)\%$; left: $(33.8 \pm 11.2)\%$].

The Pi/ATP ratios increased significantly during exercise in all muscles due to the accumulation of Pi ($p < .001$). The mixed model analysis revealed significant interaction between *muscle* and *state* ($p < .015$) with significant Pi/ATP differences between the right ES and the left muscles during load, but no significant inter-muscular differences at rest. Exercise-induced Pi/ATP increases (Pi_{inc}) were higher in the MF muscles [right: $(138.5 \pm 55.3)\%$; left: $(128.9 \pm 51.0)\%$] than in ES muscles [right: $(123.7 \pm 58.6)\%$; left: $(96.3 \pm 42.7)\%$]. Compared to the left ES ($p = .001$) and left MF ($p = .006$), Pi_{inc} was significantly stronger in the right MF. The pH values showed significant exercise-induced decreases ($p < .001$) with no muscle-specific differences, neither in absolute levels nor in relative pH changes.

Table 4.1: Metabolic quantities for the four lower back muscles (mean \pm SD).

	right ES (1)	right MF (2)	left MF (3)	left ES (4)
PCr _{rest} /ATP _{rest}	2.37 \pm 0.27	2.33 \pm 0.32	2.19 \pm 0.24	2.10 \pm 0.25
PCr _{load} /ATP _{load}	1.65 \pm 0.26* _{†3,4}	1.54 \pm 0.24* _{†3,4}	1.44 \pm 0.24* _{†1,2}	1.47 \pm 0.29* _{†1,2}
PCr _{drop} [%]	29.8 \pm 10.5	33.4 \pm 11.9	33.8 \pm 11.2	29.7 \pm 12.5
Pi _{rest} /ATP _{rest}	0.33 \pm 0.06	0.29 \pm 0.05	0.29 \pm 0.06	0.34 \pm 0.07
Pi _{load} /ATP _{load}	0.72 \pm 0.13*	0.68 \pm 0.12*	0.66 \pm 0.14*	0.65 \pm 0.13*
Pi _{inc} [%]	123.8 \pm 58.6	138.5 \pm 55.3* _{†3,4}	128.9 \pm 51.0 _{†2}	96.3 \pm 42.7 _{†2}
pH _{rest}	6.99 \pm 0.04	6.98 \pm 0.04	6.99 \pm 0.03	6.99 \pm 0.03
pH _{load}	6.93 \pm 0.03*	6.95 \pm 0.04*	6.94 \pm 0.04*	6.94 \pm 0.05*
ΔpH	0.06 \pm 0.05	0.04 \pm 0.04	0.05 \pm 0.05	0.06 \pm 0.05

* Significantly different compared to the rest state ($p < .0125$); † Significant inter-muscular differences ($p < .0083$) where index indicates compared muscle; p -values were Bonferroni-corrected based on $\alpha = 0.05$ and the number of comparisons.

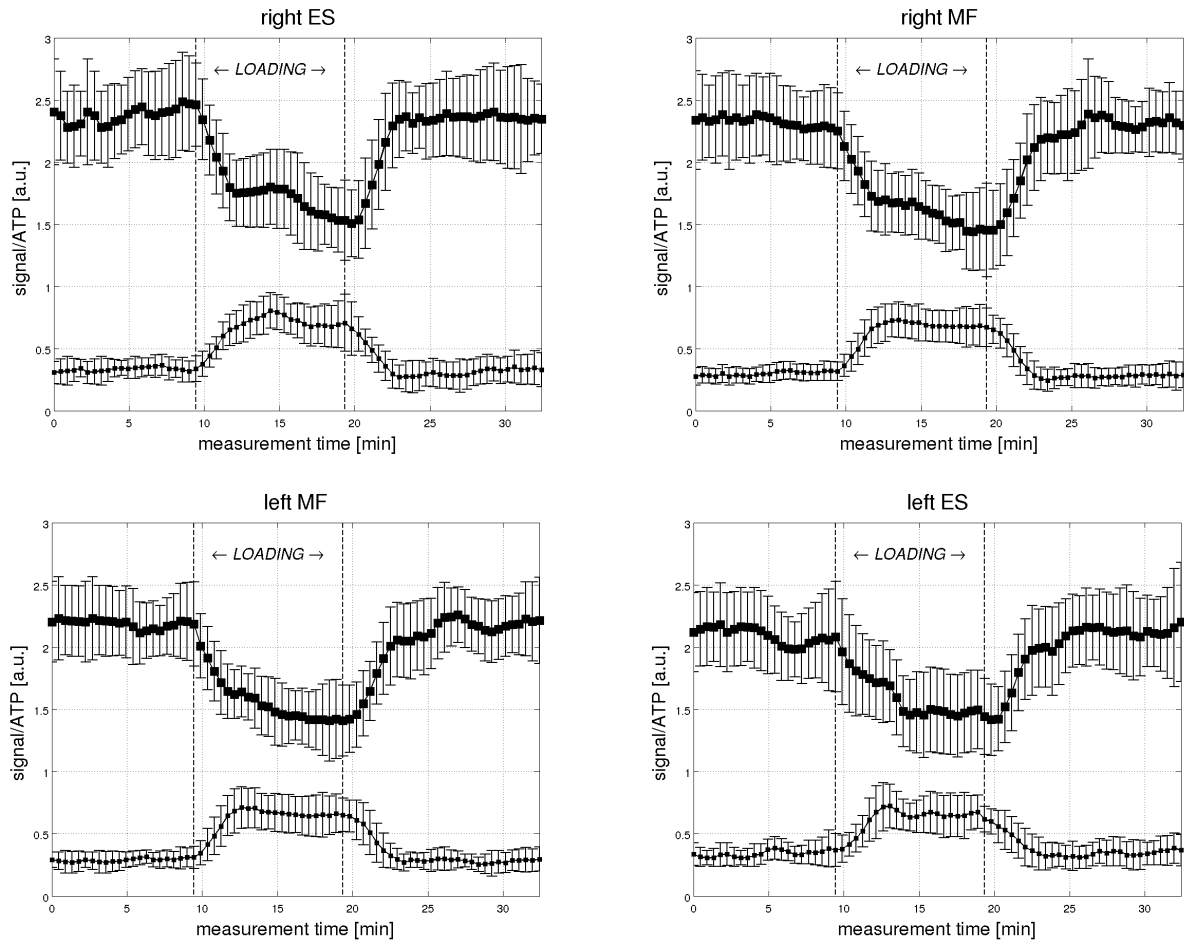


Figure 4.18: Mean time courses of normalized PCr (upper curve) and Pi (lower curve) levels that were determined bilaterally in the back muscles ES and MF. The error bars represent the SD of the examined cohort. All muscles reveal similar transient PCr and Pi changes during the first half of exercise and similar metabolic steady-state levels during the second half of exercise.

Muscle functional MR imaging

Fig. 4.19 displays representative T_2 maps of a single subject before and after exercise. Load-induced increases of T_2 are clearly observed in all muscles as reflected by the change in the map colors from predominantly yellow in the pre-exercise maps to distinctly more red in the post-exercise maps. On closer inspection, the post-exercise T_2 maps reveal inhomogeneous patterns of increased values across the muscles with higher T_2 in the inner low back muscles, which is even better seen in the ROI-based histograms, illustrating the muscle-specific distributions of T_2 values with a positive shift of the corresponding mean T_2 values. Table 4.2 summarizes the ROI-based mean baseline and post-exercise T_2 values ($T_{2,\text{rest}}$, $T_{2,\text{load}}$) together with the mean relative T_2 changes ($T_{2,\text{inc}}$, see Eq. 4.17) for the four muscles, averaged over all subjects. Baseline T_2 values were similar in all muscles ($T_{2,\text{rest}} \approx 27$ ms). The applied linear mixed model of pre- and post-exercise T_2 values identified an interaction between *state* and *muscle* ($p = .009$) with significant differences between pre- and post-load T_2 in the right ES, right MF

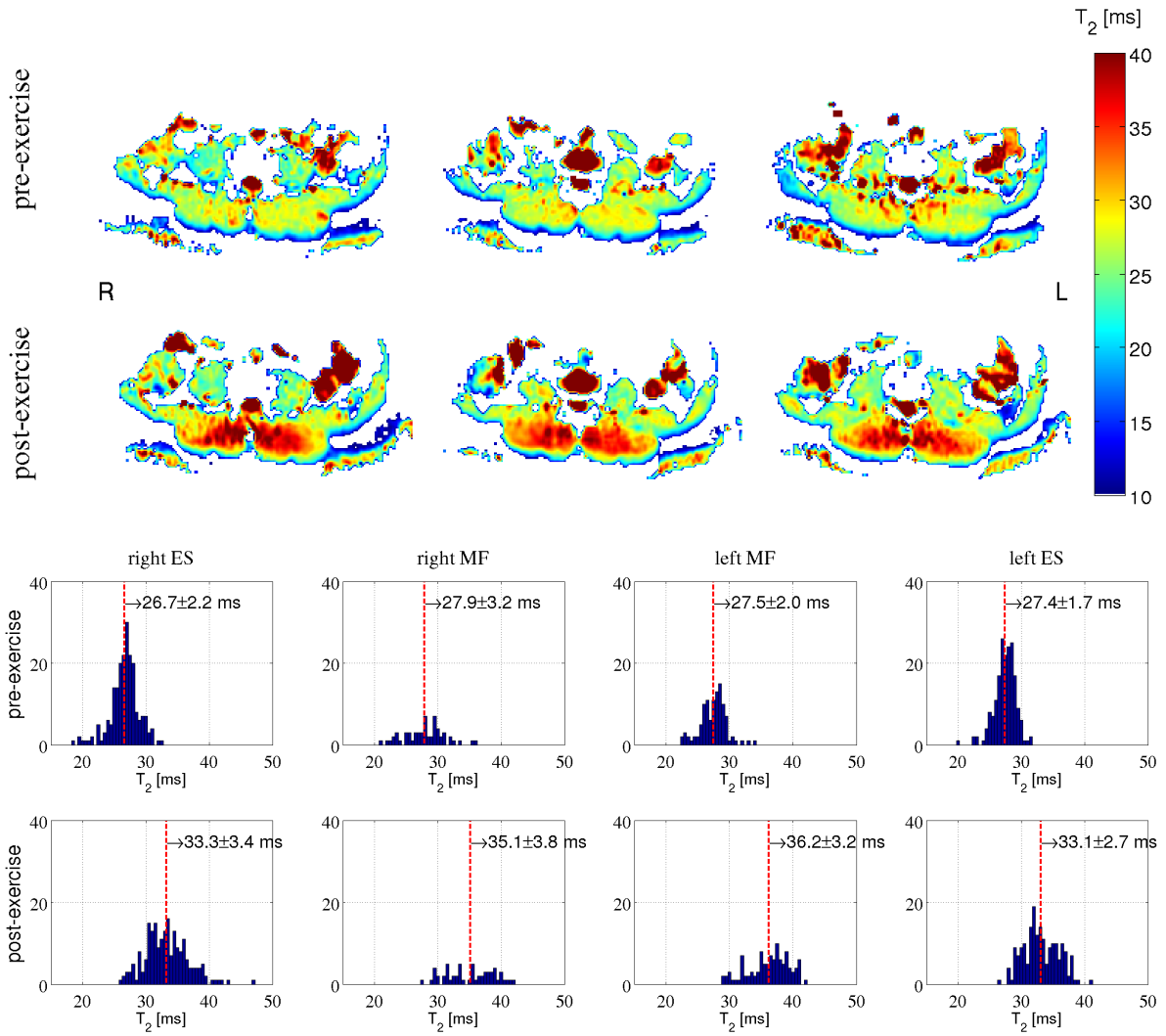


Figure 4.19: Representative pre- and post-exercise T_2 maps of a single subject (three slices acquired in both states; for illustration purposes bilinear interpolation by a factor of 2 was applied) and corresponding T_2 histograms based on ROI-analysis of the four low back muscles. Inhomogeneous activation patterns are observable with higher T_2 increases in the MF compared to ES muscles (see mean T_2 values indicated by red vertical lines in the histograms).

and left MF ($p < .001$), but not in the left ES ($p = .067$). A clear right-left asymmetry of exercise-induced T_2 changes was observed, with higher $T_{2,\text{inc}}$ values in the right than in the left muscles [right ES: $T_{2,\text{inc}} = (11.8 \pm 9.9)\%$; left ES: $T_{2,\text{inc}} = (4.6 \pm 6.6)\%$]. Accordingly, $T_{2,\text{inc}}$ was significantly higher in the right ES and right MF compared to the left ES ($p < .007$).

Exemplary pre- and post-exercise maps of the IVIM parameters D and f are shown in Fig. 4.20. Similar to the T_2 maps, the f maps obtained in this particular subject showed larger exercise-induced increases in the MF muscles. This was not observable on the D maps. The local PCA denoising approach enabled reliable assessment of small perfusion fractions - as they prevail prior to exercise (only few pixels left with $f \leq 0\%$) - and provided sufficient IVIM

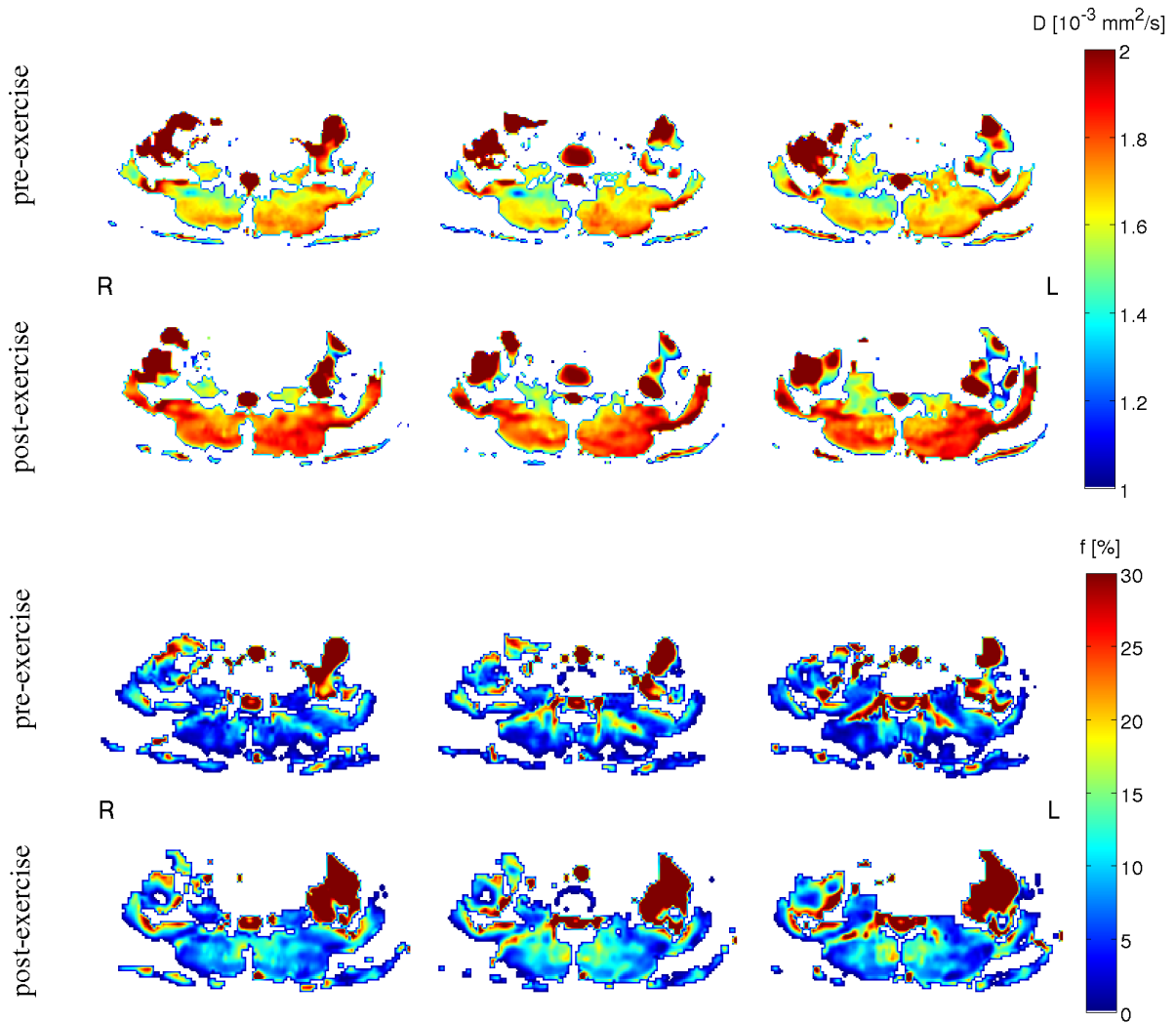


Figure 4.20: Representative pre- and post-exercise D and f maps calculated based on denoised IVIM data (same subject as in Fig. 4.19; bilinear interpolation by a factor of 2). Both parameters show inhomogeneous exercise response patterns with highest exercise-induced changes in of the vascular volume fraction f in the MF muscles (analogous to T_2 changes). Of note, the inferior *vena cava*, spinal cord and left kidney reveal highest f values independent of state.

parameter mapping quality. With denoised IVIM data the fit precision was nearly doubled compared to raw IVIM data fitting ($\text{MSE}_{\text{raw data}}/\text{MSE}_{\text{PCA data}} = 1.87$), reflecting a reduction in the uncertainty of the fit. Table 4.2 further lists muscle-specific mean D and f values derived from denoised data together with the corresponding load-induced response factors (as defined in Eq. 4.17-4.19). All muscles showed significantly increased diffusion coefficients D after exercise ($p = .007$) with a significant effect of *muscle* ($p = .036$). Similar to $T_{2,\text{inc}}$, higher D_{inc} values were found in the right back muscles compared to the left body side. However, following α adjustment for multiple comparisons pairwise inter-muscular differences became insignificant ($p = .324$). Similarly, vascular volume fractions f were significantly increased after the exercise

Table 4.2: MRI parameters obtained before and after muscle load (mean \pm SD).

	right ES (1)	right MF (2)	left MF (3)	left ES (4)
$T_{2,\text{rest}}$ [ms]	26.7 ± 1.7	26.8 ± 1.2	27.1 ± 1.0	27.3 ± 1.5
$T_{2,\text{load}}$ [ms]	$29.8 \pm 2.8^*$	$29.4 \pm 2.7^*$	$29.4 \pm 2.5^*$	28.5 ± 2.1
$T_{2,\text{inc}}$ [%]	$11.8 \pm 9.9_{\dagger 4}$	$9.7 \pm 9.3_{\dagger 4}$	8.9 ± 9.3	$4.6 \pm 6.6_{\dagger 1,2}$
D_{rest} [10^{-3} mm 2 /s]	1.69 ± 0.04	1.70 ± 0.05	1.69 ± 0.05	1.69 ± 0.08
D_{load} [10^{-3} mm 2 /s]	$1.73 \pm 0.06^*$	$1.76 \pm 0.04^*$	$1.73 \pm 0.07^*$	$1.73 \pm 0.07^*$
D_{inc} [%]	2.9 ± 3.4	3.6 ± 3.6	2.0 ± 4.6	2.3 ± 4.2
f_{rest} [%]	5.2 ± 2.3	8.0 ± 3.1	8.4 ± 3.9	5.5 ± 3.2
f_{load} [%]	$8.7 \pm 2.5^*_{\dagger 2,3}$	$11.5 \pm 3.2^*_{\dagger 1,4}$	$11.0 \pm 4.0^*_{\dagger 1,4}$	$8.2 \pm 3.7^*_{\dagger 2,3}$
Δf [pp]	3.6 ± 3.1	3.5 ± 4.1	2.5 ± 3.9	2.7 ± 3.8

* Significantly different compared to the rest state ($p < .0125$); † Significant inter-muscular differences ($p < .0083$) where index indicates compared muscle; p -values were Bonferroni-corrected based on $\alpha = 0.05$ and the number of comparisons.

Table 4.3: Matrix of correlation coefficients and corresponding p -values (in brackets) based on pairwise Pearson correlations between RPE, mfMRI and ^{31}P -MRS parameters changes.

	PCr_{drop}	P_{inc}	ΔpH	$T_{2,\text{inc}}$	D_{inc}	Δf
RPE	0.32 (.26)	0.33 (.24)	0.27 (.34)	0.58 (.03)	0.53 (.05)	0.64 (.01)
PCr_{drop}	-	-0.01 (.96)	0.69 (.01)	0.59 (.03)	0.52 (.06)	0.15 (.61)
P_{inc}	-	-	-0.35 (.22)	-0.04 (.90)	0.12 (.69)	-0.10 (.75)
ΔpH	-	-	-	0.37 (.20)	0.48 (.08)	0.29 (.31)
$T_{2,\text{inc}}$	-	-	-	-	0.72 (.00)	0.65 (.01)
D_{inc}	-	-	-	-	-	0.49 (.08)

Significant correlations are marked in bold ($p < .05$).

($p = .002$) with non-significantly higher Δf in the right muscles ($p = .369$). Absolute f_{rest} and f_{load} values were elevated in the MF compared to the ES indicating higher perfusion fraction in the inner medial than in the outer lateral lower back muscles ($p < .001$).

Associations between MRI and MRS parameter changes

As can be seen in Tab. 4.1 and Tab. 4.2, the load-induced mfMRI and MRS parameter changes ($T_{2,\text{inc}}$, D_{inc} , Δf , PCr_{drop} , P_{inc} , ΔpH) show large SDs, which may be ascribed to differences in individual fatigue. These differences were assessed by means of RPE numbers, whose mean values were 14.3 ± 3.0 and 11.4 ± 3.9 in the MRI and MRS session, respectively. These RPE values correspond to an exertion level ranging between 'fairly light' to 'hard'. Results of pairwise Pearson correlations between RPE and mfMR parameter changes as well as between the parameters $T_{2,\text{inc}}$, D_{inc} , Δf , PCr_{drop} , P_{inc} and ΔpH are summarized in Tab.4.3. While the ^{31}P -MRS parameter changes (PCr_{drop} , P_{inc} , ΔpH) revealed only a trend for a positive asso-

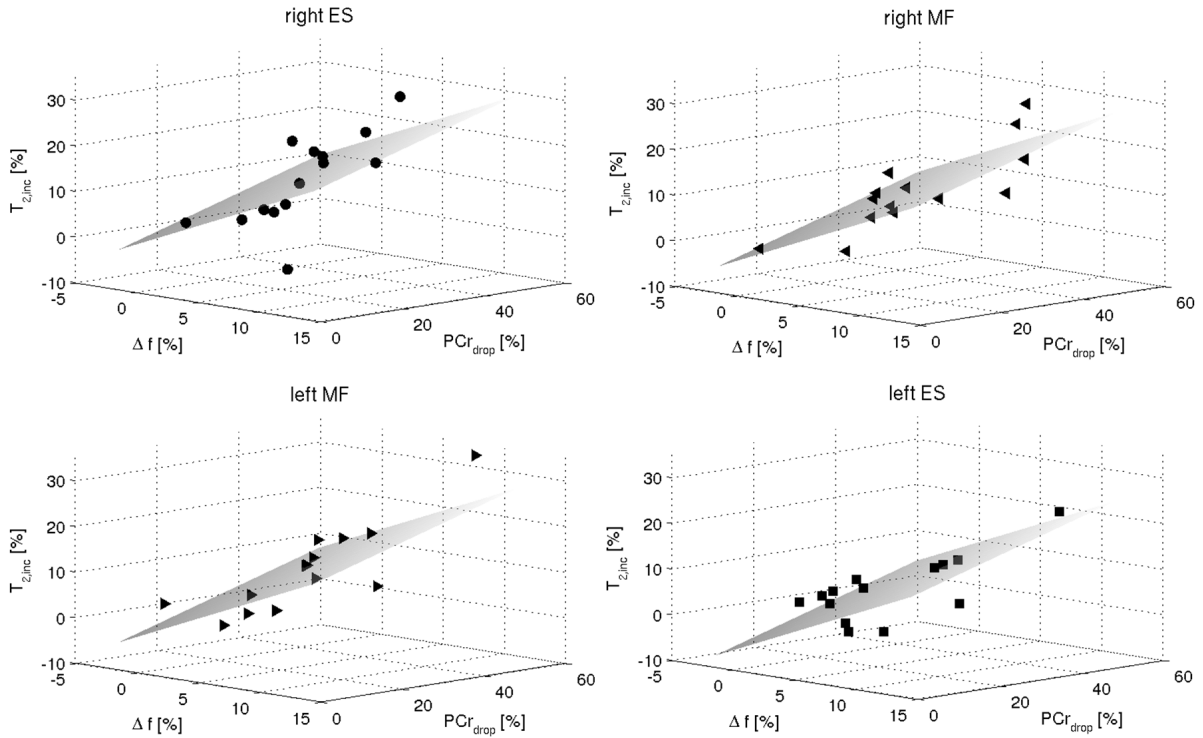


Figure 4.21: Combined relationship of PCr, perfusion fraction and T_2 changes as assessed by means of a mixed model including PCr_{drop} and Δf as independent covariates and $T_{2,inc}$ as dependent variable accounting for different muscles. For all muscles this covariate combination revealed significant associations of PCr_{drop} ($p = .001$) and Δf ($p < .001$) with $T_{2,inc}$.

ciation with RPE ($\rho = 0.27 - 0.33$, $p = .24 - .34$), $T_{2,inc}$ and Δf both showed strong positive correlations with RPE ($\rho > 0.58$, $p = .03$) and were also positively correlated among each other ($\rho = 0.65$, $p = .01$). D_{inc} showed only a non-significant trend of a positive relation with RPE ($\rho = 0.53$, $p > .05$), but was significantly associated with $T_{2,inc}$ ($\rho = 0.7$, $p < .01$). PCr_{drop} was positively correlated with ΔpH ($\rho = 0.69$, $p = .01$) and $T_{2,inc}$ ($\rho = 0.59$, $p = .03$), but not with Pi_{inc} . In addition, PCr_{drop} showed a trend with D_{inc} ($\rho = 0.52$, $p = .06$). Trends for positive associations were also observed between ΔpH and $T_{2,inc}$ ($\rho = 0.37$, $p = .20$) as well as between ΔpH and D_{inc} ($\rho = 0.48$, $p = .08$). Correlations were found neither between vascular volume changes Δf and metabolic parameters ($p > .31$) nor between Pi_{inc} and MRI parameters ($p > .69$). The linear mixed model analysis for $T_{2,inc}$ including all MR parameters yielded that only PCr_{drop} and Δf , but not Pi_{inc} , ΔpH and D_{inc} , significantly affected $T_{2,inc}$. The reduced model including only PCr_{drop} ($p = .001$) and Δf ($p < .001$) as covariates confirmed the results of the full model supporting the assumption that T_2 alterations ($T_{2,inc}$) are simultaneously related to changes in vascular volume fraction and metabolism. This can be also seen in Fig. 4.21 for the different muscles using the estimated regression coefficients of the model. The second reduced mixed model including D_{inc} and Δf as covariates yielded only a significant effect of Δf on $T_{2,inc}$ ($p < .001$) but not for D_{inc} ($p = .460$).

4.4.3 Discussion

The aim of this study was to examine exercise-induced metabolic, vascular and diffusion changes in skeletal muscles and to explore whether these changes underlie T_2 alterations. To this end, dynamic ^{31}P -CSI, diffusion-weighted and T_2 -weighted MRI were applied in the lower back muscles of a group of fourteen healthy volunteers. Load-induced changes of T_2 of $\approx 10\%$ confirm recent findings [ABABNEH et al., 2008; TAWARA et al., 2009; TAWARA et al., 2011], and PCr depletion of about $\approx 30\%$ are in line with previous work [BOESCH, 2007; KEMP et al., 2007; RZANNY et al., 2006]. Tissue diffusion D and perfusion fraction f were assessed by applying a novel imaging and data processing strategy including outer-volume suppressed trace-weighted DWI with multiple b-values, PCA-based data denoising and mono-exponential DWI signal fitting. The sequence is sensitive to the micro-circulation of blood through muscle tissue and enables determination of the most relevant measure of O_2 delivery to muscle tissue. The denoising approach appropriately filters the DWI signal attenuation curve [MANJON et al., 2013], which is subsequently analyzed by mono-exponential fitting the high b-value regime ($b > 100 \text{ s/mm}^2$). This simplified IVIM approach allows differentiating between molecular diffusion and perfusion-related signal attenuation, provides reliable IVIM parameter mapping and is thus capable of providing insight into the spatial adaptation of perfusion to the needs of skeletal muscle tissue in the lower back (Fig. 4.20).

Determined load-induced increases of vascular volume fractions (f) and molecular diffusion (D) are in good agreement with previously reported studies of human forearm muscles [MORVAN, 1995; FILLI et al., 2015] and can be ascribed to the different underlying physiologic processes, such as capillary perfusion (interstitium) and myofibrillar response (intra-cellular space), respectively. More precisely, increased f and D during exercise can be explained by increases in capillary recruitment and in extra-vascular water content or in temperature, respectively [MORVAN, 1995]. Since exercise-induced D changes, however, mainly depend on changes of the radial diffusibility (perpendicular to the fiber direction) and thus are related to the mean fiber diameter [DEUX et al., 2008; SCHWENZER et al., 2009; SIGMUND et al., 2014], they primarily represent myocellular responses. Higher f values observed in the MF compared to the ES muscles before and after exercise can be ascribed to larger blood vessels in the MF since both muscles show similar capillary densities [JORGENSEN et al., 1993].

Interestingly, T_2 , D and f maps showed higher load-induced changes in the right MF and right ES compared to the left side. It can be argued that these heterogeneous patterns are related to asymmetric muscle activation, potentially due to the right-handedness of the examined subjects. However, larger comparative studies including left-handed subjects are required to verify this hypothesis. PCr and pH did not show significant asymmetric load-induced changes, which is possibly due to technical limitations, such as low spatial resolution and partial volume effects as described below. Moreover, high inter-subject variability of all mfMR response factors (PCr_{drop} , Pi_{inc} , ΔpH , $T_{2,\text{inc}}$, D_{inc} and Δf) were observed, which may reflect various levels of muscle activity or fatigue of the investigated persons. In fact, the finding of significant

positive Pearson correlations between Δf and RPE as well as between $T_{2,\text{inc}}$ and RPE ($p \leq .03$, Tab. 4.3) seems to support this assumption, since RPE quantifies the individually perceived exertion and is associated with the heart rate as a physiological measure for the demand of oxygen [BORG, 1990]. In contrast to the imaging parameters, load-induced metabolic changes were not correlated with RPE indicating lower sensitivity of these measures to individually perceived exertion levels in the present study. This may be again due to technical limitations reducing the sensitivity to local activation spots or due to the fact that the individual metabolic capacity is only an indirect measure of the subject's felt exertion during sustained load.

Strong positive correlations were detected between Δf and $T_{2,\text{inc}}$, D_{inc} and $T_{2,\text{inc}}$ as well as between PCr_{drop} and $T_{2,\text{inc}}$ (Tab. 4.3). This is in accordance with the previously reported assumption of metabolic, extra-cellular and/or vascular effects on T_2 during muscle load. The weaker associations between Δf and PCr_{drop} as well as between Δf and D_{inc} suggest independent effects of vascular and PCr changes on T_2 alterations. Linear mixed models were applied to analyze combined effects of metabolism and extra-cellular and/or vascular fluid volumes on load-induced T_2 changes while accounting for the different muscles. The most important findings were that alterations in vascular volume fraction (Δf) rather than changes in diffusion (D_{inc}) are associated with T_2 changes and that Δf as well as PCr_{drop} both have significant effects on $T_{2,\text{inc}}$. Hence, the results obtained in this work support the assumptions that T_2 changes are associated to intra-cellular metabolic accumulations [BENDAHAN et al., 2004; DAMON et al., 2002b; PATTEN et al., 2003; SAAB et al., 2000] and that they are simultaneously affected by altered tissue perfusion [ABABNEH et al., 2008; DAMON and GORE, 2005].

Since initial investigations based on NNLS fitting showed that T_2 measured by means of SE-EPI (applying echo times in the range of $\text{TE} = 20 - 70$ ms) is not directly sensitive to the signal originating from the vascular component (sec. 4.3.3), it can be concluded that both T_2 and f are independent measures and that exchanges between the vascular and tissue component (extra and intra-cellular spaces, see Fig. 4.8) may be responsible for the observed association between T_2 and f changes. The impact of changes in temperature or myofibrillar structure on T_2 as indicated by a significant correlation between D_{inc} and $T_{2,\text{inc}}$ (averaged across different muscles) became insignificant compared to Δf when accounting for different muscles.

Dynamic ^{31}P -chemical shift imaging (CSI) was used to monitor the metabolic time evolution during exercise with a nominal spatial and temporal resolution of $30 \times 30 \times 25$ mm³ and 27 s, respectively. Due to the low sensitivity of ^{31}P -MRS spatial and temporal averaging of localized spectra is required, which resulted in effective spatial and temporal resolutions of $45 \times 90 \times 25$ mm³ (caused by PSF-blurring as described in 4.2.4) and 135 s, respectively. This represents a major limitation of this approach, where the low effective spatial localization does not allow analysis of intra-muscular activation patterns and induces signal contamination between the MF and ES muscles. The latter has to be considered when interpreting the data and may limit the interrelations with mfMRI parameters. However, in all muscles Pi increases were observed, which were nearly stoichiometric with the breakdown of PCr (Fig. 4.18). The Pi/PCr kinetics during the applied sub-maximal load exhibited two phases: during the first

1 – 2 min both metabolites showed initial rapid changes, followed by a second phase during which their intensities reached a steady-state. This typical time behavior is in good accordance with physiological knowledge about the different time-dependent energy pathways (detailed explanation given in sec. 4.2). Varying PCr and Pi sum intensities during exercise may arise from different T_1 saturation-related signal attenuations for PCr and Pi in the resting and loaded muscles [KEMP et al., 2007; TAYLOR et al., 1986]. Previously reported exercise-induced T_1 changes of phosphorus metabolites, such as of +58% for Pi and -20% for PCr in human calf muscles at 1.5 T [NEWCOMER and BOSKA, 1999], were not taken into account in the present study. These changes were observed during 90 s isometric plantar flexion at a workload of 62.5% of MVC. However, during steady-state aerobic exercise at low work level - as performed in this study - T_1 -relaxation times of these metabolites are not changed statistically from rest [CETTOLO et al., 2006] and may thus only lead to minimal effects related to different PCr and Pi signal attenuations during exercise.

A significant positive association between ΔpH and PCr_{drop} as determined in this work (Tab. 4.3) reflects the simultaneously ongoing PCr hydrolysis and anaerobic metabolism during the isometric load (including anaerobic glycolysis and lactic acid fermentation). However, no correlations were found between Pi_{inc} and PCr_{drop} as well as between Pi_{inc} and ΔpH based on the reported data, which is potentially due to the low SNR of the spectra. At last, due to the low effective temporal resolution and motion artifacts at the end of exercise (caused by re-positioning of the subject) analysis of the PCr recovery kinetics, which provides information of the oxidative capacity and the composition of recruited muscles fibers [FORBES et al., 2009; WRAY et al., 2009], was not reliably possible based on the data obtained in the present study. However, as can be seen in Fig. 4.18, the PCr/ATP levels at the end of the recovery period did vary across the study group. Additional analysis showed that these levels were significantly related to ΔpH ($\rho = -0.64$, $p = 0.01$). This finding is in good agreement with literature, where higher ΔpH and longer PCr recovery times are ascribed to stronger activation of the anaerobic energy supply typically occurring in type II fibers [FORBES et al., 2009].

T_2 and diffusion-weighted MRI were applied in supine position to reduce respiration-caused motion artifacts. The time delay of 1.5 min between the end of exercise and the start of scanning needed for re-positioning the volunteer in the scanner appears acceptable in light of the previously reported half-life times of T_2 and diffusion increases of 7.9 ± 4.2 min and 10.9 ± 7.0 min, respectively [ABABNEH et al., 2008]. The applied SE-EPI sequence is sensitive to B_0 inhomogeneities, but insensitive to B_1 inhomogeneities and thus provide more accurate T_2 quantification compared to TSE-based approaches (described in sec. 4.3.3). However, the susceptibility to field inhomogeneities may lead to inaccurate parameter values (T_2 , D and f) close to interfaces between soft tissue and bone. Therefore, quantitation of MRI parameters was restricted to muscle compartments, which are not in direct vicinity of bones by means of ROI eroding. Analysis of multiple T_2 components based on multi-exponential signal decay fitting as performed previously [SAAB et al., 2000] was not available in this study. This is due to the limited applicable range of TEs in SE-EPI, where the minimum TE is defined by the

refocusing rf and gradient pulse scheme as well as by the read-out duration ($TE_{\min} \approx 30$ ms) and long TEs result in strong T_2 -related signal loss.

Performing DWI with multiple low-to-intermediate b-value ranges ($0 - 600$ s/mm²) allows to extract perfusion and diffusion parameters of tissue. However, there are some inherent limitations to the IVIM approach. First, it is based on a two-compartment model (intra- and extra-vascular space), which presupposes normally distributed displacement of spins [MORVAN, 1995]. This model does not entirely reflect the complexity of tissue micro-structure, because both diffusion and pseudo-diffusion are anisotropic and predominantly occur parallel to muscle fibers [KARAMPINOS et al., 2010; SCHWENZER et al., 2009]. However, performing IVIM imaging with diffusion sensitizing gradients in three orthogonally aligned directions (trace-weighted DWI) provides assessment of a mean and directionally independent total vascular volume fraction as previously demonstrated [CALLOT et al., 2003; FILLI et al., 2015; KARAMPINOS et al., 2010]. Of note, applying separate diffusion weightings only along the main fiber direction may better take into account this anisotropy of the capillary network and may enhance the sensitivity to determine exercise-induced vascular changes with IVIM-based DWI of skeletal muscles. It would also provide a more appropriate assessment of the actual vascular volume fraction [CALLOT et al., 2003].

Second, based on recent studies that applied arterial spin labeling (ASL) and reported short-term exercise-induced perfusion increases during ≈ 1 min [WRAY et al., 2009] and up to ≈ 7 min of recovery [BOSS et al., 2006], it may be argued that vascular changes (in low back muscles) are reduced during multiple IVIM data acquisitions (three repetitions within $TA = 4.3$ min) and that temporal resolution of IVIM is thus not sufficient to resolve temporal adaptations of hyperemic responses. However, ROI-based analysis of data obtained in this study showed only a slight, non-significant trend towards decreasing Δf during the multiple acquisitions. In line with this, a recently published IVIM study also demonstrated that load-induced significant f increases (in forearm muscles), which were determined by multi-step bi-exponential analysis of the DWI signal course, persist over a time period of 20 min [FILLI et al., 2015]. The proposed fitting approach in that work is similar to our presented approach and is based on mono-exponential signal fitting at high b-values ($b > 50$ s/mm²) providing higher stability in the calculation of dynamic changes of IVIM parameters compared to conventional bi-exponential fitting. As an extension to our approach, by calculating f and D via mono-exponential fitting and subsequently using these results to constrain a bi-exponential fit ('segmented fitting'), the authors assessed both vascular volume fraction f and the pseudo-diffusion coefficient D^* . The latter also showed significant exercise-induced increases and was still significantly elevated in loaded muscles after 20 min of recovery. Hence, this multi-step bi-exponential approach may serve as a useful extension to the presented IVIM quantitation method in future studies, potentially providing additional information of muscle perfusion properties that are essential for understanding of the pathophysiology.

However, as recent research indicated that the characteristic timescale of the incoherent motion is not in the appropriate range for assuming the pseudo-diffusion limit [WETSCHEREK et al.,

2015], further efforts are needed to determine the characteristic timescale and velocity of the incoherent motion in skeletal muscles, which allows for an estimate of D^* . In addition, because the arterial blood signal is the main contributing factor causing the non-mono-exponential signal decay, and the relaxation time of arterial blood differs strongly from the surrounding muscle tissue, echo times have to be considered when determining f in future works [LEMKE et al., 2011]. Applying minimum TE reduces the effect of biased f values, which is due to the weighting of the signal fractions of the compartments by different relaxation decay rates. Another factor potentially causing corrupted f values is the exchange of protons between compartments that are neglected in the IVIM model [LE BIHAN et al., 1988]. This effect is, however, also unlikely to play a major role as the typical water exchange time between myo-cellular and blood compartment is on the order of 0.5 s [WACKER et al., 2002]. Nevertheless, an extended model taking into account exchange rates, and the T_1 and T_2 of each compartment has to be developed in the future.

Lastly, the intra-muscular activation distribution is discussed. Unluckily, the interrelations of metabolic, diffusion and perfusion changes with T_2 was limited in this work due to the low spatial resolution of ^{31}P -CSI. Consequently, detailed analysis of intra-muscular activation patterns was omitted and the great potential of mfMRI approaches could not be fully demonstrated. However, subsequent analysis showed that the results obtained in this work can be transferred to voxel-based analysis. Based on partial correlations (adjusted for *state*) associations between pre- and post-load T_2 and f voxel values could be identified yielding mean correlation coefficients (averaged across the subjects) of $\rho_p = 0.37$ ($p < 0.01$), $\rho_p = 0.39$ ($p = 0.10$), $\rho_p = 0.39$ ($p = 0.13$) and $\rho_p = 0.32$ ($p = 0.06$) for the right ES, right MF, left MF and left ES, respectively (demonstrated in Fig. 4.22). No correlations were observed between T_2 and D values, also in line with the ROI-based mfMRI correlations. In future, since even within synergistic muscle groups, mfMRI responses from individual voxels can be quite heterogeneous, as demonstrated in T_2 , D and f maps (see Fig. 4.19, 4.20 and 4.22), voxel-based analysis of activation patterns, like cluster analysis, could be more sensitive to muscle functional compartmentation than traditional (ROI-based) analysis [DAMON et al., 2003]. Thereby, future research studies should benefit from the high spatial resolution in mfMRI enabling functional distinctions between regions of muscle that are not seen with traditional analysis.

4.5 Age-related changes in muscle function and structure of low back muscles

4.5.1 Materials and Methods

In a subsequent study, fourteen healthy late-middle-aged male subjects were investigated in addition to the fourteen healthy young volunteers of the previous section. All participants were right-handers and were interviewed for their physical activity on a scale ranging from "1" - no physical activity at all - to "5" - high physical activity during training or work with

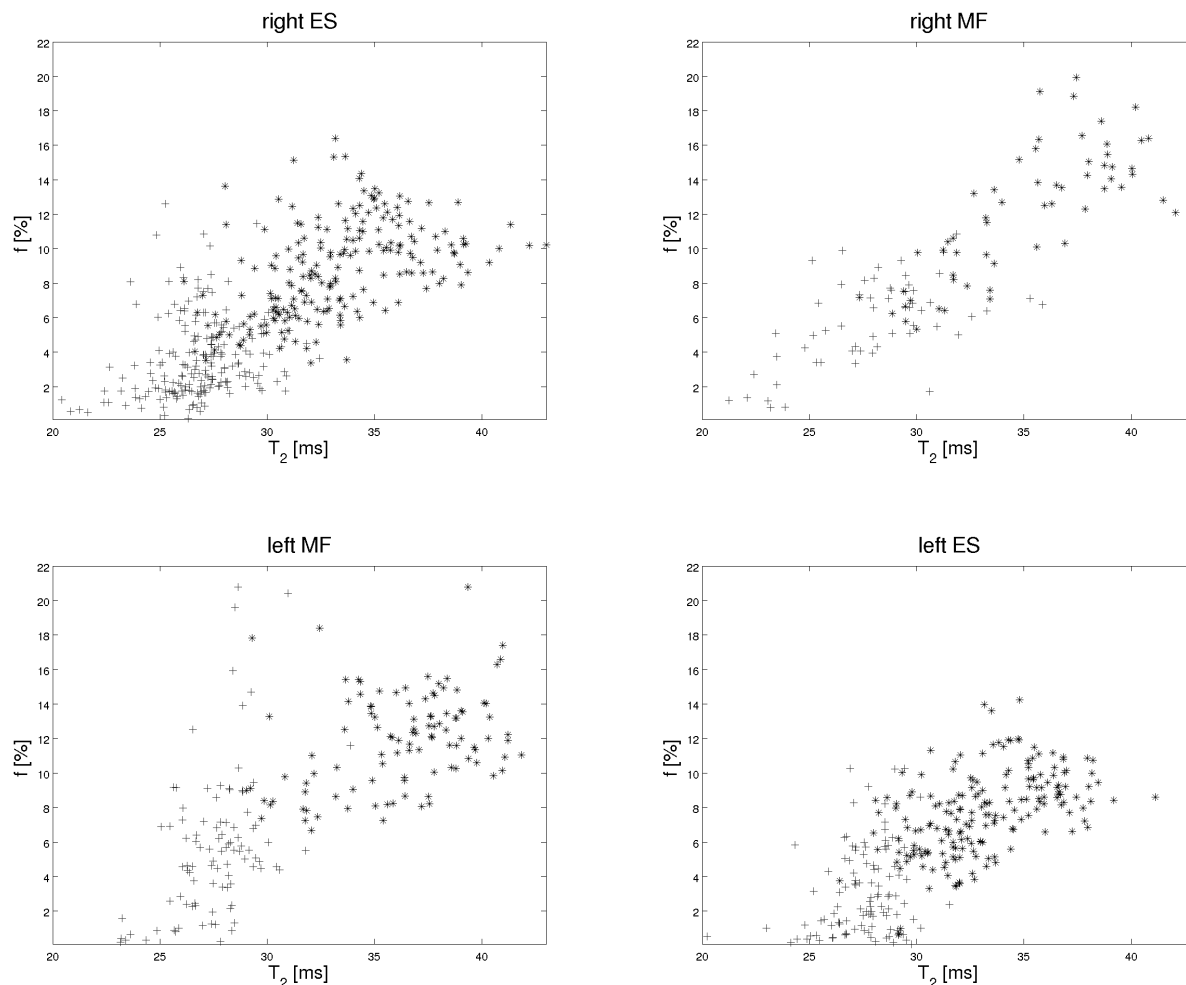


Figure 4.22: Voxel-wise comparison between T_2 and f maps obtained pre- (gray + symbols) and post-exercise (black * symbols) in the back muscles of a representative subject. The muscle-specific scatter plots indicate that the observed finding of associated (ROI-based) T_2 and f changes can be transferred to voxel-based analysis. The latter provides great potential in assessing intra-muscular activation patterns or functional clusters.

daily duration > 1 h. For both groups a median physical activity of "3" was recorded, which corresponds to normal physical activity including 2-4 physical exertions per week. Mean body mass index (BMI) and body fat fraction (measured via an impedance scale) were significantly higher in the late-middle-age group ($p < 0.05$). The upper body mass (UBM) and the isometric maximum voluntary contraction (MVC) force during back extension were both determined in a separate experiment by using the computer-supported test and training device Centaur®, BfMC, Leipzig, Germany [ANDERS et al., 2008]. Mean UBM and MVC values were lower in the late-middle-aged subjects as was the upper body torque ratio (UBTR), which corresponds to the anthropometrically normalized MVC [KURZ et al., 2014]. The age-related reduction of UBTR ($p = 0.8$) is in line with previously reported studies of back muscles [CHAMPAGNE et al., 2009; YASSIERLI et al., 2007]. Table 4.4 summarizes these group specific characteristics.

Table 4.4: Subject characteristics of two age groups of healthy, male volunteers (presented as mean \pm SD or mean and interquartile range - IQR).

	young ($n = 14$)	late-middle-age ($n = 14$)	
age [yr]	22.5 \pm 1.4	55.3 \pm 3.6	
body height [cm]	179.2 \pm 5.8	174.0 \pm 7.3	*
body weight [kg]	74.7 \pm 7.5	76.6 \pm 10.1	
physical activity	3 (IQR = 1)	3 (IQR = 1)	
body mass index (BMI) [kg/m ⁻²]	23.2 \pm 1.8	25.3 \pm 2.8	*
body fat percentage [%]	17.6 \pm 4.6	21.5 \pm 6.8	*
upper body mass (UBM) [kg]	34.1 \pm 2.6	35.7 \pm 4.7	
maximum voluntary contraction (MVC) [Nm]	270.1 \pm 44.0	230.7 \pm 77.0	
upper body torque ratio (UBTR) [a.u.]	2.45 \pm 0.39	2.07 \pm 0.68	†

* Statistical difference between both age groups with ($p < .05$) or † with ($p < .10$).

A detailed description of the applied methodology together with the results obtained in the young subjects has already been presented in section 4.4. In this study, the acquired T_1 -weighted anatomic MR images were further processed by an offline intensity correction method (FSL 4.1, FMRIB Software Library, University of Oxford, UK) before being used for ROI-based analyses including determination of muscle-specific cross-sectional areas (CSA) and fat infiltration. ROIs of the MF and ES muscles were bilaterally outlined manually on two transverse T_1 -weighted images at the height of L3 and L4 by an experienced observer using segmentation software (<http://www.mitk.org/>). Based on these ROIs, mean CSA and mean anthropometrically normalized CSA (nCSA, CSA normalized to the product of UBM and upper body segment length) were determined. Intensity distributions within these muscle-specific ROIs were analyzed by means of descriptive statistical measures including skewness (MATLAB, The Mathworks, Inc., USA), which was presumed to provide a rough estimate of tissue composition and thus muscular fat infiltration [HEBERT et al., 2014].

Remark - Due to increased subcutaneous fat fractions in late-middle-aged subjects and reduced SNR of ^{31}P -MR spectra, prolonged repetition times were applied in the older age group (TR = 1.5s, TA = 44s instead of TR = 0.92s, TA = 27s). In addition, changes were applied to the reconstruction pipelines of dynamic ^{31}P -MR spectra and mfMRI data as compared to the methods described in sec. 4.4. In order to further increase the SNR of dynamic ^{31}P -MR spectra the inner 4×4 (instead of 2×4) voxels of the 8×8 CSI matrix were used for column-wise spatial averaging. Furthermore, since initial observations such as ROI-specific f histogram analysis showed many negative, physiologically non-plausible f values in the late-middle-aged subjects (especially prior to loading), these voxel-values were set to zero. All data acquired in young subjects were again reconstructed using the modified post-processing steps.

Statistical analysis

Similar to the previous work [HIEPE et al., 2014a], several statistical analyses were performed based on the obtained data in the two different age groups using SAS 9.4:

- Age-related and load-induced changes of T_2 , diffusion, vascular and metabolic parameters were examined with respect to particular muscles using linear mixed models. Differences of pre- ($T_{2,\text{rest}}$, D_{rest} , f_{rest} , $\text{PCr}_{\text{rest}}/\text{ATP}_{\text{rest}}$, $\text{Pi}_{\text{rest}}/\text{ATP}_{\text{rest}}$, pH_{rest}) and post-exercise mfMR parameters ($T_{2,\text{load}}$, D_{load} , f_{load} , $\text{PCr}_{\text{load}}/\text{ATP}_{\text{load}}$, $\text{Pi}_{\text{load}}/\text{ATP}_{\text{load}}$, pH_{load}) were evaluated between both age groups, different muscles and states by subsequently exploring individual profile diagrams and applying separate mixed models for each mfMR parameter. Results of the model analyses are presented using p -values of the fixed effects *state*, *age* and *muscle*. To test for different state effects in both groups and thus for differences in muscle activation level between young and late-middle-aged subjects, an interaction was included in the model accounting for the (fixed) effects between *state* and *age*. Furthermore, muscle-independent state- and age-specific effects were postulated, so that interactions between *muscle* and *age* or between *muscle* and *state* were not included in the models. This was because of the limited number of included subjects in our study and since those interactions were outside the scope of our research questions (analysis of muscle activation patterns in young subjects has already been reported in section 4.4). Due to the observed non-constant variances in the profile diagrams a state-specific random effect was included. Presumed correlations between data in the different states and muscles were incorporated.
- Previously reported hypotheses that T_2 alterations are linked to changes in metabolism and diffusion or vascular volume fraction were tested by calculating mfMRI and MRS response factors ($Y_{\text{rf}} = Y_{\text{load}}/Y_{\text{rest}}$; except for f given in %, for which the response factor f_{rf} was defined as the difference between f_{load} and f_{rest} , given in percentage point, p.p.). With the response factor $T_{2,\text{rf}}$ chosen as the dependent variable, the fixed effect of *state* was replaced by including the response factors ($\text{PCr}/\text{ATP}_{\text{rf}}$, $\text{Pi}/\text{ATP}_{\text{rf}}$, pH_{rf} , D_{rf} and f_{rf}) as a covariate in separate mixed models (together with random intercept). Thereby, their effect on $T_{2,\text{rf}}$ was examined, while these models also included the fixed effects *muscle* and *age* as well as the interaction between *age* and the corresponding covariate.
- The effect of the individual degree of perceived exertion (RPE) on the different MR response factors was investigated by means of linear mixed models, which included a random intercept and the fixed effects *age* and *muscle* as well as mean RPE (averaged over both sessions) as a covariate. To account for a potential age-specific effect of RPE on the response factors an interaction between *age* and RPE was included in the model.
- Age-related changes of muscle cross-sectional area (CSA, nCSA) and fat infiltration (represented by the skewness of the histogram distribution of the T_1 -weighted scan) were assessed with repeated measurement ANOVAs.

- Partial correlations between morphological and functional MR parameters adjusted for age group were performed to test whether CSA or nCSA of MF and ES were related to MVC or UBTR. Therefore, these values were bilaterally summed and separately correlated. To unveil further potential relationships between muscle strength (MVC, UBTR), muscle function (pre- and post-exercise mfMR parameters, which were intra-individually averaged across the different muscles), fat infiltration (skewness) and subject characteristics (BMI, body fat fraction), these parameters were also correlated to each other. The results are presented as partial correlation coefficients ρ_p with corresponding p -values.

4.5.2 Results

Muscle functional MRI and MRS

All subjects tolerated the back extension exercise over the entire exercise-period of 10 min while sustaining the reference upper body position. The mean degrees of perceived exertion (RPE) during the MRI (young: 14.3 ± 2.9 ; late-middle-age: 12.4 ± 4.8) and MRS session (young: 11.4 ± 3.9 ; late-middle-age: 12.4 ± 4.0) were similar with no significant differences between both groups. Figure 4.23 displays the ratios of all pre- and post-exercise mfMR parameters together with the response factors between late-middle-aged and young subjects. Mean mfMRI parameters are summarized in Tab. 4.5 for both age groups. T_2 values showed significant load-induced increases in all muscles of both cohorts (significance of mixed model effect *state*: $p < .001$) as well as a trend of lower $T_{2,\text{rest}}$ and $T_{2,\text{load}}$ in the late-middle-aged subjects, independent of *state* (*age*: $p = .107$, see Fig. 4.23a and b). The exercise effect on T_2 was not significantly different between both groups, which indicates similar levels of muscle activation (due to non-significant interaction between *state* and *age*: $p = .501$). Except for the left ES, the response factors $T_{2,\text{rf}}$ were approximately 2-5% lower for the late-middle-aged subjects (Fig. 4.23c). Similar to T_2 , post-load vascular volume fractions (f_{load}) were significantly elevated in both age groups and all muscles compared to f_{rest} values (*state*: $p = .001$, Tab. 4.5), but had significantly reduced values in the late-middle-age group by approximately 50% for the averaged fractions (*age*: $p < .001$, Fig. 4.23). Interestingly, the load-induced vascular volume changes f_{rf} were also similar for both age groups (interaction between *state* and *age*: $p = .199$, Fig. 4.23c). The extracted diffusion coefficients during rest (D_{rest}) and load (D_{load}) were again significantly reduced in the late-middle-age group (*age*: $p = .008$; Fig. 4.23), but the exercise-induced changes were not significant in both cohorts (*state*: $p = .152$, Tab. 4.5) with higher changes (D_{rf}) in the young age group (Fig. 4.23c). Lastly, disregarding the effects of *state* and *age*, significant differences between examined muscles were observed for T_2 and f values (both highest in the MF; *muscle*: $p < .001$) as well as for D (highest in the ES).

As demonstrated previously (sec. 4.4), the normalized mean PCr and Pi signal-time courses showed similar PCr/Pi equilibrium levels during the second half of the exercise in all muscles (Fig. 4.24). Table 4.6 summarizes all spectroscopic values and their age-related ratios are displayed in Fig. 4.23. As expected from muscle physiology, PCr hydrolysis was consistently

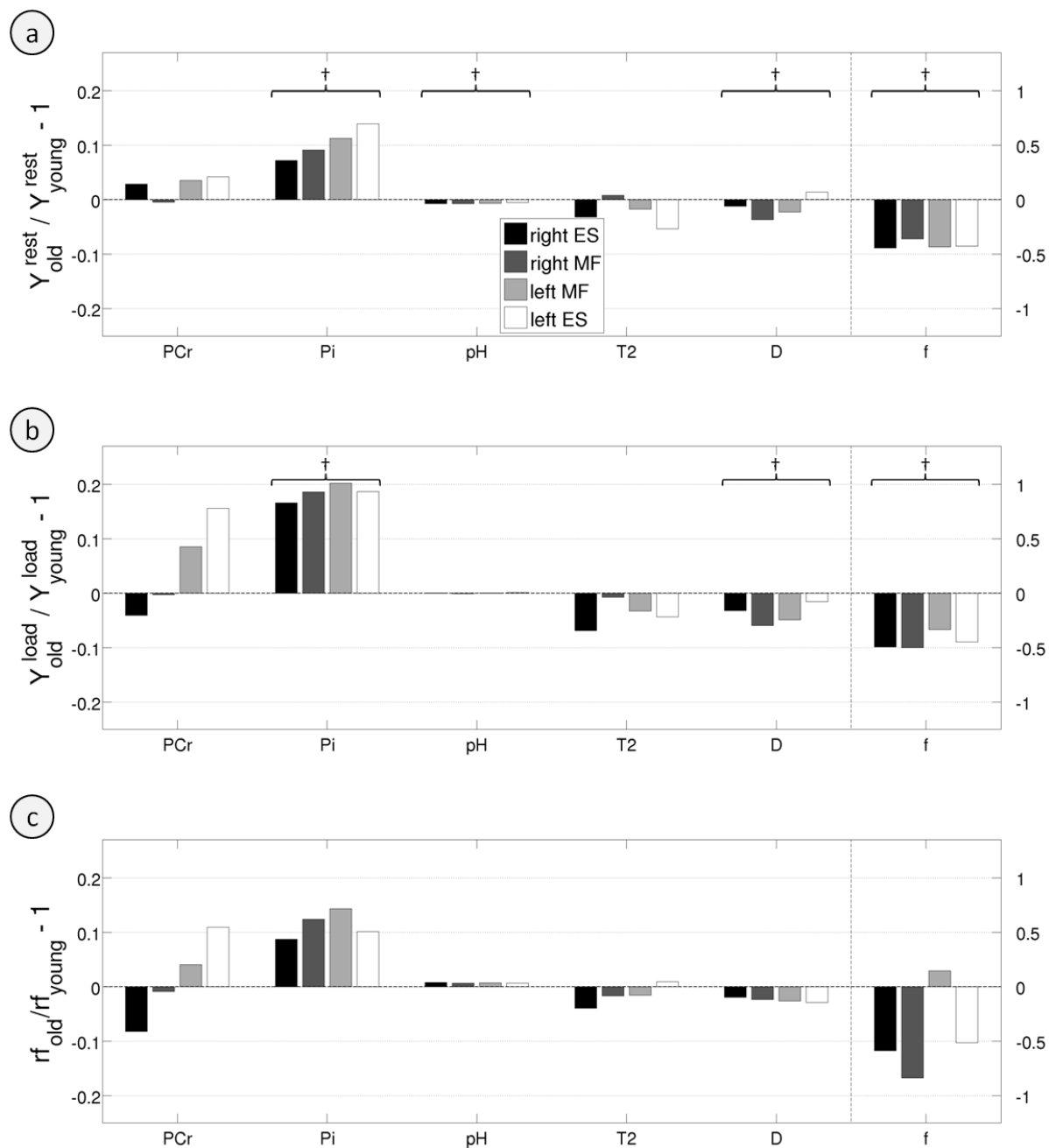


Figure 4.23: Age-related differences of pre- (a) and post-exercise (b) muscle functional MR parameters as well as their response factors (c) for the different lower back muscles (gray-shaded bars). For illustration purposes, vascular volume fractions (f) were re-scaled in each bar plot (see labeling of the right y-axes). Mixed model analyses yielded significant differences between young and late-middle-aged subjects over all muscles for pre- and post-exercise Pi/ATP, D and f values and for pH obtained during rest ($p < .05$, marked with †).

reflected in significantly reduced PCr/ATP levels ($\approx 30\%$) during exercise in all muscles (*state*: $p < .001$). No PCr/ATP differences were observed between the groups (*age*: $p = .476$).

Table 4.5: Extracted pre- and post-exercise mfMRI parameters (mean \pm SD).

		right ES	right MF	left MF	left ES	
$T_{2,\text{rest}}$ [ms]	young	26.5 \pm 1.8	26.7 \pm 1.4	27.2 \pm 1.2	27.4 \pm 1.5	
	old	25.7 \pm 1.1	26.9 \pm 1.0	26.7 \pm 1.3	25.9 \pm 1.1	
$T_{2,\text{load}}$ [ms]	young	29.6 \pm 3.1	29.1 \pm 2.9	29.2 \pm 2.6	28.6 \pm 2.2	*
	old	27.5 \pm 1.5	28.9 \pm 1.9	28.3 \pm 1.5	27.3 \pm 1.7	*
$(T_{2,\text{rf}} - 1) \cdot 100\%$	young	11.72 \pm 11.07	9.27 \pm 10.59	7.53 \pm 9.73	4.36 \pm 7.11	
	old	7.27 \pm 4.95	7.40 \pm 5.85	5.85 \pm 5.78	5.33 \pm 5.27	
f_{rest} [%]	young	5.74 \pm 2.11	7.92 \pm 2.88	8.86 \pm 3.59	6.32 \pm 3.08	†
	old	3.20 \pm 2.44	5.08 \pm 2.39	5.02 \pm 2.38	3.62 \pm 2.44	†
f_{load} [%]	young	8.89 \pm 2.27	11.28 \pm 2.55	10.71 \pm 3.23	8.42 \pm 3.12	* †
	old	4.49 \pm 2.86	5.62 \pm 3.35	7.13 \pm 3.48	4.64 \pm 3.38	* †
f_{rf} [p.p.]	young	3.14 \pm 2.92	3.36 \pm 3.73	1.85 \pm 3.06	2.10 \pm 3.15	
	old	1.30 \pm 2.16	0.54 \pm 2.98	2.12 \pm 4.02	1.01 \pm 2.89	
D_{rest} [10^{-3} mm ² /s]	young	1.69 \pm 0.06	1.70 \pm 0.05	1.69 \pm 0.05	1.69 \pm 0.09	†
	old	1.67 \pm 0.06	1.64 \pm 0.07	1.65 \pm 0.05	1.72 \pm 0.07	†
D_{load} [10^{-3} mm ² /s]	young	1.74 \pm 0.08	1.75 \pm 0.05	1.72 \pm 0.07	1.72 \pm 0.09	†
	old	1.68 \pm 0.07	1.64 \pm 0.05	1.64 \pm 0.06	1.70 \pm 0.09	†
$(D_{\text{rf}} - 1) \cdot 100\%$	young	3.13 \pm 3.44	3.26 \pm 4.50	2.03 \pm 4.68	1.81 \pm 4.81	
	old	1.69 \pm 0.06	1.70 \pm 0.05	1.69 \pm 0.05	1.69 \pm 0.09	

* Significant differences between pre- and post-exercise values in both age groups and over all muscles ($p < .05$); † Significant differences between young and late-middle-aged subjects in each state and over all muscles ($p < .05$).

Hence, the effect of exercise on PCr/ATP was not significantly different between young and late-middle-aged subjects, albeit showing an inhomogeneous response factor pattern across the different muscles (Fig. 4.23c). Rest and load Pi/ATP ratios were both significantly higher in the late-middle-age group (*age*: $p = .022$, Fig. 4.23). Due to the simultaneous accumulation of Pi with PCr hydrolysis, mean exercise-induced Pi/ATP increases between approximately 85-135% and 104-165% were observed in the young and late-middle-aged subjects, respectively (*state*: $p < .001$, Tab. 4.6). Thereby, a trend toward stronger Pi/ATP increases in the late-middle-aged subjects was observed for all muscles (interaction between *state* and *age*: $p = .101$; Fig. 4.23c). Phosphorus spectra were further analyzed to determine pH during rest and load, which showed significant decreases during exercise only in the muscles of young subjects (significant interaction between *state* and *age*: $p = .003$). The late-middle-aged subjects had significantly lower pH during rest, which remained nearly constant during load (Fig. 4.23a; Tab. 4.6). Hence, exercise-induced pH changes of late-middle-aged subjects were significantly lower compared to the young age group.

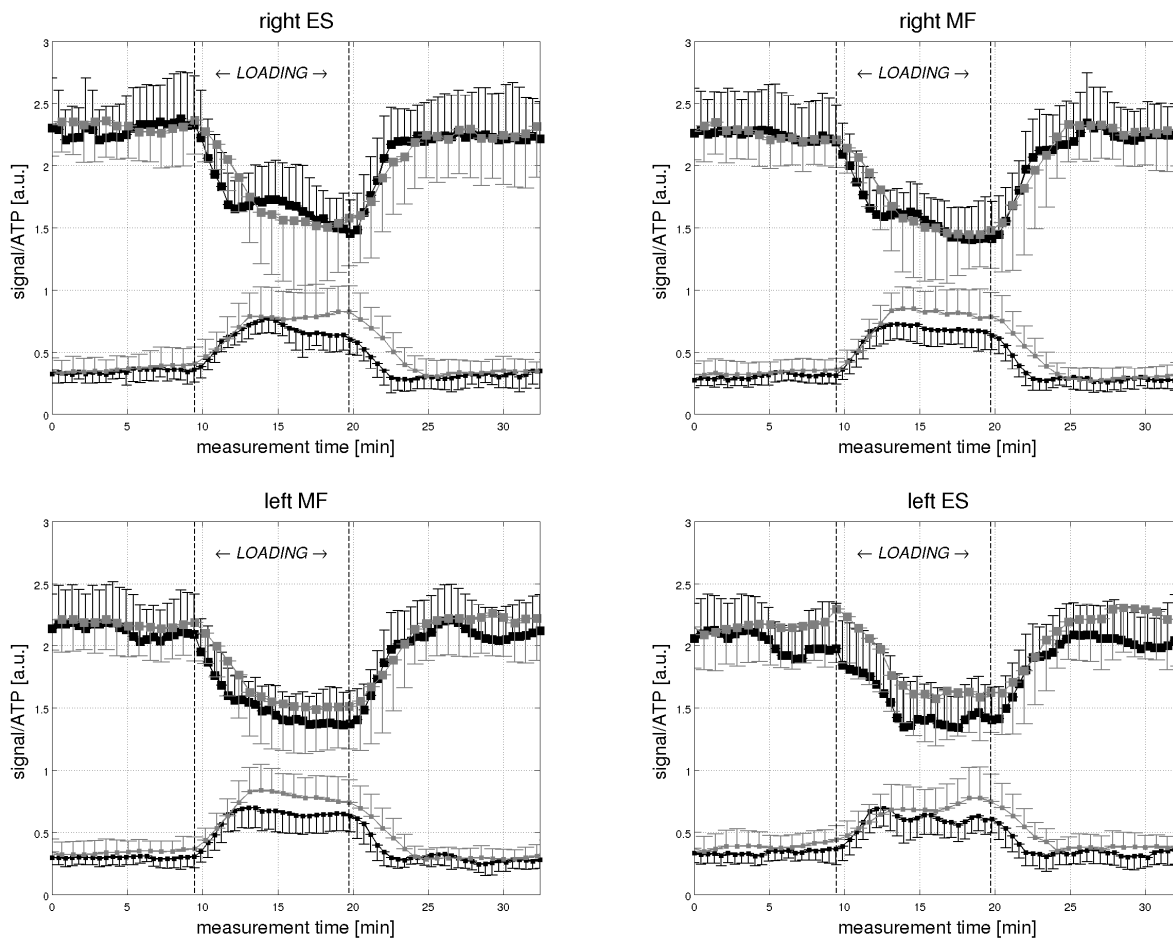


Figure 4.24: Comparison of normalized mean PCr (upper curve) and Pi (lower curve) time courses obtained in different low back muscles of young (black symbols) and late-middle-aged subjects (gray symbols). The unilateral error bars indicate the SD of each group. In general, all muscles show similar transient metabolic changes in both age groups. However, late-middle-aged subjects showed higher Pi/ATP increases in all muscles.

Interrelations between MR response factors and RPE

Statistical results (p -values) of the mixed model analyses that were obtained by modeling the mfMR response factors are summarized in Tab. 4.7. First, it was tested whether the response factor $T_{2,rf}$ was affected by the response factors of diffusion, vascular volume fraction and metabolism. In this connection, the response factors D_{rf} ($p = .019$), f_{rf} ($p < .001$) and PCr/ATP_{rf} ($p = .011$) serving as covariates each revealed a significant and age-dependent effect on $T_{2,rf}$ (interaction between *covariate* and *age*: $p < .05$; except for D_{rf}), whereas pH_{rf} and Pi/ATP_{rf} did not. All investigated mixed models for $T_{2,rf}$ listed in Tab. 4.7 yielded a significant effect of *muscle*, with $T_{2,rf}$ of the right ES being significantly higher compared to the left ES. Concerning *age*, only the mixed model with covariate PCr/ATP_{rf} revealed a significant effect on $T_{2,rf}$. Overall, these findings support the hypothesis that T_2 alterations are causally determined by changes in muscle metabolism, diffusion and vascular volume fraction,

Table 4.6: Determined ^{31}P -MRS quantities during rest and load (mean \pm SD).

		right ES	right MF	left MF	left ES	
$\text{PCr}_{\text{rest}}/\text{ATP}_{\text{rest}}$ [a.u.]	young	2.26 \pm 0.28	2.27 \pm 0.29	2.12 \pm 0.25	2.05 \pm 0.24	
	old	2.33 \pm 0.26	2.26 \pm 0.22	2.19 \pm 0.23	2.13 \pm 0.26	
$\text{PCr}_{\text{load}}/\text{ATP}_{\text{load}}$ [a.u.]	young	1.62 \pm 0.25	1.48 \pm 0.23	1.40 \pm 0.22	1.40 \pm 0.25	*
	old	1.55 \pm 0.45	1.48 \pm 0.35	1.52 \pm 0.35	1.61 \pm 0.34	*
$(\text{PCr}/\text{ATP}_{\text{rf}} - 1) \cdot 100\%$	young	-27.9 \pm 12.6	-34.1 \pm 11.1	-33.7 \pm 10.1	-31.5 \pm 11.0	
	old	-33.9 \pm 15.9	-34.7 \pm 12.8	-31.0 \pm 12.7	-24.0 \pm 14.3	
$\text{Pi}_{\text{rest}}/\text{ATP}_{\text{rest}}$ [a.u.]	young	0.34 \pm 0.06	0.30 \pm 0.06	0.30 \pm 0.05	0.33 \pm 0.06	†
	old	0.36 \pm 0.12	0.33 \pm 0.10	0.33 \pm 0.09	0.38 \pm 0.11	†
$\text{Pi}_{\text{load}}/\text{ATP}_{\text{load}}$ [a.u.]	young	0.68 \pm 0.09	0.68 \pm 0.12	0.65 \pm 0.13	0.61 \pm 0.11	*†
	old	0.81 \pm 0.17	0.81 \pm 0.17	0.78 \pm 0.16	0.72 \pm 0.17	*†
$(\text{Pi}/\text{ATP}_{\text{rf}} - 1) \cdot 100\%$	young	111.2 \pm 60.5	135.7 \pm 54.7	122.5 \pm 42.7	85.2 \pm 40.5	
	old	129.7 \pm 60.1	164.8 \pm 77.0	154.3 \pm 90.8	103.9 \pm 85.7	
pH_{rest}	young	6.99 \pm 0.05	6.98 \pm 0.04	6.99 \pm 0.03	6.99 \pm 0.03	‡
	old	6.94 \pm 0.03	6.93 \pm 0.03	6.94 \pm 0.03	6.95 \pm 0.04	‡
pH_{load}	young	6.94 \pm 0.05	6.94 \pm 0.04	6.94 \pm 0.04	6.93 \pm 0.04	
	old	6.94 \pm 0.07	6.93 \pm 0.04	6.94 \pm 0.05	6.94 \pm 0.05	
$(\text{pH}_{\text{rf}} - 1) \cdot 100\%$	young	-0.72 \pm 0.76	-0.62 \pm 0.68	-0.69 \pm 0.70	-0.81 \pm 0.66	
	old	0.02 \pm 1.11	-0.01 \pm 0.49	0.03 \pm 0.48	-0.16 \pm 0.76	

* Significant differences between pre- and post-exercise values in both age groups and over all muscles ($p < .05$); † Significant differences between young and late-middle-aged subjects in each state and over all muscles ($p < .05$); ‡ Significant differences between young and late-middle-aged subjects only in the corresponding state and independent of muscle ($p < .05$).

whereas muscle activation induced by sustained load seems not markedly associated with age. Secondly, effects of the individually perceived exertion (RPE) on the different mfMR response factors were evaluated separately (Tab. 4.7). Significant effects of RPE on $T_{2,\text{rf}}$ ($p = .003$) and f_{rf} ($p = .044$) were found, while only a (strong) trend was observed with regards to D_{rf} ($p = .066$). Except for $T_{2,\text{rf}}$ (interaction between *covariate* and *age*: $p = .048$), these effects were independent of age. Slight trends of RPE in affecting $\text{PCr}/\text{ATP}_{\text{rf}}$ ($p = .149$) or $\text{Pi}/\text{ATP}_{\text{rf}}$ ($p = .187$) were also seen and RPE was associated with pH_{rf} dependent of age group (due to absence of pH changes in late-middle-aged subjects, this association can be assigned to pH_{rf} of young subjects). Significant effects of *muscle* in models of the different response factors adjusted for the covariate RPE were observed for $T_{2,\text{rf}}$ (inter-muscular differences between right muscles and left ES), D_{rf} (not locatable), $\text{PCr}/\text{ATP}_{\text{rf}}$ (right MF vs. left ES) and $\text{Pi}/\text{ATP}_{\text{rf}}$ (right ES vs. right MF and left ES vs. bilateral MF). Contrary, no significant effect of *age* was observed in the different models, which support the notion that the level of muscle activation measured by T_2 - and IVIM-based mfMRI is maintained during healthy aging and is associated with the perceived level of exertion.

Table 4.7: Determined p -values of corresponding mixed model effects (covariates) on different mfMRI/MRS response factors (dependent variables).

dependent variable	covariate	effect of muscle	effect of age group	effect of covariate	interaction between covariate and age
$T_{2,rf}$	PCr/ATP _{rf}	<.001	0.030	0.011	0.002
$T_{2,rf}$	Pi/ATP _{rf}	0.003	0.966	0.507	0.417
$T_{2,rf}$	pH _{rf}	0.001	0.932	0.219	0.307
$T_{2,rf}$	f _{rf}	0.009	0.489	<.001	0.025
$T_{2,rf}$	D _{rf}	0.011	0.868	0.019	0.288
$T_{2,rf}$	RPE	<.001	0.073	0.003	0.048
PCr/ATP _{rf}	RPE	0.034	0.652	0.149	0.619
Pi/ATP _{rf}	RPE	<.001	0.936	0.187	0.694
pH _{rf}	RPE	0.626	0.124	0.854	0.018
f _{rf}	RPE	0.620	0.151	0.044	0.076
D _{rf}	RPE	0.043	0.701	0.066	0.451

Bold: Statistical significance of the fixed effect in the mixed model ($p < .05$).

Structural parameters and their effect on muscle function

Structural features of the lower back muscles were examined by analyzing the high-resolution T_1 -weighted MR images. The ROI based results are summarized in Tab. 4.8. Cross-sectional muscle areas (CSA) and anthropometric normalized CSA (nCSA) of the MF and the right ES were lower in late-middle-aged subjects although statistically not significant. The skewness of the intensity histograms, which was selected as a marker of age-related fat infiltration, was significantly higher in the late-middle-aged compared to the young subjects ($p < .05$). Higher positive skewness values indicated more right-shifted asymmetric voxel intensity distributions due to fat accumulation in muscle tissue (compare Fig. 4.25).

Table 4.8: Structural parameters obtained via anatomic MRI analysis (mean \pm SD).

		right ES	right MF	left MF	left ES	
CSA [cm ²]	young	16.56 \pm 3.30	7.39 \pm 1.77	7.85 \pm 2.31	15.91 \pm 2.57	
	old	16.14 \pm 2.25	6.39 \pm 1.28	6.48 \pm 1.40	15.94 \pm 2.25	
nCSA [cm ² /kg m]	young	1.34 \pm 0.30	0.60 \pm 0.18	0.64 \pm 0.22	1.29 \pm 0.24	
	old	1.31 \pm 0.28	0.51 \pm 0.10	0.52 \pm 0.10	1.29 \pm 0.27	
skewness [a.u.]	young	0.27 \pm 0.50	0.50 \pm 0.68	0.56 \pm 0.87	0.13 \pm 0.50	†
	old	0.93 \pm 0.43	0.94 \pm 0.60	0.76 \pm 0.63	0.85 \pm 0.45	†

† Significant differences between both cohorts independent of muscle ($p < .05$).

Partial correlations between MVC, UBTR, CSA, nCSA, skewness and mfMR parameters (pre- and post-exercise MR values and response factors, which were intra-individually averaged across the muscles) were computed while considering the effects of age. A positive partial

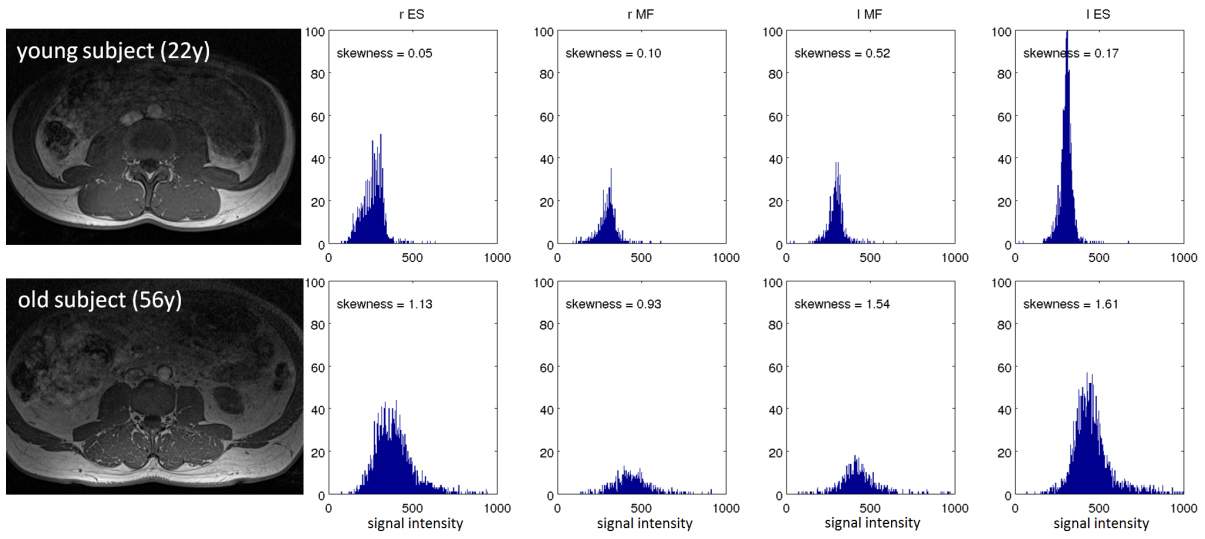


Figure 4.25: Comparison of anatomic T_1 -weighted MR images and corresponding ROI-specific signal intensity distributions in a young (top row) and in a late-middle-aged subject (bottom row) yielding more asymmetric (right-tailed) histograms in the older volunteer, thus indicating higher intra-muscular fat infiltration with age.

correlation coefficient was obtained between the bilaterally summed nCSA of MF and UBTR ($\rho_p = 0.42$, $p = .03$; illustrated in Fig. 4.26a), whereas the nCSA values of ES exhibited only a trend with higher UBTR values ($\rho_p = 0.27$, $p = .17$; Fig. 4.26b). On the other hand, partial correlations between CSA and MVC revealed no positive relationships (not shown), indicating the importance of considering anthropometric measures when analyzing mass and strength of back extensor muscles. UBTR showed significant partial correlations with mean $T_{2,\text{rest}}$ ($\rho_p = 0.41$, $p = .03$; Fig. 4.26c) and body fat fraction ($\rho_p = -0.44$, $p = .02$; Fig. 4.26e), but only insignificant associations with mean $\text{Pi}/\text{ATP}_{\text{rest}}$ ($\rho_p = -0.26$, $p = .19$; Fig. 4.26d) and mean skewness ($\rho_p = -0.27$, $p = .18$; Fig. 4.26f). Skewness was positively correlated with body fat fraction ($\rho_p = 0.39$, $p = .04$; Fig. 4.26g) and BMI ($\rho_p = 0.35$, $p = .07$), and yielded a significant inverse relationship with f_{load} ($\rho_p = -0.45$, $p = .02$; Fig. 4.26i) but not with f_{rest} ($\rho_p = -0.19$, $p = .33$; Fig. 4.26h). Lastly, f_{load} correlated well with BMI ($\rho_p = -0.46$, $p = .02$) and body fat fraction ($\rho_p = -0.45$, $p = .02$). Other partial correlations revealed that neither parameters of muscle strength (MVC, UBTR) or muscle mass (CSA, nCSA) nor fat infiltration (skewness) had any significant effect on muscle activation or basal MR parameters (except for $T_{2,\text{rest}}$).

4.5.3 Discussion

The aim of this study was to examine age-related differences in spin-spin relaxation, metabolic, perfusion and diffusion parameters and their load-induced changes in isometrically exercised lower back muscles. Additionally, muscle cross-sectional areas and fat infiltration into muscle tissue were determined by analyzing T_1 -weighted MRI data. In light of the similar mfMR

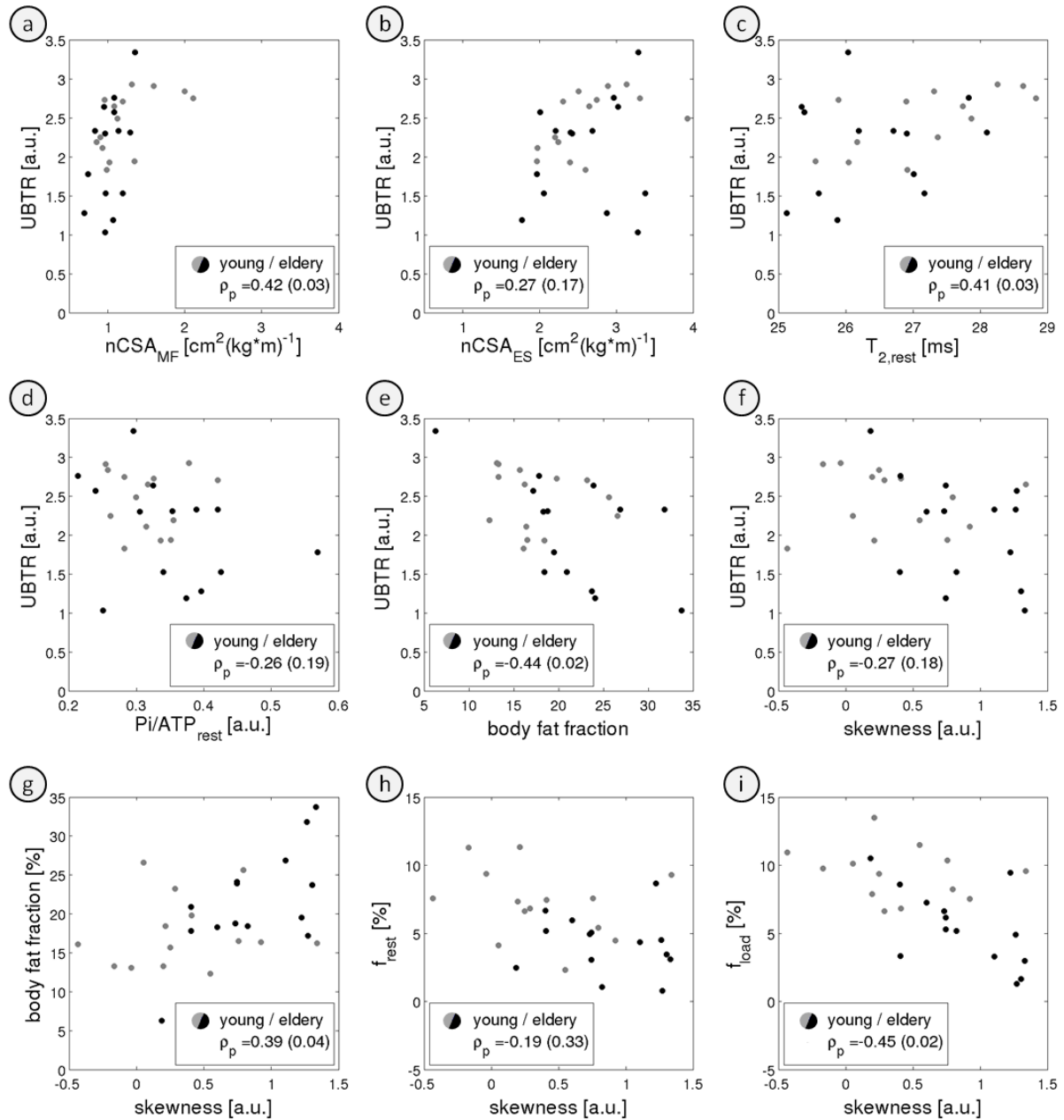


Figure 4.26: Associations between muscle strength UBTR and different parameters (a-f) as well as between body fat fraction and skewness (g), and vascular volume fraction and skewness (h-i) determined by partial correlations of data obtained in young (gray) and late-middle-aged (black) subjects. UBTR was separately compared with bilaterally summed nCSA of the MF (a) and ES (b), with mean $T_{2,rest}$ (c), mean Pi/ATP_{rest} (d), body fat fraction (e) and mean skewness values (f). The legends list determined partial correlation coefficients and the corresponding p -values (in brackets).

response factors (except for pH) and comparable RPE values in both age groups, muscle activation following moderate loads appears to be age independent. This is in line with previous studies, which reported similar endurance times and RPE in young and late-middle-aged sub-

jects during Sørensen trunk holding tests [CHAMPAGNE et al., 2009; YASSIERLI et al., 2007]. However, the mfMR response factors and RPE in our study showed high inter-subject variability that was analyzed by means of mixed models to explore age-specific associations between particular parameters. Thereby, significant effects of RPE on the response factors $T_{2,rf}$, f_{rf} and nearly on D_{rf} and pH_{rf} (only in the young cohort) were documented indicating a link between mfMRI parameter changes and the perceived exertion level (Tab. 4.7). Furthermore, the models including RPE as covariate yielded no age-specific differences of different response factors, which again support the notion that moderate muscle activation during sustained back extension does not change with age.

The metabolic parameters were not associated with RPE, but PCr/ATP_{rf} showed significant interrelation with $T_{2,rf}$ (Tab. 4.7), which supports the previously reported hypothesis that metabolic changes underlie exercise-induced T_2 alterations [BENDAHAN et al., 2004; DAMON et al., 2002a; SAAB et al., 2000]. With reference to recent reports of increased extra-cellular fluid volume [ABABNEH et al., 2008; MORVAN and LEROY-WILLIG, 1995] and elevated micro-vascular perfusion associated with load-induced T_2 changes [HIEPE et al., 2014a; SCHEWZOW et al., 2015], the response factors D_{rf} and f_{rf} were separately included in the mixed models of $T_{2,rf}$. Here, both age groups showed a significant effect of both response factors on $T_{2,rf}$, which is in agreement with the above mentioned studies. The impact of D_{rf} on $T_{2,rf}$ was, however, smaller than compared to f_{rf} . The latter finding is in line with the previously reported study [HIEPE et al., 2014a]. Regarding the fact, that diffusion changes reflect the swelling of the muscle cells during exercise due to intra-cellular water accumulation (myofibrillar response), the observed association between D_{rf} and $T_{2,rf}$ can be ascribed to the relation between fiber size (fiber CSA) and muscle T_2 . Overall, combined application of T_2 and diffusion-weighted mfMRI as well as of ^{31}P -CSI was able to identify the tight couplings between metabolic, structural and vascular activity with muscle T_2 in both age groups.

Heterogeneous activation patterns across the exercised low back muscles were observed in both groups with higher T_2 changes in the right body side (significant difference between the $T_{2,rf}$ of the right and the left ES). Compared to young subjects, this asymmetric activation pattern was not observed for D and f and was less pronounced for T_2 in the late-middle-age group. However, it can be argued that these patterns are related to the right-handedness of the examined subjects and that larger comparative studies including left-handed subjects are required to verify this hypothesis in the future.

Reduced UBTR with age together with unchanged fatigability during sustained loads [CHAMPAGNE et al., 2009; YASSIERLI et al., 2007] and similar recovery times [KURZ et al., 2014] is in good agreement with findings of previous back muscle studies. In order to identify morphological factors potentially underlying this age-related muscle strength decline and individual fatigability during moderate loads, muscle cross-sectional area (CSA) and anthropometrically-normalized CSA (nCSA, Tab. 4.8) were analyzed in this study. As a result, there was only a non-significant trend of lower CSA and nCSA in late-middle-aged subjects with higher age-related changes of CSA and nCSA in the MF compared to the ES. Hence, lower UBTR with

age cannot be solely caused by a loss of muscle mass, but obviously includes other factors as reported previously [GOODPASTER et al., 2006]. However, the individually normalized muscle volume was positively correlated with muscle strength in both age groups (nCSA vs. UBTR), which is in line with literature [GOODPASTER et al., 2006]. As these correlations were only significant in MF but not in ES, it may be concluded that MF is the main contributor during back extension at maximum voluntary intensity. This notion is supported by a previous mfMRI study, which reported larger T_2 increases in MF than in ES at different exercise intensities [MAYER et al., 2005]. Contrary to the observed association between muscle nCSA and UBTR, these parameters were not significantly associated with different mfMR response factors indicating that muscle activation at moderate work loads is independent of morphology and strength of back muscles.

The age-related decline of maximum force capacity has partly been ascribed to a loss of (contractile) muscle mass due to decreased numbers of muscle fibers and motor units as well as to the atrophy of type II fibers [GOODPASTER et al., 2006; KORHONEN et al., 2006; NILWIK et al., 2013]. **Molecular diffusion coefficients** are sensitive to muscle fiber structure and were found to be reduced with age (Tab. 4.5), which is in good agreement with a previous lumbar muscle study [YANAGISAWA et al., 2009]. Since lower D values in muscle are mainly due to by reduced radial diffusibility [DEUX et al., 2008; SCHWENZER et al., 2009; SIGMUND et al., 2014], this finding can be ascribed to a reduction of the mean fiber diameter as it occurs during atrophic processes with age. However, D was not associated with CSA, nCSA or UBTR indicating that age-related fiber-atrophic processes are not the only cause for the decline of muscle mass or muscle strength. Muscle activation as reflected in the mfMR response factors was also not affected by the reduced diffusion coefficients. The exercise-induced D increases, which were insignificant in the present study and are caused by higher radial diffusibility due to osmotic-driven intra-cellular water accumulation with accompanying cell swelling, showed no statistical differences with age. The trend for smaller D changes in the late-middle-aged subjects can be ascribed to less cell swelling due to atrophic processes.

The reduction of the apparent vascular volume fraction f with age in all muscles before and after load represents one of the main findings of the present study (Tab. 4.5). This may be ascribed again to age-related atrophic processes leading to reduced capillary density (schematically illustrated in Fig. 4.27), which is in good agreement with a previous DWI study of lumbar muscles [YANAGISAWA et al., 2009] and other studies based on biopsy [RYAN et al., 2006] or ASL [WRAY et al., 2009]. In addition, f mapping allowed us to identify muscle-specific vascular volume fractions, which were significantly higher in MF compared to ES in both cohorts (discussed in section 4.4.3). After exercise, both age groups showed significant f increases in all muscles confirming results of previous studies that applied ultrasound [KRUX et al., 2010], ASL [WRAY et al., 2009] or T_2^* -weighted imaging [DAMON et al., 2007; SLADE et al., 2011]. Late-middle-aged subjects, however, revealed smaller f changes indicating an age-related reduction in the ability to adapt O_2 delivery to muscle tissue, which is again in line with previous studies [SLADE et al., 2011; WRAY et al., 2009].

This adaptation typically comprises rapid blood flow increase (hyperemic response) at the beginning of the load and its stabilization during exercise, which is closely coupled to the metabolic demand and thus to the generated muscle work [KRIX et al., 2010]. As blood flow is regulated by the interplay between neural vasoconstrictor activity and locally released vasoactive substances inducing vasodilatation, adaptation of mean blood flow velocity (cardiac response) or mean vessel cross-sectional area (vascular response) is obviously affected by age. In line, peripheral vascular health, characterized by pulsatile arterial function and artery compliance of the vessel walls, is well documented to decline with advancing age in humans [MCVEIGH et al., 1999] and it was shown that the arteriolar vasodilatory capacity and rate are reduced with age in rats [BRADLEY et al., 2010; JACKSON et al., 2010]. However, neither the reduced blood volume fractions (f_{rest} and f_{load}) nor the lower vascular responses (f_{rf}) affected muscle strength or muscle activation significantly, which again supports the hypothesis that muscle function at moderate loads is not markedly impaired during healthy aging.

Muscular fat infiltration is considered to be one major determinant of impaired muscle function. Therefore, histogram skewness of the intensity distributions was analyzed based on T_1 -weighted MR images (Fig. 4.25, Tab. 4.8). Previously, anatomic MR images were frequently used to evaluate the intra-muscular fat content [HEBERT et al., 2014; KJAER et al., 2007; YOUNG et al., 2015]. However, the proposed approach provides only a rough estimate of intra-muscular fat infiltration and does not enable direct determination of the fat fraction, like the gold-standard method employing chemical shift-based water-fat MRI [TRIPLETT et al., 2014]. Nevertheless, significantly higher skewness values were observed in the late-middle-aged subjects confirming similar results observed in previous low back muscle studies [HEBERT et al., 2014; KJAER et al., 2007]. Interestingly, determined skewness values were negatively associated with post-load vascular volume f (Fig. 4.26i), suggesting that fat inclusion significantly affects vascular capacity and thus impairs muscle function with long-lasting, highly intense loads. This observation is a major finding of the present study, which has not been reported before and indicates that elevated fat infiltration lowers the hyperemic response by affecting micro-vascular structure and circulation of vasoactive substances. Furthermore, skewness and post-load f values were significantly related to the body fat fraction and BMI, whilst the relationship between BMI and proton mobility in lumbar muscles has been reported previously [JONES et al., 2013], and negative associations were found between body fat fraction and UBTR (significant) as well as between skewness and UBTR (non-significant). Hence, age-related fat infiltration represents an important marker for muscle function as it reduces vascular capacity and potentially affects muscle strength and fatigability at high work levels. It is assumed that atrophic processes lead to the replacement of contractile muscle and vascular tissue by fatty connective tissue (as indicated by lower D and f values, respectively) and result in declined force capacities with age.

Fiber type composition analysis based on histological studies indicated that age-related changes in fiber typing may affect muscle strength negatively [KORHONEN et al., 2006; NILWIK et al., 2013]. As described above, the changes of the fiber composition may arise due to atro-

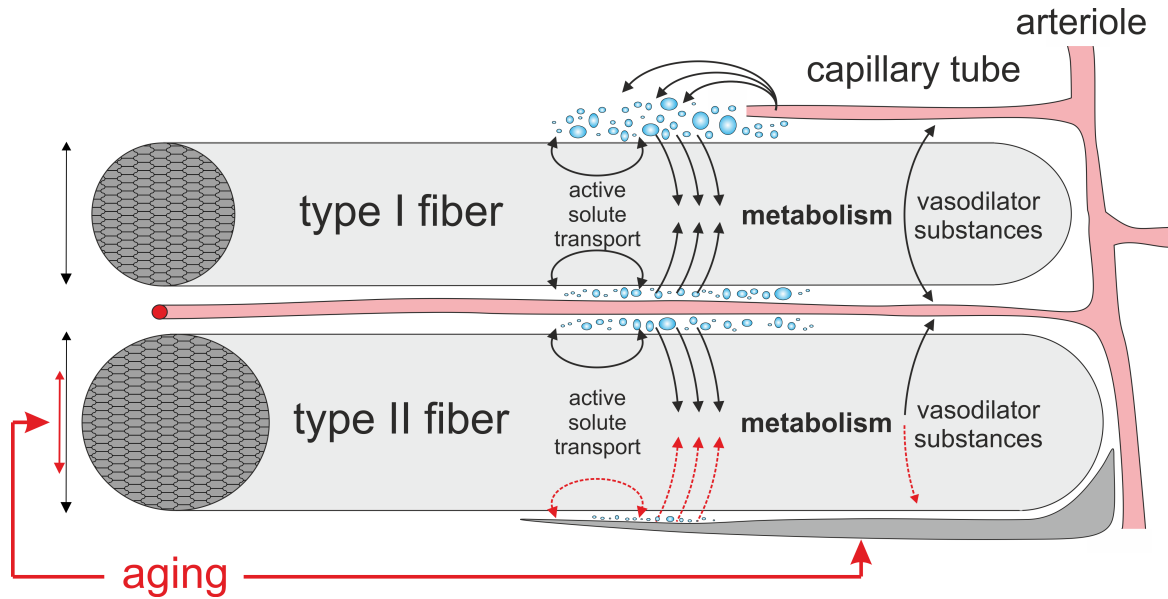


Figure 4.27: Age-related changes of skeletal muscle physiology based on a three-compartment model as viewed from the proposed multi-parametric mfMRI approach. The assumed model includes a vascular, an extra- and an intra-cellular component as well as exchange between these compartments. As indicated by the presented results, aging results in reduced cell diameters of type II fibers and leads to fat infiltration, which hampers tissue perfusion and water-molecule exchange.

phy and/or conversion of type II fibers. In our study, significantly higher P_i/ATP ratios were observed in the late-middle-age group indicating reduced type II fiber fraction as reported previously [MADHU et al., 1996]. The presumption of age-related reduced type II fiber fractions is further supported by significantly weaker pH shifts during exercise in the late-middle-age group [HOUTMAN et al., 2001]. Furthermore, since resting state T_2 [KUNO et al., 1988] and diffusibility D [SCHEEL et al., 2013] are positively related to type II fiber content, the reductions of these parameters seem again to confirm age-related type II fiber atrophy. Although only a slight trend of lower UBTR with higher P_i/ATP_{rest} was observed here, it was, however, demonstrated that $T_{2,rest}$ and UBTR were significantly associated (Fig. 4.26). Regarding the mentioned relationship between resting state T_2 and type II fiber content, this finding reflects the age-related decline of muscle strength due to atrophy or conversion of type II fibers. However, considering the fact that T_2 comprises multiple contributors, such as intra-cellular water content, fiber size, vascularity, fat infiltration and fiber type composition, the present findings may be interpreted as follows: T_2 of low back muscles predicts maximum force capacity when taking fiber structure (as indicated by D), composition (P_i/ATP), vascularity (f) and fat infiltration into account. Observations of lower muscle T_2 in subjects with a history of recurrent LBP can consequently not be ascribed solely to higher glycolytic fiber fractions as has been done before [D’HOOGE et al., 2013], but have to be regarded in light of potential vascular and structural impairments.

However, all results still have to be interpreted with caution due to the small sample size ($n = 14$ in each group). To partly compensate for this, only male right-handed healthy volunteers were included, allowing to avoid possible gender- and handedness-specific effects. Future work is certainly needed on whether and how the results can be transferred to other age groups, females, or left-handed subjects. Further limitations are due to the restricted comparability between the mfMRI and MRS parameters as they were obtained in two separate sessions and different TRs were applied for the age groups (0.92 s and 1.5 s). The latter leads to different T_1 -saturation-related signal attenuations for PCr and Pi, which, however, were corrected based on resting state T_1 -values from the literature. During steady-state aerobic exercise, as performed in this study, T_1 -relaxation times of phosphorus metabolites are not changed statistically from rest [CETTOLO et al., 2006], and effects of different PCr and Pi signal attenuations in both age groups can thus be neglected. Further issues, which are directly related to the applied MR acquisition techniques, have already been discussed in sec. 4.4.3.

4.6 Limitations and open questions

Technical improvements of the proposed mfMR approach will certainly be beneficial for future work. For instance, spatial resolution of T_2 -based mfMRI can be improved by using dual-echo steady-state sequences, which further allow simultaneous quantitation of T_2 and D in less than a minute [STAROSWIECKI et al., 2012]. The micro-circulation in the muscular vasculature, whose importance in controlling blood flow was highlighted in the present work and which showed compromised arteriolar function with aging, can be alternatively investigated by means of T_2^* -weighted MRI [DAMON et al., 2007; SCHMID et al., 2014] or ASL [SCHEWZOW et al., 2015; WRAY et al., 2009]. These techniques potentially provide higher sensitivity against small vascular effects compared to IVIM. In addition, quantitative T_2^* mapping can be performed based on data acquired with PROPELLER MRI, which is less prone to motion [KRÄMER et al., 2012] and thus could provide information about muscle activation parameters, such as blood oxygenation level and blood volume, during exercise [HIEPE et al., 2014c]. Improved differentiation of exercise-induced changes of the fiber structure, as observed in the present study, should be possible by applying single-shot STEAM DTI [HIEPE et al., 2014b] with (differently) prolonged diffusion times in conjunction with the recently introduced random permeable barrier model [SIGMUND et al., 2014]. Alternatively, time and direction-dependent diffusion parameters measured by means of diffusion kurtosis imaging are promising markers for characterizing muscle tissue structure [MARSCHAR et al., 2015]. Future research should further benefit from high spatial resolution mfMRI by precisely analyzing activation patterns, such as by means of cluster analysis, which potentially enables functional distinctions between regions of muscle that were not seen with traditional analysis [DAMON et al., 2003].

Direct combination of mfMRI and dynamic ^{31}P -MRS measurements during exercise should improve the investigations on the relationships between load-induced changes in T_2 , diffusion, perfusion and energy metabolism, which were limited in the current studies due to separate

acquisition of imaging and spectroscopic data. To this end, however, a novel design of an MR-compatible ergometer is required, which allows isometric loading of the back muscles in supine position and avoids movements of the subject during load. Such developments are currently being undertaken in our lab [HIEPE et al., 2014c] and may over and above enable reliable analysis of PCr recovery kinetics, which offers an alternate possibility to gain information about the distribution of fiber types in muscles [FORBES et al., 2009; WRAY et al., 2009]. Furthermore, quantitative fat-water MRI techniques [TRIPLETT et al., 2014] should be applied in order to obtain better understanding of fat infiltration processes and their consequences as recent investigations demonstrated a general increase of intra-muscular fat infiltration in lean muscle tissue during muscle degeneration after recovery from LBP [D'HOOGHE et al., 2012] or during current low back and leg pain [HEBERT et al., 2014].

Finally, in order to analyze muscle activation with respect to neuronal activity, which becomes increasingly important in clinical decision making to guide, e.g., exercise therapy interventions for LBP patients, mfMRI could be combined with electromyography measurements [CLARK et al., 2009; D'HOOGHE et al., 2013; DICKX et al., 2010b]. These research efforts are warranted to further characterize lumbar muscle degeneration and to establish relationships between changes in structural, vascular or neuronal properties and the risk of LBP. In particular, mfMRI has tremendous potential for the evaluation of muscle recruitment patterns in LBP patients providing insight into LBP pathology and may thus help to improve exercise programs in current rehabilitation strategies. From this clinical perspective, the presented low-load exercise protocol is highly relevant to identify lumbar muscle dysfunction during the remission of LBP and may be valuable to optimize rehabilitation strategies, which focus on stabilizing muscles [D'HOOGHE et al., 2013]. Moreover, the proposed multi-parametric mfMRI can be applied to other muscles as well (where imaging does not suffer from motion-induced artifacts) and may indeed prove themselves as being indispensable by providing valuable information about degeneration-related changes and functional impairments in skeletal muscles.

5 Conclusion and Outlook

In the first part of this thesis the feasibility of extracting the 3D architecture of skeletal muscles *in vivo* with high spatial resolution on a clinical MRI scanner was demonstrated by introducing turbo-STEAM DTI and using an animal model [HIEPE et al., 2014b]. Although the resolution of MRI generally precludes direct observations at the microscopic scale, high-resolution turbo STEAM DTI with subsequent fiber tractography allowed for indirect inferences about the micro-architecture of rabbit shank muscles and provided a multitude of functionally significant structural information. The subsequent *post mortem* validation study confirmed the architectural parameters, like pennation angle and fascicle length, derived from the DTI data [SCHENK et al., 2013]. Turbo-STEAM DTI therefore represents a promising approach for high-resolution DTI of skeletal muscle tissue enabling the delineation of small muscle cross-sections and divergent fiber patterns in multi-pennate muscles.

In a human pilot study turbo-STEAM DTI was applied to a cohort of volunteers and patients in order to identify structural changes due to muscle injuries induced by surgical posterior spinal fusion. Thereby, it was demonstrated that the proposed method is sensitive to degenerative changes of the back muscles and it was concluded that with further improvements of the DTI sequence and the post-processing routines turbo-STEAM DTI will play a prominent role in performing clinical studies of degenerative muscle tissue changes. Another important aspect of the future applications based on turbo-STEAM DTI relies on the implementation of sophisticated bio-mechanical finite element (FE) models. The techniques' capability to provide 3D information of the muscle architecture may serve as the basis for the generation of individualized 3D bio-mechanical finite element (FE) models, which help to simulate contractile behavior realistically, and that can be used to obtain deeper insights into fatigue effects and damage aspects as well as to design prostheses or medical devices.

The second part of this work analyzed in great detail the effects of different *muscle functional MRI* (mfMRI) parameters in exercised human back muscles. In particular, the effects of the high-energy metabolite turnover and vascular volume fraction on load-induced T_2 changes in the low back muscles of young, healthy subjects were determined [HIEPE et al., 2014a]. To this end, quantitative T_2 -weighted MRI, ^{31}P -CSI and diffusion-weighted MRI (DWI) were combined during functional MRI investigations of back extensor muscles, which were loaded by using a dedicated MR-compatible ergometer. Despite some limitations regarding the number of study participants and the comparability between the separately determined parameters from the imaging and spectroscopic experiments, the proposed multi-parametric mfMRI approach enabled the examination of the combined metabolic and vascular effects on muscle T_2 . It was

demonstrated that exercise-induced T_2 increases strongly vary among subjects and that they are associated with changes in vascular volume fraction f and high-energy metabolite PCr as well as with the degree of perceived exertion (RPE). Overall, the results impressively suggest that T_2 - and perfusion-sensitive mfMRI based on DWI are able to identify and monitor important physiological changes during muscle fatigue with high spatial resolution. Additionally, the results underpin the validity of the applied set of MRI techniques and strengthen the evidence that these techniques, though rather complementary than competitive, can be used independently to assess muscle activity.

As a first attempt to understand the complex physiological interplay that takes place during muscle activation under normal conditions with respect to age, the proposed set of mfMRI techniques was applied to the back muscles of young and late-middle-aged healthy subjects [HIEPE et al., 2015]. The mfMRI protocol was extended by T_1 -weighted anatomic MRI, which provides information about muscle cross-sectional area (CSA) and fat infiltration. Significant age-related changes of CSA, fat infiltration, T_2 relaxation times, diffusibility (D), vascular volume fraction (f) and metabolic parameters (PCr, Pi, pH) were identified. These changes were attributed to atrophic processes, which result in a loss of contractile muscle tissue, decreased fiber size, reduced vascular capacity and modified fiber type composition. Interestingly, fat infiltration and vascular volume fraction (measured post-exercise) showed an inverse association, which was so far reported for the first time. The late-middle-aged group had reduced maximum force capacity of the back extensors (UBTR) compared to the young age group, which was linked to elevated fat infiltration limiting the vascular capacity and to atrophy of type II fibers rather than to changes of the back muscle volume. Although muscle quality was reduced, the older age group nevertheless showed statistically unchanged exercise-induced MR parameter changes (response factors) indicating maintained muscle endurance of moderately exercised low back muscles. In addition, both age groups yielded mfMRI response factors that were associated with RPE and correlated among each other supporting the hypothesis that T_2 changes in exercised skeletal muscle are closely linked to blood volume and metabolic changes.

Overall, investigation of physiological mechanisms influencing force capacity and endurance of skeletal muscles with respect to age provide deeper insights into muscle physiology. Furthermore, the data presented in this thesis may serve as basis for future research of muscle activation behavior under normal and patho-physiological conditions, such as in the field of non-specific low back pain. In addition, the proposed multi-parametric mfMRI can be used to support the implementation of bio-mechanical FE models in order to accurately simulate and investigate the processes of muscle fatigue and muscle failure. Finally, quantitation of muscle activation (patterns) may become increasingly important in clinical decision making to guide, e.g., exercise therapy interventions.

Bibliography

- [ABABNEH et al., 2008] ABABNEH, Z. Q., R. ABABNEH, S. E. MAIER, C. S. WINALSKI, K. OSHIO, A. M. ABABNEH and R. V. MULKERN (2008). *On the correlation between $T(2)$ and tissue diffusion coefficients in exercised muscle: quantitative measurements at 3T within the tibialis anterior*. *MAGMA*, 21(4):273–8.
- [ACKERMAN et al., 1980] ACKERMAN, J.J., T. GROVE, G. WONG, D. GADIAN and G. RADDA (1980). *Mapping of metabolites in whole animals by ^{31}P NMR using surface coils*. *Nature*, 283:167–70.
- [ANDERS et al., 2008] ANDERS, C., G. BROSE, G. O. HOFMANN and H. C. SCHOLLE (2008). *Evaluation of the EMG-force relationship of trunk muscles during whole body tilt*. *J Biomech*, 41(2):333–9.
- [ANDREOU et al., 2013] ANDREOU, A., D. M. KOH, D. J. COLLINS, M. BLACKLEDGE, T. WALLACE, M. O. LEACH and M. R. ORTON (2013). *Measurement reproducibility of perfusion fraction and pseudodiffusion coefficient derived by intravoxel incoherent motion diffusion-weighted MR imaging in normal liver and metastases*. *Eur Radiol*, 23(2):428–34.
- [AVANTS et al., 2008] AVANTS, B. B., C. L. EPSTEIN, M. GROSSMAN and J. C. GEE (2008). *Symmetric diffeomorphic image registration with cross-correlation: evaluating automated labeling of elderly and neurodegenerative brain*. *Med Image Anal*, 12(1):26–41.
- [BAMMER et al., 2009] BAMMER, R., S. J. HOLDSWORTH, W. B. VELDHUIS and S. T. SKARE (2009). *New methods in Diffusion Weighted and Diffusion Tensor Imaging*. *Magn Reson Imaging Clin N Am*, 17(2):175–204.
- [BARRETT et al., 2003] BARRETT, K. E., S. M. BARMAN, S. BOITANO and H. L. BROOKS (2003). *Excitable Tissue: Muscle*. In *Ganong's Review of Medical Physiology*, chap. 5, pp. 93–114. The McGraw-Hill Companies, Inc., 23 ed.
- [BASSER et al., 1994] BASSER, P. J., J. MATTIELLO and D. LEBIHAN (1994). *MR diffusion tensor spectroscopy and imaging*. *Biophys J*, 66(1):259–67.
- [BELTON et al., 1972] BELTON, P.S., R. JACKSON and K. PACKER (1972). *Pulsed NMR studies of water in striated muscle I. Transverse nuclear spin relaxation times and freezing effects*. *Biochim Biophys Acta*, 286(1):16–25.

- [BENDAHAN et al., 2004] BENDAHAN, D., B. GIANNESINI and P. J. COZZONE (2004). *Functional investigations of exercising muscle: a noninvasive magnetic resonance spectroscopy-magnetic resonance imaging approach*. Cell Mol Life Sci, 61(9):1001–15.
- [BERNSTEIN et al., 2004] BERNSTEIN, M. A., K. F. KING and X. J. ZHOU (2004). *Handbook of MRI Pulse Sequences*. Elsevier, Academic Press London.
- [BIERING-SORENSEN, 1984] BIERING-SORENSEN, F. (1984). *Physical measurements as risk indicators for low-back trouble over a one-year period*. Spine (Phila Pa 1976), 9(2):106–19.
- [BLEMKER et al., 2007] BLEMKER, S. S., D. S. ASAKAWA, G. E. GOLD and S. L. DELP (2007). *Image-based musculoskeletal modeling: Applications, advances, and future opportunities*. J Magn Reson Imaging, 25(2):441–51.
- [BLOCH, 1946] BLOCH, F. (1946). *Nuclear Induction*. Physical Review, 70(7):460–474.
- [BLOCK et al., 2007] BLOCK, K. T., M. UECKER and J. FRAHM (2007). *Undersampled radial MRI with multiple coils. Iterative image reconstruction using a total variation constraint*. Magn Reson Med, 57(6):1086–98.
- [BOESCH, 2007] BOESCH, C. (2007). *Musculoskeletal spectroscopy*. J Magn Reson Imaging, 25(2):321–338.
- [BOGNER et al., 2009] BOGNER, W., M. CHMELIK, A. I. SCHMID, E. MOSER, S. TRATTNIG and S. GRUBER (2009). *Assessment of $(31)P$ relaxation times in the human calf muscle: a comparison between 3 T and 7 T in vivo*. Magn Reson Med, 62(3):574–82.
- [BÖL et al., 2013] BÖL, M., K. LEICHSENRING, C. WEICHERT, M. STURMAT, P. SCHENK, R. BLICKHAN and T. SIEBERT (2013). *Three-dimensional surface geometries of the rabbit soleus muscle during contraction: input for biomechanical modelling and its validation*. Biomech Model Mechanobiol, 12(6):1205–20.
- [BÖL et al., 2011] BÖL, M., H. STARK and N. SCHILLING (2011). *On a phenomenological model for fatigue effects in skeletal muscles*. J Theor Biol, 281(1):122–32.
- [BORG, 1990] BORG, G. (1990). *Psychophysical scaling with applications in physical work and the perception of exertion*. Scand J Work Environ Health, 1:55–8.
- [BOSS et al., 2006] BOSS, A., P. MARTIROSIAN, C. CLAUSSEN and F. SCHICK (2006). *Quantitative ASL muscle perfusion imaging using a FAIR-TrueFISP technique at 3.0 T*. NMR Biomed, 19(1):125–32.
- [BRADLEY et al., 2010] BRADLEY, J., B. J. BEHNKE and M. D. DELP (2010). *Aging blunts the dynamics of vasodilation in isolated skeletal muscle resistance vessels*. J Appl Physiol, 108(1):14–20.

- [BROWN, 1828] BROWN, R. (1828). *A brief account of microscopical observations made in the months of June, July and August, 1827, on the particles contained in the pollen of plants; and on the general existence of active molecules in organic and inorganic bodies.* Phil Mag, 4:161–73.
- [BROWN et al., 1982] BROWN, T. R., B. M. KINCAID and K. UGURBIL (1982). *NMR chemical shift imaging in three dimensions.* Proc Natl Acad Sci, 79(11):3523–6.
- [BUDZIK et al., 2007] BUDZIK, J. F., V. LE THUC, X. DEMONDION, M. MOREL and A. CHECHIN, D. COTTEN (2007). *In vivo MR tractography of thigh muscles using diffusion imaging: initial results.* Eur Radiol, 17(12):3079–85.
- [BURSTEIN, 1996] BURSTEIN, DEBORAH (1996). *Stimulated Echoes: Description, Applications, Practical Hints.* Concepts Magn Reson, 8:269–278.
- [CALLOT et al., 2003] CALLOT, V., E. BENNETT, U. K. DECKING, R. S. BALABAN and H. WEN (2003). *In vivo study of microcirculation in canine myocardium using the IVIM method.* Magn Reson Med, 50(3):531–40.
- [CANNON et al., 2013] CANNON, D. T., F. A. HOWE, B. J. WHIPP, S. WARD, D. J. MCINTYRE, C. LADROUE, J. R. GRIFFITHS, G. J. KEMP and H. B. ROSSITER (2013). *Muscle metabolism and activation heterogeneity by combined ^{31}P chemical shift and T_2 imaging, and pulmonary O_2 uptake during incremental knee-extensor exercise.* J Appl Physiol, 115(6):839–49.
- [CARR and PURCELL, 1954] CARR, H. Y. and E. M. PURCELL (1954). *Effects of Diffusion on Free Precession in Nuclear Magnetic Resonance Experiments.* Physical Review, 94(3):630–8.
- [CETTOLO et al., 2006] CETTOLO, V., C. PIORICO, C. ATTINA and M. P. FRANCESCATO (2006). *Estimation of the phosphocreatine T_1 time constant using a clinical NMR scanner.* Radiol Med, 111(3):420–31.
- [CHAMPAGNE et al., 2009] CHAMPAGNE, A., M. DESCARREAU and D. LAFOND (2009). *Comparison between elderly and young males' lumbopelvic extensor muscle endurance assessed during a clinical isometric back extension test.* J Manipulative Physiol Ther, 32(7):521–6.
- [CHO et al., 2012] CHO, G. Y., S. KIM, J. H. JENSEN, P. STOREY, D. K. SODICKSON and E. E. SIGMUND (2012). *A versatile flow phantom for intravoxel incoherent motion MRI.* Magn Reson Med, 67(6):1710–20.
- [CLARK et al., 2009] CLARK, B. C., S. WALKOWSKI, R. R. CONATSER, D. C. ELAND and J. N. HOWELL (2009). *Muscle functional magnetic resonance imaging and acute low back pain: a pilot study to characterize lumbar muscle activity asymmetries and examine the effects of osteopathic manipulative treatment.* Osteopath Med Prim Care, 3:7.

- [CLEVELAND et al., 1976] CLEVELAND, G. G., D. C. CHANG, C. F. HAZLEWOOD and H. E. RORSCHACH (1976). *Nuclear magnetic resonance measurement of skeletal muscle: anisotropy of the diffusion coefficient of the intracellular water*. *Biophys J*, 16(9):1043–53.
- [CRANE et al., 2010] CRANE, J. D., M. C. DEVRIES, A. SAFDAR, M. J. HAMADEH and M. A. TARNOPOLSKY (2010). *The Effect of Aging on Human Skeletal Muscle Mitochondrial and Intramyocellular Lipid Ultrastructure*. *J Gerontol A Biol Sci Med Sci*, 65(2):199–128.
- [CSAPO et al., 2014] CSAPO, R., V. MALIS, U. SINHA, J. DU and S. SINHA (2014). *Age-Associated differences in triceps surae muscle composition and strength - an MRI-based cross-sectional comparison of contractile, adipose and connective tissue*. *BMC Musculoskeletal Disord*, 15:209.
- [DAMON et al., 2002a] DAMON, B. M., Z. DING, A. W. ANDERSON, A. S. FREYER and J. C. GORE (2002a). *Validation of diffusion tensor MRI-based muscle fiber tracking*. *Magn Reson Med*, 48(1):97–104.
- [DAMON and GORE, 2005] DAMON, B. M. and J. C. GORE (2005). *Physiological basis of muscle functional MRI: predictions using a computer model*. *J Appl Physiol*, 98(1):264–73.
- [DAMON et al., 2002b] DAMON, B. M., C. D. GREGORY, K. L. HALL, H. J. STARK, V. GULANI and M. J. DAWSON (2002b). *Intracellular acidification and volume increases explain $R(2)$ decreases in exercising muscle*. *Magn Reson Med*, 47(1):14–23.
- [DAMON et al., 2007] DAMON, B. M., J. L. HORNBERGER, M. C. WADINGTON, D. A. LANS-DOWN and J. A. KENT-BRAUN (2007). *Dual gradient-echo MRI of post-contraction changes in skeletal muscle blood volume and oxygenation*. *Magn Reson Med*, 57(4):670–9.
- [DAMON et al., 2013] DAMON, B. M., T. TOWSE, A. K. W. BUCK, K. LI, N. BRYANT, Z. DING and J. H. PARK (2013). *Quantitative structural and functional MRI of skeletal muscle*. In MUFTULER, L. T., ed.: *Quantifying Morphology and Physiology of the Human Body Using MRI*, chap. 7, pp. 209–34. CRC Press, Taylor & Francis Group.
- [DAMON et al., 2003] DAMON, B. M., D. M. WIGMORE, Z. DING, J. C. GORE and J. A. KENT-BRAUN (2003). *Cluster analysis of muscle functional MRI data*. *J Appl Physiol*, 95(3):1287–96.
- [DAWSON, 1982] DAWSON, M. J. (1982). *Quantitative analysis of metabolite levels in normal human subjects by 31P topical magnetic resonance*. *Biosci Rep*, 2(9):727–33.
- [DEUX et al., 2008] DEUX, J. F., P. MALZY, N. PARAGIOS, G. BASSEZ, A. LUCIANI, P. ZER-BIB, F. ROUDOT-THORAVALL, A. VIGNAUD, H. KOBEITER and A. RAHMOUNI (2008). *Assessment of calf muscle contraction by diffusion tensor imaging*. *Eur Radiol*, 18(10):2303–10.

- [D'HOOGHE et al., 2013] D'HOOGHE, R., B. CAGNIE, G. CROMBEZ, G. VANDERSTRAETEN, E. ACHTEN and L. DANNEELS (2013). *Lumbar muscle dysfunction during remission of unilateral recurrent nonspecific low- back pain: evaluation with muscle functional MRI*. Clin J Pain, 29(3):187–94.
- [D'HOOGHE et al., 2012] D'HOOGHE, R., B. CAGNIE, G. CROMBEZ, G. VANDERSTRAETEN, M. DOLPHENS and L. DANNEELS (2012). *Increased intramuscular fatty infiltration without differences in lumbar muscle cross-sectional area during remission of unilateral recurrent low back pain*. Man Ther, 17(6):584–8.
- [DICKX et al., 2010a] DICKX, N., B. CAGNIE, E. ACHTEN, P. VANDEMAELE, T. PARLEVLIEET and L. DANNEELS (2010a). *Differentiation between deep and superficial fibers of the lumbar multifidus by magnetic resonance imaging*. Eur Spine J, 19(1):122–8.
- [DICKX et al., 2010b] DICKX, N., R. D'HOOGHE, B. CAGNIE, E. DESCHEPPER, K. VERSTRAETE and L. DANNEELS (2010b). *Magnetic resonance imaging and electromyography to measure lumbar back muscle activity*. Spine (Phila Pa 1976), 35(17):836–42.
- [EINSTEIN, 1905] EINSTEIN, A. (1905). *Über die von der molekularkinetischen Theorie der Wärme geforderte Bewegung von in ruhenden Flüssigkeiten suspendierten Teilchen*. Ann Phys, 322(8):549–60.
- [FICK, 1855] FICK, A. E. (1855). *Über Diffusion*. Poggendorf's Annalen der Physik, 94:59–86.
- [FILLI et al., 2015] FILLI, L., A. BOSS, M. C. WURNIG, D. KENKEL, G. ANDREISEK and R. GUGGENBERGER (2015). *Dynamic intravoxel incoherent motion imaging of skeletal muscle at rest and after exercise*. NMR Biomed, 28(2):240–6.
- [FINSTERBUSCH and FRAHM, 2000] FINSTERBUSCH, J. and J. FRAHM (2000). *Diffusion tensor mapping of the human brain using single-shot line scan imaging*. J Magn Reson Imaging, 12(3):388–94.
- [FINSTERBUSCH and FRAHM, 2002] FINSTERBUSCH, J. and J. FRAHM (2002). *Half-Fourier single-shot STEAM MRI*. Magn Reson Med, 47(3):611–5.
- [FISCHER et al., 2013] FISCHER, M. A., D. NANZ, A. SHIMAKAWA, T. SCHIRMER, R. GUGGENBERGER, A. CHHABRA, J. A. CARRINO and G. ANDREISEK (2013). *Quantification of muscle fat in patients with low back pain: comparison of multi-echo MR imaging with single-voxel MR spectroscopy*. Radiology, 266(2):555–63.
- [FISHER et al., 1990] FISHER, M. J., R. A. MEYER, G. R. ADAMS, J. M. FOLEY and E. J. POTCHEN (1990). *Direct relationship between proton T2 and exercise intensity in skeletal muscle MR images*. Invest Radiol, 25(5):480–5.

- [FLECKENSTEIN et al., 1988] FLECKENSTEIN, J. L., R. C. CANBY, R. W. PARKEY and R. M. PESHOCK (1988). *Acute effects of exercise on MR imaging of skeletal muscle in normal volunteers*. AJR Am J Roentgenol, 151(2):231–7.
- [FORBES et al., 2009] FORBES, S. C., J. M. SLADE, R. M. FRANCIS and R. A. MEYER (2009). *Comparison of oxidative capacity among leg muscles in humans using gated ^{31}P 2-D chemical shift imaging*. NMR Biomed, 22(10):1063–71.
- [FORNAGE, 2000] FORNAGE, B. D. (2000). *The case for ultrasound of muscles and tendons*. Semin Musculoskelet Radiol, 4(4):375–391.
- [FRAHM et al., 1986] FRAHM, J., A. HAASE and D. MATTHAEI (1986). *Rapid NMR imaging of dynamic processes using the FLASH technique*. Magn Reson Med, 3(2):321–7.
- [FROELING et al., 2012] FROELING, M., A. J. NEDERVEEN, D. F. HEIJTEL, A. LATASTER, C. BOS, K. NICOLAY, M. MAAS, M. R. DROST and G. J. STRIJKERS (2012). *Diffusion-tensor MRI reveals the complex muscle architecture of the human forearm*. J Magn Reson Imaging, 36(1):237–48.
- [FROUIN et al., 2006] FROUIN, F., S. DUTEIL, D. LESAGE, P. G. CARLIER, A. HERMENT and A. LEROY-WILLIG (2006). *An automated image-processing strategy to analyze dynamic arterial spin labeling perfusion studies. Application to human skeletal muscle under stress*. Magn Reson Imaging, 24(7):941–51.
- [GASTIN, 2001] GASTIN, P. B. (2001). *Energy system interaction and relative contribution during maximal exercise*. Sports Med, 31(10):725–41.
- [GONDIN et al., 2014] GONDIN, J., C. VILMEN, P. J. COZZONE, D. BENDAHAN and G. DUHAMEL (2014). *High-field (11.75T) multimodal MR imaging of exercising hindlimb mouse muscles using a non-invasive combined stimulation and force measurement device*. NMR Biomed, 27(8):870–9.
- [GOODPASTER et al., 2006] GOODPASTER, B. H., S. W. PARK, T. B. HARRIS, S. B. KRITCHEVSKY, M. NEVITT, A. V. SCHWARTZ, E. M. SIMONSICK, F. A. TYLAVSKY, M. VISSER and A. B. NEWMAN (2006). *The loss of skeletal muscle strength, mass, and quality in older adults: the health, aging and body composition study*. J Gerontol A Biol Sci Med Sci, 61(10):1059–64.
- [GRISWOLD et al., 2002] GRISWOLD, M. A., P. M. JAKOB, R. M. HEIDEMANN, M. NITTKA, V. JELLUS, J. WANG, B. KIEFER and A. HAASE (2002). *Generalized autocalibrating partially parallel acquisitions (GRAPPA)*. Magn Reson Med, 47(6):1202–10.
- [HAACKE et al., 1999] HAACKE, E. M., R. W. BROWN, M. R. THOMPSON and R. VENKATESAN (1999). *Magnetic Resonance Imaging - Physical Principles and Sequence Design*. John Wiley & Sons, Inc., 1 ed.

- [HAGBERG, 1981] HAGBERG, M. (1981). *Muscular endurance and surface electromyogram in isometric and dynamic exercise*. J Appl Physiol, 51(1):1–7.
- [HAHN, 1950] HAHN, E. L. (1950). *Spin Echoes*. Physical Review, 80(4):580–94.
- [HAHN et al., 2012] HAHN, K., S. PRIGARIN and K. M. HASAN (2012). *Fitting of two-tensor models without ad hoc assumptions to detect crossing fibers using clinical DWI data*. Magn Reson Imaging, 31(4):585–95.
- [HAHN et al., 2010] HAHN, K., S. PRIGARIN, K. RODENACKER and K. M. HASAN (2010). *Denoising for diffusion tensor imaging with low signal to noise ratios: method and monte carlo validation*. Int J Biomath Biostat, 1:63–81.
- [HAZLEWOOD et al., 1974] HAZLEWOOD, C. F., D. C. CHANG, B. L. NICHOLS and D. E. WOESSNER (1974). *Nuclear magnetic resonance transverse relaxation times of water protons in skeletal muscle*. Biophys J, 14(8):583–606.
- [HEBERT et al., 2014] HEBERT, J. J., P. KJAER, J. M. FRITZ and B. F. WALKER (2014). *The relationship of lumbar multifidus muscle morphology to previous, current, and future low back pain: a 9-year population-based prospective cohort study*. Spine (Phila Pa 1976), 39(17):1417–25.
- [HEEMSKERK et al., 2006] HEEMSKERK, A. M., M. R. DROST, G. S. VAN BOCHOVE, M. F. VAN OOSTERHOUT, K. NICOLAY and G. J. STRIJKERS (2006). *DTI-based assessment of ischemia-reperfusion in mouse skeletal muscle*. Magn Reson Med, 56(2):272–81.
- [HEEMSKERK et al., 2010] HEEMSKERK, A. M., T. K. SINHA, K. J. WILSON, Z. DING and B. M. DAMON (2010). *Repeatability of DTI-based skeletal muscle fiber tracking*. NMR Biomed, 23(3):294–303.
- [HEEMSKERK et al., 2007] HEEMSKERK, A. M., G. J. STRIJKERS, M. R. DROST, G. S. VAN BOCHOVE and K. NICOLAY (2007). *Skeletal muscle degeneration and regeneration after femoral artery ligation in mice: monitoring with diffusion MR imaging*. Radiology, 243(2):413–21.
- [HEEMSKERK et al., 2005] HEEMSKERK, A. M., G. J. STRIJKERS, A. VILANOVA, M. R. DROST and K. NICOLAY (2005). *Determination of mouse skeletal muscle architecture using three-dimensional diffusion tensor imaging*. Magn Reson Med, 53(6):1333–40.
- [HENKELMAN et al., 1994] HENKELMAN, R. M., J. J. NEIL and Q. S. XIANG (1994). *A quantitative interpretation of IVIM measurements of vascular perfusion in the rat brain*. Magn Reson Med, 32:464–9.
- [HIEPE et al., 2014a] HIEPE, P., A. GUSSEW, R. RZANNY, C. ANDERS, M. WALTHER, H.-C. SCHOLLE and J. R. REICHENBACH (2014a). *Interrelations of muscle functional MRI*,

- diffusion-weighted MRI and (31)P-MRS in exercised lower back muscles*. NMR Biomed, 27(8):958–70.
- [HIEPE et al., 2015] HIEPE, P., A. GUSSEW, R. RZANNY, E. KURZ, C. ANDERS, M. WALTHER, H.-C. SCHOLLE and J. R. REICHENBACH (2015). *Age-related structural and functional changes of low back muscles*. Exp Gerontol, 65:23–34.
- [HIEPE et al., 2014b] HIEPE, P., K.-H. HERRMANN, D. GÜLLMAR, C. ROS, T. SIEBERT, R. BLICKHAN, K. HAHN and J. R. REICHENBACH (2014b). *Fast low-angle shot diffusion tensor imaging with stimulated echo encoding in the muscle of rabbit shank*. NMR Biomed, 27(2):146–57.
- [HIEPE et al., 2011] HIEPE, P., K.-H. HERRMANN, C. ROS and J. R. REICHENBACH (2011). *Diffusion weighted inner volume imaging of lumbar disks based on turbo-STEAM acquisition*. Z Med Phys, 21(3):216–27.
- [HIEPE et al., 2014c] HIEPE, P., M. KRÄMER, A. GUSSEW and J. R. REICHENBACH (2014c). *Multi-component T2* mapping in the calf muscle during plantar flexion using a multi-echo radial GRE sequence*. Proc International Society for Magnetic Resonance in Medicine (ISMRM), 22:1222.
- [HOLL et al., 2008] HOLL, N., A. ECHANIZ-LAGUNA, G. BIERRY, M. MOHR, J. P. LOEFFLER, T. MOSER, J. L. DIETEMANN and S. KREMER (2008). *Diffusion-weighted MRI of denervated muscle: a clinical and experimental study*. Skeletal Radiol, 37(12):1111–7.
- [HOULT et al., 1974] HOULT, D. I., S. J. BUSBY, D. G. GADIAN, G. K. RADDA, R. E. RICHARDS and P. J. SEELEY (1974). *Observation of tissue metabolites using 31P nuclear magnetic resonance*. Nature, 252:285–7.
- [HOUTMAN et al., 2001] HOUTMAN, C. J., A. HEERSCHAP, M. J. ZWARTS and D. F. STEGEMAN (2001). *pH heterogeneity in tibial anterior muscle during isometric activity studied by (31)P-NMR spectroscopy*. J Appl Physiol, 91(1):191–200.
- [HU et al., 2008] HU, Y., H. B. LEUNG, W. W. LU and K. D. LUK (2008). *Histologic and electrophysiological changes of the paraspinal muscle after spinal fusion: an experimental study*. Spine (Phila Pa 1976), 33(13):1418–22.
- [HUXLEY, 1957] HUXLEY, H. E. (1957). *The double array of filaments in cross-striated muscle*. J Biophys Biochem Cytol, 3(5):631–48.
- [HUXLEY, 1969] HUXLEY, H. E. (1969). *The mechanism of muscular contraction*. Science, 164:1356–65.
- [ITO et al., 2010] ITO, D., E. TANAKA and S. YAMAMOTO (2010). *A novel constitutive model of skeletal muscle taking into account anisotropic damage*. J Mech Behav Biomed Mater, 3(1):85–93.

- [JACKSON et al., 2010] JACKSON, D. N., A. W. MOORE and S. S. SEGAL (2010). *Blunting of rapid onset vasodilatation and blood flow restriction in arterioles of exercising skeletal muscle with ageing in male mice*. J Physiol, 588:2269–82.
- [JEONG et al., 2006] JEONG, E. K., S. E. KIM, E. G. KHOLMOVSKI and D. L. PARKER (2006). *High-resolution DTI of a localized volume using 3D single-shot diffusion-weighted STimulated echo-planar imaging (3D ss-DWSTEPI)*. Magn Reson Med, 56(6):1173–81.
- [JIANG et al., 2002] JIANG, H., X. GOLAY, P. C. VAN ZIJL and S. MORI (2002). *Origin and minimization of residual motion-related artifacts in navigator-corrected segmented diffusion-weighted EPI of the human brain*. Magn Reson Med, 47(4):818–22.
- [JOLLIFFE, 1986] JOLLIFFE, I. T. (1986). *Principal component analysis (Vol. 487)*. New York: Springer-Verlag.
- [JONES and BASSER, 2004] JONES, D. K. and P. J. BASSER (2004). *Squashing peanuts and smashing pumpkins: how noise distorts diffusion-weighted MR data*. Magn Reson Med, 52(5):979–93.
- [JONES et al., 2013] JONES, G. E., D. A. KUMBHARE, S. HARISH and M. D. NOSEWORTHY (2013). *Quantitative DTI assessment in human lumbar stabilization muscles at 3 T*. J Comput Assist Tomogr, 37(1):98–104.
- [JORGENSEN et al., 1993] JORGENSEN, K., C. MAG, T. NICOLAISEN and M. KATO (1993). *Muscle fiber distribution, capillary density and enzymatic activities in the lumbar paravertebral muscles of young men*. Spine, 18(11):1439–50.
- [KAN et al., 2009] KAN, J. H., A. M. HEEMSKERK, Z. DING, A. GREGORY, G. MENCIO, K. SPINDLER and B. M. DAMON (2009). *DTI-based muscle fiber tracking of the quadriceps mechanism in lateral patellar dislocation*. J Magn Reson Imaging, 29(3):663–70.
- [KARAMPINOS et al., 2012] KARAMPINOS, D. C., S. BANERJEE, K. F. KING, T. M. LINK and S. MAJUMDAR (2012). *Considerations in high-resolution skeletal muscle diffusion tensor imaging using single-shot echo planar imaging with stimulated-echo preparation and sensitivity encoding*. NMR Biomed, 25(5):766–78.
- [KARAMPINOS et al., 2009] KARAMPINOS, D. C., K. F. KING, B. P. SUTTON and J. G. GEORGIADIS (2009). *Myofiber ellipticity as an explanation for transverse asymmetry of skeletal muscle diffusion MRI in vivo signal*. Ann Biomed Eng, 37(12):2532–46.
- [KARAMPINOS et al., 2010] KARAMPINOS, D. C., K. F. KING, B. P. SUTTON and J. G. GEORGIADIS (2010). *Intravoxel partially coherent motion technique: characterization of the anisotropy of skeletal muscle microvasculature*. J Magn Reson Imaging, 31(4):942–53.

- [KEMP et al., 2007] KEMP, G. J., M. MEYERSPEER and E. MOSER (2007). *Absolute quantification of phosphorus metabolite concentrations in human muscle in vivo by ^{31}P MRS: a quantitative review*. NMR Biomed, 20(6):555–65.
- [KENNAN et al., 1994] KENNAN, R. P., J. H. GAO, J. ZHONG and J. C. GORE (1994). *A general model of microcirculatory blood flow effects in gradient sensitized MRI*. Med Phys, 21(4):539–45.
- [KHALIL et al., 2010] KHALIL, C., J. F. BUDZIK, E. KERMARREC, V. BALBI, V. LE THUC and A. COTTEN (2010). *Tractography of peripheral nerves and skeletal muscles*. Eur J Radiol, 76(3):391–7.
- [KIM et al., 2006] KIM, K. T., S. H. LEE, K. S. SUK and S. C. BAE (2006). *The quantitative analysis of tissue injury markers after mini-open lumbar fusion*. Spine (Phila Pa 1976), 31(6):712–6.
- [KIM et al., 2005] KIM, S., G. CHI-FISHMAN, A. S. BARNETT and C. PIERPAOLI (2005). *Dependence on diffusion time of apparent diffusion tensor of ex vivo calf tongue and heart*. Magn Reson Med, 54(6):1387–96.
- [KJAER et al., 2007] KJAER, P., T. BENDIX, J. S. SORENSEN, L. KORSHOLM and C. LEBOEUF-YDE (2007). *Intravoxel partially coherent motion technique: characterization of the anisotropy of skeletal muscle microvasculature*. BMC Med, 5(2):1–10.
- [KORHONEN et al., 2006] KORHONEN, M. T., A. CRISTEA, M. ALEN, K. HAKKINEN, S. SIPILA, A. MERO, J. T. VIITASALO, L. LARSSON and H. SUOMINEN (2006). *Aging, muscle fiber type, and contractile function in sprint-trained athletes*. J Appl Physiol, 101(3):906–17.
- [KRÄMER et al., 2012] KRÄMER, M., T. H. JOCHIMSEN and J. R. REICHENBACH (2012). *Functional magnetic resonance imaging using PROPELLER-EPI*. Magn Reson Med, 68(1):140–51.
- [KREULEN and SMEULDERS, 2008] KREULEN, M. and M. J. SMEULDERS (2008). *Assessment of flexor carpi ulnaris function for tendon transfer surgery*. J Biomech, 41(10):2130–5.
- [KRIX et al., 2010] KRIX, M., M. A. WEBER, H. U. KAUCZOR, S. DELORME and H. KRAKOWSKI-ROOSEN (2010). *Changes in the micro-circulation of skeletal muscle due to varied isometric exercise assessed by contrast-enhanced ultrasound*. Eur J Radiol, 76(1):110–16.
- [KUNG et al., 2011] KUNG, G. L., T. C. NGUYEN, A. ITOH, S. SKARE, N. B. INGELS JR, D. C. MILLER and D. B. ENNIS (2011). *The presence of two local myocardial sheet populations confirmed by diffusion tensor MRI and histological validation*. J Magn Reson Imaging, 34(5):1080–91.

- [KUNO et al., 1988] KUNO, S., S. KATSUTA, T. INOUE, I. ANNO, K. MATSUMOTO and M. AKISADA (1988). *Relationship between MR relaxation time and muscle fiber composition*. Radiology, 169(2):567–8.
- [KURZ et al., 2014] KURZ, E., C. ANDERS, M. WALTHER, P. SCHENK and H. C. SCHOLLE (2014). *Force Capacity of Back Extensor Muscles in Healthy Males - Effects of Age and Recovery Time*. J Appl Biomech, 30(6):713–21.
- [LANSDOWN et al., 2007] LANSDOWN, D. A., Z. DING, M. WADINGTON, J. L. HORNBERGER and B. M. DAMON (2007). *Quantitative diffusion tensor MRI-based fiber tracking of human skeletal muscle*. J Appl Physiol, 103(2):673–81.
- [LAUTERBUR, 1973] LAUTERBUR, P. C. (1973). *Image formation by induced local interactions. Examples employing nuclear magnetic resonance*. Nature, 242:190–1.
- [LE BIHAN, 2008] LE BIHAN, D. (2008). *Intravoxel Incoherent Motion Perfusion MR Imaging: A Wake-Up Call*. Radiology, 249(3):748–52.
- [LE BIHAN and BRETON, 1985] LE BIHAN, D. and E. BRETON (1985). *Imagerie de diffusion in vivo par resonance magnetique nucleaire*. C R Acad Sci Paris, 301:1109–12.
- [LE BIHAN et al., 1988] LE BIHAN, D., E. BRETON, D. LALLEMAND, M.-L. AUBIN, J. VIGNAUD and M. LAVAL-JEANTET (1988). *Separation of Diffusion and Perfusion in Intravoxel Incoherent Motion MR Imaging*. Radiology, 168(2):497–505.
- [LE BIHAN et al., 1986] LE BIHAN, D., E. BRETON, D. LALLEMAND, P. GRENIER, E. CABANIS and M. LAVAL-JEANTET (1986). *MR Imaging of Intravoxel Incoherent Motions: Application to Diffusion and Perfusion in Neurologic Disorders*. Radiology, 161(2):401–7.
- [LEMKE et al., 2009] LEMKE, A., F. B. LAUN, M. KLAU, T. J. RE, D. SIMON, S. DELORME, L. R. SCHAD and B. STIELTJES (2009). *Differentiation of pancreas carcinoma from healthy pancreatic tissue using multiple b-values: comparison of apparent diffusion coefficient and intravoxel incoherent motion derived parameters*. Invest Radiol, 44(12):769–75.
- [LEMKE et al., 2011] LEMKE, A., B. STIELTJES, L. R. SCHAD and F. B. LAUN (2011). *Toward an optimal distribution of b values for intravoxel incoherent motion imaging*. Magn Reson Imaging, 29(6):766–76.
- [LIEBER and BLEVINS, 2000] LIEBER, R.L. and F. T. BLEVINS (2000). *Skeletal muscle architecture of the rabbit hindlimb: functional implications of muscle design*. J Morphol, 199(1):93–101.
- [LIEBER and FRIDEN, 2000] LIEBER, R.L. and J. FRIDEN (2000). *Functional and clinical significance of skeletal muscle architecture*. Muscle Nerve, 23(11):1647–66.

- [LOUIE et al., 2009] LOUIE, E.A., D. GOCHBERG, M. DOES and B. DAMON (2009). *Transverse relaxation and magnetization transfer in skeletal muscle: effect of pH*. Magn Reson Med, 61(3):560–69.
- [LUCIANI et al., 2008] LUCIANI, A., A. VIGNAUD, M. CAVET, J. TRAN VAN NHIEU, A. MALLAT, L. RUEL, A. LAURENT, J.-F. DEUX, P. BRUGIERES and A. RAHMOUNI (2008). *Liver cirrhosis: intravoxel incoherent motion MR imaging - pilot study*. Radiology, 249(3):891–9.
- [MADHU et al., 1996] MADHU, B., K. LAGERWALL and B. SOUSSI (1996). *Phosphorus metabolites in different muscles of the rat leg by ^{31}P image-selected in vivo spectroscopy*. NMR Biomed, 9(8):327–32.
- [MAIER et al., 2003] MAIER, C. F., S. G. TAN, H. HARIHARAN and H. G. POTTER (2003). *T2 quantitation of articular cartilage at 1.5 T*. J Magn Reson Imaging, 17(3):358–64.
- [MANJON et al., 2013] MANJON, J. V., P. COUPE, L. CONCHA, A. BUADES, D. L. COLLINS and M. ROBLES (2013). *Diffusion weighted image denoising using overcomplete local PCA*. PLoS One, 8(9):e73021.
- [MANJON et al., 2009] MANJON, J. V., N. A. THACKER, J. J. LULL, G. GARCIA-MARTI, L. MARTI-BONMATI and M. ROBLES (2009). *Multicomponent MR Image Denoising*. Int J Biomed Imaging, 2009:756897.
- [MANSFIELD and GRANNELL, 1973] MANSFIELD, P. and P. K. GRANNELL (1973). *NMR Diffraction in Solids*. J Phys C Solid State, 6(22):422–26.
- [MARSCHAR et al., 2015] MARSCHAR, A. M., T. A. KUDER, B. STIELTJES, A. M. NAGEL, P. BACHERT and F. B. LAUN (2015). *In vivo imaging of the time-dependent apparent diffusional kurtosis in the human calf muscle*. J Magn Reson Imaging, 41(6):1581–90.
- [MATHIEU-COSTELLO, 1987] MATHIEU-COSTELLO, O. (1987). *Capillary tortuosity and degree of contraction or extension of skeletal muscle*. Microvasc Res, 33(1):98–117.
- [MAYER et al., 2005] MAYER, J. M., J. E. GRAVES, B. C. CLARK, M. FORMIKELL and L. PLOUTZ-SNYDER L (2005). *The use of magnetic resonance imaging to evaluate lumbar muscle activity during trunk extension exercise at varying intensities*. Spine (Phila Pa 1976), 30(22):2556–63.
- [MCMILLAN et al., 2011] MCMILLAN, A. B., D. SHI, S. J. PRATT and R. M. LOVERING (2011). *Diffusion tensor MRI to assess damage in healthy and dystrophic skeletal muscle after lengthening contractions*. J Biomed Biotechnol, 2011:970726.
- [MCVEIGH et al., 1999] MCVEIGH, G. E., C. W. BRATTELI, D. J. MORGAN, C. M. ALINDER, S. P. GLASSER, S. M. FINKELSTEIN and J. N. COHN (1999). *Age-related abnormalities in arterial compliance identified by pressure pulse contour analysis: aging and arterial compliance*. Hypertension, 33(6):1392–8.

- [MERBOLDT et al., 2000] MERBOLDT, K. D., J. FINSTERBUSCH and J. FRAHM (2000). *Reducing inhomogeneity artifacts in functional MRI of human brain activation-thin sections vs gradient compensation*. J Magn Reson, 145(2):184–91.
- [MERBOLDT et al., 1992] MERBOLDT, K. D., W. HÄNICKE, H. BRUHN, M. L. GYNGELL and J. FRAHM (1992). *Diffusion imaging of the human brain in vivo using high-speed STEAM MRI*. Magn Reson Med, 23(1):179–92.
- [MEYER and PRIOR, 2000] MEYER, R. A. and B. M. PRIOR (2000). *Functional magnetic resonance imaging of muscle*. Exerc Sport Sci Rev, 28(2):89–92.
- [MIN et al., 2009] MIN, S. H., M. H. KIM, J. B. SEO, J. Y. LEE and D. H. LEE (2009). *The quantitative analysis of back muscle degeneration after posterior lumbar fusion: comparison of minimally invasive and conventional open surgery*. Asian Spine J, 3(2):89–95.
- [MORI and BARKER, 1999] MORI, S. and P. B. BARKER (1999). *Diffusion magnetic resonance imaging: its principle and applications*. Anat Rec, 257(3):102–9.
- [MORI et al., 1999] MORI, S., B. J. CRAIN, V. P. CHACKO and P. C. VAN ZIJL (1999). *Three-dimensional tracking of axonal projections in the brain by magnetic resonance imaging*. Ann Neurol, 45(2):265–9.
- [MORVAN, 1995] MORVAN, D. (1995). *In vivo measurement of diffusion and pseudo-diffusion in skeletal muscle at rest and after exercise*. Magn Reson Imaging, 13(2):193–9.
- [MORVAN and LEROY-WILLIG, 1995] MORVAN, D. and A. LEROY-WILLIG (1995). *Simultaneous measurements of diffusion and transverse relaxation in exercising skeletal muscle*. Magn Reson Imaging, 13(7):943–8.
- [NAPADOW et al., 2001] NAPADOW, V. J., Q. CHEN, V. MAI, P. T. SO and R. J. GILBERT (2001). *Quantitative analysis of three-dimensional-resolved fiber architecture in heterogeneous skeletal muscle tissue using nmr and optical imaging methods*. Biophys J, 80(6):2968–75.
- [NEWCOMER and BOSKA, 1999] NEWCOMER, B. R. and M. D. BOSKA (1999). *T1 measurements of 31P metabolites in resting and exercising human gastrocnemius/ soleus muscle at 1.5 Tesla*. Magn Reson Med, 41(3):486–94.
- [NILWIK et al., 2013] NILWIK, R., T. SNIJDERS, M. LEENDERS, B. B. GROEN, J. VAN KRANENBURG, L. B. VERDIJK and L. J. VAN LOON (2013). *The decline in skeletal muscle mass with aging is mainly attributed to a reduction in type II muscle fiber size*. Exp Gerontol, 48(5):492–8.
- [NOEHREN et al., 2015] NOEHREN, B., A. ANDERSEN, T. FEIWEIER, B. DAMON and P. HARDY (2015). *Comparison of twice refocused spin echo versus stimulated echo diffusion tensor imaging for tracking muscle fibers*. J Magn Reson Imaging, 41(3):624–32.

- [NOLTE et al., 2000] NOLTE, U. G., J. FINSTERBUSCH and J. FRAHM (2000). *Rapid isotropic diffusion mapping without susceptibility artifacts: whole brain studies using diffusion-weighted single-shot STEAM MR imaging*. Magn Reson Med, 44(5):731–6.
- [NOSEWORTHY et al., 2003] NOSEWORTHY, M. D., D. P. BULTE and J. ALFONSI (2003). *BOLD magnetic resonance imaging of skeletal muscle*. Semin Musculoskelet Radiol, 7(4):307–15.
- [NOSEWORTHY et al., 2010] NOSEWORTHY, M. D., A. D. DAVIS and A. H. ELZIBAK (2010). *Advanced MR imaging techniques for skeletal muscle evaluation*. Semin Musculoskelet Radiol, 14:257–68.
- [OKAMOTO et al., 2012] OKAMOTO, Y., S. MORI, Y. KUJIRAOKA, K. NASU, Y. HIRANO and M. MINAMI (2012). *Diffusion property differences of the lower leg musculature between athletes and non-athletes using 1.5T MRI*. MAGMA, 25(4):277–84.
- [PANJABI, 2003] PANJABI, M. M. (2003). *Clinical spinal instability and low back pain*. J Electromyogr Kinesiol, 13(4):371–9.
- [PATTEN et al., 2003] PATTEN, C., R. A. MEYER and J. L. FLECKENSTEIN (2003). *T2 mapping of muscle*. Semin Musculoskelet Radiol, 7(4):297–305.
- [PEKAR et al., 1992] PEKAR, J., C. T. MOONEN and P. C. VAN ZIJL (1992). *On the precision of diffusion/perfusion imaging by gradient sensitization*. Magn Reson Med, 23(4):122–9.
- [PLOUTZ-SNYDER et al., 1997] PLOUTZ-SNYDER, L. L., S. NYREN, T. G. COOPER, E. J. POTCHEN and R. A. MEYER (1997). *Different effects of exercise and edema on T2 relaxation in skeletal muscle*. Magnetic Resonance in Medicine, 37(5):676–82.
- [PRUESSMANN et al., 1999] PRUESSMANN, K. P., M. WEIGER, M. B. SCHEIDEGGER and P. BOESIGER (1999). *SENSE: sensitivity encoding for fast MRI*. Magn Reson Med, 42(5):952–62.
- [PURCELL et al., 1946] PURCELL, E. M., H. C. TORREY and R. V. POUND (1946). *Resonance Absorption by Nuclear Magnetic Moments in a Solid*. Physical Review, 69(1-2):37–38.
- [QI et al., 2008] QI, J., N. J. OLSEN, R. R. PRICE, J. A. WINSTON and J. H. PARK (2008). *Diffusion weighted imaging of inflammatory myopathies: polymyositis and dermatomyositis*. J Magn Reson Imaging, 27(1):212–7.
- [REISER and SEMMLER, 2002] REISER, M. F. and W. SEMMLER (2002). *Basics of magnetic resonance imaging and magnetic resonance spectroscopy*. In *Magnetic resonance tomography*. Springer.

- [ROBSON et al., 2004] ROBSON, M. D., M. BENJAMIN, P. GISHEN and G. M. BYDDER (2004). *Magnetic resonance imaging of the Achilles tendon using ultrashort TE (UTE) pulse sequences*. *Clinical Radiology*, 59(8):727–35.
- [RÖHRLE, 2010] RÖHRLE, O. (2010). *Simulating the electro-mechanical behavior of skeletal muscles*. *Comput Sci Eng*, 12(6):48–58.
- [RÖHRLE et al., 2012a] RÖHRLE, O., J. B. DAVIDSON and A. J. PULLAN (2012a). *Bridging scales: a three dimensional electro-mechanical finite element model of skeletal muscle*. *SIAM J Sci Comput*, 30(6):2882–904.
- [RÖHRLE et al., 2012b] RÖHRLE, O., J. B. DAVIDSON and A. J. PULLAN (2012b). *A physiologically based, multi-scale model of skeletal muscle structure and function*. *Front Physiol*, 3:358.
- [ROSATELLI et al., 2008] ROSATELLI, A. L., K. RAVICHANDIRAN and A. M. AGUR (2008). *Three-dimensional study of the musculotendinous architecture of lumbar multifidus and its functional implications*. *Clin Anat*, 21:539–46.
- [ROUSSEL et al., 2003] ROUSSEL, M., J. MATTEI, Y. LE FUR, B. GHATTAS, P. COZZONE and D. BENDAHAN (2003). *Metabolic determinants of the onset of acidosis in exercising human muscle: a ³¹P-MRS study*. *J Appl Physiol*, 94(3):1145–52.
- [RYAN et al., 2006] RYAN, N. A., K. A. ZWETSLOOT, L. M. WESTERKAMP, R. C. HICKNER, W. E. POFAHL and T. P. GAVIN (2006). *Lower skeletal muscle capillarization and VEGF expression in aged vs. young men*. *J Appl Physiol*, 100(1):178–85.
- [RZANNY et al., 2006] RZANNY, R., R. GRASSME, J. R. REICHENBACH, H. C. SCHOLLE and W. A. KAISER (2006). *Investigations of back muscle fatigue by simultaneous ³¹P MRS and surface EMG measurements*. *Biomed Tech (Berl)*, 51(5-6):305–13.
- [RZANNY et al., 2016] RZANNY, R., N. STUTZIG, P. HIEPE, A. GUSSEW, H.-A. THORHAUER and J. R. REICHENBACH (2016). *The reproducibility of different metabolic markers for muscle fiber type distributions investigated by functional ³¹P-MRS during dynamic exercise*. *Z Med Phys*, 26(4):323–38.
- [SAAB et al., 2000] SAAB, G., R. T. THOMPSON and G. D. MARSH (2000). *Effects of exercise on muscle transverse relaxation determined by MR imaging and in vivo relaxometry*. *J Appl Physiol*, 88(1):226–33.
- [SCHEEL et al., 2013] SCHEEL, M., P. VON ROTH, T. WINKLER, A. ARAMPATZIS, T. PROKSCHA, B. HAMM and G. DIEDERICHS (2013). *Fiber type characterization in skeletal muscle by diffusion tensor imaging*. *NMR Biomed*, 26(10):1220–4.

- [SCHENK et al., 2013] SCHENK, P., T. SIEBERT, P. HIEPE, D. GÜLLMAR, J. R. REICHENBACH, C. WICK, R. BLICKHAN and M. BÖL (2013). *Determination of three-dimensional muscle architectures: validation of the DTI-based fiber tractography method by manual digitization*. J Anatomy, 223(1):61–8.
- [SCHEWZOW et al., 2015] SCHEWZOW, K., G. B. FIEDLER, M. MEYERSPEER, S. GOLUCH, E. LAISTLER, M. WOLZT, E. MOSER and A. I. SCHMID (2015). *Dynamic ASL and T2*-weighted MRI in exercising calf muscle at 7T: A feasibility study*. Magn Reson Med, 73(3):1190–5.
- [SCHMID et al., 2014] SCHMID, A. I., K. SCHEWZOW, G. B. FIEDLER, S. GOLUCH, E. LAISTLER, M. WOLZT, E. MOSER and M. MEYERSPEER (2014). *Exercising calf muscle T2* changes correlate with pH, PCr recovery and maximum oxidative phosphorylation*. NMR Biomed, 27(5):553–60.
- [SCHRAML et al., 2011] SCHRAML, C., N. F. SCHWENZER, P. MARTIROSIAN, C. D. CLAUSSEN and F. SCHICK (2011). *Temporal course of perfusion in human masseter muscle during isometric contraction assessed by arterial spin labeling at 3T*. Magn Reson Mater Phys Biol Med, 24(4):201–9.
- [SCHRODER et al., 2005] SCHRODER, L., C. SCHMITZ and P. BACHERT (2005). *Cumulative "roof effect" in high-resolution in vivo P-31 NMR spectra of human calf muscle and the Clebsch-Gordan coefficients of ATP at 1.5 T*. J Magn Reson, 174(1):68–77.
- [SCHWENZER et al., 2009] SCHWENZER, N. F., G. STEIDLE, P. MARTIROSIAN, C. SCHRAML, F. SPRINGER, C. D. CLAUSSEN and F. SCHICK (2009). *Diffusion tensor imaging of the human calf muscle: distinct changes in fractional anisotropy and mean diffusion due to passive muscle shortening and stretching*. NMR Biomed, 22(10):1047–53.
- [SIEBEN et al., 2016] SIEBEN, J. M., I. VAN OTTEN, A. LATASTER, M. FROELING, A. J. NEDERVEEN, G. J. STRIJKERS and M. R. DROST (2016). *In Vivo Reconstruction of Lumbar Erector Spinae Architecture Using Diffusion Tensor MRI*. J Spinal Disord Tech, 29(3):E139–45.
- [SIEBERT et al., 2012] SIEBERT, T., M. GÜNTHER and R. BLICKHAN (2012). *A 3D-geometric model for the deformation of a transversally loaded muscle*. J Theor Biol, 298:116–21.
- [SIEBERT et al., 2015] SIEBERT, T., K. LEICHSENRING, C. RODE, C. WICK, N. STUTZIG, H. SCHUBERT, R. BLICKHAN and M. BÖL (2015). *Three-Dimensional Muscle Architecture and Comprehensive Dynamic Properties of Rabbit Gastrocnemius, Plantaris and Soleus: Input for Simulation Studies*. PLoS One, 10(6):e0130985.
- [SIEBERT et al., 2014] SIEBERT, T., O. TILL and R. BLICKHAN (2014). *Work partitioning of transversally loaded muscle: Experimentation and simulation*. Comput Methods Biomech Biomed Eng, 17(3):217–29.

- [SIGMUND et al., 2014] SIGMUND, E. E., D. S. NOVIKOV, D. SUI, O. UKPEBOR, S. BAETE, J. S. BABB, K. LIU, T. FEIWEIER, J. KWON, K. MCGORTY, J. BENCARDINO and E. FIEREMANS (2014). *Time-dependent diffusion in skeletal muscle with the random permeable barrier model (RPBM): Application to normal controls and chronic exertional compartment syndrome patients*. NMR Biomed, 27(5):519–28.
- [SINHA and SINHA, 2011] SINHA, S. and U. SINHA (2011). *Reproducibility analysis of diffusion tensor indices and fiber architecture of human calf muscles in vivo at 1.5 Tesla in neutral and plantarflexed ankle positions at rest*. J Magn Reson Imaging, 34(1):107–19.
- [SINHA et al., 2015] SINHA, USHA, R. CSAPO, V. MALIS, Y. XUE and S. SINHA (2015). *Age-related differences in diffusion tensor indices and fiber architecture in the medial and lateral gastrocnemius*. Journal of Magnetic Resonance Imaging, 41(4):941–53.
- [SKALAK and SCHMID-SCHINBEIN, 1986] SKALAK, T. C. and G. W. SCHMID-SCHINBEIN (1986). *The microvasculature in skeletal muscle. A model of the capillary network*. Microvasc Res, 32(3):333–47.
- [SLADE et al., 2011] SLADE, J. M., T. F. TOWSE, V. GOSSAIN and R. A. MEYER (2011). *Peripheral microvascular response to muscle contraction is unaltered by early diabetes, but decreases with age*. J Appl Physiol, 111(5):1361–71.
- [SLED et al., 1998] SLED, J. G., A. P. ZIJDENBOS and A. C. EVANS (1998). *A nonparametric method for automatic correction of intensity nonuniformity in MRI data*. IEEE Trans Med Imaging, 17(1):87–97.
- [STAROSWIECKI et al., 2012] STAROSWIECKI, E., K. L. GRANLUND, M. T. ALLEY, G. E. GOLD and B. A. HARGREAVES (2012). *Simultaneous estimation of $T(2)$ and apparent diffusion coefficient in human articular cartilage in vivo with a modified three-dimensional double echo steady state (DESS) sequence at 3 T*. Magn Reson Med, 67(4):1086–96.
- [STEIDLE and SCHICK, 2006] STEIDLE, G. and F. SCHICK (2006). *Echoplanar diffusion tensor imaging of the lower leg musculature using eddy current nulled stimulated echo preparation*. Magn Reson Med, 55(3):541–8.
- [STEJSKAL and TANNER, 1965] STEJSKAL, E. O. and J. E. TANNER (1965). *Spin Diffusion Measurements: Spin Echoes in the Presence of a Time-Dependent Field Gradient*. The Journal of Chemical Physics, 42(1):288–92.
- [SUWA et al., 2000] SUWA, H., J. HANAKITA, N. OHSHITA, K. GOTOH, N. MATSUOKA and A. MORIZANE (2000). *Postoperative changes in paraspinal muscle thickness after various lumbar back surgery procedures*. Neurol Med Chir (Tokyo), 40:151–4.

- [TAWARA et al., 2009] TAWARA, N., O. NITTA, H. KURUMA, M. NIITSU, A. HOSHIKAWA, T. OKUWAKI and A. ITOH (2009). *Functional $T(2)$ mapping of the trunkal muscle*. Magn Reson Med Sci, 8(2):81–3.
- [TAWARA et al., 2011] TAWARA, N., O. NITTA, H. KURUMA, M. NIITSU and A. ITOH (2011). *$T2$ mapping of muscle activity using ultrafast imaging*. Magn Reson Med Sci, 10(2):85–91.
- [TAYLOR et al., 1986] TAYLOR, D. J., P. STYLES, P. M. MATTHEWS, D. A. ARNOLD, D. G. GADIAN, P. BORE and G. K. RADDI (1986). *Energetics of human muscle: exercise-induced ATP depletion*. Magn Reson Med, 3(1):44–54.
- [TORREY, 1956] TORREY, H. C. (1956). *Bloch Equations with Diffusion Terms*. Physical Review, 104(3):563–565.
- [TRIPLETT et al., 2014] TRIPLETT, W. T., C. BALIGAND, S. C. FORBES, R. J. WILLCOCKS, D. J. LOTT, S. DEVOS, J. POLLARO, W. D. ROONEY, H. L. SWEENEY, C. BÖNNEMANN, D.-J. WANG, K. VANDENBORNE and G. A. WALTER (2014). *Chemical shift-based MRI to measure fat fractions in dystrophic skeletal muscle*. Magn Reson Med, 72(1):8–19.
- [TSCHIESCHE et al., 2014] TSCHIESCHE, K., M. ROTHAMEL, R. RZANNY, A. GUSSEW, P. HIEPE and J. REICHENBACH (2014). *MR-compatible pedal ergometer for reproducible exercising of the human calf muscle*. Med Eng Phys, 36(7):933–7.
- [URSELL, 2011] URSELL, T. S. (2011). *The Diffusion Equation: A Multi-dimensional Tutorial*. Technical report, Department of Applied Physics, California Institute of Technology.
- [VAN DONKELAAR et al., 1999] VAN DONKELAAR, C. C., L. J. KRETZERS, P. H. BOVENDEERD, L. M. LATASTER, K. NICOLAY, J. D. JANSSEN and M. R. DROST (1999). *Diffusion tensor imaging in biomechanical studies of skeletal muscle function*. J Anat, 194(1):79–88.
- [VANDENBORNE et al., 2000] VANDENBORNE, K., G. WALTER, L. PLOUTZ-SNYDER, G. DUDLEY, M. A. ELLIOTT and K. DE MEIRLEIR (2000). *Relationship between muscle $T2^*$ relaxation properties and metabolic state: a combined localized $31P$ -spectroscopy and $1H$ -imaging study*. Eur J Appl Physiol., 82(1-2):76–82.
- [VANHAMME et al., 1997] VANHAMME, L., A. VAN DEN BOOGAART and S. VAN HUFFEL (1997). *Improved method for accurate and efficient quantification of MRS data with use of prior knowledge*. J Magn Reson, 129(1):35–43.
- [WACKER et al., 2002] WACKER, C. M., F. WIESMANN, M. BOCK, P. JAKOB, J. J. SANDSTEDDE, A. LEHNING, G. ERTL, L. R. SHAD, A. HAASE and W. R. BAUER (2002). *Determination of regional blood volume and intra-extracapillary water exchange in human myocardium using Feruglose: first clinical results in patients with coronary artery disease*. Magn Reson Med, 47(5):1013–6.

- [WETSCHEREK et al., 2015] WETSCHEREK, A., B. STIELTJES and F. B. LAUN (2015). *Flow-compensated intravoxel incoherent motion diffusion imaging*. *Magn Reson Med*, 74(2):410–9.
- [WRAY et al., 2009] WRAY, D.W., S. NISHIYAMA, A. MONNET, C. WARY, S. DUTEIL, P. CARLIER and R. RICHARDSON (2009). *Multiparametric NMR-based assessment of skeletal muscle perfusion and metabolism during exercise in elderly persons: preliminary findings*. *J Gerontol A Biol Sci Med Sci*, 64(9):968–74.
- [WU et al., 2011] WU, Y., L. J. ZHANG, C. ZOU, H. F. TSE and E. X. WU (2011). *Transmural heterogeneity of left ventricular myocardium remodeling in postinfarct porcine model revealed by MR diffusion tensor imaging*. *J Magn Reson Imaging*, 34(1):43–9.
- [YANAGISAWA et al., 2009] YANAGISAWA, O., D. SHIMAO, K. MARUYAMA, M. NIELSEN, T. IRIE and M. NIITSU (2009). *Diffusion-weighted magnetic resonance imaging of human skeletal muscles: gender-, age- and muscle-related differences in apparent diffusion coefficient*. *Magn Reson Imaging*, 27(1):69–78.
- [YASSIERLI et al., 2007] YASSIERLI, M. A. NUSSBAUM, H. IRIDIASTAD and L. A. WOJCIK (2007). *The influence of age on isometric endurance and fatigue is muscle dependent: a study of shoulder abduction and torso extension*. *Ergonomics*, 50(1):26–45.
- [YOUNG et al., 2015] YOUNG, H. J., N. T. JENKINS, Q. ZHAO and K. K. MCCULLY (2015). *Measurement of Intramuscular Fat by Muscle Echo Intensity*. *Muscle Nerve*, 52(6):963–71.
- [ZARAIKAYA et al., 2006] ZARAIKAYA, T., D. KUMBHARE and M. D. NOSEWORTHY (2006). *Diffusion tensor imaging in evaluation of human skeletal muscle injury*. *J Magn Reson Imaging*, 24(2):402–8.
- [ZHANG et al., 2008] ZHANG, J., G. ZHANG, B. MORRISON, S. MORI and K. A. SHEIKH (2008). *Magnetic resonance imaging of mouse skeletal muscle to measure denervation atrophy*. *Exp Neurol*, 212(2):448–57.
- [ZHANG et al., 2010] ZHANG, J. L., E. E. SIGMUND, H. CHANDARANA, H. RUSINEK, Q. CHEN, P. H. VIVIER, B. TAOULI and V. S. LEE (2010). *Variability of renal apparent diffusion coefficients: limitations of the monoexponential model for diffusion quantification*. *Radiology*, 254(3):783–92.
- [ZÖLLNER et al., 2012] ZÖLLNER, A. M., O. J. ABILEZ, M. BÖL and E. KUHL (2012). *Stretching skeletal muscle: chronic muscle lengthening through sarcomerogenesis*. *PLoS One*, 7(10):e45661.

List of Figures

2.1	Hierarchical organization of skeletal muscles	6
2.2	Relative contributions of different energy systems to the total energy supply . .	7
2.3	FID signal and its Fourier spectrum	13
2.4	Slice-selective rf excitation	14
2.5	Schematic illustration of frequency encoding	15
2.6	MR image reconstruction based on k -space data	17
2.7	Brownian motion and Gaussian distribution of diffusing particles	18
2.8	Rf pulse scheme of the spin-echo sequence	20
2.9	PGSE sequence based on Stejskal Tanner method	22
3.1	Schematic illustration of the diffusion tensor and the fiber tracking method . .	25
3.2	Fascicle orientations in parallel and pennate muscles	27
3.3	Signal attenuation curves and FA as function of the diffusion time	28
3.4	Rf pulse and gradient diagram of the turbo-STEAM DTI sequence	30
3.5	Signal difference between STEAM and SE depended on diffusion and echo time	30
3.6	Simplified vector diagram describing the formation of a stimulated echo	31
3.7	Fiber tracking based on combined anatomic MRI and turbo-STEAM DTI	34
3.8	Experimental set-up DTI measurements in a rabbit shank	35
3.9	T_2 -weighted high-resolution images of a rabbit's shank	38
3.10	Native turbo-STEAM DTI of a rabbit shank and motion artifact analysis	39
3.11	DW turbo-STEAM images and DTI maps based on raw and denoised data	40
3.12	DW turbo-STEAM images and DTI maps based on raw and denoised data	42
3.13	Fiber tracking results based on turbo-STEAM DTI of the rabbit's hind leg	42
3.14	Evaluation of reconstructed fiber tracts for the SOL and GM muscles	43
3.15	Simulated evolution of the STEAM magnetization during FLASH readout	45
3.16	Anatomical preparation and digitization of a histologically fixed muscle	49
3.17	DW images of fixed vertebrae bodies pre and post-filtering	53
3.18	MRI and FA values of patients after lumbar trauma and healthy controls	54
3.19	Photograph and fiber tracts of lumbar muscles	55
4.1	Non-localized ^{31}P -MR spectrum of resting human calf muscles	64
4.2	Dynamic ^{31}P -MRS in human calf muscles	67
4.3	Localized ^{31}P -MRS using CSI in the back	69

4.4	Pulse timing diagram of a FSE-MRI sequence	74
4.5	Pulse timing diagram of the SE-EPI sequence	75
4.6	T_2 -weighted MR images of the human calf acquired pre- and post-exercise	77
4.7	Reconstructed T_2 maps of exercised calf muscles	78
4.8	Biological models assumed by the IVIM theory	80
4.9	DWI signal attenuation curve as function of the diffusion weighting	81
4.10	DWI signal attenuation curves obtained in exercised calf muscle	84
4.11	Approximation error of mono-exponential IVIM fitting	85
4.12	Reconstructed D and f maps of exercised calf muscles	86
4.13	Noise reduction of simulated signal attenuation curves by PCA	88
4.14	Noise reduction by PCA depended of the b-value array and the patch size	89
4.15	Reconstructed D and f maps of exercised calf muscles based on denoised data	90
4.16	Experimental set-up and MR examination protocol during low back muscle exercise	92
4.17	Position of the CSI and mfMRI slices	93
4.18	Mean time courses of normalized PCr and Pi levels in young subjects	98
4.19	Pre- and post-exercise T_2 maps and histograms	99
4.20	Pre- and post-exercise D and f maps	100
4.21	Combined relationship of PCr, perfusion fraction and T_2 changes	102
4.22	Voxel-wise comparison of pre- and post-exercise T_2 and f maps	108
4.23	Age-related differences of pre- and post-exercise mfMR parameters	112
4.24	Comparison of PCr and Pi time courses obtained in two age groups	114
4.25	Anatomic MR images and corresponding ROI-specific signal intensity distributions	117
4.26	Partial correlations between muscle strength and different MR parameters	118
4.27	Age-related changes in skeletal muscles based on a three-compartment model	122

List of Tables

2.1	List of isotopes that are relevant for NMR experiments	10
3.1	Mean values and SD of ADC, FA, λ_{1-3} , CP, θ and ϕ values	41
4.1	Metabolic quantities for the four lower back muscles (mean \pm SD).	97
4.2	MRI parameters obtained before and after muscle load (mean \pm SD).	101
4.3	Pearson correlation between mfMR parameters	101
4.4	Subject characteristics of two age groups	109
4.5	Extracted pre- and post-exercise mfMRI parameters (mean \pm SD).	113
4.6	Determined ^{31}P -MRS quantities during rest and load (mean \pm SD).	115
4.7	Determined p -values of mixed model effects on mfMRI/MRS response factors .	116
4.8	Structural parameters obtained via anatomic MRI analysis (mean \pm SD).	116

Curriculum Vitae

Name: Patrick Hiepe
Adresse: Brucknerstraße 12a
Wohnort: 88167 München
Geburtsdatum: 27.09.1984
Geburtsort: Gera
E-mail: phiepe@gmail.com

Schulbildung

1991–1995 4. Grundschule Gera
1995–2003 Goethe - Gymnasium, Rutheneum seit 1608

Wissenschaftlicher Werdegang

2004–2009 Studium
Dipl. Ing. (FH) der Biomedizintechnik
Fachhochschule Jena
07703 Jena

2010–2015 Wissenschaftlicher Mitarbeiter
Medical Physics Group
Institut für Diagnostische und Interventionelle Radiologie
Universitätsklinikum Jena

2012–2015 Doktorand am Institut für Biomedizinische Technik und Informatik
Technische Universität Ilmenau

Auszeichnungen

P. Hiepe. Gewinner des 1. Preises des Gorter-Award 2014 der Deutschen Sektion der International Society for Magnetic Resonance in Medicine für den Beitrag **Funktionelle Muskeluntersuchung mittels ^{31}P -MR-Spektroskopie, T_2 - und diffusionsgewichteter MR-Bildgebung**

P. Hiepe. Posterpreis auf der Tagung 19. Erfurter Tage 2012 für den Beitrag **^{31}P -MR-Spektroskopie zur Messung metabolischer Änderungen in der Rückenmuskulatur bei selbst kontrollierter, isometrischer Belastung**

Original Papers

P. Hiepe, A. Gussew, R. Rzanny, E. Kurz, C. Anders, M. Walther, H.-C. Scholle, J. R. Reichenbach. **Age-related changes in muscle structure and activation during isometric back extension exercise.** *Exp Geront* 2015. 65:23-34

P. Hiepe, A. Gussew, R. Rzanny, C. Anders, M. Walther, H.-C. Scholle, J. R. Reichenbach. **Interrelations of muscle functional MRI, diffusion-weighted MRI and ^{31}P -MRS in exercised lower back muscles.** *NMR Biomed* 2014. 27(8):958-70.

P. Hiepe, K.-H. Herrmann, D. Güllmar, C. Ros, T. Siebert, R. Blickhan, K. Hahn, J. R. Reichenbach. **Fast low-angle shot diffusion tensor imaging with stimulated echo encoding in the muscle of rabbit shank.** *NMR Biomed* 2014. 27(2):146-57.

P. Hiepe, K.-H. Herrmann, C. Ros, J. R. Reichenbach. **Diffusion weighted inner volume imaging of lumbar disks based on turbo-STEAM acquisition.** *Z Med Phys* 2011. 21(3):216-27.

Conference Proceedings

P. Hiepe, A. Gussew, R. Rzanny, C. Anders, M. Walther, H.-C. Scholle, J. R. Reichenbach. **Funktionelle Muskeluntersuchung mittels ^{31}P -MR-Spektroskopie, T_2 - und diffusionsgewichteter MR-Bildgebung.** Tagungsband der Deutschen Sektion der International Society for Magnetic Resonance in Medicine, vol. 17, 2014, G1

P. Hiepe, A. Gussew, R. Rzanny, J. R. Reichenbach. **Quantitative T_2^* -gewichtete MR-Bildgebung und dynamische ^{31}P -MR-Spektroskopie in belasteter Rückenmuskulatur.** Tagungsband der Deutschen Sektion der International Society for Magnetic Resonance in Medicine, vol. 17, 2014, P6

P. Hiepe, A. Gussew, R. Rzanny, H.-C. Scholle, J. R. Reichenbach. **Age-related changes in muscle structure and fatigue.** Beitragsband des Workshop Molekulare Bildgebung 2014 des Interdisziplinären Netzwerkes Molekulare Bildgebung (INMB), 2014, L19

P. Hiepe, Krämer M, A. Gussew, J. R. Reichenbach. **Multi-component T_2^* mapping in the calf muscle during plantar flexion using a multi-echo radial GRE sequence.** Proceedings of the International Society for Magnetic Resonance in Medicine, vol. 22, 2014, 1222

P. Hiepe, A. Gussew, R. Rzanny, J. R. Reichenbach. **Functional T_2 measurements in lower back muscles before and after isometric muscle contraction.** Proceedings of the International Society for Magnetic Resonance in Medicine, vol. 21, 2013, 3512

P. Hiepe, A. Gussew, R. Rzanny, J. R. Reichenbach. **Functional ^{31}P -MR chemical shift imaging in lower back muscles during isometric load.** Proceedings of the International Society for Magnetic Resonance in Medicine, vol. 21, 2013, 3505

P. Hiepe, Gllmar D, A. Gussew, R. Rzanny J. R. Reichenbach. **Improved IVIM image quantitation of exercised lower back muscles by principle component analysis.** Proceedings of the International Society for Magnetic Resonance in Medicine, vol. 21, 2013, 3491

P. Hiepe, R. Rzanny, A. Gussew, C. Anders, H.-C. Scholle, J. R. Reichenbach. **Functional diffusion weighted MRI for assessment of muscle fatigue in the lower back muscles.** Biomed Tech. 2012; 57, 512

P. Hiepe, R. Rzanny, A. Gussew, C. Anders, H.-C. Scholle, J. R. Reichenbach. **Functional T_2 weighted MRI for investigation of muscle fatigue in the lower back muscles.** Biomed Tech. 2012; 57, 511

P. Hiepe, D. Gllmar, C. Ros, T. Siebert, A. Gussew, R. Rzanny, J. R. Reichenbach. **Functional DTI in Voluntary Contracted Human Calf Muscles Using an MR Compatible Ergometer.** Proceedings of the International Society for Magnetic Resonance in Medicine, vol. 20, 2012, 578

P. Hiepe, D. Gllmar, K.-H. Herrmann, C. Kpper, T. Siebert, J. R. Reichenbach. ***In-vivo* Fiber-Tracking der Wadenmuskulatur von Kaninchen basierend auf diffusionsgewichteter STEAM-MR-Bildgebung.** Rfo - Fortschritte auf dem Gebiet der Rntgenstrahlen und der bildgebenden Verfahren, vol. 92, 2011

P. Hiepe, K.-H. Herrmann, C. Ros, J. R. Reichenbach. **Diffusionsgewichtete MR-Bildgebung lumbaler Bandscheiben mittels Inner-Volume-STEAM-Technik.** Rfo - Fortschritte auf dem Gebiet der Rntgenstrahlen und der bildgebenden Verfahren, vol. 92, 2011

P. Hiepe, D. Gllmar, K.-H. Herrmann, C. Kpper, T. Siebert, J. R. Reichenbach. ***In-vivo* Fiber Tractography of Muscle Anatomy in Rabbits based on turbo-STEAM DWI and long Diffusion Times.** Annual Meeting of the European Society for Magnetic Resonance in Medicine and Biology, vol. 28, 2011

P. Hiepe, R. Rzanny, A. Gussew, J. R. Reichenbach. **Longitudinal ^{31}P -MRS Study for Assessing the Distribution of Fiber Types in Human Calf Muscles.** Annual Meeting of the European Society for Magnetic Resonance in Medicine and Biology, vol. 28, 2011

P. Hiepe, J. R. Reichenbach. **Functional Muscle MRI in Human Calf Muscle using IVIM.** Proceedings of the International Society for Magnetic Resonance in Medicine, vol. 19, 2011

P. Hiepe, C. Ros, J. R. Reichenbach, K.-H. Herrmann. **Diffusion Weighted ZOOM Imaging in the Lumbar Spine Based on Single-Shot STEAM.** Tagungsband des World Congress on Medical Physics and Biomedical Engineering, vol. 11, 2009

P. Hiepe, K.-H. Herrmann, M. E. Bellemann, J. R. Reichenbach. **STEAM DWI: Erste *in-vitro* und *in-vivo* Ergebnisse bei unterschiedlichen Akquisitionsmodi.** Tagungsband der Jahrestagung der Deutschen Sektion der International Society for Magnetic Resonance in Medicine, vol. 11, 2008

Book Chapters

P. Hiepe, R. Rzanny, A. Gussew, C. Anders, H.-C. Scholle, J. R. Reichenbach. **Beiträge der funktionellen T_2 - und diffusionsgewichteten Magnetresonanz-Bildgebung zur Charakterisierung der Ermüdungsphysiologie der Rückenmuskulatur.** In: 18. Erfurter Tage 2011, Prävention von arbeitsbedingten Gesundheitsgefahren und Erkrankungen, Grieshaber R, Stadeler M, Scholle HC (Hrsg.), Verlag Bussert & Stadeler, Jena 2012, ISBN 978-3-942115-18-6:211-223

P. Hiepe, R. Rzanny, A. Gussew, C. Anders, H.-C. Scholle, J. R. Reichenbach. **Die Anwendung multimodaler Methoden der MR-Bildgebung und MR-Spektroskopie zur Bestimmung muskulärer Leistungsparameter in gesunden Probanden.** In: 19. Erfurter Tage 2012, Prävention von arbeitsbedingten Gesundheitsgefahren und Erkrankungen, Kirchner CJ, Stadeler M, Scholle HC (Hrsg.), Verlag Bussert & Stadeler, Jena 2013, ISBN 978-3-942115-25-4:341-356.

Ehrenwörtliche Erklärung

Ich versichere, dass ich die vorliegende Arbeit ohne unzulässige Hilfe Dritter und ohne Benutzung anderer als der angegebenen Hilfsmittel angefertigt habe. Die aus anderen Quellen direkt oder indirekt übernommenen Daten und Konzepte sind unter Angabe der Quelle gekennzeichnet. Bei der Auswahl und Auswertung folgenden Materials haben mir die nachstehend aufgeführten Personen in der jeweils beschriebenen Weise unentgeltlich geholfen:

1. *Unterstützung bei der Korrektur und Interpretation von ^{31}P -MR-Spektren*
Alexander Gussew, Dr.-Ing.
Medizinische Physik, Institut für Diagnostische und Interventionelle Radiologie
Universitätsklinikum Jena, Jena, Deutschland
2. *Unterstützung bei der Implementierung von DWI-Bildverarbeitungstechniken*
Daniel Güllmar, Dr.-Ing.
Medizinische Physik, Institut für Diagnostische und Interventionelle Radiologie
Universitätsklinikum Jena, Jena, Deutschland
3. *Unterstützung bei der Implementierung von DWI-STEAM-Sequenzen*
Karl-Heinz Herrmann, Dr.
Medizinische Physik, Institut für Diagnostische und Interventionelle Radiologie
Universitätsklinikum Jena, Jena, Deutschland
4. *Unterstützung bei der statistischen Analyse der Ergebnisse*
Mario Walther, Dr.
Institut für Medizinische Statistik, Informatik und Dokumentation (IMSID)
Universitätsklinikum Jena, Jena, Deutschland
5. *Unterstützung bei der Interpretation der Ergebnisse in der gesamten Arbeit*
Jürgen R. Reichenbach, Prof. Dr.
Medizinische Physik, Institut für Diagnostische und Interventionelle Radiologie
Universitätsklinikum Jena, Jena, Deutschland

Weitere Personen waren an der inhaltlich-materiellen Erstellung der vorliegenden Arbeit nicht beteiligt. Insbesondere habe ich hierfür nicht die entgeltliche Hilfe von Vermittlungs- bzw. Beratungsdiensten (Promotionsberater oder anderer Personen) in Anspruch genommen. Niemand hat von mir unmittelbar oder mittelbar geldwerte Leistungen für Arbeiten erhalten, die im Zusammenhang mit dem Inhalt der vorgelegten Dissertation stehen. Die Arbeit wurde bisher weder im In- noch im Ausland in gleicher oder ähnlicher Form einer Prüfungsbehörde vorgelegt. Weiterhin bin ich darauf hingewiesen worden, dass die Unrichtigkeit der vorstehenden Erklärung als Täuschungsversuch bewertet wird und gemäß §7 Abs. 10 der Promotionsordnung den Abbruch des Promotionsverfahrens zur Folge hat.

München, 2. Oktober 2017

Danksagung

Entgegen der üblichen Abfolge, möchte ich mich an erster Stelle herzlich bei meiner Mutter, Ute Hiepe, bedanken, die leider die Fertigstellung meiner Doktorarbeit nicht mehr erleben durfte. Sie lehrte mich schwierige Situationen im Leben zu meistern und dabei das Ziel nie aus den Augen zu verlieren.

Folgend möchte ich mich bei all jenen bedanken, die mir bei der Anfertigung dieser Dissertation geholfen und mich stets auf meinem Schaffensweg unterstützt haben. Ein ganz besonderer Dank gilt Herrn Prof. Dr. Jürgen R. Reichenbach aus dem Institut für Diagnostische und Interventionelle Radiologie der Friedrich-Schiller-Universität (Arbeitsgruppe Medizinische Physik), der mir die Anfertigung dieser Arbeit ermöglichte und mich stets mit großem Engagement unterstützte. Zusätzlich möchte ich meinem Kollegen Dr. Alexander Gussev für unseren stets konstruktiven sowie freundschaftlichen Austausch danken. Des Weiteren gebühren Prof. Dr.-Ing. Jens Haueisen (Fakultät für Informatik und Automatisierung, TU Ilmenau) und Prof. Dr. Hans-Christoph Scholle (Funktionsbereich Motorik, Pathophysiologie und Biomechanik, Universitätsklinikum Jena) ein großer Dank, da sie durch ihre Betreuung - respektive Organisation von Forschungsmitteln (Förderung durch die Berufsgenossenschaft Nahrungsmittel und Gastgewerbe) - einen unabdingbaren Beitrag zu dieser Promotionsarbeit geleistet haben.

Nachdem ich zu Beginn bereits meine Mutter erwähnte, möchte ich mich an dieser Stelle herzlich bei meinem Großvater, Gerhardt Fröhlich, sowie bei meiner Schwester, Nadja Hiepe, bedanken. Eure Unterstützung ist mir sehr viel wert und hat erheblich zum Gelingen dieser Arbeit beigetragen. Zum Abschluss möchte ich mich bei meinen Freunden und vor allem bei meiner Freundin, Melanie Schröpfer, bedanken. Ihr habt mich auch in Situationen großer Hindernisse stets ermuntert und, genau wie meine Familie, immer an mich geglaubt.

Patrick Hiepe
München im Februar 2017

